UNIVERSITAT POLITÈCNICA DE CATALUNYA
BARCELONATECH
Departament d'Enginyeria Electrònica

"AUTOMATIC SUPERVISION OF PV SYSTEMS AND DEGRADATION ANALYSIS OF THIN FILM PV MODULES"

Thesis submitted in partial fulfilment of the requirement for the PhD Degree issued by the Universitat Politècnica de Catalunya, in its Electronic Engineering Program.

Sofiane Kichou

Director: *Santiago Silvestre Berges*

January 2017

To my dear parents, brothers and sisters for their support...

Acknowledgment

First and foremost, I would like to express my utmost gratitude to my supervisor Prof. Santiago Silvestre Berges for his precious advices, help, support, and his excellent guidance during all my research period. He is one of the most exceptional persons I have ever known and I am proud to have worked with him. Besides my supervisor, I would like to express my gratitude to all the professors of the UPC I met and all co-authors for their information, help and encouragement (Aissa Chouder, Gustavo Nofuentes, Dani Guasch, …).

Next, I would like to thank all members of electronic engineering department for their amiability and help. I can't forget to thank all my colleagues and friends for their support and the good moments shared together (David, Dani, Didac, Chenna, ….).

Last but not the least, I would like to thank my parents for supporting me throughout all my life in general, my brothers and sisters. I express my wholehearted gratitude to my brother Hassane Baghdad for everything he did for me, without him nothing would be the same.

Thank you very much.

Abstract

Monitoring and regular performance analysis of Grid-Connected Photovoltaic (GCPV) systems are of primal importance in order to ensure an optimal energy harvesting and reliable power production at competitive costs. Main faults in GCPV systems are caused by short-circuits or open-circuits in PV modules, inverter disconnections, PV module degradation and the presence of shadows on the PV array plane. Detecting these faults can minimize generated losses by reducing the time in which the PV system is working below its optimum point of power generation. In addition, the degradation of Tin Film PV (TFPV) modules under outdoor exposure is still not fully understood and is currently object of research. A better understanding on this topic would be important for selecting the best PV technology for the appropriate climatic condition and for improving the reliability and performance of PV systems.

Simulations play a crucial role in both outdoor behaviour forecasting and automatic fault detection of GCPV systems. Two PV module/array models have been used in the present thesis in order to simulate the outputs of GCPV systems of different topologies and solar cell technologies, as well as in the fault detection procedure. Moreover, five different algorithms were used for estimating the unknown parameters of both PV models in order to see how these estimated parameters affect their accuracy in reproducing the outdoor behaviour of three GCPV systems. The obtained results show that the metaheuristic algorithms are more efficient than the Levenberg-Marquardt algorithm (LMA) especially in bad weather conditions and both PV models perform well when used in the automatic fault detection procedure.

A new approach for automatic supervision and remote fault detection of GCPV systems by means of OPC technology-based monitoring is presented in this thesis. The fault detection procedure used for the diagnosis of GCPV systems is based on the analysis of the current and voltage indicators evaluated also from monitored data and expected values of current and

voltage obtained from the model of the PV generator. Three GCPV systems having different sizes, topologies and cell technologies have been used for the experimental validation of the proposed fault detection method. The analysis of current and voltage indicators has demonstrated effectiveness in the detection of most probable faults occurred in the PV arrays in real time. Furthermore, obtained results show that the combination of OPC monitoring along with the proposed fault detection procedure is a robust tool which can be very useful in the field of remote supervision and diagnosis of GCPV systems.

Finally, the study of degradation issues of TFPV modules corresponding to four technologies: a-Si:H, a-Si:H/μc-Si:H, CIS and CdTe, deployed under outdoor conditions for long term exposure is also addressed in the present thesis. The impact of the degradation on the output power of the PV modules is analysed, in order to determine their annual degradation rate and their stabilization period. The degradation rate is obtained through a procedure based on the evolution of the module effective peak power over time. The stabilization period is evaluated by means of two methods: the evolution of DC-output power of the PV module, and the power-irradiance technique. The obtained results show that the CIS PV module is the most stable compared to the other technologies, when deployed under Continental-Mediterranean Climate. The a-Si:H and a-Si:H/μc-Si:H PV modules also perform quite well, showing degradation rates and stabilization periods similar to the expectations. The CdTe module shows poor performances, with the highest degradation rate, and long stabilization period of 32 months. Lastly, the parameter extraction technique has been also applied to analyse the evolution of model parameters for a-Si:H and a-Si:H/μc-Si:H arrays working in outdoor conditions for long term exposure.

Resumem

La monitorización y el seguimiento regular del comportamiento de los sistemas fotovoltaicos conectados a la red (SFCR) son de primordial importancia para asegurar una generación de energía óptima a costes competitivos. Los fallos principales en los SFCR son causados por cortocircuitos o circuitos abiertos en módulos fotovoltaicos, desconexiones de inversores, degradación de módulos fotovoltaicos y presencia de sombras en el plano del generador fotovoltaico. La detección de estos fallos puede minimizar las pérdidas generadas al reducir el tiempo en que el sistema fotovoltaico está funcionando por debajo de su punto óptimo de generación de energía. Por otro lado, la degradación de los módulos fotovoltaicos de capa delgada (TFPV) en condiciones reales de trabajo sigue siendo actualmente objeto de investigación. Una mejor comprensión de este tema es importante para seleccionar la tecnología fotovoltaica más adecuada para cada condición climática específica y mejorar así tanto la fiabilidad como el rendimiento de los sistemas fotovoltaicos.

Las simulaciones desempeñan un papel crucial tanto en el pronóstico del comportamiento real como en la detección automática de fallos en los SFCR. En la presente tesis se han utilizado dos modelos de módulos fotovoltaicos para simular las salidas de los sistemas de diferentes topologías y tecnologías de células solares, así como en el procedimiento de detección de fallos. Se han utilizado cinco algoritmos diferentes para estimar los parámetros de ambos modelos con el fin de ver cómo estos parámetros estimados afectan su precisión en la reproducción del comportamiento real de tres SFCR. Los resultados obtenidos muestran que los algoritmos meta-heurísticos son más eficientes que el algoritmo de Levenberg-Marquardt (LMA) especialmente en malas condiciones climáticas, aunque ambos modelos pueden ser utilizados para la supervisión y la detección automática de fallos.

En esta tesis se presenta un nuevo enfoque para la supervisión automática y la detección remota de fallos en SFCR mediante la monitorización basada en la tecnología OPC. El procedimiento de detección de fallos utilizado para el diagnóstico de SFCR se basa en el análisis de los indicadores de corriente y tensión evaluados también a partir de datos monitorizados y valores esperados de corriente y tensión obtenidos a partir del modelo del generador fotovoltaico. Se han utilizado tres SFCR de diferentes tamaños, topologías y tecnologías fotovoltaicas para la validación experimental del método de detección de fallos propuesto. El análisis de los indicadores de corriente y tensión ha demostrado efectividad en la detección de los fallos más probables en generadores fotovoltaicos en tiempo real. Además, los resultados obtenidos muestran que la combinación de monitorización OPC junto con el procedimiento de detección de fallos propuesto es una herramienta robusta que puede ser muy útil en el campo de la supervisión remota y el diagnóstico de SFCR.

Finalmente, en la presente tesis se aborda el estudio de los problemas de degradación de módulos fotovoltaicos de capa delgada correspondientes a cuatro tecnologías: a-Si:H, a-Si:H/μc-Si:H, CIS y CdTe, en condiciones de trabajo a la intemperie durante periodos prolongados de exposición. Se analiza el impacto de la degradación en la potencia de salida de los módulos fotovoltaicos para determinar su tasa de degradación anual y su período de estabilización. La tasa de degradación se obtiene a través de un procedimiento basado en la evolución de la potencia máxima efectiva del módulo a lo largo del periodo de exposición. El período de estabilización se evalúa mediante dos métodos: El estudio de la evolución de la potencia de salida del módulo fotovoltaico y la técnica de Potencia-Irradiancia. Los resultados obtenidos muestran que el módulo fotovoltaico CIS es el más estable comparado con las otras tecnologías, cuando trabajan en condiciones de clima continental mediterráneo. Los módulos fotovoltaicos a-Si:H y a-Si:H/μc-Si:H también presentan un buen comportamiento, mostrando tasas de degradación y períodos de estabilización similares a los esperados. El módulo de CdTe muestra las peores prestaciones, con una mayor tasa de degradación y un largo período de estabilización de 32 meses. Por último, se ha aplicado también la técnica de extracción de parámetros para analizar la evolución de los parámetros del modelo para generadores fotovoltaicos de módulos de a-Si: H y a-Si:H/μc-Si:H en condiciones reales de trabajo durante largos periodos de tiempo.

Resum

El monitoratge i el seguiment regular del comportament dels sistemes fotovoltaics connectats a la xarxa (SFCX) són de cabdal importància per assegurar una generació òptima d'energia a costos competitius. Les fallades principals en els SFCX són causats per curtcircuits o circuits oberts en mòduls fotovoltaics, desconnexions d'inversors, degradació de mòduls fotovoltaics i presència d'ombres en el pla del generador fotovoltaic. La detecció d'aquests errors pot minimitzar les pèrdues generades en reduir el temps en què el sistema fotovoltaic està funcionant per sota del seu punt òptim de generació d'energia. D'altra banda, la degradació dels mòduls fotovoltaics de capa prima (TFPV) en condicions reals de treball segueix sent actualment objecte d'investigació. Una millor comprensió d'aquest tema és important per seleccionar la tecnologia fotovoltaica més adequada per a cada condició climàtica específica i millorar així tant la fiabilitat com el rendiment dels sistemes fotovoltaics.

Les simulacions tenen un paper crucial tant en el pronòstic del comportament real com en la detecció automàtica de fallades en els SFCX. En la present tesi s'han utilitzat dos models de mòduls fotovoltaics per simular les sortides dels sistemes de diferents tipologies i tecnologies de cèl·lules solars, així com en el procediment de detecció de fallades. S'han utilitzat 5 algoritmes diferents per estimar els paràmetres de tots dos models per tal de veure com aquests paràmetres estimats afecten la seva precisió en la reproducció del comportament real de tres SFCX. Els resultats obtinguts mostren que els algoritmes meta-heurístics són més eficients que l'algorisme de Levenberg-Marquardt (LMA) especialment en males condicions climàtiques, encara que tots dos models poden ser utilitzats per a la supervisió i la detecció automàtica de fallades.

En aquesta tesi es presenta un nou enfocament per a la supervisió automàtica i la detecció remota de fallades en SFCX mitjançant el monitoratge basat en la tecnologia OPC. El

procediment de detecció de fallades utilitzat per al diagnòstic de SFCX es basa en l'anàlisi dels indicadors de corrent i tensió avaluats també a partir de dades monitoritzades i valors esperats de corrent i tensió obtinguts a partir del model del generador fotovoltaic. S'han utilitzat tres SFCR de diferents potencies, topologies i tecnologies fotovoltaiques per a la validació experimental del mètode de detecció de fallades proposat. L'anàlisi dels indicadors de corrent i tensió ha demostrat efectivitat en la detecció de les fallades més probables en generadors fotovoltaics en temps real. A més, els resultats obtinguts mostren que la combinació de monitorització OPC juntament amb el procediment de detecció de fallades proposat és una eina robusta que pot ser molt útil en el camp de la supervisió remota i el diagnòstic de SFCX.

Finalment, en la present tesi s'aborda l'estudi dels problemes de degradació de mòduls fotovoltaics de capa prima corresponents a quatre tecnologies: a-Si:H, a-Si:H / μc-Si:H, CIS i CdTe, en condicions de treball a la intempèrie durant períodes prolongats d'exposició. S'analitza l'impacte de la degradació en la potència de sortida dels mòduls fotovoltaics per determinar la seva taxa de degradació anual i el seu període d'estabilització. La taxa de degradació s'obté a través d'un procediment basat en l'evolució de la potència màxima efectiva del mòdul al llarg del període d'exposició. El període d'estabilització s'avalua mitjançant dos mètodes: L'estudi de l'evolució de la potència de sortida del mòdul fotovoltaic i la tècnica de Potència-Irradiància. Els resultats obtinguts mostren que el mòdul fotovoltaic CIS és el més estable comparat amb les altres tecnologies, quan treballen en condicions de clima continental mediterrani. Els mòduls fotovoltaics a-Si:H i a-Si:H/μc-Si:H també presenten un bon comportament, mostrant taxes de degradació i períodes d'estabilització similars als esperats. El mòdul de CdTe mostra les pitjors prestacions, amb una major taxa de degradació i un llarg període d'estabilització de 32 mesos. Finalment, s'ha aplicat també la tècnica d'extracció de paràmetres per analitzar l'evolució dels paràmetres del model per a generadors fotovoltaics de mòduls de a-Si:H i a-Si:H/μc-Si:H en condicions reals de treball durant llargs períodes de temps.

Contents

Nomenclatures

ABC	*Artificial Bee Colony*
AC	*Alternative Current*
AM	*Air Mass*
a-Si:H	*Hydrogenated amorphous silicon*
a-Si:H/µc-Si:H	*Micromorph silicon (Hybrid amorphous microcrystalline silicon)*
CdTe	*Cadmium Telluride*
CIS ($CuInS_2$)	*Copper Indium Diselenide*
c-Si	*Crystalline silicon*
DBMS	*DataBase Management System*
DC	*Direct Current*
DE	*Differential Evolution*
FF	*Fill Factor*
G	*Solar irradiance (W/m²)*
GA	*Genetic Algorithm*
HDA	*Historical Data Access*
IP	*Internet Protocol*
$k = 1.38066E^{-23} J/K$	*Boltzmann's constant*
LID	*Light Induced Degradation*
LMA	*Levenberg-Marquardt algorithm*
MPPT	*Maximum Power Point Tracking*
OLE	*Object Linking and Embedding*
OPC	*OLE for Process Control*
PSO	*Particle Swarm Optimization*
PV	*Photovoltaic*
PR	*Performance Ratio*
$q = 1.60218E^{-19}$ C	*Elementary charge*
RMSE	*Root Mean Square Error*
SQL92	*Structured Query Language92*
STC	*Standard Test Conditions ($G = 1000$ W/m², $T_c = 25$ ºC)*
SWE	*Staebler-Wronski Effect*
Tc	*Solar cell temperature (ºC)*
TF	*Thin Film*
VPN	*VPN*
$V_t = k*T/q$	*Thermal voltage ($T = 300K$)*
W_p	*Watt-peak*

List of Figures

List of Tables

1. Introduction

The share of renewable energy technologies has been steadily increasing worldwide, particularly with regards to the energy sector. Renewable energy provided an estimated 19.2% of global final energy consumption in 2014, and the growth of their capacity and power generation continued in 2015 [1]. This growth is driven by several developments that all have a bearing on renewable energy, including a dramatic decline in global fossil fuel prices recorded in 2015; a series of announcements regarding the lowest-ever prices for renewable power long-term contracts; a significant increase in attention to energy storage; and a historic climate agreement in Paris that brought together the global community [1,2].

Among all the renewable energy sources, solar energy is one of the most promising sources for the generation of clean energy. Solar photovoltaic (PV) technology is one from the technologies that can harvest this abundant energy source [1]. PV technology converts sunlight directly into electricity, and its market share has steadily increased in the last years [3]. The large diffusion of PV technology is mainly due to its cost trend, which experienced a decrease of 75% in less than ten years. This makes PV a cost competitive source of electricity in a growing number of countries, with prices often below 1 €/W_p in European markets [4].

The performance of PV systems is influenced by several factors such as soiling, PV module degradation, shading, bypassed PV modules, faulty strings, mismatch, spectral distribution and operating temperature. However, the development of methods for regular performance supervision and fault detection is crucial to ensure an optimal energy harvesting and reliable power production PV systems. In addition, cost-effective procedures for faults detection in PV systems make the PV technology even more attractive for customers and investors.

PV modules are a key element of PV systems, which are based on different cell technologies for the conversion of sunlight into electrical energy. PV modules can be divided into two main categories: crystalline silicon and thin film technologies. Although crystalline silicon technologies are currently more efficient and dominate the market, Thin Film Photovoltaic (TFPV) modules have become an important technology. In 2015, TFPV modules covered the 7% of the market, with an annual production of 4.2 GW_p [3].

The main advantages of TFPV modules are their lower production costs and lower temperature coefficients compared to crystalline PV modules [5,6]. However, the main problems that this technology has to deal with are, the degradation phenomena after outdoor exposure [7–10] and the lower efficiencies compared to crystalline silicon PV modules.

The degradation and the behaviour of TFPV modules under outdoor exposure are still not fully understood and are currently object of research. A better understanding on this topic would be important for selecting the best PV technology for the appropriate climatic condition and for improving the reliability and performance of TFPV modules.

The outlined goals and objectives of the present work, as well as the thematic and the contributions of the thesis are described in sections below.

1.1. Aim and objectives

The present thesis is conducted in order to progress the state of the art of the supervision and diagnosis of photovoltaic systems, as well as modelling and the study of degradation of thin film PV modules.

On one hand, the aim of the thesis is to develop a cost effective technique for the diagnosis and automatic detection of the most probable faults which can occur during the functioning of a grid-connected PV system. On the other hand, the evaluation of performance and the estimation of degradation rates and the stabilization period of TFPV modules based on different cell technologies are the others goals to achieve in this thesis.

To successfully accomplish the thesis goals, the following specific objectives shall be achieved:

1- Modelling and simulation of the individual system components:

- ✓ Modelling of PV cell/ PV module/ PV generator.

- ✓ Modelling of the inverter.

2- Identification and validation of the system components models with experimental data:

- ✓ Using different algorithms for the model parameter extraction (LMA, DE, GA, PSO and ABC algorithm).
- ✓ Model parameter extraction from I-V curves and from dynamic behaviour: From monitoring data of the PV system working in real conditions.

3- Development of an automatic supervision procedure for PV systems:

- ✓ Identification of most probably source of faults present in the PV system.
- ✓ Fault detection method through OPC.

4- Characterization of PV systems in real operation conditions and degradation analysis of different PV cell technologies:

- ✓ Estimation of yields and performance ratios (comparison with expected energy production).
- ✓ Study of degradation rates of PV modules of different technologies: Amorphous silicon (a-Si:H), micromorph tandem silicon (a-Si:H/μc-Si:H), cadmium telluride (CdTe) and copper indium diselenide (CIS).
- ✓ Analysis of the stabilization period of the different technologies.
- ✓ Study of the PV module model parameters evolution along the degradation process.

1.2. Thematic

The thematic of the present thesis covers three important fields that are crucial in conceiving reliable grid-connected photovoltaic systems.

1.2.1. Parameter extraction of the PV module model

The PV cell/module models include several parameters that used to be unknown and are not provided by the PV module manufacturers. To adequately simulate the real behaviour of a PV module, an accurate parameter identification procedure is highly significant.

Several methods for parameters estimation of PV cell/module model have been proposed in the literature and they are categorized into: analytical methods [11], numerical methods [12,13] and bio-inspired methods [14–20].

The analytical methods for parameters estimation of PV cell/module model require some key points from the I-V characteristic curve, such as the maximum power point, the short-circuit current, the open-circuit voltage, and the slopes at the axis intersections [21]. These methods allow a relatively simple and fast calculation of the unknown parameter values. However, the accuracy of the extracted parameters heavily depends on the accuracy of these key points. Unfortunately, these methods provide high uncertainties because measured data usually contains noise due to device inaccuracy and other electrical disturbances.

To overcome the uncertainties in the analytical methods, many researchers have explored numerical methods, such Newton-Raphson (NR) and Levenberg-Marquardt (LM) based methods [12,13]. In general, these numerical methods provide good predictions however, they fail under certain conditions, such as fast varying of weather or presence of shadows in the plane of the PV array.

The bio-inspired methods based on the Genetic Algorithm (GA) [14], Particle Swarm Optimization (PSO) [15], Simulated Annealing (SA) [16], Harmony Search (HS) [17], Pattern Search (PS) [18], Differential Evolution (DE) [19] and Artificial Bee Colony (ABC) [20], are becoming the best solution in the modelling of PV systems because of their good accuracy.

In most works available in the literature, the extraction of the model parameters of the PV module model is carried out from measured I-V characteristics; this means using constant values of solar cell temperature and solar irradiance. Nevertheless, in the present research, the parameters are extracted directly from the monitored outputs of the PV module/array taking into account the variation of solar irradiance and cell temperature, in real working conditions.

1.2.2. Fault detection in PV systems

A grid-connected PV system can be divided in three main parts; AC-side, DC-side and the inverter in between. The three parts are susceptible to failures with different degree of complexity. The AC-side and the inverter failures can be easily identified due to advanced point reached by the researchers in developing robust devices. Compared to AC-side, the failures present in the DC-side of a grid-connected PV system are difficult to analyse, and their causes

are difficult to identify, because different faults have similar effects on the outputs of the PV array.

The faults in the DC-side of grid-connected PV systems can be classified into two main categories considering that energy losses result of faults may be temporary or permanent. Table 1.2.1 lists the possible origins of faults that may occur in the DC-side of a grid-connected PV system.

Table 1.2. 1 List of possible faults and their origins which affect the DC side of PV system.

Failure type	Failure name	Affected components	Possible origins
Permanent failures	Degradation [22,23]	Cell, module	- Deterioration of cells, crack, hot spots. - Penetration of humidity, degradation of interconnections, corrosion of cell's connections. - Mismatch. - Shorted Modules, reversed modules.
	Soiling [24]	Cell, module, string, array, ref-cell	- Waste, pollution, sand.
	Breakdown [23]	Cell, module, ref-cell, pyranometer, junction box, Protection diodes.	- Torn or broken module. - Short-circuit in electrical circuit. - Current surges due to lightning storms. - Absence or non-operation of diodes. - Reverse diode's polarity, faulty connection.
Temporary failures	Shading [25,26]	Cell, module, string, array, ref-cell	- Obstacles: clouds, buildings, trees…
	Grid outage [27]	Cables, inverter	- Faulty wiring - Corrosion of connections and contacts. - Destruction of wires.
	MPP-Tracking [25]	Inverter (DC-DC converter)	- Internal error, ageing of the component
	Total blackout [28]	String, array	- Disconnection of wiring, activation of DC-protection (fuses Blocking diode…)

With a view to the high implementation degree of grid-connected PV systems, the necessity to develop efficient diagnosis methods is particularly important in order to minimize outage periods and optimize their reliability and performance.

Several researches [29–31] have been carried out, using climate data from satellites observation to generate the necessary data at the desired location. This is a cost-effective approach, since no climate sensors are needed on the plant, although it provides low accuracy in estimating expected energy yields in some specific climatic conditions [31].

Other studies combined the computing techniques with local sensors which collected the meteorological data in order to estimate the energy production. An example can be found in

[32], where a method based on the extended correlation function and the matter-element model is proposed to detect faults in a small PV plant. Furthermore, in another work [33] the matter-element model is combined with a neural network to build an intelligent fault diagnosis system. Both proposals use a PV system simulator to collect power generation data of PV modules during normal and faulty operations.

Even more, some works were carried out using artificial intelligent techniques [34–36] and statistical data analysis for the supervision of PV systems [37]. However, these techniques have not been yet optimized for fault detection analysis and clear identification of the kind of fault present in the system.

Other interesting techniques were presented in the literature [38–40]. Authors proposed an automatic monitoring and fault detection system based on power losses analysis and yields analysis. This diagnostic procedure integrates monitoring, modelling, simulation, and fault diagnosis in a complete package designed in LabVIEW software. In this way the method allows at the same time PV model module parameters extraction, dynamic system simulation, monitoring of electrical and weather variables, and finally the detection of faults.

A new procedure for automatic fault detection in grid-connected PV systems defining new current and voltage indicators has been reported in the literature [41]. This method is based on previous works [42,43], that reduced both, computational analysis and the number of monitoring sensors. In concrete, irradiance and a temperature sensors are the only needed to supervise each sub-array connected to each inverter present in the PV system. The measurement of output current and voltage of the PV array is carried out by the inverter. The main idea is that this method of fault detection can be integrated into the inverter without using simulation software or additional external hardware.

Recently Hariharan et al. [44] presented a method for detecting permanent fault and partial shading in PV arrays. The method relies in defining two variables, and uses just the measured values of irradiance, voltage and current of the PV array. The use of this method allows distinguishing between permanent faults and temporary shading effects on the PV array. However, the nature of the permanent fault cannot be defined. Furthermore, neglecting the temperature effect leads to less significant results.

In this thesis the method proposed in [41] has been improved. Apart from the detection of several permanent faults, the method has been applied for detecting temporal faults like partial

shadows and inverter disconnections. Furthermore, now the procedure is able to give an equivalent number of faulty strings or bypassed modules in the PV array.

1.2.3. Degradation of PV modules

Several factors such as soiling, spectral distribution, mismatch and temperature strongly affect the performance of PV modules after a period of exposure under outdoor conditions. The degradation is mainly associated to the PV module technology. Several studies have reported that the TFPV modules degrade more sternly than the crystalline ones [45,46].

Previous studies present in the literature [7–9] were carried out in order to estimate the degradation rate of different TFPV modules technologies deployed outdoor for long term exposure in different climate conditions. The studies presented in references [8,47,48] demonstrate that the Staebler-Wronski Effect (SWE) [49] is the main cause of degradation in thin film hydrogenated single-junction amorphous silicon (a-Si:H) PV modules.

The characterization and the study of the degradation of four different TFPV modules is one of the goals of the present thesis. Moreover, parameter extraction techniques are used in order to study the degradation effects on the model parameters to understand the physical mechanisms associated to the degradation.

1.3. Contributions of the present thesis

The analysis of degradation of TFPV modules of different technologies in different climatic conditions can help selecting the best PV technology for each specific site. Thus, understanding the origin of the degradation modes and how they affect the performance of PV modules is important to improve their reliability.

The relevant contributions achieved along the present thesis rely mainly on the acquired information from the evolution of the extracted parameters of the PV cell model in order to achieve a better understanding of the performance changes of TFPV modules. The five parameters of the one-diode model have been extracted from dynamic response of the two PV generators based on a-Si:H and micromorph PV modules respectively, and evaluated along the monitoring campaign.

Moreover, the contributions of this thesis can also be found in the works published along the investigation period, related to:

- PV module/array modelling and parameter extraction techniques,
- Supervision and fault detection methods,
- Characterization and degradation study of TFPV modules.

Furthermore, as the field of PV is still progressing, the results and the methods given in the present thesis may open doors to further investigations.

A brief description of each publication is given bellow:

− The first paper [50] is related to PV module modelling and parameters extraction techniques. Two PV module models based on five different parameter identification methods were compared.

− The second paper [51] presents a cost effective method for the detection of the overall faults that may occur in the DC-side of a PV system.

− The third one [52] is an application of the fault detection method in an OPC platform used for remote supervision of PV systems.

− The characterization and the study of degradation of two PV systems of different TFPV modules technologies under outdoor long term exposure are done in [53,54]. Moreover, the evolution of the extracted parameters of the PV array model along the outdoor monitoring period reflects the degradation of the PV modules.

− Finally, the results of the analysis of degradation of four thin film photovoltaic modules deployed under outdoor long term exposure in continental climate conditions are given in [55].

The full-text of each publication and the discussions of the obtained results are detailed in the following chapters.

References

[1] Kristin Seyboth, Sverrisson F, Appavou F, Brown A, Epp B, Leidreiter A, et al. Renewables 2016 Global Status Report. Glob Status Rep 2016:272. http://www.ren21.net/status-of-renewables/global-status-report/ (accessed October 20, 2016).

[2] European Commission. Paris Agreement - European Commission. Clim Action 2016. http://ec.europa.eu/clima/policies/international/negotiations/paris/index_en.htm (accessed November 1, 2016).

[3] Fraunhofer Institute for Solar Energy Systems, ISE. Photovoltaics Report. Freiburg 2016. https://www.ise.fraunhofer.de/de/downloads/pdf-files/aktuelles/photovoltaics-report-in-englischer-sprache.pdf (accessed October 20, 2016).

[4] Solar Power Europe, "Global Market Outlook for Solar Power 2015-2019," Glob. Mark. Outlook, 2014 2015. http://helapco.gr/pdf/Global_Market_Outlook_2015_-2019_lr_v23.pdf (accessed November 1, 2016).

[5] Tossa AK, Soro YM, Thiaw L, Azoumah Y, Sicot L, Yamegueu D, et al. Energy performance of different silicon photovoltaic technologies under hot and harsh climate. Energy 2016;103:261–70. doi:10.1016/j.energy.2016.02.133.

[6] Friesen G, Pavanello D, Virtuani A. Overview of Temperature Coefficients of Different Thin Film Photovoltaic Technologies. 25th Eur Photovolt Sol Energy Conf Exhib / 5th World Conf Photovolt Energy Conversion, 6-10 Sept 2010, Val Spain 2010:4248–52. doi:10.4229/25thEUPVSEC2010-4AV.3.83.

[7] Jordan DC, Kurtz SR. Photovoltaic degradation rates - An Analytical Review. Prog Photovoltaics Res Appl 2013;21:12–29. doi:10.1002/pip.1182.

[8] Meyer EL, van Dyk EE. Characterization of degradation in thin-film photovoltaic module performance parameters. Renew Energy 2003;28:1455–69. doi:10.1016/S0960-1481(02)00062-9.

[9] Mendoza-Pérez R, Sastre-Hernández J, Contreras-Puente G, Vigil-Galán O. CdTe solar cell degradation studies with the use of CdS as the window material. Sol Energy Mater Sol Cells 2009;93:79–84. doi:10.1016/j.solmat.2008.09.016.

[10] Muñoz-García MA, Marin O, Alonso-García MC, Chenlo F. Characterization of thin film PV modules under standard test conditions: Results of indoor and outdoor measurements and the effects of sunlight exposure. Sol Energy 2012;86:3049–56.

[11] Hejri M, Mokhtari H, Azizian MR, Ghandhari M, Söder L. On the parameter extraction of a five-parameter double-diode model of photovoltaic cells and modules. IEEE J Photovoltaics 2014;4:915–23. doi:10.1109/JPHOTOV.2014.2307161.

[12] Ameen AM, Pasupuleti J, Khatib T. Modeling of photovoltaic array output current based on actual performance using artificial neural networks. J Renew Sustain Energy 2015;7:53107. doi:10.1063/1.4931464.

[13] Ikegami T, Maezono T, Nakanishi F, Yamagata Y, Ebihara K. Estimation of equivalent circuit parameters of PV module and its application to optimal operation of PV system. Sol Energy Mater Sol Cells 2001;67:389–95. doi:10.1016/S0927-0248(00)00307-X.

[14] Zagrouba M, Sellami A., Bouaïcha M, Ksouri M. Identification of PV solar cells and modules parameters using the genetic algorithms: Application to maximum power extraction. Sol Energy 2010;84:860–6. doi:10.1016/j.solener.2010.02.012.

[15] Ye M, Wang X, Xu Y. Parameter extraction of solar cells using particle swarm optimization. J Appl Phys 2009;105. doi:10.1063/1.3122082.

[16] El-Naggar KM, AlRashidi MR, AlHajri MF, Al-Othman A. K. Simulated Annealing algorithm for photovoltaic parameters identification. Sol Energy 2012;86:266–74.

[17] Askarzadeh A, Rezazadeh A. Parameter identification for solar cell models using harmony search-based algorithms. Sol Energy 2012;86:3241–9.

[18] AlHajri MF, El-Naggar KM, AlRashidi MR, Al-Othman a. K. Optimal extraction of solar cell parameters using pattern search. Renew Energy 2012;44:238–45. doi:10.1016/j.renene.2012.01.082.

[19] Ishaque K, Salam Z, Mekhilef S, Shamsudin A. Parameter extraction of solar photovoltaic modules using penalty-based differential evolution. Appl Energy 2012;99:297–308. doi:10.1016/j.apenergy.2012.05.017.

[20] Garoudja E, Kara K, Chouder A, Silvestre S. Parameters extraction of photovoltaic module for long-term prediction using artifical bee colony optimization. 2015 3rd Int Conf Control Eng Inf Technol 2015:1–6. doi:10.1109/CEIT.2015.7232993.

[21] Cubas J, Pindado S, Farrahi A. New method for analytical photovoltaic parameter extraction. Proc 2013 Int Conf Renew Energy Res Appl ICRERA 2013 2013:873–7. doi:10.1109/ICRERA.2013.6749874.

[22] Alonso-García MC, Ruiz JM, Chenlo F. Experimental study of mismatch and shading effects in the I-V characteristic of a photovoltaic module. Sol Energy Mater Sol Cells 2006;90:329–40. doi:10.1016/j.solmat.2005.04.022.

[23] Smith RM, Jordan DC, Kurtz SR. Outdoor PV module degradation of current-voltage parameters. World Renew Energy Forum 2012:1–9.

[24] Zorrilla-Casanova J, Piliougine M. Analysis of dust losses in photovoltaic modules. World Renew … 2011:2985–92. doi:10.3384/ecp110572985.

[25] Patel H, Agarwal V. Maximum power point tracking scheme for PV systems operating under partially shaded conditions. IEEE Trans Ind Electron 2008;55:1689–98.

[26] Ramabadran R. Effect of Shading on Series and Parallel Connected Solar PV Modules. Mod Appl Sci 2009;3:P32. doi:10.5539/mas.v3n10p32.

[27] Pigazo A, Liserre M, Mastromauro RA, Moreno VM, Dell'Aquila A. Wavelet-Based Islanding Detection in Grid-Connected PV Systems. IEEE Trans Ind Electron 2009;56:4445–55. doi:10.1109/TIE.2008.928097.

[28] Hanitsch RE, Schulz D, Siegfried U. Shading Effects on Output Power of Grid Connected Photovoltaic Generator Systems. Renew Energy 2001:93–9.

[29] Drews A, de Keizer A. C, Beyer HG, Lorenz E, Betcke J, van Sark WGJHM, et al. Monitoring and remote failure detection of grid-connected PV systems based on satellite observations. Sol Energy 2007;81:548–64.

[30] Stettler S, Toggweiler P, Remund J. Spyce: Satellite Photovoltaic Yield Control and Evaluation. 21st Eur Photovolt Sol Energy Conf 2006:2613–6.

[31] Muselli M, Notton G, Canaletti JL, Louche A. Utilization of meteosat satellite-derived radiation data for integration of autonomous photovoltaic solar energy systems in remote areas. Energy Convers Manag 1998;39:1–19.

[32] Chao KH, Ho SH, Wang MH. Modeling and fault diagnosis of a photovoltaic system. Electr Power Syst Res 2008;78:97–105. doi:10.1016/j.epsr.2006.12.012.

[33] Chao KH, Chen CT, Wang MH, Wu CF. A novel fault diagnosis method based-on modified neural networks for photovoltaic systems. Lect Notes Comput Sci (Including Subser Lect Notes Artif Intell Lect Notes Bioinformatics) 2010;6146 LNCS:531–9.

[34] Ducange P, Fazzolari M, Lazzerini B, Marcelloni F. An intelligent system for detecting faults in photovoltaic fields. Int Conf Intell Syst Des Appl ISDA 2011:1341–6.

[35] Mellit A, Kalogirou S A. ANFIS-based modelling for photovoltaic power supply system: A case study. Renew Energy 2011;36:250–8.

[36] Karatepe E, Hiyama T. Controlling of artificial neural network for fault diagnosis of photovoltaic array. Intell Syst Appl to 2011:1–6.

[37] Vergura S, Acciani G, Amoruso V, Patrono GE, Vacca F. Descriptive and inferential statistics for supervising and monitoring the operation of PV plants. IEEE Trans Ind Electron 2009;56:4456–64. doi:10.1109/TIE.2008.927404.

[38] Chouder A, Silvestre S, Taghezouit B, Karatepe E. Monitoring, modelling and simulation of PV systems using LabVIEW. Sol Energy 2013;91:337–49. doi:10.1016/j.solener.2012.09.016.

[39] Gokmen N, Karatepe E, Celik B, Silvestre S. Simple diagnostic approach for determining of faulted PV modules in string based PV arrays. Sol Energy 2012;86:3364–77. doi:10.1016/j.solener.2012.09.007.

[40] Chouder A., Silvestre S. Automatic supervision and fault detection of PV systems based on power losses analysis. Energy Convers Manag 2010;51:1929–37.

[41] Silvestre S, Silva MA Da, Chouder A, Guasch D, Karatepe E. New procedure for fault detection in grid connected PV systems based on the evaluation of current and voltage indicators. Energy Convers Manag 2014;86:241–9.

[42] Chine W, Mellit A., Pavan A. M, Kalogirou S A. Fault detection method for grid-connected photovoltaic plants. Renew Energy 2014;66:99–110. doi:10.1016/j.renene.2013.11.073.

[43] Silvestre S, Chouder A, Karatepe E. Automatic fault detection in grid connected PV systems. Sol Energy 2013;94:119–27. doi:10.1016/j.solener.2013.05.001.

[44] Hariharan R, Chakkarapani M, Saravana Ilango G, Nagamani C. A Method to Detect Photovoltaic Array Faults and Partial Shading in PV Systems. IEEE J Photovoltaics 2016;6:1278–85. doi:10.1109/JPHOTOV.2016.2581478.

[45] Pierro M, Bucci F, Cornaro C. Full characterization of photovoltaic modules in real operating conditions: theoretical model, measurement method and results. Prog Photovoltaics Res Appl 2015;23:443–61. doi:10.1002/pip.2450.

[46] Spataru S, Hacke P, Sera D, Packard C, Kerekes T, Teodorescu R. Temperature-dependency analysis and correction methods of in situ power-loss estimation for crystalline silicon modules undergoing potential-induced degradation stress testing. Prog Photovoltaics Res Appl 2015;23:1536–49. doi:10.1002/pip.2587.

[47] van Dyk EE, Audouard A., Meyer EL, Woolard CD. Investigation of the degradation of a thin-film hydrogenated amorphous silicon photovoltaic module. Sol Energy Mater Sol Cells 2007;91:167–73. doi:10.1016/j.solmat.2006.08.001.

[48] Radue C, van Dyk EE. A comparison of degradation in three amorphous silicon PV module technologies. Sol Energy Mater Sol Cells 2010;94:617–22.

[49] Staebler DL, Wronski CR. Reversible conductivity changes in discharge-produced amorphous Si. Appl Phys Lett 1977;31:292. doi:10.1063/1.89674.

[50] Kichou S, Silvestre S, Guglielminotti L, Mora-López L, Muñoz-Cerón E. Comparison of two PV array models for the simulation of PV systems using five different algorithms for the parameters identification. Renew Energy 2016;99:270–9.

[51] Silvestre S, Kichou S, Chouder A, Nofuentes G, Karatepe E. Analysis of current and voltage indicators in grid connected PV (photovoltaic) systems working in faulty and partial shading conditions. Energy 2015;86:42–50. doi:10.1016/j.energy.2015.03.123.

[52] Silvestre S, Mora-López L, Kichou S, Sánchez-Pacheco F, Dominguez-Pumar M. Remote supervision and fault detection on OPC monitored PV systems. Sol Energy 2016;137:424–33. doi:10.1016/j.solener.2016.08.030.

[53] Kichou S, Silvestre S, Nofuentes G, Torres-Ramírez M, Chouder A, Guasch D. Characterization of degradation and evaluation of model parameters of amorphous silicon photovoltaic modules under outdoor long term exposure. Energy 2016;96:231–41. doi:10.1016/j.energy.2015.12.054.

[54] Kichou S, Elif A, Silvestre S, Nofuentes G, Torres-Ramírez M, Chouder A. Study of degradation and evaluation of model parameters of micromorph silicon photovoltaic modules under outdoor long term exposure in Jaén, Spain. Energy Convers Manag 2016;120:109–19. doi:10.1016/j.enconman.2016.04.093.

[55] Silvestre S, Kichou S, Guglielminotti L, Nofuentes G, Alonso-Abella M. Degradation analysis of thin film photovoltaic modules under outdoor long term exposure in Spanish continental climate conditions. Sol Energy 2016;139:599–607.

2. Methodology

An important aspect to consider during the development of this research work is the methodology to be employed during the investigation period in order to reach the main objectives stated previously in section 1.1. In Fig. 2.1 it is depicted the flowchart of the methodology followed:

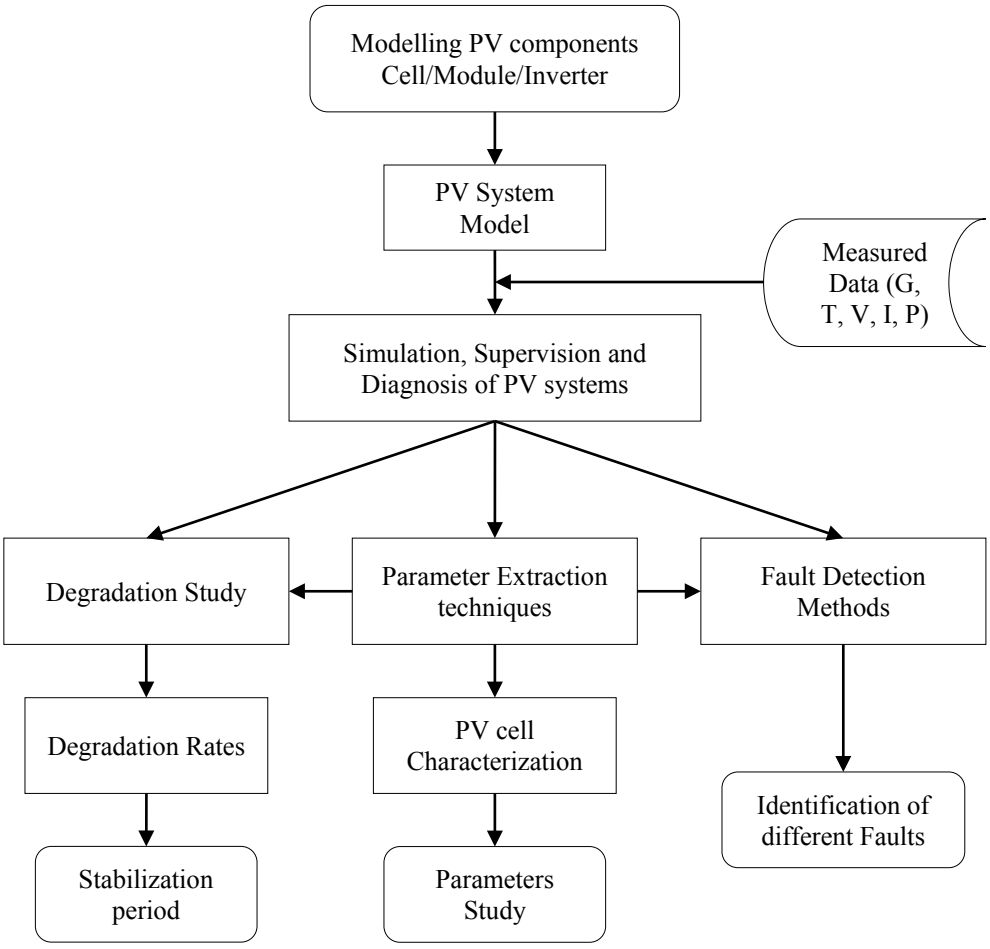

Figure 2. 1 Flowchart of the methodology.

Both, design tools and PV components models, were selected based on the literature review of the state of the art and the advancement in the field of PV systems. After selecting the models of the PV components, the whole PV systems is modelled, and a platform for simulation, supervision and diagnosis of PV systems is developed on MATLAB/Simulink. By using measured data of solar irradiance and cell temperature, the outputs of the PV system can be simulated and compared with monitored ones.

The parameter extraction technique is very important in order to optimize the PV model parameters which permit the reproduction of the exact behaviour of the PV system with good accuracy. Moreover, the parameter extraction technique is used in the study of degradation of TFPV modules, as well as in the development of efficient fault detection procedure which will be able to detect the most probable faults.

Finally, two procedures for the study of the degradation of TFPV modules and the assessment of stability period have been employed.

The main elements of the methodology described by the flowchart are detailed in the following sections.

2.1. Design and analysis tools

A wide variety of software tools now exist for the analysis, simulation and sizing of PV systems. These tools present different degrees of complexity and accuracy, depending on the specific tasks for which each tool has been developed.

It is useful to distinguish between sizing tools; which determine the component size and configuration [1–3], and simulation or modelling tools; which analyse the system output and performance once its specifications are known [4–8].

The development of the thesis has been carried out by using MATLAB software, which is a powerful technical computing environment that can be complemented by a wide set of associated toolboxes offered by Mathworks [8]. It allows the modelling and simulation of PV systems and components. Moreover, it can also be combined with the Simulink interface which is a friendly modular graphical environment of simulation, resulting in a very powerful modelling and simulation platform.

2.2. PV system modelling

Modelling is the basis for computer simulation of a real system. It is usually based on a theoretical analysis of several physical processes occurring in the system and the respective factors that influence these processes. Modelling of PV system components requires a good understanding of both, the principle operation of each component and the interaction between the rests of components.

Accurate modelling of PV module and the inverter is an important requirement for designing efficient PV system simulations since they are the basis elements of the PV system.

2.2.1. PV cell/module/array modelling

A detailed approach to solar cell based on a physical description and the electrical equivalent circuit of the solar cell is given in [9,10]. Several models with different degree of complexity and accuracy were elaborated in order to simulate and understand the behaviour of a PV cell [11–18].

The one diode model and Sandia model described below were used in the simulations of PV systems and PV modules carried out in the present thesis:

a) One diode model

The one diode model of a solar cell, also known as five-parameter model includes a parallel combination of a photogenerated controlled current source I_{ph}, a diode, described by the well-known single-exponential Shockley equation [10,19], a shunt resistance R_{sh} and a series resistance R_s modelling the power losses as shown in Fig. 2.2.1.

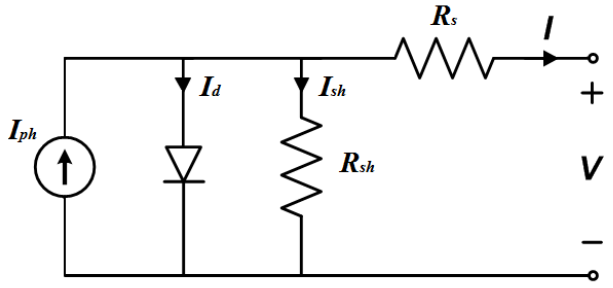

Figure 2.2. 1 One diode model of PV cell.

The current-voltage (I-V) characteristic of a solar cell could be derived from Kirchoff's current law and it is given by the implicit and nonlinear equation as follows:

$$I = I_{ph} - I_o\left(e^{\left(\frac{V+R_sI}{nV_t}\right)} - 1\right) - \left(\frac{V + R_sI}{R_{sh}}\right) \quad (2.2\text{-}1)$$

where I_o and n are the reverse saturation current and ideality factor of the diode respectively and V_t is the thermal voltage.

Eq. (*2.2*-1) can also be written as follows,

$$I = I_{ph} - I_d - I_{sh} \quad (2.2\text{-}2)$$

where I_d and I_{sh} are the currents across the diode and shunt resistance respectively.

The photogenerated current can be evaluated for any arbitrary value of irradiance, G, and cell temperature, T_c, by using the following equation:

$$I_{ph} = \frac{G}{G^*} I_{sc} + k_i(T_c - T_c^*) \quad (2.2\text{-}3)$$

where G^* and T_c^* are respectively the irradiance and cell temperature at standard test conditions (STC): 1000 W/m^2 (AM1.5) and 25ºC, k_i (A/ºC) is the temperature coefficient of the current and I_{sc} (A) is the solar cell short-circuit current at STC.

Some PV modules are formed by parallel strings of solar cells connected in series. However, most PV modules include one single string of solar cells. Therefore, the model of the solar cell can be scaled up to the model of the PV module using the following equations (*2.2*-4) – (*2.2*-8):

$$I_M = N_p\, I \quad (2.2\text{-}4)$$

$$I_{scM} = N_p\, I_{sc} \quad (2.2\text{-}5)$$

$$V_M = N_s\, V \quad (2.2\text{-}6)$$

$$V_{ocM} = N_s\, V_{oc} \quad (2.2\text{-}7)$$

$$R_{sM} = \frac{N_s}{N_p}\, R_s \quad (2.2\text{-}8)$$

where subscript M stands for 'Module', N_s is the number of solar cells connected in series and N_p is the number of parallel branches of solar cells forming the module.

Then, the output current of the PV module, I_M, is obtained rewriting Eq. (*2.2*-2) as follows:

$$I_M = N_p\left(I_{ph} - I_{dM} - I_{shM}\right) \quad (2.2\text{-}19)$$

The diode current, I_{dM}, included in Eq (*2.2*-9) is given by:

$$I_{dM} = I_{oM}\left(e^{\left(\frac{V_M + I_M R_{sM}}{n\, N_s V_t}\right)} - 1\right) \tag{2.2-10}$$

where V_M (V) and I_M (A), are the output voltage and current of the PV module respectively.

The saturation current of the diode I_{oM} (A) depends strongly on temperature and it is given by:

$$I_{oM} = \frac{I_{scM} e^{\left(\frac{E_{go}}{V_{to}} - \frac{E_g}{V_t}\right)}}{N_p\left(e^{\left(\frac{V_{ocM}}{n\, N_s V_{to}}\right)} - 1\right)}\left(\frac{T_c}{T_c^*}\right)^3 \tag{2.2-11}$$

where I_{scM} is the short-circuit current of the PV module, V_{ocM} is the open-circuit voltage of the PV module, V_{to} is the thermal voltage at STC, E_g the energy bandgap of the semiconductor and E_{go} is the energy bandgap at $T = 0$ K.

The value of the energy bandgap of the semiconductor at any cell temperature T_c is given by:

$$E_g = E_{go} - \frac{\alpha_{gap}\, T_c^2}{\beta_{gap} + T_c} \tag{2.2-12}$$

where α_{gap} and β_{gap} are characteristic parameters of the semiconductor.

Finally, the current I_{shM}, also included in Eq. (*2.2*-9) is given by the following equation:

$$I_{shM} = \frac{V_M + I_M R_{sM}}{N_p R_{shM}} \tag{2.2-13}$$

The same procedure can be applied to scale up the model of the PV module to the model of a PV array by taking into account the number of PV modules connected in series by string, N_{sg}, and the number of parallel strings in the PV array, N_{pg} [9].

b) Sandia model

The Sandia Array Performance Model (SAPM) developed at Sandia National Laboratories [20], is an empirical model described by the fundamental Eqs. (*2.2*-14) – (*2.2*-20).

The model contains several coefficients and parameters that are unknown and not provided by the PV module's manufacturer. By knowing these model parameters, as well as the solar radiation and the PV modules operating temperature, the output power of the PV array is predicted by using the following equations:

$$Ee = G/G_n \tag{2.2-14}$$

$$Iscg = N_{pg}[Isco \cdot Ee \cdot \{1 + \alpha_{Isc} \cdot (Tc - To)\}] \quad (2.2\text{-}15)$$

$$mpg = N_{pg}\left[Impo \cdot \{C_0 \cdot Ee + C_1 \cdot Ee^2\} \cdot \left\{1 + \alpha_{Imp} \cdot (Tc - To)\right\}\right] \quad (2.2\text{-}16)$$

$$\delta(Tc) = n \cdot k \cdot (Tc + 273.15)/q \quad (2.2\text{-}17)$$

$$Vocg = N_{sg}[Voco + N_s \cdot \delta(Tc) \cdot ln(Ee) + \beta_{Voc}(Ee) \cdot (Tc - To)] \quad (2.2\text{-}18)$$

$$Vmpg = N_{sg}\left[Vmpo + C_2 \cdot N_s \cdot \delta(Tc) \cdot ln(Ee) + C_3 \cdot N_s \cdot \{\delta(Tc) \cdot ln(Ee)\}^2 + \beta_{Vmp}(Ee) \cdot (Tc - To)\right] \quad (2.2\text{-}19)$$

$$Pmpg = Impg \cdot Vmpg \quad (2.2\text{-}20)$$

where; *Ee*: effective solar irradiance. *G*: measured irradiance (W/m^2). G_n: reference irradiance at STC. *To*: reference cell temperature at STC. *Tc*: measured cell temperature inside module (°C). *Isco*: PV module short-circuit current at STC (A). α_{Isc}: normalized temperature coefficient for *Isc*, (°C^{-1}). *Iscg*: PV array short-circuit current (A). N_{pg}: number of modules connected in parallel. *Impo*: PV module current at the maximum power point at STC (A). *Impg*: PV array current at the maximum power point (A). α_{Imp}: the normalized temperature coefficient for Imp, (°C^{-1}). C_0 and C_1 are empirically determined coefficients which relate *Imp* to the effective irradiance, $C_0+C_1=1$, (dimensionless). $\delta(Tc)$: thermal voltage per cell at temperature Tc. *q*: elementary charge. *k*: Boltzmann's constant. *n*: diode ideality factor. *Voco*: PV module open-circuit voltage at STC (V). β_{Voc}: temperature coefficient for module *Voc* at standard irradiance, (V/°C). N_s: number of cells in series per PV module. N_{sg}: number of modules connected in series. *Vocg*: PV array open-circuit voltage (V). *Vmpo*: PV module voltage at the maximum power point at STC (V). β_{Vmp}: temperature coefficient for module *Vmp* at standard irradiance, (V/°C). *Vmpg*: PV array voltage at the maximum power point (V). C_2 and C_3 are empirically determined coefficients which relate *Vmp* to the effective irradiance (C_2 is dimensionless, and the unit of C_3 is (V^{-1})). *Pmp*: PV array power at the maximum power point (W).

In order to solve the system equations formed by the Eqs. (*2.2*-14) – (*2.2*-20) described above and reproduce the behaviour of the whole PV system with a good accuracy, it is necessary to apply specific methods to determine the empirical coefficients included in the model equations.

2.2.2. Inverter modelling

PV Inverters convert the DC-power from the PV array into an AC-power compatible with the utility power grid. The inverter's model can be used in conjunction with a photovoltaic

array's model to calculate expected system performance and to verify the compatibility of inverter and PV array electrical features. In addition, the inverter's model is used to continuously monitor inverter performance characteristics that may indicate the need for repair or maintenance [20,21].

The Sandia Inverter Performance Model (SIPM) for grid-connected systems has been assumed in the present thesis, because of its efficiencies characterized in the conversion process from DC-power to AC-power using an empirical method. Moreover, the SIPM is characterized by taking into account a quadratic function of input power and voltage, and coefficients that can be used in the model [21].

The following equations define the model used to relate the inverter's AC-power output to both the DC-power and the DC-voltage:

$$P_{ac} = \{(P_{aco}/(A-B)) - C \cdot (A-B)\} \cdot (P_{dc} - B) + C \cdot (P_{dc} - B)^2 \quad (2.2\text{-}21)$$

$$A = P_{dco} \cdot \{1 + C_1 \cdot (V_{dc} - V_{dco})\} \quad (2.2\text{-}22)$$

$$B = P_{so} \cdot \{1 + C_2 \cdot (V_{dc} - V_{dco})\} \quad (2.2\text{-}23)$$

$$C = C_o \cdot \{1 + C_3 \cdot (V_{dc} - V_{dco})\} \quad (2.2\text{-}24)$$

where; P_{ac}: AC-power output from inverter based on input power and voltage, (W). P_{dc}: DC-power input to inverter, assumed to be equal to the PV array maximum power, (W). V_d: DC-voltage input, assumed to be equal to the PV array maximum power voltage, (V). P_{aco}: Maximum AC-power "rating" for inverter at nominal operating conditions, assumed to be an upper limit value, (W). P_{dco}: DC-power level at which the AC-power rating is achieved at the reference operating condition, (W). V_{dco}: DC-voltage level at which the AC-power rating is achieved at the reference operating conditions, (V). P_{so}: DC-power required for starting the inversion process, or self-consumption by inverter, strongly influences inverter efficiency at low power levels, (W). P_{nt}: AC-power consumed by inverter at night (night tare) to maintain circuitry required to sense PV array voltage, (W). C_o: parameter defining the curvature (parabolic) of the relationship between AC-power and DC-power at the reference operating conditions, default value of zero gives a linear relationship, (1/W). C_1: empirical coefficient allowing P_{dco} to vary linearly with dc-voltage input, default value is zero, (1/V). C_2: empirical coefficient allowing P_{so} to vary linearly with DC-voltage input, default value is zero, (1/V). C_3: empirical coefficient allowing C_o to vary linearly with DC-voltage input, default value is zero, (1/V).

2.3. Parameters extraction techniques

To adequately predict the real behaviour of the PV module/array, a good estimation of the model parameters is crucial.

The parameter extraction techniques employed in this thesis are based on five different optimization algorithms (LMA, GA, DE, PSO, and ABC), which can be applied to linear and nonlinear systems. Moreover, the extraction of the parameters could be carried out by using static or dynamic responses of the PV module/array.

The parameter extraction techniques evaluate the model parameters of the two PV module/array models described before, using as inputs measured data of solar irradiance and module temperature together with DC-output current and voltage.

For the five-parameter model of the PV module, the model parameters: I_{ph}, I_o, n, R_s, and R_{sh}, are evaluated by using Eqs. (*2.2*-9) – (*2.2*-13). Regarding the SAPM, the same idea is considered for the estimation of the empirical coefficients of the model parameters: C_0, C_1, C_2, C_3, n, α_{Imp} and β_{Vmp} using Eqs. (*2.2*-14) – (*2.2*-20).

The nonlinear regression method based on the Levenberg–Marquardt algorithm uses the following quadratic objective function given by Eq. (*2.3*-1) [22]. Where, the objective function for optimization using metaheuristic algorithms (GA, DE, PSO and ABC) is defined as the root mean square error (RMSE) of all data points given by Eq. (*2.3*-2) [23,24], where the *N* represent the number of measured data, *Vi* and *Ii* represent the measured voltage and current of the data point *i*.

$$S(\theta) = \sum_{i=1}^{N} [Ii - I(Vi, \theta)]^2 \qquad (2.3\text{-}1)$$

$$S(\theta) = \sqrt{\frac{1}{N} \sum_{i=1}^{N} [Ii - I(Vi, \theta)]^2} \qquad (2.3\text{-}2)$$

where θ = f (I_{ph}, I_o, n, R_s, R_{sh}) for the five parameter model and θ = f (C_0, C_1, C_2, C_3, n, α_{Imp}, β_{Vmp}) for the SAPM.

The parameter extraction algorithms implemented in MATLAB/Simulink environment are executed until function $S(\theta)$ is minimized. Thus, the result of the parameter extraction algorithms is a set of PV module model parameters that allow the best approach to the real daily evolution of DC-output current and voltage of the PV arrays.

2.3.1. Levenberg–Marquardt (LM) algorithm

The LM algorithm is an iterative technique that locates a local minimum of a multivariate function that is expressed as the sum of squares of several non-linear, real-valued functions. It has become a standard technique for nonlinear least-squares problems, widely adopted in various disciplines for dealing with data-fitting applications. LM can be thought of as a combination of "steepest descent" and "Gauss-Newton" methods [25,26]. When the current solution is far from a local minimum, the algorithm behaves like a steepest descent method: slow, but guaranteed to converge. When the current solution is close to a local minimum, it becomes a Gauss-Newton method and exhibits fast convergence rate [27]. The automatic switching between the two methods (steepest descent and Gauss-Newton) is ensured by the control parameter λ named damping factor. Therefore, the parameters $\theta = f(I_{ph}, I_o, n, R_s, R_{sh})$ (case of the one diode model) to be identified are updated at each iteration according to the following expression:

$$\theta_{k+1} = \theta_k - \left[\frac{J'\varepsilon}{J'J + \lambda_k I}\right]_{\theta=\theta_k} \qquad (2.3\text{-}3)$$

where, ε is the error between the measured current and the calculated one using Eq. (*2.2*-9), J is the Jacobian matrix $\left(\frac{\partial F(\theta)}{\partial \theta}\right)$ contains the de derivatives of the function $F(I_M, V_M, \theta)$ according to each parameter of the vector θ and, I is the Identity matrix.

In the present thesis, the nonlinear regression method based on the LM algorithm has been used directly from the provided functions in MATLAB environment.

2.3.2. Genetic algorithm (GA)

The GA algorithm was developed by John Holland in the 1970s for solving constrained and unconstrained optimization problems inspired from the biological evolution [28]. In GA each individual represents a solution, considering the one-diode model, each individual i is a set of parameters (I_{phi}, I_{oi}, n_i, R_{si} and R_{shi}). Several researches applied GA to extract the parameters of the PV model from measured I–V curves [29,30].

The GA starts with the initial population containing a set of individuals created randomly in the research range. To create the new generation, the algorithm selects some individuals of the current population as "Parents" to contribute part of their genes (the PV model parameters) to create "Children". Those children are the individuals of the new generation.

The children are divided in three types: Elite, Crossover and Mutation. The Elite children are the individuals of the present generation with the lowest cost function values. The Crossover children are those created by combining the genes or vectors of two parents; therefore, each child has information of the genes of both parents. Finally, the Mutation children are created by modifying the genes of the parents randomly, in other words a Mutation child is created by modifying one parent only.

In general, the GA continues creating new generations until a stop condition is fulfilled. Some typical stopping conditions are: desired fitness function range, maximum number of generations, time limit or the relative change in the fitness function.

The GA available in the Global Optimization toolbox of MATLAB has been used for minimizing the objective function given by Eq. (*2.3*-2) [29].

2.3.3. Differential evolution (DE)

The DE algorithm was proposed by Rainer Storn and Kenneth Price in 1997 [31]. Similar to other evolutionary algorithms, DE is a population based, derivative-free function optimizer. An advantage of DE over GA is that DE treats possible solutions as real-number strings, and thus encoding and decoding are not required.

The target vector $x = [x_1, x_2, \ldots, x_i]$ where $i = 1,2,\ldots, NP$ represents a population of NP random candidate solutions. The vector of the i-th particle, x_i indicates a series of parameters to be extracted, e.g. $x_i = [I_{ph}, I_o, n, R_s, R_{sh}]$ for the one-diode model and $x_i = [C_0, C_1, C_2, C_3, n, \alpha_{Imp}, \beta_{Vmp}]$ for the SAPM. For a d dimension optimization problem, a random candidate solution is given by:

$$x_j^{low} \leq x_{i,j} \leq x_j^{up} \qquad (2.3\text{-}4)$$

where x_j^{low} and x_j^{up} are the lower and the upper limits of the j-th vector component respectively, $i = 1, 2, \ldots, NP$ and $j = 1, 2, \ldots, d$.

After the initialization DE enters a loop of evolutionary operations: mutation, crossover and selection considering the maximum number of generations t_{max}, where $t = 1,2,\ldots,t_{max}$.

In the mutation step, for each x_i at generation t, three vectors x_{r0}, x_{r1} and x_{r2} are chosen randomly from the set $\{1, 2, \ldots, NP\}\backslash\{i\}$ to generate a donor vector by:

$$v_i^{t+1} = x_{r0}^t + F(x_{r1}^t - x_{r2}^t) \qquad (2.3\text{-}5)$$

where F is a differential weight, known as scaling parameter, that usually ranges in the interval [0, 1].

The crossover operation is used to decide whether to exchange the value with donor vector. By generating a random integer index $J_r \in [1, d]$ and a randomly distributed number $k_i \in [0, 1]$, the j-th dimension of v_i, namely $u_{i,j}$, is updated according to:

$$u_{i,j}^{t+1} = \begin{cases} v_{i,j}^{t+1}, & k_i \leq CR \text{ or } i = J_r \\ x_{i,j}^{t}, & k_i > CR \text{ and } i \neq J_r \end{cases} \quad (2.3\text{-}6)$$

where CR is a crossover probability in the interval [0, 1]. The crossover scheme formulated by Eq. (*2.3*-6) used in the present work is called binomial strategy.

The selection operation, selects the best one from the parent vector x_i^t, and the trial vector u_i^{t+1} solution with the minimum objective value, using the following expression:

$$x_i^{t+1} = \begin{cases} u_i^{t+1}, & f(u_i^{t+1}) \leq f(x_i^t) \\ x_i^t, & otherwise \end{cases} \quad (2.3\text{-}7)$$

where $f(x)$ is the fitness function to be minimized. Therefore, if a particular trial vector is found to result in lower fitness value, it will replace the existing target vector; otherwise, the target vector is retained.

2.3.4. Particle swarm optimization (PSO)

The PSO is a population based stochastic optimization technique developed by Kennedy and Eberhart [32] and is inspired by the social behaviour of bird flocking or fish schooling.

The PSO searches a possible solution in a given space by adjusting the trajectories of particles. The best position encountered of the particle i is designed by $pbest_i$. In a swarm of particles, there are N local best positions, and the best solution is denoted by *gbest*.

The velocities and positions of particles, as well as the algorithm parameters, inertia weight w and learning parameters α, β, are firstly initialized. In an iteration t, the fitness of particles is evaluated individually by the objective function. By attracted toward $pbest_i$ and *gbest*, the particle moves according to the following expression:

$$x_i^{t+1} = x_i^t + v_i^{t+1} \quad (2.3\text{-}8)$$

where v_i^{t+1} is the velocity, expressed as:

$$v_i^{t+1} = wv_i^t + \alpha\epsilon_1(x_i^t - gbest^t) + \beta\epsilon_2(x_i^t - pbest_i^t) \quad (2.3\text{-}9)$$

The random vectors ϵ_1 and ϵ_2 are in the range [0, 1]. α = 1.5, β = 2. The w is the inertia weight, used to balance global and local search abilities, it is considered constant and set equal to 0.9.

Finally, lower and upper boundaries are set to ensure that particles are within the predetermined range. The PSO will continue to search for better solutions until it meets the stopping criterion.

2.3.5. Artificial bee colony algorithm (ABC)

The ABC algorithm is an optimization algorithm inspired by the natural foraging behaviour of honey bees. As reported in literature, it was successfully applied in the parameter extraction of solar cell models [23,24]. In the ABC, there are food sources representing the solutions of the optimization problems and honey bees (classified into employed bees, onlooker bees and scout bees) representing the operations to the solutions. The employed bees investigate potential food sources and share information with onlooker bees. The food sources of higher quality will have higher possibility to be selected by onlooker bees. If the quality of the employed bees' food sources is relatively low, they will change its role to scout bees to randomly explore new potential food sources. Consequently, the exploitation is promoted by employed and onlooker bees while the exploration is maintained by scout bees.

The ABC algorithm is an iterative process similar to other swarm-based approaches. The implementation of the ABC algorithm in MATLAB is carried out by following the same steps given in the previous works [23,24,33]. It starts with initializing a population of randomly generated solution (food sources) as follow:

$$x_{i,j} = l_j + rand(0,1) \cdot \left(u_j - l_j\right) \qquad (2.3\text{-}10)$$

where $x_{i,j}$ is a food source (target vector), the index i (i = 1,2,…,NP) corresponds to i-th food source and j (j=1,2,…,d) is the j-th dimension of the search space. l_j and u_j are the lower and upper bound in each dimension.

After the initialization, the following steps are executed until reaching a stopping criterion -i.e: iteration limit, tolerance value,…-:

a. Send the employed bees

The number of employed bees that are used to generate new solutions is the same as the number of food sources. The entire number of population is divided by two (NP/2), one half

corresponds to the employed bees and the second half corresponds to the onlooker bees [34,35]. Then, to generate the new source food using the employed bee operator, in a randomly way is selected a *k* food source in the *j* dimension. If a parameter of an employed bee food source $B_{i,j}$ exceeds the boundaries, it should be adjusted in order to fit the appropriate range.

$$B_{i,j} = x_{i,j} + \emptyset_{i,j}(x_{i,j} - x_{k,j}), \quad \forall\, i \neq k \tag{2.3-11}$$

where, $\emptyset_{j,i}$ is a random value selected between [-1, 1], and $k \in \text{rand}\{1, NP\}$.

After this process, it is calculated the fitness value associated with each solution. The fitness value is used to evaluate the quality of a food source. For minimization purposes it can be obtained using the following expression:

$$fit_i = \begin{cases} \dfrac{1}{1 + J_i} & if\ J_i \geq 0 \\ 1 + abs(J_i) & if\ J_i < 0 \end{cases} \tag{2.3-12}$$

where J_i is the objective function value of the candidate solution x_i. In our context, J_i represents the RMSE (Eq. (*2.3*-2)) value associated to a candidate model x_i. The next process consists in applying a greedy selection between the values of the employed bee food sources contained in B_i and the initial food sources vector x_i. Meaning that if the nectar amount (fitness value) of B_i is better, then the solution x_i is replaced by B_i otherwise, x_i is preserved.

b. Select the food sources using the onlooker bees

The food sources are modified several times depending on the fitness value Eq. (*2.3*-12). For a food source selection, it is necessary to obtain a probability factor that is computed based on the fitness.

$$Prob_i = \frac{fit_i}{\sum_{i=1}^{NP} fit_i} \tag{2.3-13}$$

where, fit_i corresponds to the fitness value of the *i*-th food source and is related to the objective function of the food source *i*. If the fitness of a food source increases, then the probability of being selected by an onlooker is bigger. When a food source is selected, a new value is obtained using Eq. (*2.2*-9), its fitness is computed and the greedy process is applied to modify (or not) its position.

c. Determinate the scout bees

The final step is the scout bee process. Here the bees are applied if a food source *i* cannot be improved through a predetermined trial "limit" number, then the food source is considered

to be abandoned and instead to be modified by and onlooker bee, is modified by a scout bee using Eq. (*2.3*-10). The predefined "limit" is a counter assigned to each food source and is incremented when the fitness is not improved [23].

2.4. PV system simulation and monitoring

This subsection discusses the solution and the simulation of the I-V characteristic of the PV cell given by Eq. (*2.2*-1). Moreover, the effects of solar irradiance and cell temperature, as well as the variation of the five parameters of the PV cell model on the I-V characteristic are analysed. Finally, the monitoring method used in the present work based on OPC is described.

2.4.1. Solution and simulation of the PV module characteristic

The Eq. (*2.2*-1) given by the one diode (five-parameter) PV model is implicit and nonlinear. The Newton-Raphson algorithm is the most suitable method for solving this kind of iterative problems [22,36].

For a given value of V, the PV module output current, I, is calculated individually according to the voltage input point so that the following equation is satisfied:

$$F(V_i, I_i) = 0 \qquad (2.4\text{-}1)$$

The main idea of the Newton-Raphson algorithm is to find the PV modules current I_i which is the root of the Eq. (*2.2*-1) for a given voltage V_i. Starting from a given initial value I_0, the Newton-Raphson algorithm evaluates the following iterations:

$$I_{i+1} = I_i - \frac{F(V, I_i)}{\frac{\partial F(V, I_i)}{\partial I}} \qquad (2.4\text{-}2)$$

where I_{i+1} is the actual current values, I_i is the previous value of the calculated current.

The iterative process continues till reaching a predefined absolute value ε between two consecutive iterations:

$$|I_{i+1} - I_i| < \varepsilon \qquad (2.4\text{-}3)$$

The graphical representation of the solution of the implicit nonlinear equation given by Eq. (*2.2*-1), for constant values of solar irradiance (G) and cell temperature (T_c) is shown in Fig. 2.4.1.

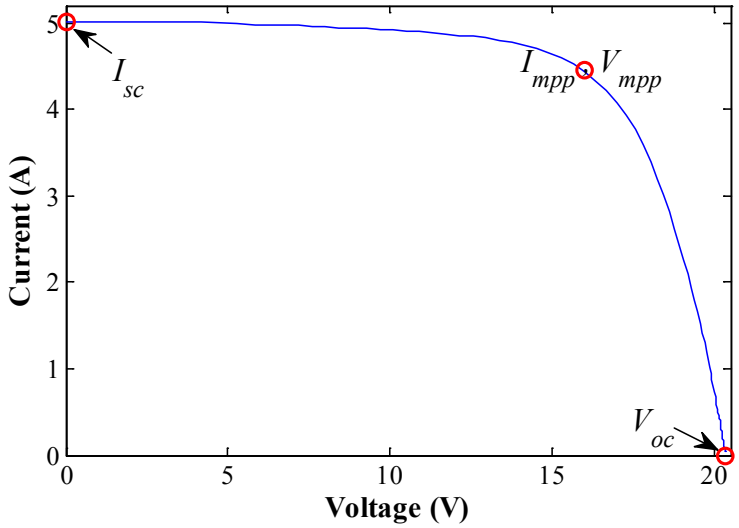

Figure 2.4. 1 I-V characteristic of a PV module.

Four important parameters represented in the I-V characteristic namely are the short-circuit current (I_{sc}), open-circuit voltage (V_{oc}) and the current and voltage maximum power points (I_{mpp} and V_{mpp}) respectively. These points are shown in Fig. 2.4.1 and are given in the manufacturer's PV module data sheet.

The maximum efficiency of PV cell/module is the ratio between the maximum power and the incident light power, given by:

$$\eta_{max} = \frac{P_{mpp}}{P_{in}} = \frac{V_{mpp} \cdot I_{mpp}}{A\phi} \qquad (2.4\text{-}4)$$

where; ϕ is the incident irradiance and A is the cell/module area.

The Fill factor gives an indication of the quality of a cell's semiconductor junction and measures of how well a solar cell is able to collect the carriers generated by light. It is represented by the ratio of the maximum power that can be delivered to the load and the product of I_{sc} and V_{oc} as follow:

$$FF = \frac{V_{mpp} \cdot I_{mpp}}{I_{sc} \cdot V_{oc}} \qquad (2.4\text{-}5)$$

The performance ratio, PR, is used as an indicator of outdoor modules performance and is defined as a ratio of the final yield (Y_f) and the reference yield (Y_r):

$$PR = \frac{Y_f}{Y_r} \qquad (2.4\text{-}6)$$

The final yield (Y_f) is defined as the annual, monthly or daily net AC-energy output of the system E_{ac} (Wh) divided by the installed peak power P^* (W) of the PV array at STC. And it is calculated using Eq. (*2.4*-7).

$$Y_f = \frac{E_{ac}}{P^*} \qquad (2.4\text{-}7)$$

The reference yield is the total in-plane solar insolation H_t (kWh/m^2) divided by the array reference irradiance G^* (W/m^2), given by Eq. (*2.4*-8).

$$Y_r = \frac{H_t}{G^*} \qquad (2.4\text{-}8)$$

Another yield known as array yield (Y_A) is usually used in the estimation of the power losses related to PV array. It is defined as the annual, monthly or daily energy output of the PV array E_{dc} (Wh) divided by the installed peak power P^* (W) of the PV array at STC, and it is calculated by Eq. (*2.4*-9).

$$Y_a = \frac{E_{dc}}{P^*} \qquad (2.4\text{-}9)$$

2.4.3. Impacts of temperature and irradiance on the I-V characteristic

PV modules rarely operate under standard test conditions. The electrical output and the shape of the I-V curves of PV modules depend upon temperature and irradiance and some other external effect like shadows. Thus PV modules are usually operating under variable conditions of temperature and irradiance, so nominal outputs are rarely reached.

The changes in solar irradiance affect the module's current most of all since the current is directly dependent upon the irradiance. When irradiance drops by half, the output power of the PV module is also reduced by half. By contrast, the MPP voltage value stays relatively constant with changing irradiance as it is shown in Fig. 2.4.2-(a).

On the other hand, module's voltage is affected mostly by module temperature, as it is illustrated in Fig. 2.4.2-(b). The change in voltage of the module determines the system voltage and therefore the design of the entire PV system.

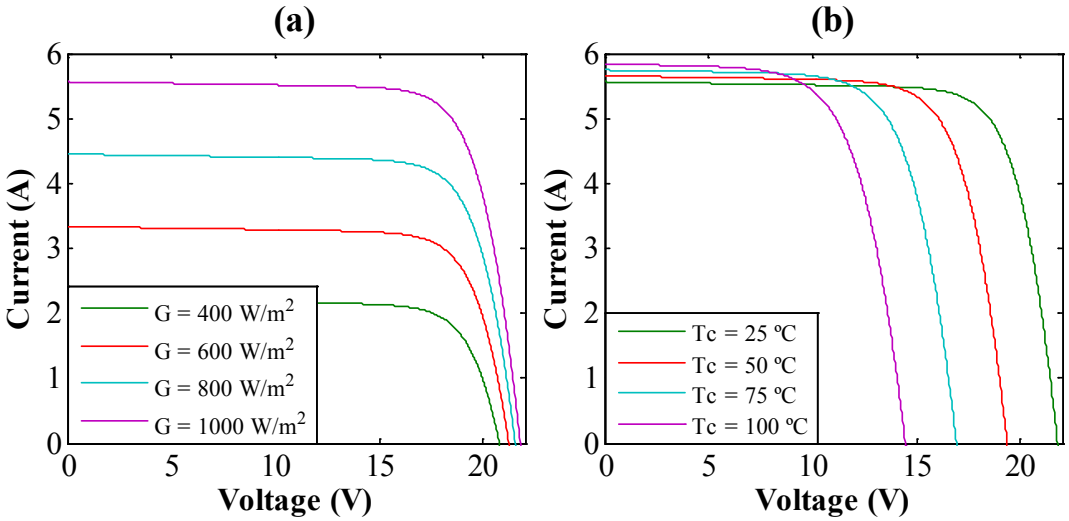

Figure 2.4. 2 Effect of varying temperature and irradiance on PV module characteristics.

2.4.4. Impacts of the PV model's parameters on the I-V characteristic

The five parameters of the one-diode model of a PV cell (I_{ph}, I_o, n, R_s, and R_{sh}) have a significant influence on the I-V characteristic. Each parameter influences a specific region of the I-V curve. Hereafter, the influence of the variation of each parameter (supposing the other parameters remaining constant) is shown graphically.

- ***Variation of the photogenerated current, I_{ph}***

The I_{ph} parameter depends on the solar irradiance and cell temperature (Eq. (*2.2*-3)). From Fig. 2.4.3, it can be seen that the variation of the I_{ph} affects the shape of the I-V curve at the short-circuit current.

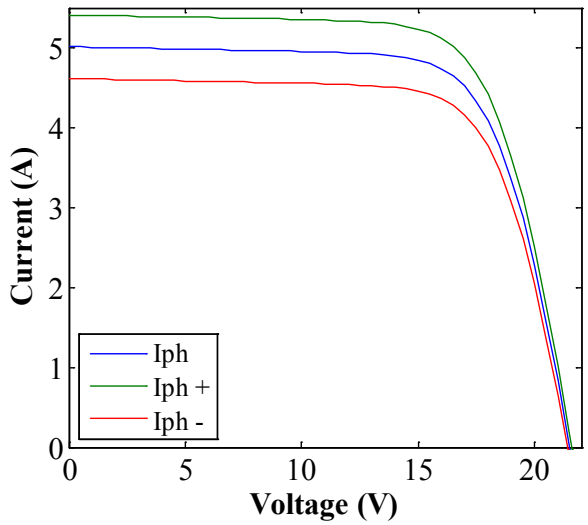

Figure 2.4. 3 Effects of the photogenerated current, I_{ph}, on the I-V curve.

- ***Variation of the reverse saturation current, I_o***

The expression of the reverse saturation current given by Eq. (*2.2*-11) shows that the I_o depends on temperature, and the bandgap of the semiconductor. In practice, the bandgap energy of the semiconductors used for manufacturing PV cells varies from 1 to 1.7 eV [37]. The variation of the magnitude of I_o strongly affects the I-V curve at the open-circuit voltage, as it is shown in Fig. 2.4.4.

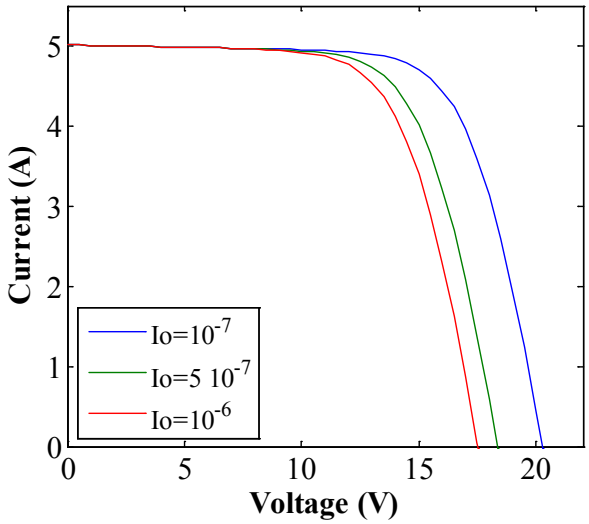

Figure 2.4. 4 Effects of the reverse saturation current, I_o, on the I-V curve.

- ***Variation of the diode ideality factor, n***

From the variation of the values of the ideality factor, *n*, illustrated in Fig. 2.4.5, it can be seen that the regions of open-circuit voltage and short-circuit current are not affected. However, the variation of *n* affects only the maximum power point (MPP) coordinates (I_{mpp} and V_{mpp}).

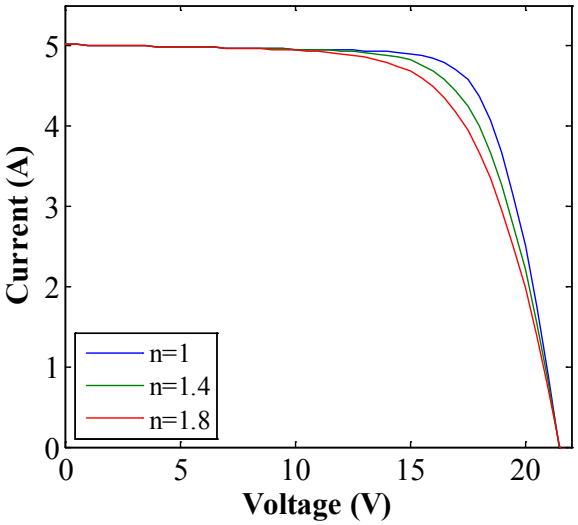

Figure 2.4. 5 Effects of the diode ideality factor, n, on the I-V curve.

- ***Variation of the series resistance, R_s***

Figure 2.4.6 shows that the increase of the series resistance value reduces significantly the voltage at the MPP, as well as the fill factor. However excessively high values of R_s may also reduce the short-circuit current.

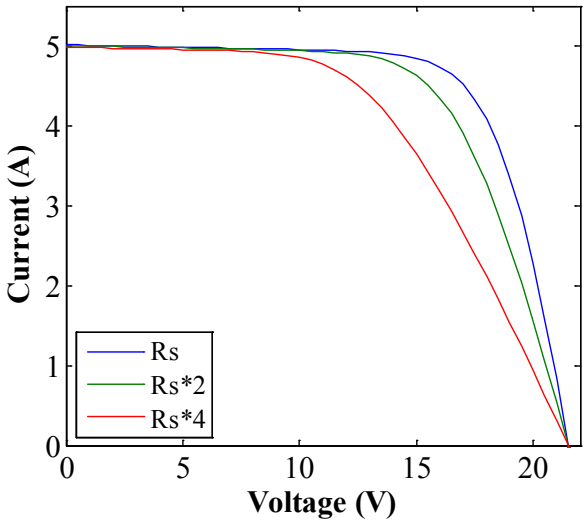

Figure 2.4. 6 Effects of the series resistance, R_s, on the I-V curve.

- ***Variation of the shunt resistance, R_{sh}***

Unlike the series resistance, the ideal value of the shunt resistance is supposed to be infinite and the decrease of its value affects mainly the coordinates of the MPP, especially the current at MPP. The fill factor is also influenced by the decrease of the shunt resistance. The effects of the R_{sh} on the I-V characteristic are shown below in Fig. 2.4.7.

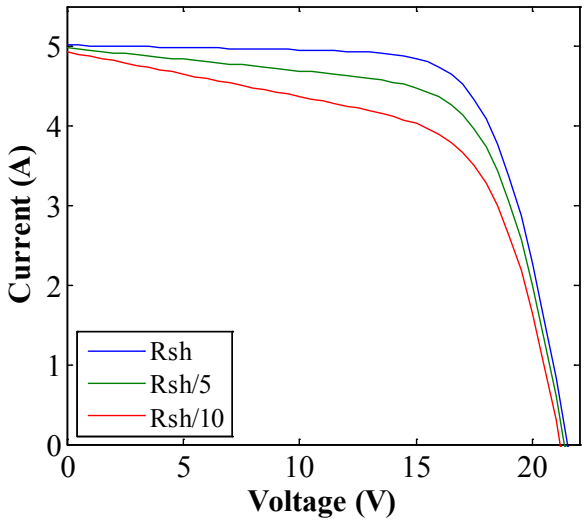

Figure 2.4. 7 Effects of the shunt resistance, R_{sh}, on the I-V curve.

Reduced values of shunt resistance cause power losses in solar cells by providing an alternate path for the photogenerated current. As a consequence, the current flowing through the solar cell junction as well as the solar cell voltage are reduced [36].

2.4.5. Remote monitoring of PV systems based on OPC

The OLE for Process Control (OPC) is a standard and consistent communication system for exchanging information. It was originally based on OLE (object Linking and Embedding) for process control [38,39], and now is available on other operation systems.

OPC allows defining the rules of handshaking between different devices using the client-server paradigm; this system has been used in industry to connect supervisory systems and data acquisition and man-machine interfaces with the physical control systems [40]. Moreover, it allows the development of components for interconnecting disperse systems providing interoperability efficiently. This technology enables software components developed by experts in one sector to be used by applications in any other sector.

The design of OPC interfaces supports distributed architectures. The Data access OPC and Historical Data Access specifications are compatible with client-server and publisher-subscriber communication models. The use of the Distributed Component Object Model (DCOM) from Microsoft makes possible the access to remote OPC servers. DCOM extends Microsoft's object-oriented Component Object Model (COM) to promote interoperation of software objects in a distributed-heterogeneous environment.

The OPC standard model of the remote monitoring of PV systems used in the present thesis is the same developed in [41]. The following parameters were monitored: Current, voltage and power of both sides DC and AC, frequency, irradiance and module temperature. Where, for data collection it was used OPC Historical Data Access (OPC HDA) specifications which provide access to information already stored in inverters and allow retrieving this information in a homogeneous and uniform way. A VPN and IP were used to connect with the facilities. The data collection interval was 5 min. Data are directly retrieved from the inverter.

Several elements are used in the monitoring process: The client software using OPC HDA technology for downloading data from the devices, the device and the OPC HDA server that knows the protocol and the procedure to download data from the device. Data were stored in a PostgreSQL DBMS compatible with the SQL92 standard [42].

Finally, for the evaluation of the performance of the PV systems, as well as the detection of anomalies, the fault detection procedure described in the following section was implemented by means of remote monitoring and control based on OPC.

2.5. Fault detection procedure

The automatic supervision and fault detection procedure employed in the present thesis relies on the two indicators of current, *NRc*, and voltage, *NRv*, defined in [43] as follows:

$$NRc = \frac{I_m}{I_{sc}} \tag{2.5-1}$$

$$NRv = \frac{V_m}{V_{oc}} \tag{2.5-2}$$

where V_m and I_m are the voltage and current of the maximum power point (MPP) at the DC-output of the PV array, I_{sc} and V_{oc} are the short-circuit current and the open-circuit voltage of the PV generator respectively.

The inverter is able to calculate both *NRc* and *NRv* indicators through MPP coordinates available at the inverter input, and the values of I_{sc} and V_{oc}, obtained for actual conditions of irradiance and temperature by the inverter itself internally in real time. For this purpose, the inverter must have MPP tracking and monitoring capabilities, which is the case of most inverters used in grid-connected PV systems. Furthermore, the inverter requires a minimum input voltage, start-up voltage to start working. So, a minimum level of irradiance on the PV array is necessary to enable the proper operation of the inverter. By taking into account this fact, a minimum level of $G = 200$ W/m^2 is considered for starting the fault detection procedure in the PV system and calculate the corresponding current and voltage indicators.

Two more parameters can be also calculated in real time: I_{mo} and V_{mo}, the current and voltage at the maximum power point of the output of the PV array in absence of faults [43]. Then, the ratios: *NRco* and *NR*vo, representing the expected values of *NRc* and *NRv,* in normal (fault-free) operation of the PV system are given by:

$$NRco = \frac{I_{mo}}{I_{sc}} \tag{2.5-3}$$

$$NRvo = \frac{V_{mo}}{V_{oc}} \tag{2.5-4}$$

For an arbitrary value of the irradiance and temperature, the short-circuit current of a PV module, I_{scm}, is given by Eq. (*2.5*-5):

$$I_{scm} = \frac{I_{scmr}}{G^*} G + \left(\frac{dI_{scm}}{dT}\right)(T_c - T_c^*) \quad (2.5\text{-}5)$$

where I_{scmr} is the short-circuit current of the PV module at STC (G^* = 1000 W/m^2 and T_c^* = 25 °C), G is the actual irradiance on the PV module and T_c is the real operating cell temperature. The open-circuit voltage of the PV module, V_{ocm}, can be written as [9]:

$$V_{ocm} = V_{ocmr} + \left(\frac{dV_{ocm}}{dT}\right)(T_c - T_c^*) + V_t \ln\left(\frac{I_{scm}}{I_{scmr}}\right) \quad (2.5\text{-}6)$$

where V_{ocmr} is the open-circuit voltage of the PV module at STC and V_t is the thermal voltage. The values of I_{scm} and V_{ocm} can be easily estimated for any condition of temperature and irradiance, by using Eqs. (*2.5*-5) and (*2.5*-6) taking into account the PV module parameters given by manufacturers at STC. Considering a PV array composed of N_{pg} parallel strings of PV modules, including a number of N_{sg} PV modules in series per string, Eqs. (*2.5*-5) and (*2.5*-6) can be scaled to calculate the I_{sc} and V_{oc} of the entire PV array as follows:

$$I_{sc} = N_{pg}\left(\frac{I_{scmr}}{G^*} G + \left(\frac{dI_{scm}}{dT}\right)(T_c - T_c^*)\right) \quad (2.5\text{-}7)$$

$$V_{oc} = N_{sg}\left(V_{ocmr} + \left(\frac{dV_{ocm}}{dT}\right)(T_c - T_c^*) + V_t \ln\left(\frac{I_{scm}}{I_{scmr}}\right)\right) \quad (2.5\text{-}8)$$

Then the ratios *NRc* and *NRv* defined by Eqs. (*2.5*-1) and (*2.5*-2) could be estimated from Eqs. (*2.5*-7) and (*2.5*-8) once the coordinates of the MPP of the PV array are known.

The values of I_{mo} and V_{mo} for a PV array of arbitrary series-parallel (N_{sg} x N_{pg}) connection of PV modules can be calculated for any condition of G and T_c by using the following equations that include parameters of the PV modules forming the PV array [9]:

$$I_{mo} = N_{pg}\left(\frac{I_{mmr}}{G^*} G + \left(\frac{dI_{scm}}{dT}\right)(T_c - T_c^*)\right) \quad (2.5\text{-}9)$$

$$I_{mm} = \frac{I_{mmr}}{G^*} G + \left(\frac{dI_{scm}}{dT}\right)(T_c - T_c^*) \quad (2.5\text{-}10)$$

$$V_{mo} = N_{sg}\left(N_s V_t \ln\left(1 + \frac{I_{scm} - I_{mm}}{I_{scm}}\left(e^{\frac{V_{ocm}}{N_s V_t}} - 1\right)\right) - I_{mm} R_{sm}\right) \quad (2.5\text{-}11)$$

where; n is the diode ideality factor, I_{mmr} is the PV module current at the MPP, N_s is the number of solar cells connected in series forming the PV module, R_{sm} is the series resistance of the PV module, I_{scm} and V_{ocm} are the short-circuit current and open-circuit voltage of the PV module given by Eqs. (*2.5*-5) and (*2.5*-6), and I_{mm} is the maximum current of the PV module given by Eq. (*2.5*-10).

In normal (fault-free) operation of the PV system, the values of the indicators *NRc* and *NRv* should be very similar to the values of *NRco* and *NRvo* given by Eqs. (*2.5*-3) and (*2.5*-4) and maintain values over specific thresholds.

The definition of thresholds for current, TNR_{cfs}, and voltage, $TNR_{vbm,}$ allows detecting short-circuits and open-circuits in the PV array as well as partial shading and inverter disconnection. These thresholds were defined by the following equations [43]:

$$TNR_{cfs} = 1.02\ \alpha\ NRco \qquad (2.5\text{-}12)$$

$$TNR_{vbm} = 1.02\ \beta\ NRvo \qquad (2.5\text{-}13)$$

where α and β given by Eqs. (*2.5*-14) and (*2.5*-15) are the relationship between the ratios of current in case of one faulty string and fault-free operation, and the ratio between the voltage ratios in case of one bypassed PV module and fault-free operation respectively [43]. The constant included in the Eqs. (*2.5*-12) and (*2.5*-13) was fixed by means of statistical procedures in order to avoid false fault detections as an offset of a 2% respect the *NRco* and *NRvo* values.

$$\alpha = 1 - \frac{1}{Np} \qquad (2.5\text{-}14)$$

$$\beta = 1 - \frac{1}{Ns} \qquad (2.5\text{-}15)$$

As it can be seen from Eqs. (*2.5*-14) and (*2.5*-15) both parameters α and β depend only on the array configuration: Number of PV modules connected in series by string, N_{sg}, and number of strings connected in parallel in the PV array, N_{pg}.

When one of the values of the indicators, *NRc* or *NRv*, is below the threshold, a fault is detected in the PV system. Moreover, an internal data logger interface of the inverter can be used for the transmission of the measured data and the alarm event to a server or a local network through a standard RS485, an Ethernet connection or optionally with a GSM Modem.

Table 2.5.1 shows the most probable faults present in the PV system based on the values of the ratios *NRc* and *NRv*.

Table 2.5. 1 Possible faults based on the values of the ratios NRc and NRv.

Possible Faults	**NRc**	**NRv**
No Fault	OK	OK
String Fault	Below Threshold	OK
Short-Circuited Modules	OK	Below Threshold
Short-Circuited Modules & String Fault.	Below Threshold	Below Threshold
Partial shadow, Inverter disconnection	Below threshold for (short duration)	Below threshold for (short duration)

In case of permanent faults in the PV array, short-circuits or open-circuits, the corresponding current or voltage indicators always remains below its threshold depending on the number of faulty strings and bypassed PV modules of the PV generator.

The presence of partial shadows on the PV array can also be detected by means of current and voltage indicators when they present values below their respective thresholds for short periods of time. The output current of the PV generator is reduced by the number of PV modules affected by shading. The most shaded PV module in a chain limits the total current in that chain. Moreover, there is also a reduction in the output voltage of the PV array due to shadow.

Both effects, current and voltage reduction, can be observed at the same time or separately depending on the shadow profile and the configuration of the PV array. Furthermore, in most cases these effects disappear quickly due to the dynamic behaviour of the irradiance profile on the PV field unless a PV module has been completely damaged resulting in a permanent fault.

The overall decrease in the output voltage depends on the number of bypass diodes that are activated in the PV modules that form the PV generator [44]. The following Eqs. (*2.5*-17) and (*2.5*-19) allow identifying the number of bypassed modules and the equivalent number of faulty strings in the PV array respectively in the presence of faults.

The total percentage of reduction in output voltage, ΔV, can be expressed as follows:

$$\Delta V = \left(\frac{V_{mo} - V_m}{V_{mo}}\right) = \left(1 - \frac{NRv}{NRvo}\right) \qquad (2.5\text{-}16)$$

Considering a number of N_{sg} PV modules connected in series by string in the array, the number of PV modules bypassed, *BPmod*, are given by:

$$BPmod = \Delta V \, N_{sg} \qquad (2.5\text{-}17)$$

Similarly, the normalized reduction of output current, ΔI, varies according to the following expression:

$$\Delta I = \left(\frac{I_{mo} - I_m}{I_{mo}}\right) = \left(1 - \frac{NRc}{NRco}\right) \quad (2.5\text{-}18)$$

If the PV array is formed by N_{pg} strings of PV modules connected in parallel, the output current losses can be translated to number of equivalent strings in open-circuit. The number of equivalent faulty strings, *Efs*, is given by:

$$Efs = \Delta I \, N_{pg} \quad (2.5\text{-}19)$$

The proportion of DC-power losses due to the presence of faults, *Ploss*, can also be evaluated from Eqs. (*2.5*-16) and (*2.5*-18) as follows:

$$Ploss = \left(1 - \frac{NRc}{NRco}\frac{NRv}{NRvo}\right) \quad (2.5\text{-}20)$$

The accuracy of the method depends on the errors in the estimation of main parameters involved in the equations, mainly: I_{sc}, V_{oc}, I_{mo}, V_{mo}, I_m and V_m. The RMSE in (%) between real measured data and values obtained from equations are in the range of 2–4% for voltages and currents, depending on the employed parameters extraction procedure.

It is important to apply this method by using inverters with smart maximum power point tracking (MPPT) techniques, because the accuracy on the evaluation of V_m and I_m will depend of the inverter capability to track the MPP. If the inverter is trapped at a local maximum the values of *NRc* and *NRv* will be lower than the values corresponding to the real MPP, while the values of *NRco*, *NRvo*, TNR_{cfs} and TNR_{vbm} are independent of the real value of the MPP. So, in that situation the algorithm will detect power losses due to the differences between the real MPP and the local MPP tracked by the inverter and then the presence of faults will be indicated. However, the method will not be able to tell whether the failure is due to incorrect tracking of the MPP (inverter) or shade in the photovoltaic field.

2.6. Degradation study of TFPV modules

The characterisation of degradation of TFPV modules is one of the aims of the present thesis. Two different techniques based on the analysis of the evolution of the DC-output power of the PV module were used. The combination of these two techniques allows a good approach to understand the degradation effects and helps to identify better the degradation rates, stabilization periods and seasonal variations.

2.6.1. Effective peak power technique

The effective peak power technique allows the determination of the degradation rate (R_D) per year of the PV module under study. The R_D value is obtained from the linear trend line of the evolution of the effective peak power, P_M^*, along the monitoring campaign.

The effective peak power of a PV module, P_M^*, at STC is given by the following equation [45,46]:

$$P_M^* = \frac{G^* P_{DC}}{G\,[1 + \gamma(T_c - T_c^*)]} \qquad (2.6\text{-}1)$$

where; P_{DC}, G and T_c are the DC-output power of the PV module, the irradiance and cell temperature respectively, γ is the power temperature coefficient of the PV modules and G^* and T_c^* are the irradiance and temperature at STC, respectively.

The power coefficient temperature γ is normally stated in the PV manufacturer's datasheet. Nevertheless, it can be calculated as follows [47]:

$$\gamma = \frac{1}{P_{max}} \frac{\partial P_{max}}{\partial T} \qquad (2.6\text{-}2)$$

where; P_{max} is the maximum power of PV module at STC.

Outdoor monitoring is subject to continuously changing operating conditions as irradiation, temperature and spectrum. The evaluation of P_M^* requires a preliminary filtering of irradiance values (G) in order to avoid the influence of operational anomalies, such as shade on the PV array, inverter saturation, inverter–off, low irradiances, etc [45,46]. Thus, the monitored data corresponding to irradiance values $G < 700$ W/m^2 were disregarded before the calculation of P_M^* values.

The degradation rate, R_D, can be analysed by a linear least square fitting method. This method is applied to the monthly effective peak power of the PV module, P_M^*, calculated by using Eq. (*2.6*-3) and monitored data. Using the trend line, the degradation per year can be calculated by linear regression (LR) equation as follows [48,49]:

Equation of the trend line:

$$y = mx + c \qquad (2.6\text{-}3)$$

where; m is the slope of line and c is the y intercept, thus the degradation per year: R_D (%) can be calculated as follows [48]:

$$R_D = 100\frac{12m}{c} \quad (2.6\text{-}4)$$

The analysis of the stabilization period of TFPV modules is based on a second monitoring data filtering process following the procedure used in previous works [50]. The aim of such data filtering is to keep the external conditions (module temperature, T_c, and irradiance, G) as steady as possible, while observing the changes of P_{DC} over the time. Therefore, one point for each month is extracted from the monitored data, which falls in a very narrow range of irradiance and temperature.

The restricted ranges of the tilted irradiance and PV module temperature are chosen according to the PV module technology and the climate of the site where the PV module is installed. For example, ranges of: 900 W/m^2 < G < 905 W/m^2 and 48.6 ºC < T_c < 54 ºC, could be selected.

Finally, the values of P_{DC} corresponding to the points obtained with this filtering process are then plotted in a graph, from which the stabilization period can be observed.

2.6.2. Power-Irradiance technique

The power-irradiance (P-G) technique is the second method used in the present thesis to assess the stabilization period of the TFPV modules. This method was defined in [50], and it is based on the observation of the variation of the real DC-output power of the PV module as a function of the solar irradiance in between two boundary indicators; predicted initial and stabilized data values of PV array DC-output power.

The two boundaries, predicted initial, Pdc_{init}, and stabilized, Pdc_{stab}, depend on the measured plane-of-array irradiance (G), module temperature (T_c), and are calculated by using the following equations:

$$Pdc_{init} = N_{sg} \cdot N_{pg} \cdot Pm_{init} \cdot \eta \cdot G_{eff} \cdot (1 + kv \cdot \Delta T) \cdot (1 - ki \cdot \Delta T) \quad (2.6\text{-}5)$$

$$Pdc_{stab} = N_{sg} \cdot N_{pg} \cdot Pm_{stab} \cdot \eta \cdot G_{eff} \cdot (1 + kv \cdot \Delta T) \cdot (1 - ki \cdot \Delta T) \quad (2.6\text{-}6)$$

$$G_{eff} = \frac{G}{G^*} \quad (2.6\text{-}7)$$

$$\Delta T = T_c - T_c^* \quad (2.6\text{-}8)$$

where; N_{sg} and N_{pg} are the number of PV modules connected in series and parallel respectively, Pm_{init} is the initial measured peak power of PV module, kv and ki are the voltage and current

temperature coefficients respectively provided in the manufacturer's data sheet ($^oC^{-1}$), Pdc_{stab} is the predicted array DC-power referred to stabilized, Pm_{stab} is the stabilized peak power of the PV module found in the manufacturer's data sheet, η is the efficiency referred to all general system losses which changes between 0.89 in summer and 0.86 in winter months, G^* and T_c^* are the reference irradiance and cell temperature respectively at STC.

This method also requires a preliminary data filtering process in order to avoid problems caused by low values of irradiance. As for the evaluation of the R_D described in section before, all data points corresponding to irradiance values $G < 700$ W/m^2 are disregarded.

A Linear Correlation Approach (LCA) was used to obtain monthly linear regression equations from the actual PV modules DC-outputs, $P_{DC,}$ as a function of the irradiance, G, by means of the following equation:

$$P_{DC} = A_{Gr}.G + C \qquad (2.6\text{-}9)$$

where; Pdc is the array DC-output power, A_{Gr} is the gradient, G is the plan-of-array irradiance and C is the ordinate value of Pdc at $G = 0$.

Finally, the monthly gradient values, A_{Gr}, of each empirical equation can be plotted to determine the stabilization period of the TFPV module under study [50].

References

[1] PVGIS. http://re.jrc.ec.europa.eu/pvgis/apps4/pvest.php
(accessed November 15, 2016).

[2] System Advisor Model (SAM). https://sam.nrel.gov/
(accessed November 15, 2016).

[3] SolarMax. http://www.solarmax.com/en/maxdesign/
(accessed November 15, 2016).

[4] PVsol. http://www.valentin-software.com/en
(accessed November 15, 2016).

[5] Insel. http://www.insel.eu/index.php?id=73&L=1
(accessed November 15, 2016).

[6] Data Design System. http://www.dds-cad.net/products/dds-cad-pv/
(accessed November 15, 2016).

[7] PVSYST. http://www.pvsyst.com/fr/software
(accessed November 15, 2016).

[8] MATLAB n.d. www.mathworks.com/
(accessed November 15, 2016).

[9] Castañer L, Silvestre S. Modelling Photovoltaic Systems using PCspice 2002. doi:10.1002/0470855541.

[10] McEvoy AJ (Augustin J, Markvart T, Castañer L. Practical handbook of photovoltaics : fundamentals and applications. Academic Press; 2012.

[11] Chenni R, Makhlouf M, Kerbache T, Bouzid a. A detailed modeling method for photovoltaic cells. Energy 2007;32:1724–30. doi:10.1016/j.energy.2006.12.006.

[12] Xiao W, Dunford WG, Capel A. A novel modeling method for photovoltaic cells. PESC Rec - IEEE Annu Power Electron Spec Conf 2004;3:1950–6. doi:10.1109/PESC.2004.1355416.

[13] Ishaque K, Salam Z, Taheri H. Simple, fast and accurate two-diode model for photovoltaic modules. Sol Energy Mater Sol Cells 2011;95:586–94. doi:10.1016/j.solmat.2010.09.023.

[14] Brendel R, Aberle A., Cuevas A., Glunz S, Hahn G, Poortmans J, et al. Considering the Distributed Series Resistance in a Two-diode Model. Energy Procedia 2013;38:167–75. doi:10.1016/j.egypro.2013.07.264.

[15] Ishaque K, Salam Z, Taheri H, Syafaruddin. Modeling and simulation of photovoltaic (PV) system during partial shading based on a two-diode model. Simul Model Pract Theory 2011;19:1613–26. doi:10.1016/j.simpat.2011.04.005.

[16] Alonso-García MC, Ruíz JM. Analysis and modelling the reverse characteristic of photovoltaic cells. Sol Energy Mater Sol Cells 2006;90:1105–20. doi:10.1016/j.solmat.2005.06.006.

[17] Bishop JW. Computer simulation of the effects of electrical mismatches in photovoltaic cell interconnection circuits. Sol Cells 1988;25:73–89. doi:10.1016/0379-6787(88)90059-2.

[18] Silvestre S, Chouder A. Effects of shadowing on photovoltaic module performance. Prog Photovoltaics Res 2008.

[19] Celik AN Acikgoz N. Modelling and experimental verification of the operating current of mono-crystalline photovoltaic modules using four and five parameter models. Appl Energy 2007:1–15.

[20] Cameron CP, Stein JS, Tasca C a. PV performance modeling workshop summary report 2011:1–92.

[21] King DL, Gonzalez S, Galbraith GM, Boyson WE. Performance Model for Grid-Connected Photovoltaic Inverters, SAND2007-5036. Contract 2007;38:655–60.

[22] Chouder A., Silvestre S. Analysis Model of Mismatch Power Losses in PV Systems. J Sol Energy Eng 2009;131:24504. doi:10.1115/1.3097275.

[23] Oliva D, Cuevas E, Pajares G. Parameter identification of solar cells using artificial bee colony optimization. Energy 2014;72:93–102. doi:10.1016/j.energy.2014.05.011.

[24] Garoudja E, Kara K, Chouder A, Silvestre S. Parameters extraction of photovoltaic module for long-term prediction using artifical bee colony optimization. 2015 3rd Int Conf Control Eng Inf Technol 2015:1–6. doi:10.1109/CEIT.2015.7232993.

[25] Lourakis MI A. A Brief Description of the Levenberg-Marquardt Algorithm Implemened by levmar. Matrix 2005;3:2. doi:10.1016/j.ijinfomgt.2009.10.001.

[26] Lampton M. Damping-undamping strategies for the Levenberg-Marquardt nonlinear least-squares method. Comput Phys 1997;11:110–5. doi:10.1063/1.168600.

[27] Dkhichi F, Oukarfi B, Fakkar A, Belbounaguia N. Parameter identification of solar cell model using Levenberg-Marquardt algorithm combined with simulated annealing. Sol Energy 2014;110:781–8. doi:10.1016/j.solener.2014.09.033.

[28] Zagrouba M, Sellami a., Bouaïcha M, Ksouri M. Identification of PV solar cells and modules parameters using the genetic algorithms: Application to maximum power extraction. Sol Energy 2010;84:860–6. doi:10.1016/j.solener.2010.02.012.

[29] Ismail MS, Moghavvemi M, Mahlia TMI. Characterization of PV panel and global optimization of its model parameters using genetic algorithm. Energy Convers Manag 2013;73:10–25. doi:10.1016/j.enconman.2013.03.033.

[30] Bastidas-Rodriguez JD, Petrone G, Ramos-Paja CA, Spagnuolo G. A genetic algorithm for identifying the single diode model parameters of a photovoltaic panel. Math Comput Simul 2015. doi:10.1016/j.matcom.2015.10.008.

[31] Storn R, Price K. Differential Evolution -- A Simple and Efficient Heuristic for global Optimization over Continuous Spaces. J Glob Optim 1997;11:341–59. doi:10.1023/A:1008202821328.

[32] Eberhart R, Kennedy J. A new optimizer using particle swarm theory. MHS'95 Proc Sixth Int Symp Micro Mach Hum Sci 1995:39–43. doi:10.1109/MHS.1995.494215.

[33] Karaboga D, Akay B. A comparative study of Artificial Bee Colony algorithm. Appl Math Comput 2009;214:108–32. doi:10.1016/j.amc.2009.03.090.

[34] Karaboga D. An idea based on honey bee swarm for numerical optimization 2005.

[35] Karaboga D, Basturk B. On the performance of artificial bee colony (ABC) algorithm. Appl Soft Comput 2008.

[36] Chouder A. Analysis, Diagnosis and Fault Detection in Photovoltaic Systems. UPC, 2010.

[37] Avrutin V, Izyumskaya N. Amorphous and micromorph Si solar cells: current status and outlook. Turkish J 2014.

[38] Gordon A. Programación con COM y COM+ 2001.

[39] Liu J, Lim K, Ho W, Tan K, Tay A. Using the OPC standard for real-time process monitoring and control. IEEE 2005.

[40] Holley DW. Understanding and using OPC for maintenance and reliability applications. Comput Control Eng 2004;15:28–31. doi:10.1049/cce:20040106.

[41] Martínez Marchena I, Sidrach-de-Cardona M, Mora-López L. Framework for Monitoring and Assessing Small and Medium Solar Energy Plants. J Sol Energy Eng 2014;137:21007. doi:10.1115/1.4028398.

[42] Martinez Marchena I. MARCO DE TRABAJO PARA LA GENERACION DE SOFTWARE PARA LA GESTION DE SISTEMAS DE ENERGIA SOLAR. University of Malaga, 2015.

[43] Silvestre S, Silva MA Da, Chouder A, Guasch D, Karatepe E. New procedure for fault detection in grid connected PV systems based on the evaluation of current and voltage indicators. Energy Convers Manag 2014;86:241–9.

[44] Dolara A, Lazaroiu GC, Leva S, Manzolini G. Experimental investigation of partial shading scenarios on PV (photovoltaic) modules 2013.

[45] Martínez-Moreno F, Lorenzo E, Muñoz J, Moretón R. On the testing of large PV arrays. Prog Photovoltaics Res Appl 2012;20:100–5. doi:10.1002/pip.1102.

[46] Muñoz J, Lorenzo E, Carrillo JM, Moretón R. Design of a twin capacitive load and its application to the outdoor rating of photovoltaic modules. Prog Photovoltaics Res Appl 2015;23:247–52. doi:10.1002/pip.2425.

[47] Spataru S, Hacke P, Sera D, Packard C, Kerekes T, Teodorescu R. Temperature-dependency analysis and correction methods of in situ power-loss estimation for crystalline silicon modules undergoing potential-induced degradation stress testing. Prog Photovoltaics Res Appl 2015;23:1536–49. doi:10.1002/pip.2587.

[48] Sharma V, Sastry OS, Kumar A, Bora B, Chandel SS. Degradation analysis of a-Si, (HIT) hetro-junction intrinsic thin layer silicon and m-C-Si solar photovoltaic technologies under outdoor conditions. Energy 2014;72:536–46. doi:10.1016/j.energy.2014.05.078.

[49] Phinikarides A, Kindyni N, Makrides G, Georghiou GE. Review of photovoltaic degradation rate methodologies. Renew Sustain Energy Rev 2014;40:143–52. doi:10.1016/j.rser.2014.07.155.

[50] Hussin MZ, Shaari S, Omar AM, Zain ZM. Amorphous silicon thin-film: Behaviour of light-induced degradation. Renew Sustain Energy Rev 2015;43:388–402. doi:10.1016/j.rser.2014.10.093.

3. Publications

3.1. Published paper in Renewable Energy 99 (2016)

Renewable Energy 99 (2016) 270 – 279
http://dx.doi.org/10.1016/j.renene.2016.07.002

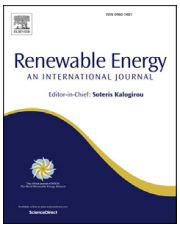

Comparison of two PV array models for the simulation of PV systems using five different algorithms for the parameters identification

Sofiane Kichou[1], Santiago Silvestre[1], Letizia Guglielminotti[1], Llanos Mora-López[2] and Emilio Muñoz-Cerón[3]*

[1] MNT Group, Electronic Engineering Department, UPC-BarcelonaTech. Barcelona, C/ Jordi Girona 1-3, Mòdul C4 Campus Nord UPC, 08034 Barcelona, Spain.

[*] Corresponding author: E-mail addresses: kichousofiane@gmail.com

[2] Dpto. Lenguajes y Ciencias de la Computación, Universidad de Málaga Campus de Teatinos, sn, Málaga 29071, Spain

[3] IDEA Research Group, University of Jaén, Campus de Las Lagunillas, 23071, Jaén, Spain.

ARTICLE INFO

Article history:

Received 19 April 2016
Received in revised form
30 June 2016
Accepted 3 July 2016

Keywords:

PV modelling,
Simulation,
Parameter extraction,
Metaheuristic algorithms.

ABSTRACT

Simulation is of primal importance in the prediction of the produced power and automatic fault detection in PV grid-connected systems (PVGCS). The accuracy of simulation results depends on the models used for main components of the PV system, especially for the PV module. The present paper compares two PV array models, the five-parameter model (5PM) and the Sandia Array Performance Model (SAPM). Five different algorithms are used for estimating the unknown parameters of both PV models in order to see how they affect the accuracy of simulations in reproducing the outdoor behaviour of three PVGCS. The arrays of the PVGCS are of three different PV module technologies: Crystalline silicon (c-Si), amorphous silicon (a-Si:H) and micromorph silicon (a-Si:H/µc-Si:H).

The accuracy of PV module models based on the five algorithms is evaluated by means of the Route Mean Square Error (RMSE) and the Normalized Mean Absolute Error (NMAE), calculated for different weather conditions (clear sky, semi-cloudy and cloudy days). For both models considered in this study, the best accuracy is obtained from simulations using the estimated values of unknown parameters delivered by the ABC algorithm. Where, the maximum error values of RMSE and NMAE stay below 6.61% and 2.66% respectively.

3.1.1. Introduction

The photovoltaic (PV) market has grown rapidly in recent years worldwide, especially in developed countries, where this growth has been exponential. One of the main reasons for the high growth of the PV industry is the reduction of the cost of PV generation as well as the improvement of the quality and performance of the electronics associated with these generation systems. The monitoring and regular performance supervision on the functioning of grid-connected PV systems is basic to ensure an optimal energy harvesting and reliable power production at competitive costs. Detecting faults in PV systems can minimize generation losses by reducing the time in which the system is working below its point of maximum power generation. In this context, the development of accurate automatic fault detection procedures is crucial [1–3]. Main faults in PV systems are caused by short-circuits or open-circuits in PV modules, inverter disconnections and the presence of shadows on the PV array plane [4–6].

On the other hand, the integration of grid-connected PV systems also requires the capability of managing the uncertainty related to the fluctuating energy output inherent to these generation plants. For this purpose, it is very important to develop accurate forecasting models in order to achieve an easy integration of PV generation plants into traditional power distribution systems [7,8].

Simulation plays a crucial role in both outdoor behaviour forecasting and automatic fault detection of grid-connected PV systems. The precision of simulation results depends on the models used for the main components of the PV system, especially the PV module models [9,10]. Moreover, the accuracy of the PV module models is strongly affected by the way of extracting their unknown parameters. Several research works discussed the topic of PV model parameters estimation, by applying different methods based on analytical [11], numerical [12,13] and bio-inspired optimization solution [14–20].

Previous works investigated the accuracy of PV module models focusing on the I-V curve of the PV module [21–24] or on the I-V characteristic of a PV array [25]. The objective of this study is to compare two PV array models to analyse the simulation of grid-connected PV systems in real conditions of work. The accuracy of the simulations in reproducing the actual behaviour of the PV system is evaluated by means of the results obtained from different parameter extraction techniques based on five algorithms: Levenberg–Marquardt algorithm (LMA), genetic algorithm (GA), particle swarm optimization (PSO), differential evolution (DE) and artificial bee colony (ABC) algorithm.

The two PV array models included in this study are the five-parameter model (5PM) [26,27] and the Sandia Array Performance Model (SAPM) developed by [28]. Three real grid-connected PV systems are included in the study to validate the accuracy of the models. Each one of the PV systems is formed by PV modules of different technologies: Crystalline silicon (c-Si), amorphous silicon (a-Si:H) and micromorph silicon (a-Si:H/μc-Si:H) in order to outline differences in the prediction due to solar cell type.

The remainder of the paper is organized as follows: In section 2, the PV systems included in the study are described. The PV array models and the parameters extraction techniques used in this study are summarized in sections 3 and 4 respectively. Results obtained are shown in section 5. Finally, conclusions are detailed in section 6.

3.1.2. Description of the PV systems

Three grid connected PV systems formed by PV modules of different technologies were used in this study.

The first PV system is located in San Sebastián (Spain). The PV array is formed by 30 c-Si PV modules with a peak power of 4.8 kWp connected to a single phase inverter.

The other two PV systems are sited in Jaén (Spain). Each PV array is connected to single phase inverter with AC nominal powers of 1.2kW. One of the PV arrays is formed of 15 a-Si:H PV modules, rated 60-W peach, and the second PV array consists of 8 micromorph PV modules, rated 110-Wp each. Main characteristics of the PV systems and PV modules forming the arrays are given in Table 3.1.1 and Table 3.1.2 respectively.

The following parameters were monitored in the three PV arrays: Current, voltage, power (DC and AC), cosine (ϕ), frequency, irradiance and module temperature with a sampling rate of 5 min.

In the PV system located in San Sebastián, the irradiance was measured by using a calibrated solar cell installed in the plane of the modules. The module temperature was measured using a Pt100 sensor fitted to the back of the module, in the middle of a cell. The internal data acquisition card of the inverter recorded both parameters.

The monitoring system included in the PV arrays located in Jaén consists of three SMA Sunny SensorBox devices, installed in the same plane as the PV generators, capable to measure solar radiation, module and ambient temperatures together with wind speed. Two Pt100 RTD

were pasted to the rear surface of the modules under test to measure the cell temperature in each PV array. An anemometer and a temperature probe were also available. All sensors were supplied by SMA and connected to three Sunny SensorBox devices. An additional irradiance sensor, aKipp & Zonen CMP11pyranometer, was also installed and connected to one of the latter devices. The three of them were serially connected to the inverters via a RS-485 bus and then to a Sunny Webbox, from which environmental and operation could be retrieved.

Table 3.1. 1 PV systems description.

Main Parameters	**PV system 1**	**PV system 2**	**PV system 3**
PV Module	c-Si	a-Si:H/µc-Si:H	a-Si:H
Location	San Sebastián (Spain) Latitude: 43º 17' 9.8" N Longitude: 1º 59' 55.4 " W Altitude: 41 m.	Jaén (Spain) Latitude: 37º 47' 14.35" N Longitude: 3º 46' 39.73 " W Altitude: 511 m	
Nominal power	4.8 kWp	880 Wp	900 Wp
Modules per inverter	30	8	15
Modules in series (*Nsg*)	15	4	3
Strings in parallel (*Npg*)	2	2	5
Tilt - Orientation	20º - 9º East	30º - 0º South	35º- 0º South
Inverter	Ingecon SUN 5 Single-phase inverter 5kW	Sunny Boy SB1200 Single-phase inverter 1.2 kW	

Table 3.1. 2 Main parameters of PV modules.

PV module Parameters	**PV system 1**	**PV system 2**	**PV system 3**
Isc (A)	9.46	2.5	1.19
Voc (V)	22.2	71	92
Current at Maximum Power Point: Impp (A)	8.65	2.04	0.9
Voltage at Maximum Power Point: Vmpp (V)	18.5	54	67
Temperature Coefficient of Voc β_{Voc} (V/ºC)	- 0.084	-0.248	-0.280
Temperature Coefficient of Isc α_{Isc} (A/ºC)	$4.60\ 10^{-3}$	1.4010^{-3}	$0.89\ 10^{-3}$

3.1.3. PV array models

As it has been previously mentioned, the two PV array models included in this study are the 5PM [26,27,29] and the SAPM developed by [28].

The 5PM, also called one diode model, is one of the most used in simulation of PV modules and arrays. Moreover, root mean square errors (RMSE) of 4.26% [3], 4.39% [30] and 5.12% [31] were reported in the estimation of the energy produced by grid-connected PV systems in simulations of dynamic behaviour of c-Si PV generators by using this model. On the other hand, simulations of a-Si PV arrays by using the SAPM model have obtained errors below 4.1% on sunny days [32]. In our approach, the model parameters are calculated by means of parameter extraction methods having as main input data daily actual profiles of module temperature, irradiance on the PV array plane and output voltage and current of the PV array.

3.1.3.1. Five-parameter model

The 5PM of a solar cell includes a parallel combination of a photogenerated controlled current source I_{ph}, a diode, described by the well-known single-exponential Shockley equation [33], a shunt resistance R_{sh} and a series resistance R_s modelling the power losses.

The I-V characteristic of a solar cell is given by an implicit and nonlinear equation as follows:

$$I = I_{ph} - I_o\left(e^{\left(\frac{V+R_sI}{nV_t}\right)} - 1\right) - \left(\frac{V + R_sI}{R_{sh}}\right) \quad (3.1\text{-}1)$$

where I_o and n are the reverse saturation current and ideality factor of the diode respectively and V_t is the thermal voltage.

Eq. (*3.1*-1) can also be written as follows,

$$I = I_{ph} - I_d - I_{sh} \quad (3.1\text{-}2)$$

where I_d and I_{sh} are the currents across the diode and shunt resistance respectively.

The photogenerated current can be evaluated for any arbitrary value of irradiance, G, and cell temperature, T_c, by using the following equation:

$$I_{ph} = \frac{G}{G^*}I_{sc} + k_i(T_c - T_c^*) \quad (3.1\text{-}3)$$

where G^* and T_c^* are respectively the irradiance and cell temperature at standard test conditions (STC): 1000 W/m^2 (AM1.5) and 25ºC, ki (A/ºC) is the temperature coefficient of the current and I_{sc} (A) is the solar cell short-circuit current at STC.

Some PV modules are formed by parallel strings of solar cells connected in series. However, most PV modules include one single string of solar cells. Therefore, the model of the solar cell can be scaled up to the model of the PV module using the following equations (*3.1*-4) – (*3.1*-8):

$$I_M = N_pI \quad (3.1\text{-}4)$$

$$I_{scM} = N_pI_{sc} \quad (3.1\text{-}5)$$

$$V_M = N_sV \quad (3.1\text{-}6)$$

$$V_{ocM} = N_sV_{oc} \quad (3.1\text{-}7)$$

$$R_{sM} = \frac{N_s}{N_p}R_s \quad (3.1\text{-}8)$$

where subscript M stands for 'Module', N_s is the number of solar cells connected in series and N_p is the number of parallel branches of solar cells forming the module.

Then, the output current of the PV module, I_M, is obtained rewriting Eq. (*3.1*-2) as follows:

$$I_M = N_p\left(I_{ph} - I_{dM} - I_{shM}\right) \quad (3.1\text{-}9)$$

The diode current, I_{dM}, included in Eq (*3.1*-9) is given by:

$$I_{dM} = I_{oM}\left[e^{\left(\frac{V_M + I_M R_{sM}}{n\, N_s V_t}\right)} - 1\right] \quad (3.1\text{-}10)$$

where V_M (V) and I_M (A), are the output voltage and current of the PV module respectively.

The saturation current of the diode I_{oM} (A) depends strongly on temperature and it is given by:

$$I_{oM} = \frac{I_{scM} e^{\left(\frac{E_{go}}{V_{to}} - \frac{E_g}{V_t}\right)}}{N_p\left(e^{\left(\frac{V_{ocM}}{n\, N_s V_{to}}\right)} - 1\right)}\left(\frac{T_c}{T_c^*}\right)^3 \quad (3.1\text{-}11)$$

where I_{scM} and V_{ocM} are the short-circuit current and the open-circuit voltage of the PV module respectively, V_{to} is the thermal voltage at STC, E_g the energy bandgap of the semiconductor and E_{go} is the energy bandgap at T=0 K.

The value of the energy bandgap of the semiconductor at any cell temperature T_c is given by:

$$E_g = E_{go} - \frac{\alpha gap\, T_c^2}{\beta gap + T_c} \quad (3.1\text{-}12)$$

where α_{gap} and β_{gap} are fitting parameters characteristic of the semiconductor.

Finally, the current I_{shM}, also included in Eq. (*3.1*-9) is given by the following equation:

$$I_{shM} = \frac{V_M + I_M R_{sM}}{N_p R_{shM}} \quad (3.1\text{-}13)$$

The same procedure can be applied to scale up the model of the PV module to the model of a PV array by taking into account the number of PV modules connected in series by string, N_{sg}, and the number of parallel strings in the PV array, N_{pg} [27].

3.1.3.2. SAPM Model

The SAPM model is an empirical model defined by the following equations [28]. The PV array power at the maximum power point (MPP), *Pmp* (W), is evaluated as follows:

$$Pmpg = Impg \times Vmpg \quad (3.1\text{-}14)$$

where, *Impg* (A) and *Vmpg* (V) are the coordinates of the MPP of the PV array.

The model uses the normalized irradiance, *Ee,* defined as follows,

$$Ee = \frac{G}{G^*} \quad (3.1\text{-}15)$$

Then, the current and voltage of the MPP of the PV array can be calculated by using the following equations:

$$Impg = N_{pg}\left[Impo(C_0 Ee + C_1 Ee^2)\left(1 + \alpha_{Imp}(T_c - T_c^*)\right)\right] \quad (3.1\text{-}16)$$

$$Vmpg = N_{sg}\left[Vmpo + C_2 N_s \delta(T_c) ln(Ee) + C_3 N_s (\delta(T_c) ln(Ee))^2 + \beta_{Vmp} Ee(T_c - T_c^*)\right] \quad (3.1\text{-}17)$$

$$\delta(T_c) = nk(T_c + 273.15)/q \quad (3.1\text{-}18)$$

where, *Impo* (A) and *Vmpo* (V) are the PV module current and voltage of the MPP at STC, C_0 and C_1 are empirically determined coefficients (dimensionless) which relate *Imp* to the effective irradiance, $C_0+C_1=1$, α_{Imp} ($°C^{-1}$) is the normalized temperature coefficient for Imp, C_2 (dimensionless) and C_3 (V^{-1}) are empirical coefficients which relate *Vmp* to the effective irradiance, $\delta(T_c)$ is the thermal voltage per cell at temperature T_c, q is the elementary charge, $1.60218\ 10^{-19}$ (coulomb), k is the Boltzmann's constant, $1.38066\ 10^{-23}$ (J/K) and β_{Vmp} (V/°C) is the temperature coefficient for module *Vmp* at STC.

The models contain several coefficients and parameters that must be calculated because are not routinely provided by the PV module's manufacturer. For this purpose, we used the parameter extraction technique described in the following section.

3.1.4. Parameter extraction techniques

The parameter extraction techniques employed in this study are based on five optimization algorithms that evaluate the model parameters of the two PV array models in real conditions of work, using as inputs daily profiles of solar irradiance and cell temperature together with monitored DC output current and voltage.

For the five-parameter model of the PV module, the model parameters: I_{ph}, I_o, n, R_s, and R_{sh} are evaluated by using Eqs. (*3.1*-3) – (*3.1*-13) and actual daily profiles of monitored current

and voltage at the DC output of the three PV arrays included in the study, together with actual daily profiles of G and T_c at the specific locations detailed in section 2.

Regarding the SAPM, the same idea is considered for the estimation of the empirical coefficients of the model parameters: C_0, C_1, C_2, C_3, n, α_{Imp} and β_{Vmp} using Eqs. (*3.1*-15) – (*3.1*-18).

The objective function for optimization using metaheuristic algorithms is defined as the RMSE of the error of all data points given by Eq. (*3.1*-19) [19,34], where the N represent the number of measured data, Vi and Ii represent the measured voltage and current of the data point i.

$$S(\theta) = \sqrt{\frac{1}{N}\sum_{i=1}^{N}[Ii - I(Vi,\theta)]^2} \qquad (3.1\text{-}19)$$

where $\theta = f(I_{ph},I_o,n,R_s,R_{sh})$ for the five parameter model and $\theta = f(C_0, C_1, C_2, C_3, n, \alpha_{Imp}, \beta_{Vmp})$ for the SAPM.

The parameter extraction algorithms implemented in MATLAB/Simulink environment are executed until function $S(\theta)$, given by Eq. (*3.1*-19), is minimized. Figs. 3.1.1 and 3.1.2 show the Simulink block diagram of the 5PM and SAPM used in the parameter extraction procedures. Thus, the result of the parameter extraction algorithms is a set of PV module parameters for the 5PM and a set of empirical parameters for the SAPM that allow the best approach to the real daily evolution of DC output current and voltage of the PV arrays.

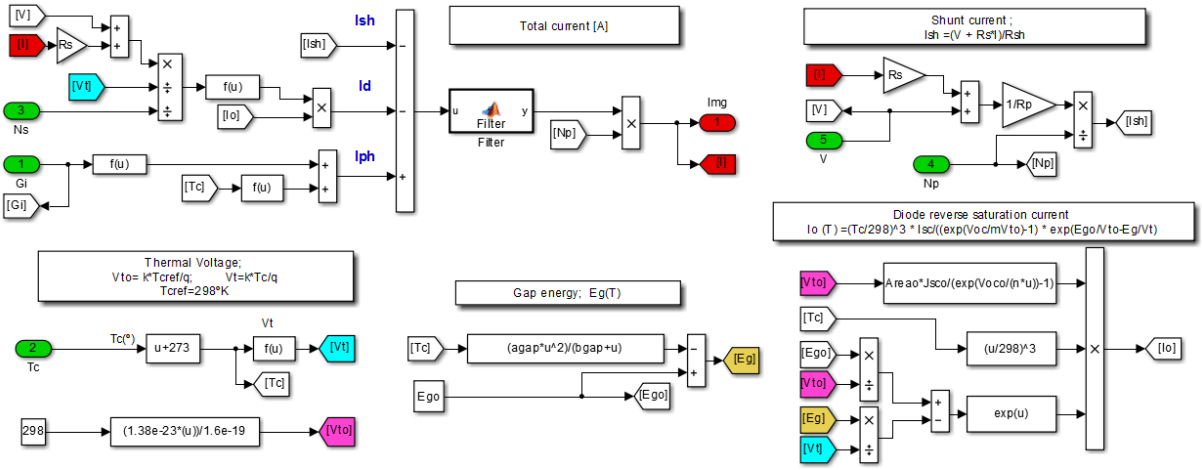

Figure 3.1. 1 Simulink block diagram for the 5PM.

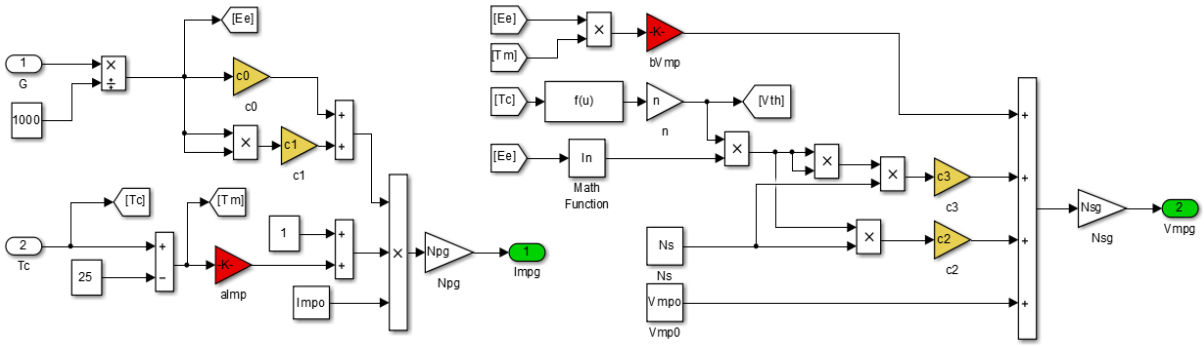

Figure 3.1. 2 Simulink block diagram for the SAPM.

Two parameter extraction methods are used in this study. The first method is a numerical solution based on Levenberg–Marquardt algorithm (LMA) detailed in a previous work [12]. The second method is based on different metaheuristic algorithms (GA, DE, PSO and ABC) which are described below.

3.1.4.1. Genetic algorithm

The Genetic Algorithm (GA) developed by John Holland in the 1970s is a technique for solving constrained and unconstrained optimization problems inspired from the biological evolution.

The optimization function is encoded as arrays of binary character strings representing the chromosomes. The fitness of chromosomes in the population is evaluated by the objective function for each iteration. Fitter chromosomes are stochastically selected in terms of the elitist strategy, which ensures the progeny chromosomes inherit the best possible combination of the genes of their parents. Some of the chromosomes in the population are modified via genetic operators like crossover and mutation, forming new chromosomes for the next generation. The reason why GA applies crossover and mutation may lie in their capability of avoiding local optima in the searching process. Several researches applied GA to extract the parameters of a PV model from measured I–V curves [17,35].

In this paper, the genetic algorithm available in the Global Optimization toolbox of MATLAB has been used for minimizing the objective function Eq. (*3.1*-19) [17].

3.1.4.2. Differential evolution

Differential evolution (DE) was proposed by Rainer Storn and Kenneth Price in 1997 [36]. Similar to other evolutionary algorithms, DE is a population based, derivative-free function

optimizer. An advantage of DE over GA is that DE treats possible solutions as real-number strings, and thus encoding and decoding are not required.

The target vector $x = [x_1, x_2, \ldots, x_i]$ where $i = 1,2,\ldots, NP$ represents a population of NP random candidate solutions. The vector of the ith particle, x_i indicates a series of parameters to be extracted, e.g. $x_i = [I_{ph}, I_o, n, R_s, R_{sh}]$ for the one-diode model and $x_i = [C_0, C_1, C_2, C_3, n, \alpha_{Imp}, \beta_{Vmp}]$. For a D-dimension optimization problem, a random candidate solution is given by:

$$x_j^{low} \leq x_{i,j} \leq x_j^{up} \qquad (3.1\text{-}20)$$

where x_j^{low} and x_j^{up} are the lower and the upper limits of the j[th] vector component respectively, $i = 1, 2, \ldots, NP$ and j = 1, 2, …, D.

After the initialization DE enters a loop of evolutionary operations: mutation, crossover and selection considering the maximum number of generations t_{max}, where $t = 1, 2,\ldots, t_{max}$.

In the mutation step, for each x_i at generation t, three vectors x_{r0}, x_{r1} and x_{r2} are chosen randomly from the set $\{1, 2, \ldots, NP\}\backslash\{i\}$ to generate a donor vector by:

$$v_i^{t+1} = x_{r0}^t + F(x_{r1}^t - x_{r2}^t) \qquad (3.1\text{-}21)$$

where F is a differential weight, known as scaling parameter, usually ranges in the interval [0, 1].

The crossover operation is used to decide whether to exchange with donor vector. By generating a random integer index $J_r \in [1, D]$ and a randomly distributed number $k_i \in [0, 1]$, the j[th] dimension of v_i, namely $u_{i,j}$, is updated according to:

$$u_{i,j}^{t+1} = \begin{cases} v_{i,j}^{t+1}, & k_i \leq CR \text{ or } i = J_r \\ x_{i,j}^t, & k_i > CR \text{ and } i \neq J_r \end{cases} \qquad (3.1\text{-}22)$$

where CR is a crossover probability in the interval [0, 1]. The crossover scheme formulated by Eq. (*3.1*-22) used in the present work is called binomial strategy.

The selection operation, selects the best one from the parent vector x_i^t, and the trial vector u_i^{t+1} solution with the minimum objective value, using the following expression:

$$x_i^{t+1} = \begin{cases} u_i^{t+1}, & f(u_i^{t+1}) \leq f(x_i^t) \\ x_i^t, & othewise \end{cases} \qquad (3.1\text{-}23)$$

where $f(x)$ is the fitness function to be minimized. Therefore, if a particular trial vector is found to result in lower fitness value, it will replace the existing target vector; otherwise, the target vector is retained.

3.1.4.3. Particle swarm optimization

Particle swarm optimization (PSO) is a population based stochastic optimization technique developed by Kennedy and Eberhart [16] and is inspired by the social behavior of bird flocking or fish schooling.

PSO search possible solution in a search space by adjusting the trajectories of particles. The best position encountered of the particle i is designed by $pbest_i$. In a swarm of particles, there are N local best positions, and the best solution is denoted by $gbest$.

The velocities and positions of particles, as well as the algorithm parameters (inertia weight w and learning parameters α, β) are firstly initialized. In an iteration t, the fitness of particles is evaluated individually by the objective function. By attracted toward $pbest_i$ and $gbest$, the particle moves according to the following expression:

$$x_i^{t+1} = x_i^t + v_i^{t+1} \quad (3.1\text{-}24)$$

where v_i^{t+1} is the velocity, expressed as:

$$v_i^{t+1} = wv_i^t + \alpha\epsilon_1(x_i^t - gbest^t) + \beta\epsilon_2(x_i^t - pbest_i^t) \quad (3.1\text{-}25)$$

$\alpha = 1.5$, $\beta = 2$. The random vectors ϵ_1 and ϵ_2 are in the range [0, 1]. The w is the inertia weight, used to balance global and local search abilities, it is considered constant and set equal to 0.9.

Finally, lower and upper boundaries are set to ensure that particles are within the predetermined range. The PSO will continue to search for better solutions until it meets the stopping criterion.

3.1.4.4. Artificial bee colony algorithm

The artificial bee colony algorithm (ABC) is an optimization algorithm inspired by the natural foraging behaviour of honey bees. It was successfully applied in the parameter extraction of solar cell models [19,34]. In the ABC, there are food sources representing the solutions of optimization problems and honey bees (classified into employed bees, onlooker bees and scout bees) representing the operations to the solutions. The employed bees investigate potential food sources and share information with onlooker bees. The food sources of higher quality will have higher possibility to be selected by onlooker bees. If the quality of the employed bees' food sources is relatively low, they will change to scout bees to randomly explore new potential food sources. Consequently, the exploitation is promoted by employed and onlooker bees while the exploration is performed by scout bees. The implementation of the

ABC algorithm in MATLAB is carried out by following the same steps of given in the previous works [19,34,37].

3.1.5. Results

The results of simulation of grid-connected PV systems in real conditions of work were obtained under different weather conditions: clear sky, semi-cloudy, and cloudy weather. The two PV array models described above were used for forecasting the output power of the three different PV systems using the extracted parameters delivered by the five algorithms.

The adjustable parameters chosen for the GA, DE, PSO and ABC algorithms and the lower and upper boundaries selected for each parameter are summarized in Table 3.1.3 and Table 3.1.4.

Table 3.1. 3 Selected parameters of each algorithm.

Algorithm parameters	**GA**	**PSO**	**DE**	**ABC**
Population (colony) size, (*NP*)	100	100	100	100
Inertia weight, (*w*)	–	0,9	–	–
α and β	–	1.5 and 2	–	–
Crossover probability (*CR*)	–	–	0.4	–
Number of onlooker bees	–	–	–	50
Limit of scout bees	–	–	–	420
Maximum number of iteration	1000	1000	1000	1000

Table 3.1. 4 Lower and upper boundaries selected for each PV module model parameter.

C_0	[0 – 2]	I_{ph} **[A]**	[0 – 10]
C_1	[-1– 1]	I_o **[A]**	[10^{-7} – 10^{-11}]
C_2	[-10 – 10]	***n***	[1 – 2]
C_3	[-10 – 100]	R_s **[Ω]**	[0 – 20]
α_{Imp} **[°C^{-1}]**	[10^{-4} – 10^{-2}]	R_{sh} **[Ω]**	[50 – 10^5]
β_{Vmp} **[V/°C]**	[-1 – 0]		

The optimization algorithms used in the parameter extraction techniques evaluate the model parameters of the PV module; I_{ph}, I_o, n, R_s, R_{sh}, in case of the 5PM, and C_0, C_1, C_2, C_3, n, α_{Imp}, β_{Vmp}, in case of SAPM.

In the case of using the extraction method based on LMA, an average number of 10 iterations are needed in order to find a set of solar cell model parameters for an input data set corresponding to one day of real operation of the PV array. On the other hand, for the extraction method relied on the metaheuristic algorithms (GA, PSO, DE and ABC) the average number of iterations is much higher, by around 500 iterations are needed.

Moreover, the parameter extraction methods were applied for each sample day separately, in order to get the optimal set of parameters of the two PV models that allows reproducing the real behaviour of the PV systems with best accuracy. As the extracted parameters values obtained by the different algorithms are very close to each other, it is decided to show the mean value of each extracted parameter. The set of the extracted parameters are listed in Tables 3.1.5 and 3.1.6.

In order to present the best variety of results, and see the performance of the two models using real conditions of solar irradiance and cell temperature, it was chosen to display the DC-output current evolution over the course of a clear sky day for PV system 1, a semi-cloudy day for PV system 2 and a cloudy day for PV system 3.

Table 3.1. 5 Mean values of the main PV module parameters obtained from the parameter extraction algorithms for the 5PM.

PV system	Day	Weather conditions	R_s [Ω]	R_{sh} [Ω]	I_o [A]	I_{ph} [A]	n
1	09/12/2013	Clear sky	0.662	660.011	$1.07\ 10^{-8}$	8.7268	1.191
	18/12/2013	Semi cloudy	0.701	651.880	$1.14\ 10^{-8}$	8.7366	1.192
	20/12/2013	Cloudy	0.701	651.894	$1.14\ 10^{-8}$	8.7366	1.192
2	05/07/2012	Clear sky	5.771	$25.96\ 10^{3}$	$2.32\ 10^{-7}$	2.2055	1.223
	12/05/2012	Semi cloudy	7.321	$20.34\ 10^{3}$	$4.90\ 10^{-7}$	2.2462	1.290
	12/11/2012	Cloudy	8.010	$21.31\ 10^{3}$	$1.20\ 10^{-7}$	2.2462	1.289
3	07/08/2011	Clear sky	12.354	$3.358\ 10^{3}$	$8.82\ 10^{-9}$	1.0751	1.343
	12/05/2012	Semi cloudy	17.915	$2.365\ 10^{3}$	$7.92\ 10^{-9}$	1.0627	1.351
	12/11/2012	Cloudy	19.796	$2.865\ 10^{3}$	$1.36\ 10^{-9}$	1.0686	1.351

Table 3.1. 6 Average values of main parameters obtained from the parameter extraction algorithms for the SAPM.

PV System	Day	Weather conditions	C_0	C_1	C_2	C_3	n	α_{Imp} [°C^{-1}]	β_{Vmp} [V/°C]
1	09/12/2013	Clear sky	1.0438	- 0.2000	2.0686	21.2425	1.1619	$4.32\ 10^{-3}$	- 0.1067
	18/12/2013	Semi cloudy	0.9138	- 0.0552	1.6104	10.9348	1.1613	$4.32\ 10^{-3}$	- 0.1168
	20/12/2013	Cloudy	0.9762	- 0.1468	2.0351	12.7702	1.162	$4.32\ 10^{-3}$	- 0.0554
2	05/07/2012	Clear sky	0.8887	0.0662	2.575	31.7208	1.2177	$5.8\ 10^{-4}$	- 0.2819
	12/05/2012	Semi cloudy	0.9237	0.0500	2.995	43.1182	1.2459	$5.8\ 10^{-4}$	- 0.2692
	12/11/2012	Cloudy	0.9208	0.0608	2.4241	20.0134	1.2466	$5.8\ 10^{-4}$	- 0.4632
3	07/08/2011	Clear sky	0.8229	0.0500	2.1346	18.999	1.3162	$7.52\ 10^{-3}$	- 0.2467
	12/05/2012	Semi cloudy	0.7973	0.0400	2.7898	27.9781	1.3537	$7.52\ 10^{-3}$	- 0.3299
	12/11/2012	Cloudy	1.0010	- 0.1086	1.7077	7.8209	1.2941	$7.52\ 10^{-3}$	- 0.4998

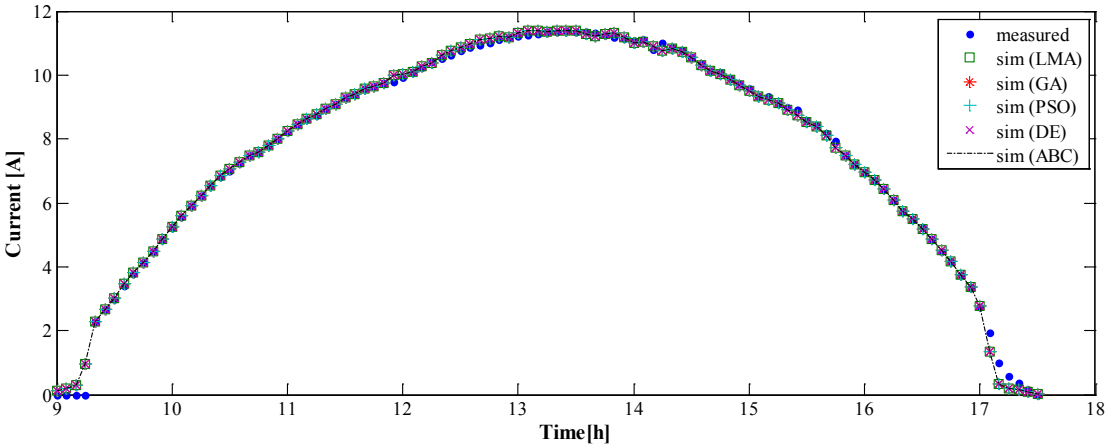

Figure 3.1. 1 Evolution of the DC-current of the PV system 1 using SAPM for clear sky day (December 09th, 2013).

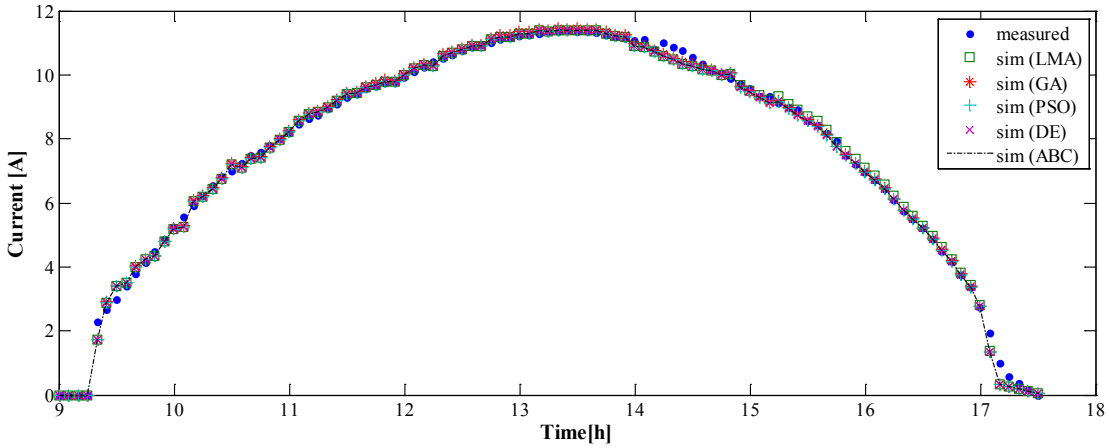

Figure 3.1. 2 Evolution of the DC-current of the PV system 1 using 5PM for clear sky day (December 09th, 2013).

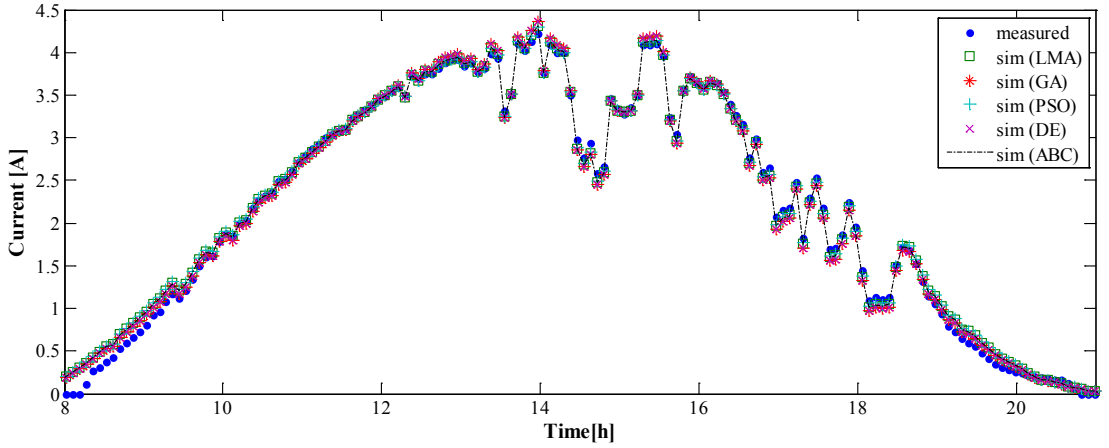

Figure 3.1. 3 Evolution of the DC-current of the PV system 2 using SAPM for semi-cloudy day (May 12th, 2012).

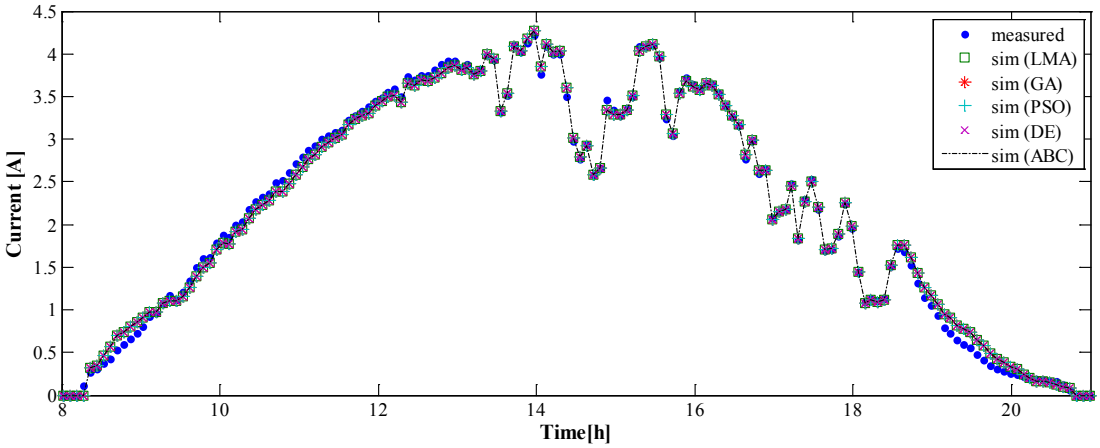

Figure 3.1. 4 Evolution of the DC-current of the PV system 2 using 5PM for semi-cloudy day (May 12th, 2012).

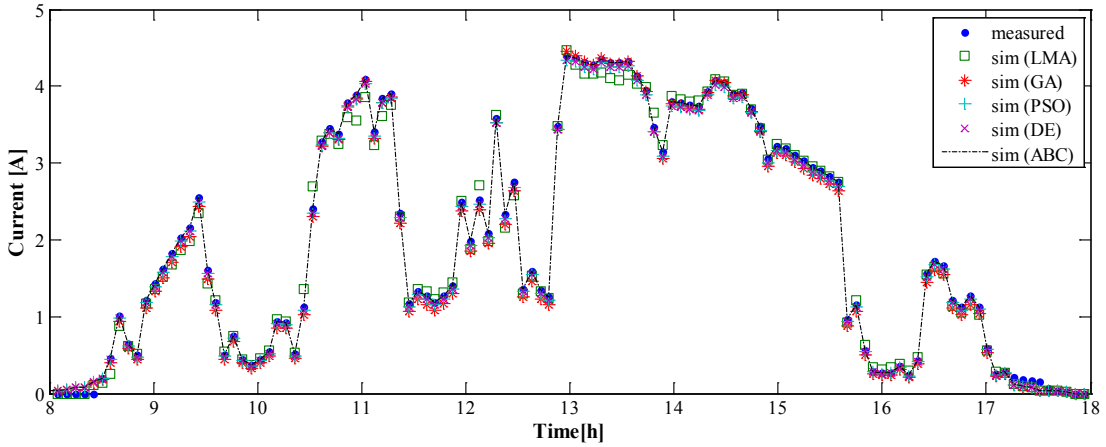

Figure 3.1. 5 Evolution of the DC-current of the PV system 3 using SAPM for cloudy day.

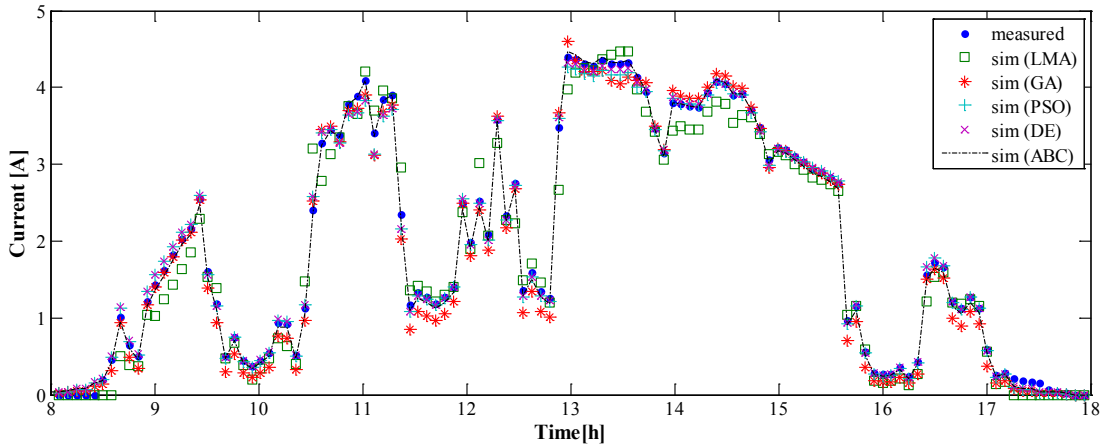

Figure 3.1. 6 Evolution of the DC-current of the PV system 3 using 5PM for cloudy day (November 12th, 2012).

Figs. 3.1.3 – 3.1.8 show the measured DC-output current of the three PV systems, compared with the simulation results obtained with the two PV array models using the extracted set of parameters estimated by the five optimization algorithms considered in this study.

As it can be seen in the figures, a good agreement is always found between the measured data and the SAPM simulation curves, while the curves obtained with the 5PM are less close to the real monitored curve. Moreover, it is found that a better agreement between real and simulated curve is always reached in clear sky days rather than in cloudy days. It is qualitatively noted that the worse the weather conditions, the more difficult is for the models to approximate real data as expected.

By comparing the optimization algorithms used for the estimation of the unknown parameters of the two PV array models, it can be clearly seen that the metaheuristic algorithms provide good results compared to the LMA in all weather conditions and for both PV models.

These considerations are confirmed by values of errors calculated for the two PV models given in Table 3.1.7 and 3.1.8. The values quantify discrepancies between measured data (DC-output current, voltage and power) versus simulated ones predicted by the two PV array models using the five algorithms (LMA, GA, PSO, DE and ABC). Two metrics were used: The Route Mean Square Error (RMSE) [32] and the Normalized Mean Absolute Error (NMAE) [10]. For the error calculation an irradiance filter was applied to the data set. Only the data corresponding to irradiance values above 200 W/m^2 were considered, since the inverters start working in these conditions. Below this irradiance value, the PV systems are in an open-circuit configuration, and the resulting values are misleading.

Table 3.1. 7 Calculated RMSE (%) and NMAE (%) for the SAPM.

PV system	*Day*	*Weather*	*Error [%]*	*LMA*			*GA*			*PSO*			*DE*			*ABC*		
				I	**V**	**P**	**I**	**V**	**P**	**I**	**V**	**P**	**I**	**V**	**P**	**I**	**V**	**P**
1	09/12/2013	clear sky	***RMSE***	0.64	2.09	1.72	0.64	1.26	1.18	0.64	0.84	1.00	0.65	0.84	0.99	0.65	0.71	063
			NMAE	0.27	1.43	0.77	0.25	0.97	0.58	0.26	0.62	0.45	0.26	0.62	0.45	0.27	0.48	0.25
	18/12/2013	semi cloudy	***RMSE***	2.91	4.09	2.87	2.51	2.98	2.68	2.50	2.98	2.63	2.50	2.90	2.59	2.50	2.89	2.59
			NMAE	1.29	2.11	1.12	0.86	1.83	0.97	0.83	1.84	0.94	0.83	1.70	0.89	0.83	1.69	0.91
	20/12/2013	cloudy	***RMSE***	6.37	5.06	6.02	6.41	4.90	5.84	6.36	4.91	5.77	6.35	4.87	5.79	6.37	4.91	5.78
			NMAE	2.43	3.51	2.40	2.54	3.34	2.35	2.44	3.34	2.26	2.44	3.32	2.27	2.44	3.35	2.26
2	05/07/2012	clear sky	***RMSE***	1.33	1.42	1.55	1.29	0.82	1.14	1.31	0.81	1.14	1.29	1.02	1.06	1.27	0.84	1.03
			NMAE	0.46	1.48	0.78	0.53	1.23	0.70	0.47	1.29	0.58	0.51	1.73	0.55	0.53	1.47	0.52
	12/05/2012	semi cloudy	***RMSE***	1.54	1.13	1.55	1.52	0.98	1.53	1.52	1.11	1.41	1.75	1.49	1.36	1.53	1.11	1.32
			NMAE	0.62	1.67	0.88	0.59	1.50	0.88	0.59	1.90	0.87	0.75	2.68	0.85	0.61	1.89	0.83
	12/11/2012	cloudy	***RMSE***	2.75	3.50	3.51	2.78	3.32	3.17	2.76	3.22	3.15	2.76	3.22	3.15	2.76	3.31	3.13
			NMAE	0.70	5.91	1.84	0.68	4.59	1.65	0.69	4.32	1.62	0.68	4.31	1.61	0.69	4.57	1.61
3	07/08/2011	clear sky	***RMSE***	1.37	0.92	1.43	1.04	0.95	1.17	1.04	0.88	1.10	1.04	0.77	0.99	1.04	0.76	0.98
			NMAE	1.25	0.56	0.78	0.90	0.64	0.66	0.90	0.56	0.59	0.91	0.64	0.51	0.90	0.61	0.48
	12/05/2012	semi cloudy	***RMSE***	1.91	0.89	2.20	1.23	0.81	1.10	1.24	0.90	0.93	1.24	0.82	1.07	1.23	0.89	0.91
			NMAE	1.70	0.81	1.07	1.05	0.68	0.49	1.08	0.82	0.43	1.07	0.68	0.48	1.07	0.81	0.41
	12/11/2012	cloudy	***RMSE***	2.67	2.39	4.00	2.40	1.87	2.16	2.42	1.62	1.98	2.42	1.68	2.07	2.25	1.62	1.42
			NMAE	2.12	3.27	1.86	1.75	2.34	1.09	1.79	2.04	0.66	1.75	2.08	1.06	1.75	2.04	1.01

The DC-output power of the PV array is obtained as a product of current and voltage in both real and simulated results.

As a general trend, the errors obtained in the case of SAPM model were smaller than in the case of the 5PM for all PV systems and weather conditions regardless of the solar cell technology. Similarly, for each PV system the error decreases with improving weather conditions: The error for clear sky day was smaller than for semi-cloudy day, while for cloudy day the largest discrepancy was always found, as anticipated from the inspection of Figs. 3.1.3 – 3.1.8.

Table 3.1. 8 Calculated RMSE (%) and NMAE (%) for the 5PM.

PV system	*Day*	*Weather*	*Error [%]*	*LMA*			*GA*			*PSO*			*DE*			*ABC*		
				I	**V**	**P**	**I**	**V**	**P**	**I**	**V**	**P**	**I**	**V**	**P**	**I**	**V**	**P**
1	09/12/2013	clear sky	***RMSE***	1.78	1.39	2.29	1.76	1.39	2.23	1.75	1.39	2.22	1.75	1.38	2.21	1.75	1.38	2.21
			NMAE	0.89	0.98	1.05	0.88	0.98	1.05	0.88	0.98	1.05	0.87	0.97	1.04	0.87	0.96	1.04
	18/12/2013	semi cloudy	***RMSE***	3.42	3.93	4.96	3.37	3.84	4.88	3.37	3.80	4.05	2.84	3.82	3.72	2.55	4.84	3.69
			NMAE	1.38	2.48	2.19	1.35	2.48	2.13	1.34	2.45	1.94	1.28	2.46	1.80	0.97	3.08	1.74
	20/12/2013	cloudy	***RMSE***	10.34	4.92	13.55	9.34	5.80	11.23	7.73	4.87	6.96	6.41	6.29	7.79	5.60	4.91	6.60
			NMAE	4.37	3.63	5.30	4.30	3.51	4.12	3.63	3.32	2.91	3.17	4.76	2.99	2.14	3.62	2.67
2	05/07/2012	clear sky	***RMSE***	1.35	2.07	2.43	1.34	2.07	2.42	1.34	2.06	2.41	1.34	2.06	2.40	1.34	1.38	2.09
			NMAE	0.48	3.03	1.59	0.48	3.02	1.59	0.48	3.03	1.59	0.47	3.01	1.57	0.47	2.47	1.45
	12/05/2012	semi cloudy	***RMSE***	1.60	2.98	3.51	1.60	2.92	3.41	1.60	2.28	3.13	1.60	2.27	3.13	1.61	2.12	3.07
			NMAE	0.64	5.40	2.50	0.65	5.24	2.42	0.65	3.71	2.10	0.65	3.70	2.10	0.64	3.72	2.08
	12/11/2012	cloudy	***RMSE***	4.13	3.24	5.01	3.16	3.25	4.86	2.44	2.98	3.98	3.70	3.24	4.60	3.50	3.14	3.64
			NMAE	1.53	5.83	3.87	1.15	5.83	3.17	0.87	5.09	2.54	1.27	5.83	2.72	1.16	5.29	2.06
3	07/08/2011	clear sky	***RMSE***	1.91	2.44	3.32	1.90	2.43	3.31	1.91	2.16	1.57	1.83	1.92	2.12	0.85	2.31	1.28
			NMAE	1.61	1.77	1.71	1.60	1.75	1.73	1.61	1.59	1.69	1.09	0.89	1.01	0.79	1.88	0.67
	12/05/2012	semi cloudy	***RMSE***	1.66	2.68	3.53	1.72	2.09	3.36	1.67	1.97	3.34	1.65	1.95	3.17	1.66	1.95	3.02
			NMAE	1.51	2.49	1.78	1.52	1.74	1.67	1.52	1.76	1.66	1.51	1.74	1.60	1.51	1.75	1.53
	12/11/2012	cloudy	***RMSE***	5.36	5.10	6.99	3.44	5.10	4.84	2.53	2.36	2.63	2.12	2.52	1.89	2.09	2.53	1.78
			NMAE	4.25	3.22	3.29	2.76	3.21	2.44	1.89	2.18	1.42	1.60	2.24	0.91	1.51	2.26	0.80

The maximum values of RMSE and NMAE obtained for the output power using the SAPM model were 6.02% and 2.40% respectively. These values were provided by simulations based on LMA of the PV system 1 with c-Si PV modules in a cloudy day. Nevertheless, for the PV systems 2 and 3 based on different PV module technologies, the RMSE and NMAE errors obtained for DC output power were below 4% and 1.86%.

On the other hand, in the simulations based on the 5PM the maximum values of RMSE and NMAE obtained regarding the DC output power were increased up to 13.55% and 5.30% for PV system 1 based on LMA. However, for the PV systems 2 and 3, even based on the LMA, the obtained values of RMSE and NMAE were 6.99% and 3.29%.

The accuracy of the PV module models in reproducing the behaviour of the PV array under outdoor conditions of solar irradiance and cell temperature depends also on the used methods for parameters estimation. As it can be seen from Tables 3.1.7 and 3.1.8, the metaheuristic

algorithms provide lower values of RMSE and NMAE than the numerical traditional method based on the LMA.

Considering the SAPM, the passage from using the LMA to GA as a main algorithm of the parameter extraction, reduces the maximum values of RMSE and NMAE of the DC-output power to 5.84% and 2.35% taking into account all the PV systems and weather conditions. This passage from LMA to GA also affects the accuracy of the 5PM, where the maximum values of RMSE and NMAE of the DC-output power were reduced to 11.23% and 4.12% respectively.

The best accuracy of simulations using the SAPM was obtained by using the ABC algorithm for the estimation of the unknown parameters. The greatest RMSE and NMAE values obtained regarding the DC-power of the PV system 1 were 5.78% and 2.26%. Otherwise for PV system 2 the errors values don't exceed 3.13% and 1.61%, and for PV system 3 the best accuracy is achieved, whatever the weather condition, the RMSE and NMAE are below 1.43% and 1.02% respectively.

On the other hand, for the 5PM, the best forecasting of the DC output power of the PV systems is also obtained from simulations using the estimated parameters provided by the ABC algorithm. Considering the worst weather condition, the RMSE and NMAE values related to DC-output power obtained for the PV system 1 are 6.6% and 2.67%. However, for the PV systems 2 and 3 the errors values remain below 3.65% and 2.07%.

Finally, regarding the DC-output current, the highest values of RMSE obtained in clear sky and semi cloudy day, are below 2.91% in case of SAPM and 3.42% in case of 5PM. In order to make the obtained results more comprehensive, other machines learning used for modelling the DC-output current of PV arrays were considered. Ameen et al [13] reported RMSE of 5.67% in a work based on artificial neural networks for forecasting the output current of a PV array. Ibrahim et al [38] published a novel machine learning consisting in using random forests technique for modelling the output current of a PV array, the RMSE provided is of 2.74%.

3.1.6. Conclusions

Two PV array models have been compared in this work for simulation purposes: The 5PM and the SAPM. These models were applied to reproduce the behaviour of three grid connected PV systems with different topologies and solar cell technologies. The models parameters were

obtained from daily monitored profiles of G, T_c, and DC-output current and voltage of the PV arrays using five different optimization algorithms (LMA, GA, PSO, DE and ABC).

The metaheuristic algorithms are more efficient than the traditional LMA algorithm in estimating the unknown parameters of both PV module models, essentially in bad weather conditions. The GA provides high values of RMSE compared to the other bio-inspired algorithms. The ABC algorithm is slightly more accurate than the DE and PSO algorithms.

The 5PM allowed simulating the dynamic behaviour of the PV systems included in this study with an acceptable accuracy degree for applications of supervision and forecasting of energy production. The RMSE obtained in the comparison of the daily evolution of main electrical parameters of the PV systems is below 8% in all cases except the case of using LMA and GA algorithms to simulate the c-Si PV module working in cloudy conditions. This effect can be explained taking into account that the values of series, R_s, and shunt, R_{sh}, resistances forming part of the model parameter set vary with the irradiance, whereas both parameters have been assumed constant in the performed simulations. An advantage of the 5PM lies in the physical meaning of the set of model parameters that provides relevant information about the PV array and allows an easy comparison between different PV modules.

On the other hand, the SAPM model is an empirical model including a set of model parameters in which some of them have little physical meaning. Nevertheless, the SAPM model showed a high accuracy degree in the simulation of the PV systems behaviour independently of the solar cell technology. The RMSE values obtained for the DC output power of the PV arrays in the simulations stayed below 6.05% for the PV system 1 even in cloudy days. For the PV system 2 this error dropped below 3.52%. However, for the PV system 3 the RMSE values are below 4% even in cloudy days and case of using LMA. The SAPM model demonstrated best potential for the simulation of PV systems in real operating conditions; this holds even when using thin film technologies of PV modules.

Acknowledgments

This work was partly supported by the Spanish Science and Innovation Ministry and the ERDF within the frame of the project ‘Estimación de la energía generada por módulos fotovoltaicos de capa delgada: influencia del espectro’ under expedient code ENE2008-05098/ALT.

References

[1] C. Ventura, G.M. Tina, Development of models for on-line diagnostic and energy assessment analysis of PV power plants: The study case of 1 MW Sicilian PV plant, Energy Procedia. 83 (2015) 248–257.

[2] S. Silvestre, M.A. Da Silva, A. Chouder, D. Guasch, E. Karatepe, New procedure for fault detection in grid connected PV systems based on the evaluation of current and voltage indicators, Energy Convers. Manag. 86 (2014) 241–249. doi:10.1016/j.enconman.2014.05.008.

[3] A. Chouder, S. Silvestre, Automatic supervision and fault detection of PV systems based on power losses analysis, Energy Convers. Manag. 51 (2010) 1929–1937. doi:10.1016/j.enconman.2010.02.025.

[4] S. Silvestre, A. Chouder, E. Karatepe, Automatic fault detection in grid connected PV systems, Sol. Energy. 94 (2013) 119–127.

[5] S. Silvestre, S. Kichou, A. Chouder, G. Nofuentes, E. Karatepe, Analysis of current and voltage indicators in grid connected PV (photovoltaic) systems working in faulty and partial shading conditions, Energy. 86 (2015) 42–50. doi:10.1016/j.energy.2015.03.123.

[6] W. Chine, A. Mellit, V. Lughi, A. Malek, G. Sulligoi, A. Massi Pavan, A novel fault diagnosis technique for photovoltaic systems based on artificial neural networks, Renew. Energy. 90 (2016) 501–512.

[7] A. Dolara, F. Grimaccia, S. Leva, M. Mussetta, E. Ogliari, A physical hybrid artificial neural network for short term forecasting of PV plant power output, Energies. 8 (2015) 1138–1153. doi:10.3390/en8021138.

[8] Y.M. Saint-Drenan, S. Bofinger, R. Fritz, S. Vogt, G.H. Good, J. Dobschinski, An empirical approach to parameterizing photovoltaic plants for power forecasting and simulation, Sol. Energy. 120 (2015) 479–493.

[9] A.K. Tossa, Y.M. Soro, Y. Azoumah, D. Yamegueu, A new approach to estimate the performance and energy productivity of photovoltaic modules in real operating conditions, Sol. Energy. 110 (2014) 543–560.

[10] A. Dolara, S. Leva, G. Manzolini, Comparison of different physical models for PV power output prediction, Sol. Energy. 119 (2015) 83–99.

[11] M. Hejri, H. Mokhtari, M.R. Azizian, M. Ghandhari, L. Söder, On the parameter extraction of a five-parameter double-diode model of photovoltaic cells and modules, IEEE J. Photovoltaics. 4 (2014) 915–923.

[12] S. Kichou, S. Silvestre, G. Nofuentes, M. Torres-Ramírez, A. Chouder, D. Guasch, Characterization of degradation and evaluation of model parameters of amorphous silicon photovoltaic modules under outdoor long term exposure, Energy. 96 (2016) 231–241. doi:10.1016/j.energy.2015.12.054.

[13] A. M. Ameen, J. Pasupuleti, T. Khatib, Modeling of photovoltaic array output current based on actual performance using artificial neural networks. Journal of Renewable and Sustainable Energy. 7(5) (2015) 1-11. 053107.

[14] M. F. AlHajri, K. M. El-Naggar, M. R. AlRashidi, A. K. Al-Othman, Optimal extraction of solar cell parameters using pattern search. Renewable Energy. 44 (2012) 238-245.

[15] D. H. Muhsen, A. B. Ghazali, T. Khatib, I. A. Abed, A comparative study of evolutionary algorithms and adapting control parameters for estimating the parameters of a single-diode photovoltaic module's model. Renewable Energy. 96 (2016) 377-389.

[16] R. Eberhart, J. Kennedy, A new optimizer using particle swarm theory, MHS'95. Proc. Sixth Int. Symp. Micro Mach. Hum. Sci. (1995) 39–43. doi:10.1109/MHS.1995.494215.

[17] M.S. Ismail, M. Moghavvemi, T.M.I. Mahlia, Characterization of PV panel and global optimization of its model parameters using genetic algorithm, Energy Convers. Manag. 73 (2013) 10–25. doi:10.1016/j.enconman.2013.03.033.

[18] J. Ma, Z. Bi, T.O. Ting, S. Hao, W. Hao, Comparative performance on photovoltaic model parameter identification via bio-inspired algorithms, Sol. Energy. 132 (2016) 606–616. doi:10.1016/j.solener.2016.03.033.

[19] E. Garoudja, K. Kara, A. Chouder, S. Silvestre, Parameters extraction of photovoltaic module for long-term prediction using artifical bee colony optimization, 2015 3rd Int. Conf. Control. Eng. Inf. Technol. (2015) 1–6. doi:10.1109/CEIT.2015.7232993.

[20] V. Jack, Z. Salam, An Improved Method to Estimate the Parameters of the Single Diode Model of Photovoltaic Module Using Differential Evolution, In *Electric Power and Energy Conversion Systems (EPECS), 4th International Conference*. IEEE (2015) 1-6.

[21] M.. de Blas, J.. Torres, E. Prieto, A. García, Selecting a suitable model for characterizing photovoltaic devices, Renew. Energy. 25 (2002) 371–380. doi:10.1016/S0960-1481(01)00056-8.

[22] G. Ciulla, V. Lo Brano, V. Di Dio, G. Cipriani, A comparison of different one-diode models for the representation of I-V characteristic of a PV cell, Renew. Sustain. Energy Rev. 32 (2014) 684–696. doi:10.1016/j.rser.2014.01.027.

[23] L. Hontoria, J. Aguilera, F. Almonacid, G. Nofuentes, P. Zufiria, Artificial neural networks applied in PV systems and solar radiation, Artif. Intell. Energy Renew. Energy Syst. (2006) 163–200.

[24] S. Lineykin, M. Averbukh, A. Kuperman, An improved approach to extract the single-diode equivalent circuit parameters of a photovoltaic cell/panel, Renew. Sustain. Energy Rev. 30 (2014) 282–289. doi:10.1016/j.rser.2013.10.015.

[25] T. Ma, H. Yang, L. Lu, Development of a model to simulate the performance characteristics of crystalline silicon photovoltaic modules/strings/arrays, Sol. Energy. 100 (2014) 31–41. doi:10.1016/j.solener.2013.12.003.

[26] R. Overstraeten, R. Mertens, Characterisation and testing of solar cells and modules, Hilger, Bristol, Engl. (1986).

[27] L. Castañer, S. Silvestre, Modelling Photovoltaic Systems using PCspice, (2002). doi:10.1002/0470855541.

[28] D.L. King, J. a Kratochvil, W.E. Boyson, Photovoltaic array performance model, Online. 8 (2004) 1–19. doi:10.2172/919131.

[29] W. De Soto, S.A. Klein, W.A. Beckman, Improvement and validation of a model for photovoltaic array performance, Sol. Energy. 80 (2006) 78–88.

[30] A.N. Celik, N. Acikgoz, Modelling and experimental verification of the operating current of mono-crystalline photovoltaic modules using four- and five-parameter models, Appl. Energy. 84 (2007) 1–15.

[31] A. Chouder, S. Silvestre, N. Sadaoui, L. Rahmani, Modeling and simulation of a grid connected PV system based on the evaluation of main PV module parameters, Simul. Model. Pract. Theory. 20 (2012) 46–58.

[32] J. Peng, L. Lu, H. Yang, T. Ma, Validation of the Sandia model with indoor and outdoor measurements for semi-transparent amorphous silicon PV modules, Renew. Energy. 80 (2015) 316–323. doi:10.1016/j.renene.2015.02.017.

[33] C. Sah, R.N. Noyce, W. Shockley, Carrier generation and recombination in P–N junctions and P–N junction characteristics. Proc of the IRE, 45 (1957) 1228–1243.

[34] D. Oliva, E. Cuevas, G. Pajares, Parameter identification of solar cells using artificial bee colony optimization, Energy. 72 (2014) 93–102. doi:10.1016/j.energy.2014.05.011.

[35] J.D. Bastidas-Rodriguez, G. Petrone, C.A. Ramos-Paja, G. Spagnuolo, A genetic algorithm for identifying the single diode model parameters of a photovoltaic panel, Math. Comput. Simul. (2015). doi:10.1016/j.matcom.2015.10.008.

[36] R. Storn, K. Price, Differential Evolution -- A Simple and Efficient Heuristic for global Optimization over Continuous Spaces, J. Glob. Optim. 11 (1997) 341–359. doi:10.1023/A:1008202821328.

[37] D. Karaboga, B. Akay, A comparative study of Artificial Bee Colony algorithm, Appl. Math. Comput. 214 (2009) 108–132. doi:10.1016/j.amc.2009.03.090.

[38] I. A. Ibrahim, A. Mohamed, T. Khatib, Modeling of photovoltaic array using random forests technique. In *Conference on Energy Conversion (CENCON),* IEEE (2015, October) 390-393.

3.2. Published paper in Energy 86 (2015)

Energy 86 (2015) 42 – 50
http://dx.doi.org/10.1016/j.energy.2015.03.123

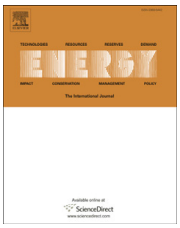

Analysis of current and voltage indicators in grid connected PV (photovoltaic) systems working in faulty and partial shading conditions

Santiago Silvestre[1], Sofiane Kichou[1], Aissa Chouder[2], Gustavo Nofuentes[3], Engin Karatepe[4]*

[1] *MNT Group, Electronic Engineering Department, UPC-BarcelonaTech. Barcelona, C/ Jordi Girona 1-3, Mòdul C4 Campus Nord UPC, 08034 Barcelona, Spain.*

[*] *Corresponding author: E-mail addresses: Santiago.silvestre@upc.edu*

[2] *Univ. M'sila, Fac. Technologies, Dep. Génie Electrique, BP 166 Ichbelia 28000 M'sila, Algeria.*

[3] *IDEA Research Group, University of Jaén, Campus de Las Lagunillas, 23071, Jaén, Spain.*

[4] *Department of Electrical and Electronics Engineering, Dokuz Eylul University, 35160 Buca, Izmir, Turkey.*

ARTICLE INFO

Article history:

Received 13 January 2015
Received in revised form
23 March 2015
Accepted 24 March 2015

Keywords:

PV systems,
Partial shadow,
Current and voltage
indicators.

ABSTRACT

To ensure the optimization of the energy generated by grid connected PV (photovoltaic) systems is necessary to plan a strategy of automatic fault detection. The analysis of current and voltage indicators has demonstrated effectiveness in the detection of permanent faults in the PV array in real time as short-circuits or open-circuits present in the system. In this paper, the analysis of the evolution of these indicators is focused on the detection of temporary faults due to partial shade on the PV array or disconnection of the inverter in case of grid fluctuations of voltage or frequency to prevent islanding. These situations can be identified by observation of the evolution of both indicators and power losses due to these effects can be evaluated from them. The analysis and experimental validation were carried out in two grid connected PV systems in Spain and Algeria.

3.2.1. Introduction

Grid connected PV (photovoltaic) systems are becoming an important part of the electricity system all around the globe, especially in most developed countries. A vigorous growth of the global PV market is still expected due to the strong PV technology price decreases and rise of electricity prices produced by conventional sources together with the clear advantages of green and renewable energy sources as PV on delivering safe and clean energy.

Monitoring, automatic supervision and fault detection of grid-connected PV systems are absolutely necessary to ensure an optimal energy harvesting, minimize the cost of the energy produced by the system and to ensure reliable power production.

The identification of failures in grid connected PV systems can be based on evaluation of the system yields and comparison with forecasted values of these parameters [1–4] or on the analysis of power losses present in the PV system in real operation [4–9]. Once a failure in the PV system operation is observed the source of the fault must be identified by means of a specific diagnostic procedure. Monitored parameters are the key to develop a successful diagnostic procedure [10–12].

Most common faults in PV arrays use to be the apparition of short-circuits in PV modules, mainly due to hot spots, the activation of bypass diodes and earth faults [13-16], overcurrent and voltage disturbances [17], and open-circuits that disconnect some strings of the array [15,18,19]. Accurate simulations of the PV system behaviour have demonstrated good results in fault detection and diagnostic of faults in PV systems [20–23]. However, these techniques require sophisticated simulation software environments and high computational cost.

In a previous work we have presented a procedure for automatic fault detection in grid connected (PV) systems based on the evaluation of current and voltage indicators [24]. The described procedure can be integrated into the inverter without using simulation software or additional external hardware and minimizing the number of sensors present in the monitoring system. Moreover, the indicators of current and voltage used as benchmarks can be calculated by the inverter itself in real time. This approach was experimentally validated and other researchers have followed this way to identify the kind of fault present in the PV system [25].

In the present work we analyse the effects of partial shading of the PV array on current and voltage indicators and how this condition of work and power losses associated to it can be clearly identified by means of these indicators.

The rest of this paper is organized as follows: First, the methodology and calculations are introduced in Section 3.2.2. Section 3.2.3 presents the experimental validation carried out in two different grid connected PV systems. Finally, the conclusions are made in the last section.

3.2.2. Methodology

3.2.2.1. Current and Voltage indicators for fault detection

Silvestre et al. [24] defined two indicators of current, *NRc*, and voltage, *NR*v, for automatic supervision and fault detection of PV systems as follows:

$$NRc = \frac{I_m}{I_{sc}} \quad (3.2\text{-}1)$$

$$NRv = \frac{V_m}{V_{oc}} \quad (3.2\text{-}2)$$

where V_m and I_m are the voltage and current of the MPP (maximum power point) at the DC output of the PV generator respectively and I_{sc} and V_{oc} the short-circuit current and V_{oc} the open-circuit voltage of the PV array respectively.

The inverter is able to calculate both NR_c and NR_v indicators through MPP coordinates available at the inverter input, and the values of I_{sc} and V_{oc}, obtained for actual conditions of irradiance and temperature by the inverter itself internally in real time. For this purpose, the inverter must have MPP tracking and monitoring capabilities. Two more parameters can be also calculated in real time: I_{mo} and V_{mo}, the current and voltage at the maximum power point of the output of the PV array in absence of faults [24]. Then, the ratios: *NRco* and *NR*vo, the expected values of *NRc* and *NRv,* in normal operation of the PV system are given by:

$$NRco = \frac{I_{mo}}{I_{sc}} \quad (3.2\text{-}3)$$

$$NRvo = \frac{V_{mo}}{V_{oc}} \quad (3.2\text{-}4)$$

The definition of thresholds for current, TNR_{cfs}, and voltage, TNR_{vbm}, allows detecting both, short-circuits and open-circuits in the PV array [24]. These thresholds were defined by the following equations:

$$TNR_{cfs} = 1.02\ \alpha\ NRco \quad (3.2\text{-}5)$$

$$TNR_{vbm} = 1.02\ \beta\ NRvo \quad (3.2\text{-}6)$$

where α and β are the relationship between the ratios of current in case of one faulty string and fault-free operation and the ratio between the voltage ratios in case of one bypassed PV module and fault-free operation respectively given by Equations (*3.2*-7) and (8). On the other hand, the constant included in Equations (*3.2*-5) and (*3.2*-6) was fixed by means of statistical procedures in order to avoid false fault detections as an offset of a 2% respect theNRco and NRvo values [24].

$$\alpha = \frac{NRcfs}{NRco} = 1 - \frac{1}{Np} \qquad (3.2\text{-}7)$$

$$\beta = \frac{NRvbm}{NRvo} = 1 - \frac{1}{Ns} \qquad (3.2\text{-}8)$$

In case of permanent faults in the PV array, short-circuits or open-circuits, the corresponding current or voltage indicators always remains below its threshold.

3.2.2.2. Partial shading of the PV array

Unavoidably, the partial shading is a condition that affects the operation of PV systems at some point and leads to reduction of the output power [26–31]. However, most times partial shading has a dynamic behaviour depending on the cloud evolution and on the position of surrounding obstacles near the PV array [32].

The output current of the PV generator is reduced by the number of PV modules affected by shading. The most shaded PV module in a chain limits the total current in that chain. Moreover, there is also a reduction in the output voltage of the PV array due to shadow. The overall decrease in the output voltage depends on the number of bypass diodes that are activated in the PV modules that form the PV generator [33].

Both effects, current and voltage reduction, can be observed at the same time or separately depending on the shadow profile and the configuration of the PV array. Furthermore, in most cases these effects disappear quickly due to the dynamic behaviour of the irradiance profile on the PV field unless a PV module has been completely damaged. So, it is possible to identify that situation by means of the current and voltage indicators described in the previous section.

The total percentage of reduction in output voltage, ΔV, can be expressed as follows:

$$\Delta V = \left(\frac{V_{mo} - V_m}{V_{mo}}\right) = \left(1 - \frac{NRv}{NRvo}\right) \qquad (3.2\text{-}9)$$

Considering a number of Ns PV modules connected in series by string in the array, the number of PV modules bypassed, *BPmod*, because of the shadow effects are given by:

$$BPmod = \Delta V\ Ns \tag{3.2-10}$$

Similarly, the normalized reduction of output current, ΔI, varies according to the following expression:

$$\Delta I = \left(\frac{I_{mo} - I_m}{I_{mo}}\right) = \left(1 - \frac{NRc}{NRco}\right) \tag{3.2-11}$$

If the PV array is formed by Np strings of PV modules connected in parallel, the output current losses can be translated to number of equivalent strings in open-circuit. The number of equivalent faulty strings, *Efs*, is given by:

$$Efs = \Delta I\ Np \tag{3.2-12}$$

So, the presence of partial shadows on the PV array can be detected by means of current and voltage indicators when they present values below their respective thresholds for short periods of time. Moreover, Equations (*3.2*-10) and (*3.2*-12) allow identifying the number of bypassed modules and the equivalent number of faulty strings in the PV array respectively in case of partial shading.

The proportion of DC power losses due to the shadowing effect, Ploss, can also be evaluated from Equations (*3.2*-9) and (*3.2*-11) as follows:

$$Ploss = \left(1 - \frac{NRc}{NRco}\frac{NRv}{NRvo}\right) \tag{3.2-13}$$

The accuracy of the method depends on the errors in the estimation of main parameters involved in the equations, mainly: Isc, Voc, Imo, Vmo, Im and Vm. The accuracy on the evaluation of Vm and Im will depend on the inverter capability to track the MPPT (maximum power point). If the inverter is trapped at a local maximum the values of NRc and NRv will be lower than the values corresponding to the real MPP, while the values of NRco, NRvo, TNRcfs and TNRvbm are independent of the real value of the MPP. So, in that situation the algorithm will detect power losses due to the differences between the real MPP and the local MPP tracked by the inverter and then the presence of faults will be indicated. However, the method will not be able to tell whether the failure is due to incorrect MPPT (inverter) or shade in the photovoltaic field. So, it is important to apply this method by using inverters with smart MPPT techniques. On the other hand, the equations used to evaluate the rest of parameters were used in previous works [5,6,12,24] with success. The RMSE (root-mean square error) (%) between real measured data and values obtained from equations are in the range of 2–4 % for voltages and currents.

3.2.3. Experimental Validation

3.2.3.1 Description of the PV systems used in the experimental validation

The analysis of the evolution of current and voltage indicators in case of partial shading in grid connected PV systems was carried out in two PVGCS (grid connected PV systems) in Spain and Algeria.

The PV system sited in Jaen was monitored uninterruptedly since July 2011 [34] while the new monitoring system of the PV system sited in Algiers was installed in 2012 [12]. The presented procedure was applied in both systems in different periods of the year to analyse different irradiance, shading and temperature conditions as well as study the behaviour of different PV technologies. Results obtained have shown the effectiveness of the proposed method in all cases. We selected the results obtained in one day of operation of each PV system to show the procedure and methodology.

The first PV system is located in Algiers (Algeria, latitude: 36°43'N, longitude: 3°15'E). This grid connected PV system of 9 kWp is divided in three sub-arrays of 3 kWp each one, which are connected to 2.5 kW (IG30 Fronius) single phase inverters. The configuration of each sub-array consist of 30 c-Si PV modules in a configuration of two parallel strings, Np = 2, of 15 PV modules in series, Ns = 15.

The monitoring system used in this PV system includes an Agilent 34970A for the data acquisition, a reference solar cell and two pyranometers (Kipp & Zonen CM 11 type) to measure irradiance at different planes. Temperature measurements were made by using k type thermocouples. A more detailed description of this monitoring system can be found elsewhere [12].

The second PV system is located in Jaén (Spain, latitude 37º45'N, longitude 3º47'). The PV array of 900Wp is formed by 15 a-Si-H thin film PV modules, with 5 parallel-connected strings of 3 series-connected PV modules each (Np = 5, Ns = 3). This PV array is connected to the grid using a SMA Sunny Boy SB1200 inverter. Three SMA Sunny SensorBox devices were also installed in the same platform as the PV systems to measure on-plane irradiance, module and ambient temperatures together with wind speed. Two Pt 100 resistive thermal detectors (RTD) were used as module temperature sensors being pasted to the rear surface of the PV modules. An additional irradiance sensor Kipp & Zonen™ CMP21 pyranometer, was also installed on a metal plate, coplanar with the PV array.

Table 3.2.1 describes the two PV arrays included in this study as well as the configuration of the PV array: Ns x Np.

Table 3.2. 1 Description of the PV arrays included in the study.

Case Study	PV module	Ns	Np	P(kW)
Algiers	106-Wp rated c-Si	15	2	3
Jaén	60Wp-rated a-SI:H	3	5	0.9

Table 3.2. 2 Main model parameters of PV modules.

Model Parameter	c-Si PV module	a-SI:H Thin film PV module
n	1.14	1.2
Io (A)	$3\ 10^{-10}$	$2.8\ 10^{-12}$
Rs (Ω)	0.33	19.5
Rsh (Ω)	199	400
Isc (A)	6.54	1.1
Solar cells (Ncs x Ncp)	36 x 2	115 x 1
Voc (V)	21.6	92
P (W)	106	60
V coeff. (mV/K)	-144.7	-280.6
I coeff. (mA/K)	2.5	0.89

Table 3.2.2 shows main model parameters of PV modules used in this study at STC: The ideality factor of the diode (n), the diode saturation current (Io), the series resistance (Rs) and the shunt resistance (Rsh), the short-circuit current (Isc), the open-circuit voltage (Voc), peak power (P), the number of solar cells per PV module (Nsc, Npc), and temperature coefficients for current and voltage.

3.2.3.2 Experiments carried out

a) PV System in Algiers

One day with partial shadows on the PV array was observed in the monitoring of the PV system and selected for the study. That day, shadows appear in the morning and afternoon. Fig. 3.2.1 shows the irradiance profile monitored where time intervals of shadowing detected by the sensor are highlighted.

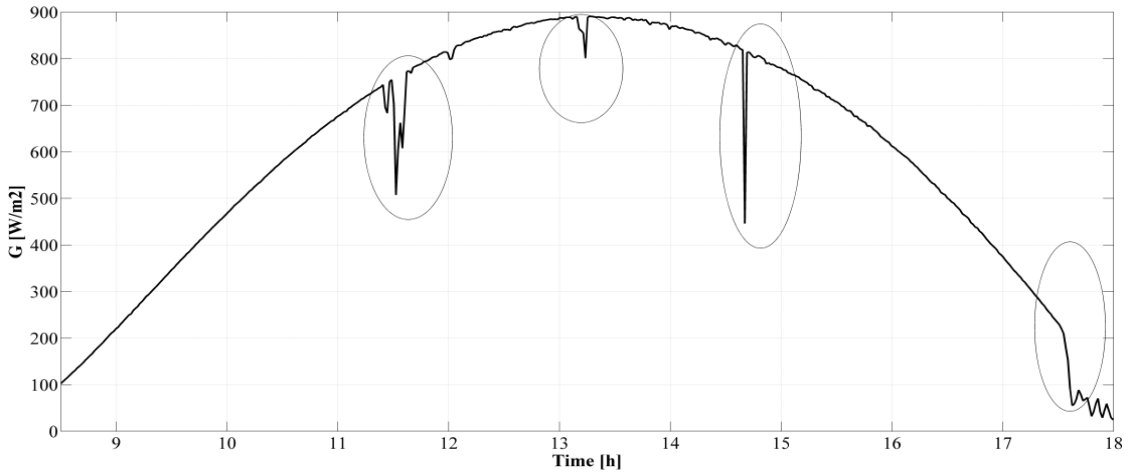

Figure 3.2. 1 Irradiance profile, Algiers.

Figure 3.2. 2 Picture of the PV system showing nearby objects responsible of shadows on the array.

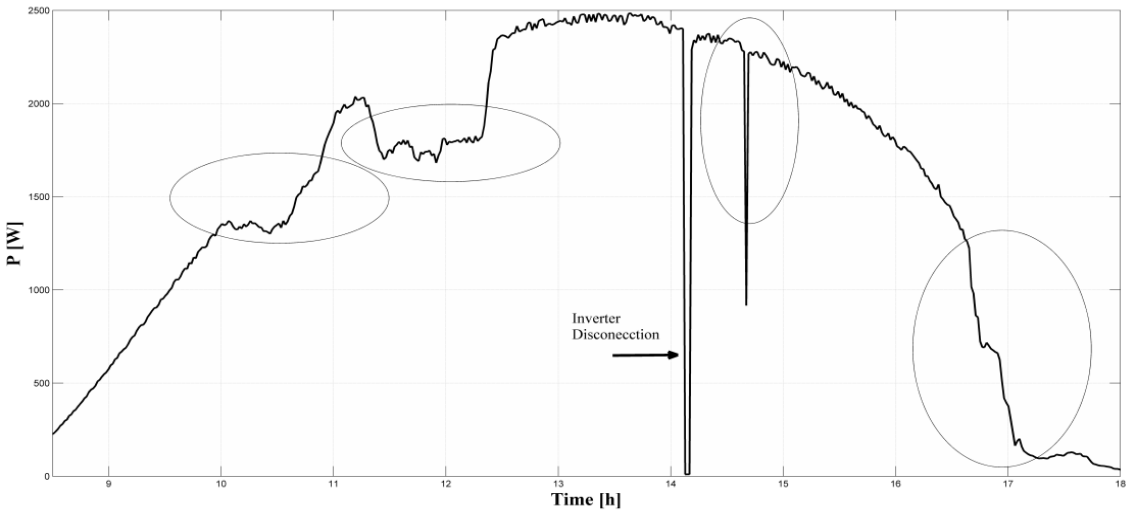

Figure 3.2. 3 DC output power of the PV array.

Fig. 3.2.3 shows the measured DC output power of the array. As shown in the figure, the same time slots are clearly identifiable except the small irradiance reduction around 13.00 h that has no effect on the output power. However, the length of the shadows appears greater than in Fig. 3.2.1. This fact indicates that the sensor remained less affected by shading than the rest of the PV array at that time. The same happens between 10.00 a.m. and 11.00 a.m., when the reduction of power due to shadowing is not detected by the irradiance sensor. On the other hand, after 2.00 p.m. an inverter disconnection is clearly identified, probably due to a short disturbance in the grid.

The PV field suffers, in winter season, an irregular shade over both strings because of a nearby pylon of telecommunications, especially in the morning, from 10h until 12h 30 min, and another shade at the end of the day due to some trees that also hides the reference cell. The effect of these shadows on the generated power was well noticed on clear days. Fig. 3.2.2 shows the nearby objects responsible for these shadows.

Fig. 3.2.4 shows the evolution of the voltage indicators, the shadows affecting the PV array between 11.30 a.m. to 12.30 p.m. and from 4.30 p.m. to 6.00 p.m. are clearly identified. During these time intervals the voltage indicator; NRv, appears below the voltage threshold TNRvbm. Nevertheless, power losses in the PV array between 10.00 a.m. to 11.00 a.m. are not due to the presence of bypassed PV modules, as can be seen in Fig. 3.2.4, where the evolution of voltage indicators is normal.

The inverter disconnection is also clearly reflected by NRv. The current at the inverter input is zero, as can be seen in Fig. 3.2.6, because of the islanding prevention and then the voltage increases.

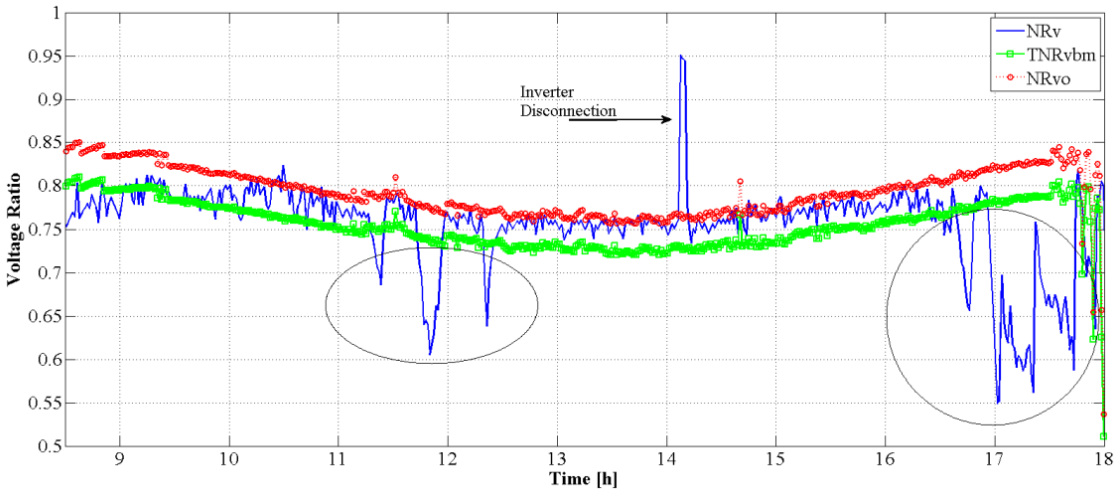

Figure 3.2. 4 Voltage indicators.

Fig. 3.2.5 shows the number of bypassed PV modules, BPmod, due to the shadowing of the PV array. The number of series connected PV modules by string in the PV generator is Ns = 15. As can be seen in the figure, the shadow effects in the morning cause the activation of bypass diodes in 3 modules of the same string near noon, while in the afternoon up to 5 PV modules are bypassed.

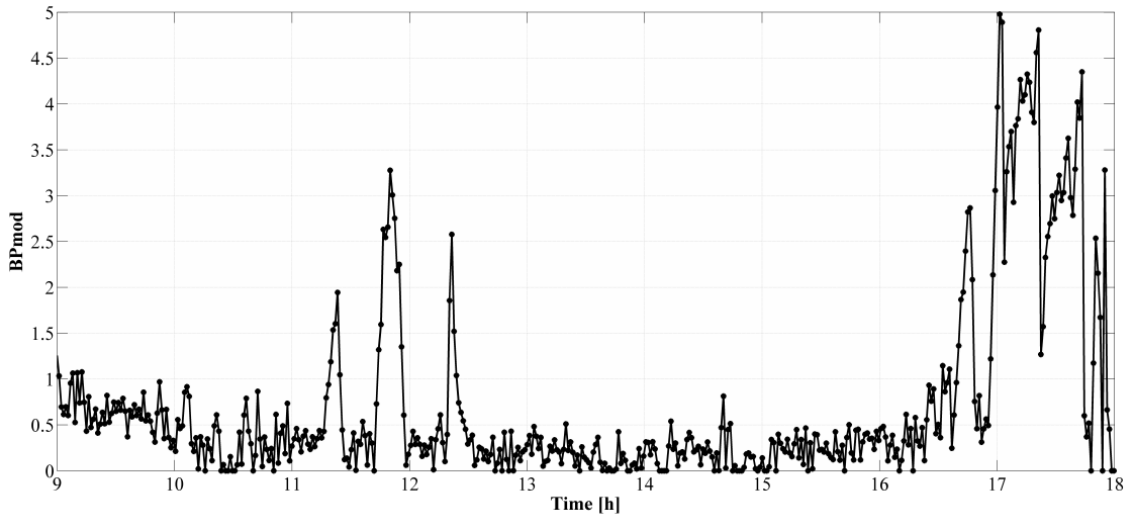

Figure 3.2. 5 Number of bypassed modules.

Figs. 3.2.6 and 3.2.7 show the evolution of the indicators of current and the number of equivalent faulty strings, Efs, reflecting the reduction in output current of the PV array respectively. As depicted in Figs. 3.2.6 and 3.2.7, the inverter disconnection and the effect of shadowing in the reduction of output current of the PV array in the afternoon are clear. The PV array is formed by two parallel strings, Np = 2. Along the inverter disconnection the output current is zero and the number of equivalent faulty strings is Efs = 2. At the moment when a grid fault occurs, the current at DC side instantly drops to zero because the inverter switches off as a safety measure to prevent islanding.

In the afternoon the reduction of current due to shadowing is equivalent to a value of Efs up to 1.6. This fact indicates that the shadowing on the PV array limits the current of the strings to a 40% of the expected value.

On the other hand, the current reduction in the morning between 10:00 a.m. to 11:00 a.m. is observed, and also between 11:30 a.m. to 12:00 p.m. However, the power reduction is smaller in the morning than in the evening, as shown in Fig. 3.2.8, where the amount of power losses calculated from Equation (*3.2*-13) is plotted.

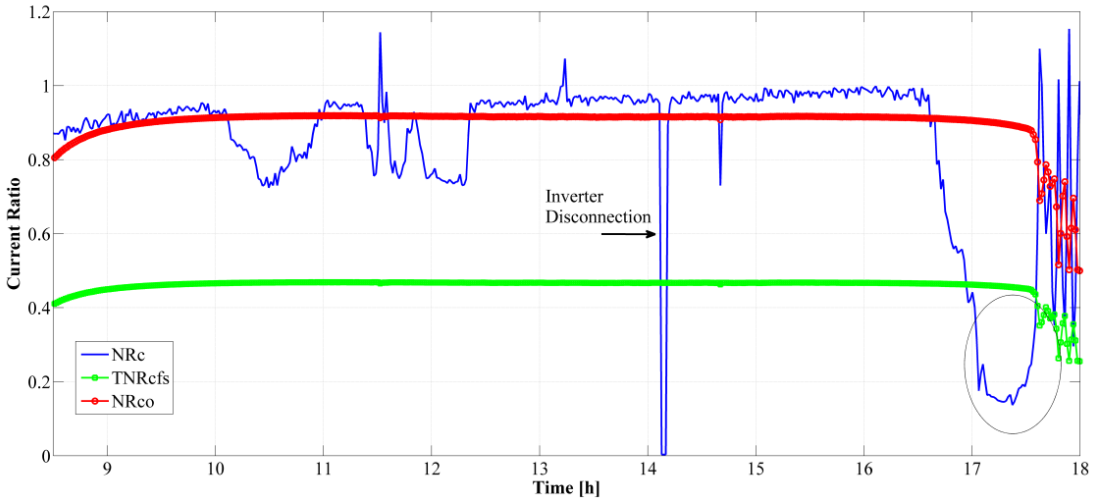

Figure 3.2. 6 Indicators of current.

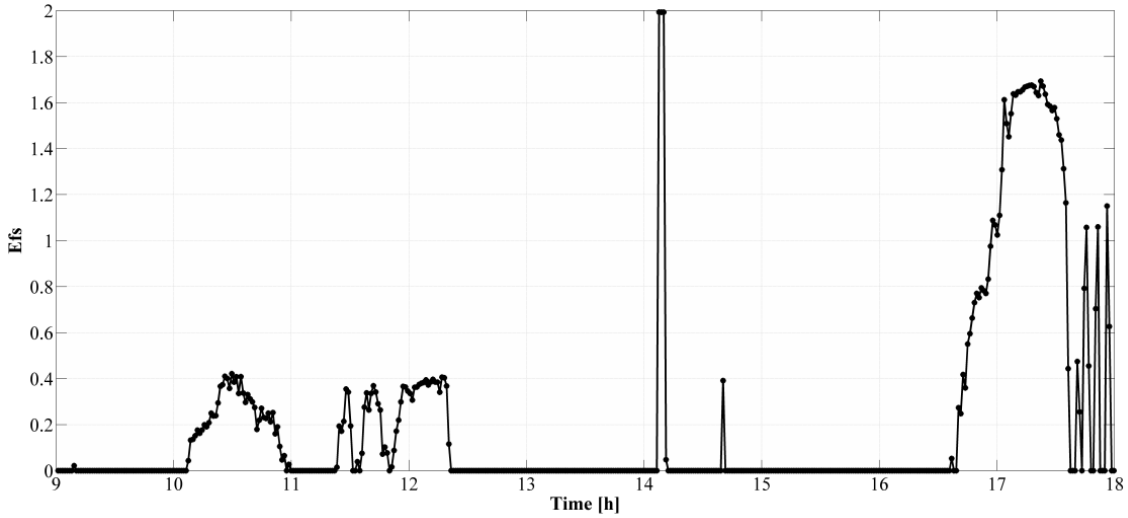

Figure 3.2. 7 Equivalent faulty strings.

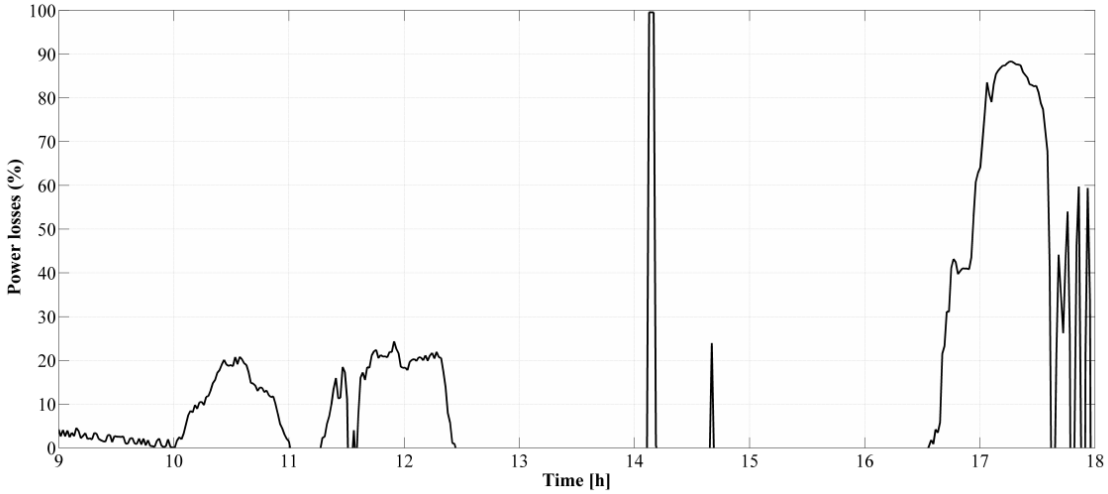

Figure 3.2. 8 Reduction of DC output power.

b) PV System in Jaén

Fig. 3.2.9 shows the irradiance profile monitored in one day of December in the PV system sited in Jaén, Spain. The irradiance sensor detects a reduction of irradiance around 12.30 p.m., before 4.00 p.m. and at 5.00 p.m.

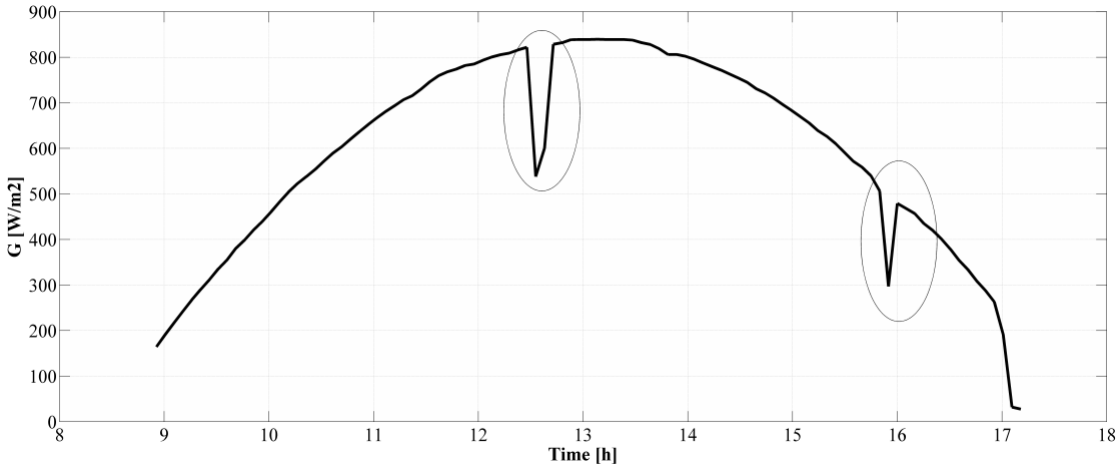

Figure 3.2. 9 Irradiance profile, Jaén.

The reduction in output power of the PV array in the same time intervals is observed in the measured output DC power given by Fig. 3.2.10.

The a-Si:H PV field experiences a minor partial shading from November to January, inclusive, which takes place by the end of the day. The shade is projected by the surrounding mountain and buildings shown in the upper left part of Fig. 3.2.11.

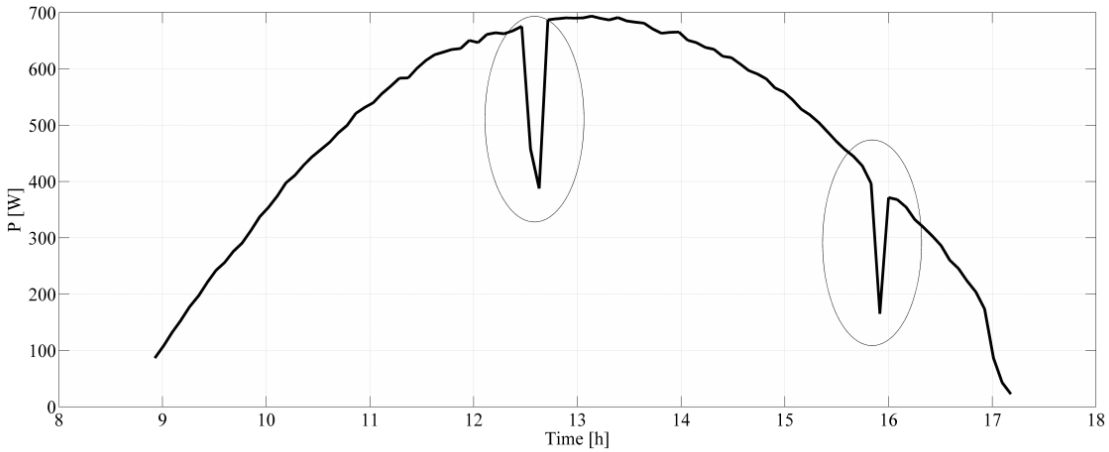

Figure 3.2. 10 Measured PV array DC output power.

Figure 3.2. 11 PVGCS analysed in the site of Jaén. The upper row of modules comprise the a-Si:H PV field under scrutiny in this work. The lower row of modules corresponds to a micromorph (heterojunction a-Si:H/μc-Si) PV field of another PVGCS.

The shadowing of the PV array has very low impact in the evolution of the voltage indicators in this case, as seen in Fig. 3.2.12. There is a reduction of voltage due to shadowing effects before 4.00 p.m. that causes also a reduction in output power of the PV array but is not so important to correspond to the presence of bypassed modules in the strings. The PV array is formed by five parallel strings, Np = 5, of three PV modules connected in series, Ns = 3. As can be seen in Fig. 3.2.13, the number of bypassed modules is always lower than one.

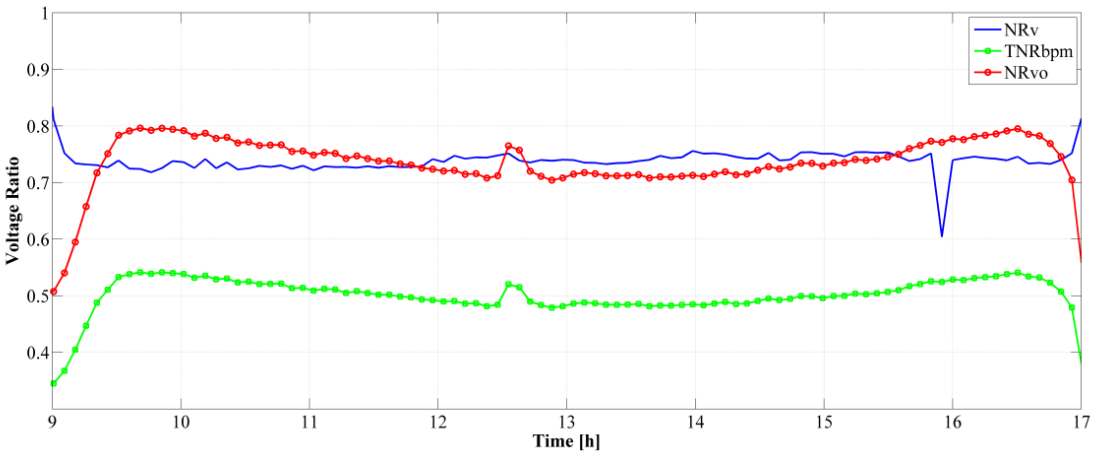

Figure 3.2. 12 Voltage indicators.

On the other hand, the evolution of the indicators of current, shown by Fig. 3.2.14, detects the reduction in current due to partial shading around noon and at 5.00 p.m. These low values of current are the cause of the output power reduction in these time intervals, being the partial

shadow on the PV array between 12.00 p.m. and 1.00 p.m. the most important one. Then, the total output current of the PV array corresponds to the output current of the PV array having one of the strings in open-circuit. The reduction of output current at 5.00 p.m. is not so important, as can be seen in Fig. 3.2.15.

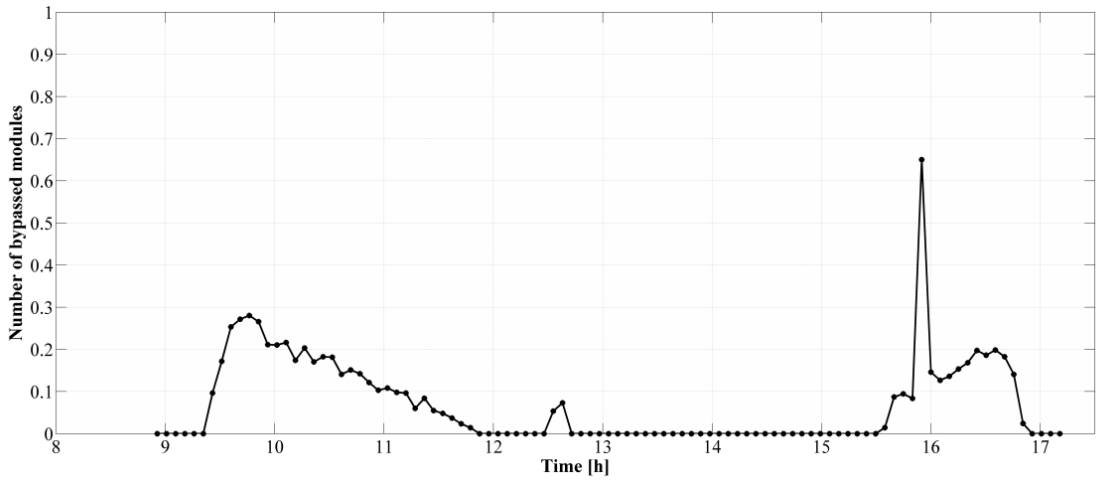

Figure 3.2. 13 Number of bypassed modules.

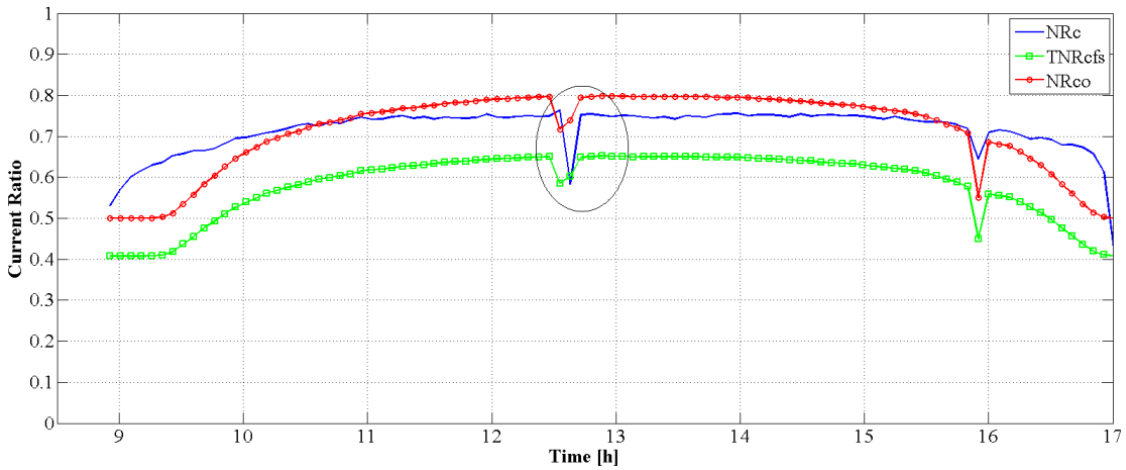

Figure 3.2. 14 Indicators of current.

Finally, Fig. 3.2.16 shows the power losses due to partial shading of the PV array. In the morning the power losses are mainly due to the lowering in voltage, while between 12:00 and 3:30 p.m. power losses are due to the reduction of output current.

On the other hand, the evolution of the indicators of current, shown by Fig. 3.2.12, detects the reduction in current due to partial shading around noon and at 5.00 p.m. These low values of current are the cause of the output power reduction in these time intervals, being the partial shadow on the PV array between 12.00 p.m. and 1.00 p.m. the most important one. Then, the

total output current of the PV array corresponds to the output current of the PV array having one of the strings in open-circuit. The reduction of output current at 5.00 p.m. is not so important, as can be seen in Fig. 3.2.13.

Finally, Fig. 3.2.14 shows the power losses due to partial shading of the PV array. In the morning the power losses are mainly due to the lowering in voltage, while between 12:00 and 3:30 p.m. power losses are due to the reduction of output current.

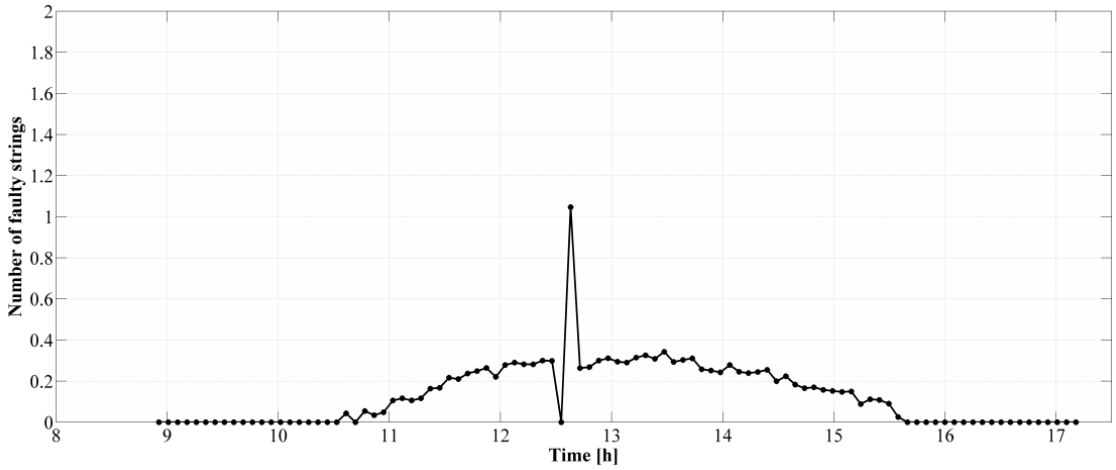

Figure 3.2. 15 Equivalent faulty strings.

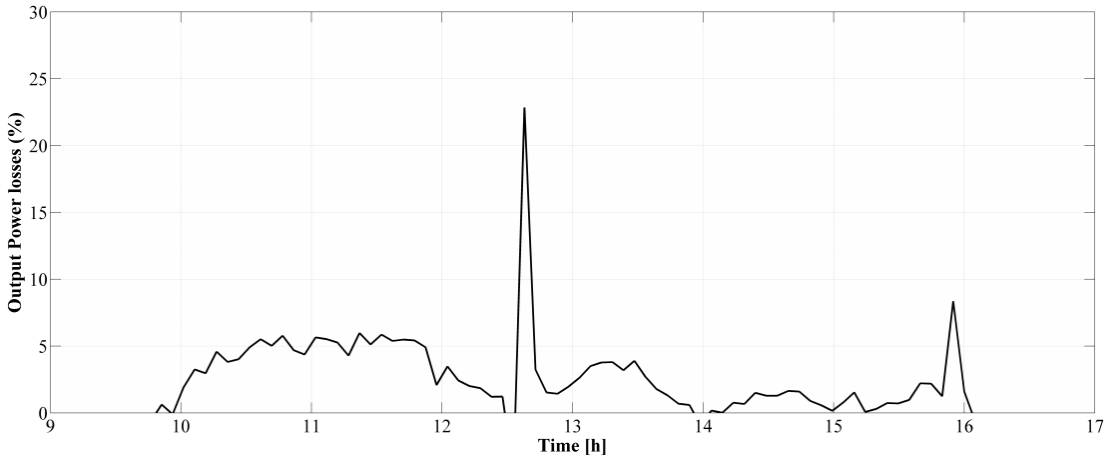

Figure 3.2. 16 Reduction of DC output power.

3.2.4. Conclusions

In this work the effect of partial shading and inverter disconnection on PV arrays based in the study of indicators of current and voltage is presented. The use of these indicators in automatic fault detection in grid connected PV systems was experimentally validated in a previous work. Main faults as short-circuits, permanently bypassed PV modules, and open-

circuits, disconnected strings, can be detected in real time by the inverter himself by using a method based on the evaluation of the ratios of current and voltage. The effects of these faults remain in time and their effect on the current and voltage ratios is permanent.

In case of partially shaded PV generators, energy losses associated are not permanent in the photovoltaic field, but detection of this situation can also be carried out through the study of the evolution of indicators current and voltage. Moreover, the amount of power losses can be estimated from the values of both indicators.

An experimental validation of the proposed procedure is shown in two grid connected PV systems having different sizes, topologies, and different solar cell technologies.

References

[1] Yagi Y, Kishi H, Hagihara R, Tanaka T, Kozuma S, Ishida T. et al. Diagnostic technology and an expert system for photovoltaic systems using the learning method. Solar Energy Material & Solar Cells 2003; 75: 655-663.

[2] Stettler S,Toggweiler P and Remund J. Spyce: satellite photovoltaic yield control and evaluation. In: Proc. of the 21st European photovoltaic solar energy conference, 2006, pp. 2613-2616.

[3] Drews A, de Keizer AC, Beyer HG, Lorenz E, Betcke J,Van Sark WGJHM et al. Monitoring and remote failure detection of grid-connected PV systems based on satellite observations. Solar Energy 2007; 81: 548-564.

[4] Leloux J, Narvarte L, Luna A and Desportes A. Automatic fault detection on BIPV systems without solar irradiation data. In Proc. of the: 29th European Photovoltaic Solar Energy Conference and Exhibition, 2014, pp. 1-7.

[5] Chouder A and Silvestre S. Automatic supervision and fault detection of PV systems based on power losses analysis. Energy Conversion and Management 2010; 51: 1929-1937.

[6] Silvestre S, Chouder A, Karatepe E. Automatic fault detection in grid connected PV systems. Solar Energy 2013; 94: 119-127.

[7] Solórzano J. and Egido MA. Automatic fault diagnosis in PV systems with distributed MPPT. Energy Conversion and Management 2013; 76: 925–934.

[8] Trillo-Montero D, Santiago I, Luna-Rodriguez JJ and Real-Calvo R. Development of a software application to evaluate the performance and energy losses of grid-connected photovoltaic systems. Energy Conversion and Management 2014; 81: 144–159.

[9] Oozeki T, Izawa T, Otani K, Kurokawa K. An evaluation method of PV systems. Sol Energy Mater Celles 2003; 75(3):687–695.

[10] Forero N, Hernández J, Gordillo G. Development of a monitoring system for a PV solar plant. Energy Conversion and Management 2006; 47:15–16.

[11] Vergura S, Acciani G, Amoruso V, Patrono GE and Vacca F. Descriptive and Inferential Statistics for Supervising and Monitoring the Operation of PV Plants. IEEE Trans. on Industrial Electronics 2009; 56: 4456-4463.

[12] Chouder A, Silvestre S, Taghezouit B and Karatepe E. Monitoring, modeling and simulation of PV systems using LabVIEW. Solar Energy 2013; 91: 337-349.

[13] Silvestre S, Boronat A and Chouder A. Study of bypass diodes configuration on PV modules. Applied Energy 2009; 86: 1632-1640.

[14] Rezgui W, Mouss L, Kinza Mouss N and Benbouzid M. A Smart Algorithm for the Diagnosis of Short-Circuit Faults in a Photovoltaic Generator. In: Proc. of the First International Conference on Green Energy ICGE, 2014, pp. 139–143.

[15] Gokmen N, Karatepe E, Celik B and Silvestre S. Simple diagnostic approach for determining of faulted PV modules in string based PV arrays. Solar Energy 2012; 86: 3364–3377.

[16] Hernández JC, Vidal PG, Medina A. Characterization of the insulation and leakage currents of PV generators: Relevance for human safety, Renewable Energy 2010; 35: 593–601.

[17] Garcia O, Hernandez JC, Jurado F. Guidelines of the insulation and leakage currents of PV generators. Adv Electr Comput Eng 2012;12(4):63–70.

[18] Ducange P, Fazzolari M, Lazzerini B and Marcelloni F. An Intelligent system for detecting faults in photovoltaic fields. In: Proc. of the 11th International conference on Intelligent Systems Design and Applications (ISDA), 2011, pp. 1341–6.

[19] Syafaruddin, Karatepe E and Hiyama T. Controlling of artificial neural network for fault diagnosis of photovoltaic array. In: IEEE 16th International Conference on Intelligent System Application to Power Systems, 2011, pp. 1–6.

[20] Chao KH, Hob SH and Wang MH. Modeling and fault diagnosis of a photovoltaic system. Electric Power Systems Research 2008; 78: 97–105.

[21] Mellit A and Kalogirou SA. ANFIS-based modelling for photovoltaic power supply system: A case study. Renewable Energy 2011; 36: 250–258.

[22] Chouder A, Silvestre S, Sadaoui N and Rahmani L. Modeling and simulation of a grid connected PV system based on the evaluation of main PV module parameters. Simulation Modelling Practice and Theory 2012; 20: 46–58.

[23] Tadj M, Benmouiza K, Cheknane A and Silvestre S. Improving the performance of PV systems by faults detection using GISTEL approach. Energy Conversion and Management 2014; 80: 298–304.

[24] Silvestre S, Aires da Silva M, Chouder A, Guasch D, and Karatepe E. New procedure for fault detection in grid connected PV systems based on the evaluation of current and voltage indicators. Energy Conversion and Management 2014; 86: 241–249.

[25] Chine W, Mellit A, Pavan AM, Kalogirou SA. Fault detection method for grid-connected photovoltaic plants. Renewable Energy 2014; 66: 99–110.

[26] Rodrigo P, Fernández EF, Almonacid F, Pérez-Higueras PJ. A simple accurate model for the calculation of shading power losses in photovoltaic generators. Solar Energy 2013; 93: 322–333.

[27] Sánchez Reinoso CR, Milone DH, Buitrago RH. Simulation of photovoltaic centrals with dynamic shading. Applied Energy 2013; 103: 278–289.

[28] Di Vincenzo MC. and Infield D. Detailed PV array model for non-uniform irradiance and its validation against experimental data. Solar Energy 2013; 97:314–331.

[29] Silvestre S, and Chouder A. Effects of shadowing on photovoltaic module performance. Progress in Photovoltaics: Research and applications 2008; 60: 141–149.

[30] Kadri R, Andrei H, Gaubert JP, Ivanovici T, Champenois G and Andrei P. Modeling of the photovoltaic cell circuit parameters for optimum connection model and real-time emulator with partial shadow conditions. Energy 2012; 42: 57–67.

[31] Bouilouta A, Mellit A, Kalogirou SA. New MPPT method for stand-alone photovoltaic systems operating under partially shaded conditions. Energy 2013; 55: 1172–1185.

[32] Celik B, Karatepe E, Gokmen N and Silvestre S. A virtual reality study of surrounding obstacles on BIPV systems for estimation of long-term performance of partially shaded PV arrays. Renewable Energy 2013; 60: 402–414.

[33] Dolara A, Lazaroiu GC, Leva S and Manzolini G. Experimental investigation of partial shading scenarios on PV (photovoltaic) modules. Energy 2013;55: 466–475.

[34] Torres-ramírez M, Nofuentes G, Silva JP, Silvestre S, Muñoz JV. Study on analytical modelling approaches to the performance of thin film PV modules in sunny inland climates. Energy 2014; 73:731–740

3.3. Published paper in Solar Energy 137 (2016)

Solar Energy 137 (2016) 424 – 433

http://dx.doi.org/10.1016/j.solener.2016.08.030

Remote supervision and fault detection on OPC monitored PV systems

Santiago Silvestre[1], Llanos Mora-López[2], Sofiane Kichou[1], Francisco Sánchez-Pacheco[3] and Manuel Dominguez-Pumar[1]*

[1] *MNT Group, Electronic Engineering Department, UPC-BarcelonaTech. Barcelona, C/ Jordi Girona 1-3, Mòdul C4 Campus Nord UPC, 08034 Barcelona, Spain*

[*] *Corresponding author: E-mail addresses: Santiago.silvestre@upc.edu*

[2] *Dpto. Lenguajes y Ciencias de la Computación, Universidad de Málaga Campus de Teatinos, sn, Málaga 29071, Spain*

[3] *Dpto. Tecnología Eléctrica, Universidad de Málaga, Campus de Teatinos, sn, Málaga 29071, Spain*

ARTICLE INFO

Article history:

Received 30 May 2016
Received in revised form 1 August 2016
Accepted 19 August 2016

Keywords:

OPC,
Monitoring,
Fault detection,
PV systems.

ABSTRACT

This paper presents a new approach for automatic supervision and remote fault detection of grid connected photovoltaic (PV) systems by means of OPC technology-based monitoring. The use of standard OPC for monitoring enables data acquisition from a set of devices that use different communication protocols as inverters or other electronic devices present in PV systems enabling universal connectivity and interoperability. Using the OPC standard allows promoting interoperation of software objects in distributed-heterogeneous environments and also allows incorporating in the system remote supervision and diagnosis for the evaluation of grid connected PV facilities. The supervision system analyses the monitored data and evaluates the expected behaviour of main parameters of the PV array: Output voltage, current and power. The monitored data and evaluated parameters are used by the fault detection procedure in order to identify possible faults present in the PV system. The methodology presented has been experimentally validated in the supervision of a grid connected PV system located in Spain. Results obtained show that the combination of OPC monitoring along with the supervision and fault detection procedure is a robust tool that can be very useful in the field of remote supervision and diagnosis of grid connected PV systems. The RMSE between real monitored data and results obtained from the modelling of the PV array were below 3.6% for all parameters even in cloudy days.

3.3.1. Introduction

One of the main difficulties involved in monitoring systems is the inability to add new devices or new ways of evaluating the performance of these systems without significantly changing the topology of the monitoring system. Firstly, the incorporation of new devices, in the absence of standard communication protocols, requires the development of software for acquiring data from these devices and it is also necessary to add the functionality of each of the data that are acquired. Moreover, in photovoltaic (PV) plants connected to the grid each inverter has its own communication protocol and issues its own program online or locally to access data and plant information. These programs do not allow the inclusion of data from other inverters or for other plants even in the case of inverters from the same manufacturer. Also, it is not possible to incorporate any functionality to them in order to make a diagnosis and evaluation of the operation of facilities, beyond including the system supplied by the manufacturer of the inverter, who usually simply presents the information of the recorded data. Therefore, it is possible to ensure that one of the most important problems when it comes to monitoring and supervising solar energy plants is the communication between devices due to the different types used. It is common to find many devices of different types and manufacturers who use different ways of communication. In order to obtain a generic system, a general mechanism is needed to communicate with any devices, irrespective of their characteristics or of the manufacturer.

To address these limitations, it has been proposed to use the OPC standard for monitoring PV systems [1,2]. OPC was originally based on OLE (Object Linking and Embedding) for Process Control [3,4]. However, OPC is now available on other operating systems. It is a standard and consistent communication system for exchanging information and it allows defining the rules of handshaking between different devices using the client-server paradigm; this system has been used in industry to connect supervisory systems and data acquisition and man-machine interfaces with the physical control systems [5]. Moreover, it allows the development of components for interconnecting disperse systems providing interoperability efficiently. This technology enables software components developed by experts in one sector to be used by applications in any other sector. The design of OPC interfaces supports distributed architectures.

The Data access OPC and Historical Data Access specifications are compatible with client-server and publisher-subscriber communication models. The use of the Distributed Component Object Model (DCOM) from Microsoft makes possible the access to remote OPC servers.

DCOM extends Microsoft's object-oriented Component Object Model (COM) to promote interoperation of software objects in a distributed-heterogeneous environment.

Using this OPC standard, an automatic assessment model for solar energy plants was proposed in [2]. The model for each installation is built using different data sources. Various daily parameters were proposed to evaluate the performance of a photovoltaic system:

- The daily output energy of the photovoltaic plant, that is, the daily energy supplied by the installation, E_{day}.
- The daily yield, Y_{a_day}, defined as the daily output energy per kW_p installed.

The daily evaluation model is treated as an element of the system. The container used for the model behaves as an OPC client with access to all data.

The operation of each plant is evaluated using a statistical analysis of the differences between the measured parameters and the estimated parameters. These differences are checked using the Jarque-Bera test [6] that informs whether these differences follow a normal distribution. This proposal allows an initial daily evaluation of the performance of the PV system. However, for a complete diagnosis of the detected problems generally related to the DC side of the PV system, it is necessary to use additional methods based on a detailed analysis of monitored data.

A list of fault detection methods for grid connected PV systems was reported in the past. Some of these methods are based on power losses analysis [7–9] or on theoretical concepts of descriptive and inferential statistics [10,11]. Bayesian [12] and neural networks [13] were also used in fault detection procedures. However, these techniques require sophisticated software environments and have a high computational cost. In this work a procedure for automatic fault detection in grid connected PV systems is used. This procedure is based on a technique for the evaluation of current and voltage indicators recently reported that was experimentally validated and can work in real time without using sophisticated software tools [14–16]. The integration of this fault detection procedure along with OPC monitoring, results in a powerful tool for automatic supervision and fault detection of grid connected PV systems. The present work shows the results obtained in the remote supervision of a grid connected PV system with a nominal power of 14.08 kW located in Spain by using diagnosis tools in combination with OPC monitoring.

3.3.2. Methodology

3.3.2.1. Description of the OPC-based monitoring

The following parameters were monitored: Current, voltage and power (DC and AC), cosine (ϕ), frequency, irradiance, partial energy and module temperature. The irradiance received was measured using a calibrated solar cell installed in the plane of the modules. Module temperature was measured using a Pt100 sensor fitted to the back of the module, in the middle of a cell, near its geometric center. Both parameters are recorded by the data acquisition of the inverter.

All data were supplied by the inverters. For data collection it was used OPC Historical Data Access (OPC HDA) specifications which provide access to information already stored in inverters and allow retrieving this information in a homogeneous and uniform way. A VPN and IP were used to connect with the facilities. The data collection interval was 5 minutes. Data are directly retrieved from the inverter. When the inverter is disconnected data are not recorded, but data previously stored in the inverter will be transmitted when the inverter is connected.

Several elements are used in the monitoring process: The client software using OPC HDA technology for downloading data from the devices, the device and the OPC HDA server that knows the protocol and the procedure to download data from the device [17].

Data were stored in a PostgreSQL DBMS compatible with the SQL92 standard. Daily evaluation and fault detection algorithms were implemented with OPC.

3.3.2.2. PV system modelling

The model of the PV array is mainly based on the Sandia PV array performance model (SAPM) [18]. This model is an empirical model described by the fundamental Eqs. (*3.3*-1) – (*3.3*-7). The model contains several coefficients and parameters that are unknown and not provided by the PV module's manufacturer, by knowing these model parameters as well as the solar radiation and the PV modules operating temperature, the output power of the PV array can be predicted by using the following equations:

$$Ee = G/G_n \tag{3.3-1}$$

$$Iscg = N_{pg}[Isco \cdot Ee \cdot \{1 + \alpha_{Isc} \cdot (Tc - To)\}] \tag{3.3-2}$$

$$Impg = N_{pg}[Impo \cdot \{C_0 \cdot Ee + C_1 \cdot Ee^2\} \cdot \{1 + \alpha_{Imp} \cdot (Tc - To)\}] \tag{3.3-3}$$

$$\delta(Tc) = n \cdot k \cdot (Tc + 273.15)/q \quad (3.3\text{-}4)$$

$$Vocg = N_{sg}[Voco + N_s \cdot \delta(Tc) \cdot ln(Ee) + \beta_{Voc}(Ee) \cdot (Tc - To)] \quad (3.3\text{-}5)$$

$$Vmpg = N_{sg}[Vmpo + C_2 \cdot N_s \cdot \delta(Tc) \cdot ln(Ee) + C_3 \cdot N_s \cdot \{\delta(Tc) \cdot ln(Ee)\}^2 + \beta_{Vmp}(Ee) \cdot (Tc - To)] \quad (3.3\text{-}6)$$

$$Pmpg = Impg \cdot Vmpg \quad (3.3\text{-}7)$$

where, *Ee* is the effective solar irradiance; *G* is the measured irradiance (W/m^2); G_n is the reference irradiance (1000 W/m^2) at standard conditions (STC); *To* is the reference cell temperature (25°C) at STC; *Tc* is the measured cell temperature inside module (°C); *Isco* is the PV module short-circuit current at STC (A); α_{Isc} is the normalized temperature coefficient for *Isc*, (°C^{-1}); *Iscg* is the PV array short-circuit current (A); N_{pg} is the number of modules connected in parallel; *Impo* is the PV module current at the maximum power point at STC (A); *Impg* is the PV array current at the maximum power point (A); α_{Imp} is the normalized temperature coefficient for Imp, (°C^{-1}); C_0 and C_1 are empirically determined coefficients which relate *Imp* to the effective irradiance, $C_0+C_1=1$, (dimensionless); $\delta(Tc)$ is the thermal voltage per cell at temperature Tc; *q* is the elementary charge, 1.60218 10^{-19} (coulomb); *k* is the Boltzmann's constant, 1.38066 10^{-23} (J/K); *n* is the diode ideality factor; *Voco* is the PV module open-circuit voltage at STC (V); β_{Voc} is the temperature coefficient for module *Voc* at standard irradiance, (V/°C); N_s is the number of cells in series per PV module; N_{sg} is the number of modules connected in series; *Vocg* is the PV array open-circuit voltage (V); *Vmpo* is the PV module voltage at the maximum power point at STC (V); β_{Vmp} is the temperature coefficient for module *Vmp* at standard irradiance, (V/°C); *Vmpg* is the PV array voltage at the maximum power point (V); C_2 and C_3 are empirically determined coefficients which relate *Vmp* to the effective irradiance (C_2 is dimensionless, and the unit of C_3 is (V^{-1}) and finally *Pmp* is the PV array power at the maximum power point (W).

In order to solve the system equations formed by the Eqs. (*3.3*-1) – (*3.3*-7) and reproduce the behaviour of the whole PV system with a good accuracy, it is necessary to apply specific methods to determine the empirical coefficients. A method based on the combination of indoor and outdoor measurements and coefficients estimation and fitting has been recently reported in the literature [19]. The set of coefficients used by the model is obtained by means of a parameter extraction procedure carried out in MATLAB/Simulink environment by using the Parameter Estimation toolbox. The monitored current and voltage of the PV array together with in-plane

irradiance (*G*) and cell temperature (*Tc*) profiles are needed to estimate the set of unknown parameters of SAPM model implemented in Simulink as illustrated in Fig. 3.3.1.

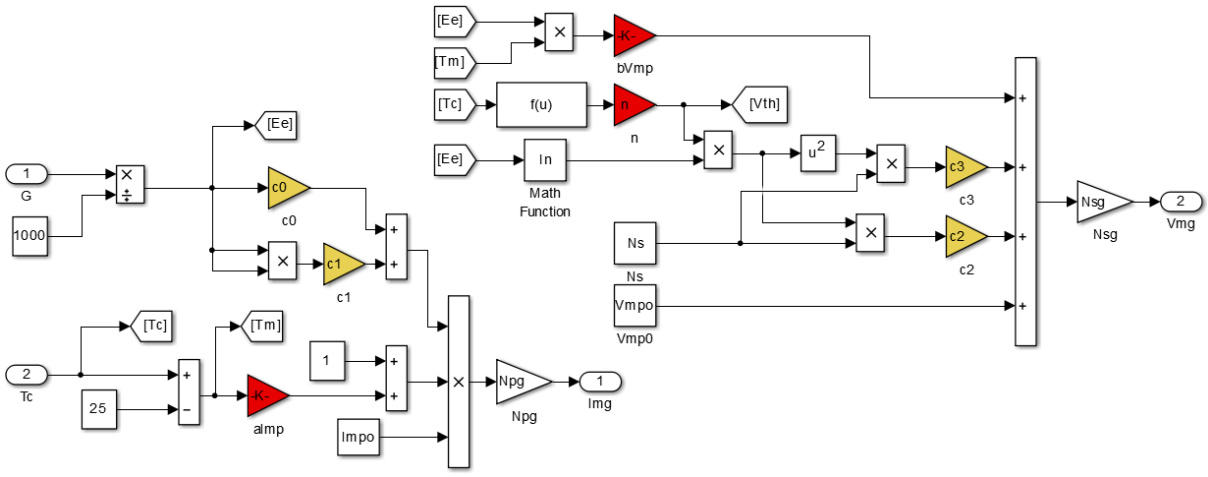

Figure 3.3. 1 Simulink block diagram of the parameter extraction algorithm.

The parameter extraction algorithm evaluates: C_0, C_1, C_2, C_3, α_{Imp}, β_{Vmp} and n by using Eq. (3) and Eq. (6). A nonlinear regression method based on the Levenberg–Marquardt algorithm was applied to both data sets: The daily monitored data from the PV array in real conditions of work and the simulation results generated by using the described model of Sandia, in order to minimize the quadratic error between the simulation results and the experimental data.

3.3.2.3. Fault detection procedure

The fault detection procedure is based on the analysis of the current and voltage indicators for fault detection, *NRc* and *NRv* respectively, defined by Silvestre et al. [14] and given by the following equations:

$$NRc = \frac{I_m}{I_{scg}} \qquad (3.3\text{-}8)$$

$$NRv = \frac{V_m}{V_{ocg}} \qquad (3.3\text{-}9)$$

where *Vm* and *Im* are the coordinates of the maximum power point (MPP) at the DC side of the PV array.

The fault detection algorithm evaluates both *NRc* and *NRv* indicators through MPP coordinates available from the monitoring data set in real time, and the values of I_{scg} and V_{ocg}, obtained for actual conditions of irradiance and temperature by using the PV array model presented in the previous section. Two more parameters can be also obtained from the model

simulations in real time: I_{mpo} and V_{mpo}, the current and voltage at the maximum power point of the output of the PV array in absence of faults and normal operation of the PV array [14]. Then, the expected values of *NRc* and *NRv*: *NRco* and *NRvo*, are given by:

$$NRco = \frac{I_{mpo}}{I_{scg}} \quad (3.3\text{-}10)$$

$$NRvo = \frac{V_{mo}}{V_{ocg}} \quad (3.3\text{-}11)$$

Silvestre et al. defined two thresholds for current, *TNRcfs*, and voltage indicators, *TNRvbm*, that allow detecting most important faults in grid connected PV systems: short-circuits and open-circuits in the PV array [14] as well as inverter disconnection or partial shading conditions of work [15]. These thresholds were defined by the following equations:

$$TNRcfs = 1.02\ \alpha\ NRco \quad (3.3\text{-}12)$$

$$TNRvbm = 1.02\ \beta\ NRvo \quad (3.3\text{-}13)$$

where α and β are the relationship between the ratios of current in case of one faulty string and fault-free operation and the ratio between the voltage ratios in case of one bypassed PV module in a string of the PV array and fault-free operation respectively [14,15].

Both parameters depend only on the PV array configuration: Number of PV modules connected in series by string, N_{sg}, and number of strings connected in parallel, N_{pg}. In case of permanent faults in the PV array, short-circuits or open-circuits, the corresponding current or voltage indicator always remains below its threshold and their effect on the current and voltage ratios is permanent, while in case of partial shading conditions of work or inverter disconnection to prevent islanding, these indicators change as quickly as do the shadows in the photovoltaic field or as soon as the inverter is reconnected to the grid. The islanding refers to the condition in which the PV generator continues to power a location even though power from the electric utility is no longer present. This situation can be dangerous to utility workers. So, the inverter must be disconnected from the grid to avoid islanding when important frequencies of voltage disturbances are observed.

The fault detection algorithm is able to detect all those faults and generate alarm signals to indicate the most probably fault present in the system. Moreover, the total amount of power losses caused by the fault as well as the equivalent number of short-circuited or bypassed PV modules present in the PV array are also evaluated by the fault detection algorithm. The equivalent number of faulty strings, E*fs*, is evaluated by using the following equation [15]:

$$Efs = Npg\left(1 - \frac{NRc}{NRco}\right) \quad (3.3\text{-}14)$$

Finally, the number of equivalent bypassed modules, BPmod, present on the PV array is estimated as follows:

$$BPmod = Nsg\left(1 - \frac{NRv}{NRvo}\right) \quad (3.3\text{-}15)$$

The proportion of DC power losses due to the shadowing effect, Ploss, is also evaluated by the automatic supervision procedure by using the following equation:

$$Ploss = \left(1 - \frac{NRc}{NRco}\frac{NRv}{NRvo}\right) \quad (3.3\text{-}16)$$

The efficiency parameters used for the energetic evaluation of the system are the performance ratio (*PR*) and the array yield (Y_a) given by the following equations:

$$Y_a = \frac{\int_0^{\Delta t} P_{ac}\ dt}{P_o} \quad (3.3\text{-}17)$$

where P_{ac} is the output power of the PV array and P_o is the nominal power of the array.

$$PR = \frac{Ya}{Yr} \quad (3.3\text{-}18)$$

where *Yr*, is the daily total irradiation H in the array plane divided by the reference daily irradiance at STC.

3.3.3. Results and discussion

The operation of a PV plant located in San Sebastián (Gipuzkoa, Spain), which is at latitude of 43° is analysed. Table 3.3.1 shows the details of the PV system and main PV module parameters used are given in Table 3.3.2.

Table 3.3. 1 PV system description.

Main Parameters	**PV system**
PV Module	IS 160
Nominal power	14.08 kWp
Number of inverters	3
Modules per inverter	28/30/30
Modules in series (*Nsg*)	14/15/15
Strings in parallel (*Npg*)	2/2/2
Tilt	20º
Orientation	9º East
Inverters	Ingecon SUN 5 Single-phase inverter
Inverters nominal power	5kWp

Table 3.3. 2 Main parameters of PV modules.

PV module Parameters	PV module IS 160
Isc (A)	9.46
Voc (V)	22.2
Current at Maximum Power Point: Impp (A)	8.65
Voltage at Maximum Power Point: Vmpp (V)	18.5
Temperature Coefficient of Voc: β_{Voc} (V/ºC)	- 0.084
Temperature Coefficient of Isc: α_{Isc} (A/ºC)	$4.6\ 10^{-3}$

This system was remotely supervised and daily evaluated by means of the OPC system. When discrepancies between expected and actual values are observed, the fault detection analysis previously described is applied. This analysis was carried out for the month of December 2014.

The result of the parameters extraction algorithm presented in section 3.3.2.2 is the set of empirical coefficients of the SAPM: C_0, C_1, C_2 and C_3, and PV module parameters: α_{Imp}, β_{Vmp} and n, that allow the best approach to the daily evolution of output current and voltage of the PV array. The values of main model parameters obtained by using the parameter extraction algorithm for the PV system under study are given in Table 3.3.3.

Table 3.3. 3 Values obtained for model parameters.

C_0	C_1	C_2 (V^{-1})	C_3	α_{Imp} (1/°C)	β_{Vmp} (V/°C)	n
0.90336	0.002202	3.8319	99.94	$3.768\ 10^{-4}$	-0.10447	1.1003

Figs. 3.3.2 and 3.3.3 illustrate the daily monitored profiles of irradiance and cell temperature of the PV array used as input data for the parameter extraction algorithm.

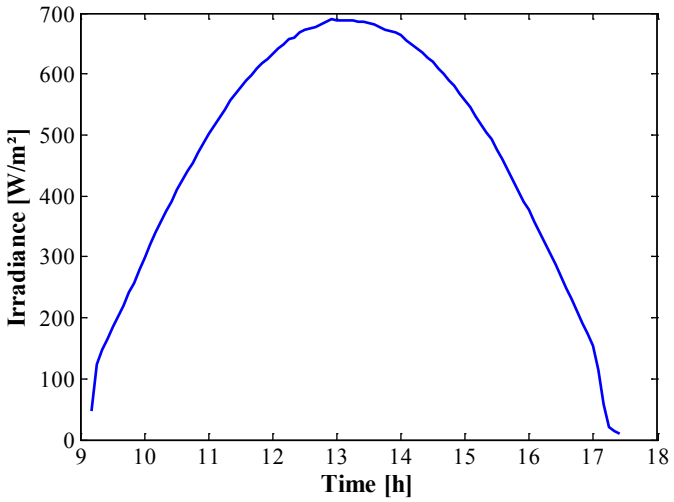

Figure 3.3. 2 Irradiance profile corresponding to 10th of December, 2014.

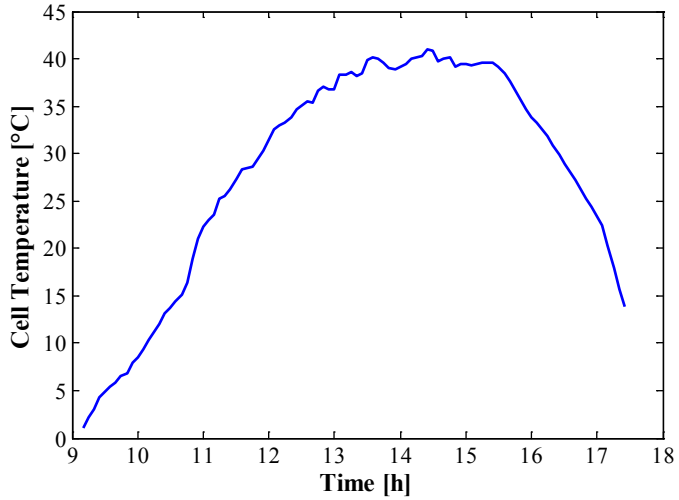

Figure 3.3. 3 Cell temperature corresponding to 10th of December, 2014.

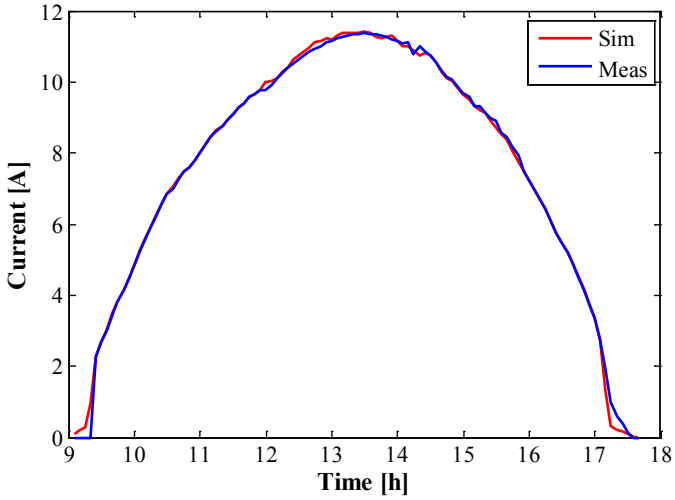

Figure 3.3. 4 Simulated and measured DC output Current corresponding to 10th of December, 2014.

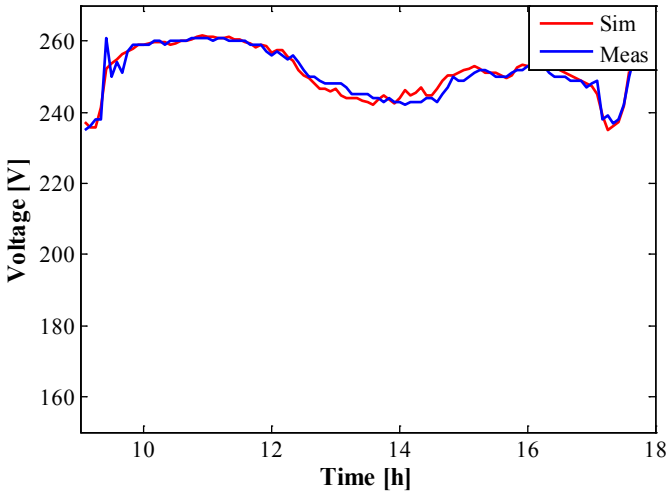

Figure 3.3. 5 Simulated and measured DC output voltage corresponding to 10th of December, 2014.

Figs. 3.3.4 and 3.3.5 show the electrical monitored DC output current and voltage, compared with the predicted results obtained by using the set of the model parameters evaluated by the parameter extraction algorithm. The DC output power of the PV array is obtained as a product of current and voltage in both real and simulated results and the obtained result is illustrated in Fig. 3.3.6.

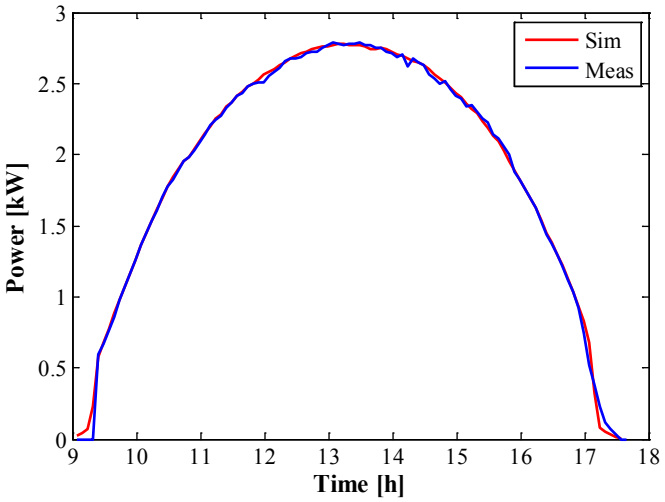

Figure 3.3. 6 Simulated and measured DC output Power corresponding to 10th of December, 2014.

As it is shown in Figs. 3.3.4 – 3.3.6, a good accordance is obtained between simulation results and the real measured data. The simulation performance was also evaluated by calculating the root mean square errors (RMSEs) of current, voltage and power between both data sets for different days with different climatic conditions.

Table 3.3.4 shows the RMSE values obtained. As it can be seen in the table, there is a good agreement between predicted and measured outputs. Furthermore, the inverters connected to the PV array require a minimum input voltage (start-up voltage) to start working. A minimum level of irradiance on the PV array is necessary to enable the proper operation of the inverters. For that reason, a minimum level of G = 200 W/m^2 is considered to start the fault detection evaluation procedure. The RMSE for current, voltage and power were evaluated after filtering the data and run the simulations for irradiance values over the selected threshold of 200 W/m^2.

Table 3.3. 4 Obtained RMSE (%) for different weather conditions.

Days	RMSE Current [%]	RMSE Voltage [%]	RMSE Power [%]
Clear sky day (G>=200)	0.635	1.229	0.677
Semi cloudy day (G>=200)	0.889	1.284	1.693
Cloudy day (G>=200)	2.573	3.591	3.397

The PV system included in this study was remotely supervised by means of the OPC system. The fault detection procedure described previously is used for analysing the present discrepancies between expected and actual values of the monitored parameters.

From the analysis carried out for the month of December 2014, Fig. 3.3.7 shows the evolution of the monitored daily yields and the expected daily yields, Ya-exp, obtained from the modelling of the PV system. As described in section 3.3.2.1, this PV system is formed by three PV arrays connected to three single-phase inverters with a nominal power of 5 kW each one. As shown in Table 3.3.1, the subgenerator 1 connected to the inverter 1 has 14 PV modules per string instead of 15. So, the subgenerator 1 has two PV modules least in the PV field that the other inverters.

As can be seen in Fig. 3.3.7 the daily yields corresponding to the inverter 3, Ya-3, are very similar to the expected daily yields, Ya-exp, evaluated by the model in most of the days, while the yields corresponding to inverters 1 and 2, Ya-1 and Ya-2 respectively, are lower than Ya-3 and Ya-exp. Furthermore, the sub-generator connected to the inverter 2 presents the lowest yield in all the days of the month.

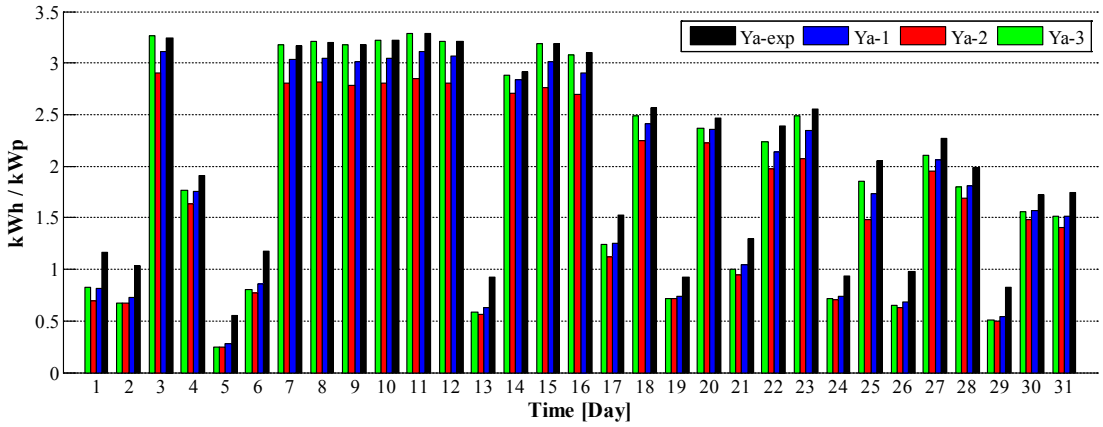

Figure 3.3. 7 Daily array yields corresponding to December 2014.

In order to analyse possible faults present in the PV system, data corresponding to December 11th was selected to show how the process performs analysis of fault detection. Figs. 3.3.2 and 3.3.3 show the irradiance and temperature profiles measured on this day of December.

Table 3.3.5 shows the daily energy generated by each sub-generator of the PV system (DC and AC) as well as the performance ratio (*PR*).

As it can be seen in Table 3.3.5, the sub-generator connected to the third inverter presents the highest value of *PR*, as it might be expected regarding the values of the yields shown in Fig.

3.3.7. On the other hand, the *PRs* corresponding to the sub-generators 1 and 2 are lower, especially the *PR* of the second array. This fact, together with low yields values shown in Fig. 3.3.7 for sub-generators 1 and 2, indicates some problems present in the PV arrays in this time period. It is necessary to study the evolution of current and voltage indicators to identify the cause of these problems.

Table 3.3. 5 Values of the PR and energy generated by the PV system corresponding to 11th of December, 2014.

	Daily *PR* (%)	**Daily DC Energy (kWh)**	**Daily AC Energy (kWh)**
Sub-generator 1	73.03	13.928	13.026
Sub-generator 2	66.96	13.683	12.797
Sub-generator 3	76.44	16.366	14.609

As mentioned above, the fault detection algorithm is performed to values of irradiance greater than G = 200 W/m^2, corresponding approximately from 10.00 a.m. to 17.00 p.m. As it can be seen in Fig. 3.3.2, the irradiance sensor did not detect any important shadow along the day. However, partial shadows on the sub-generators 1 and 2 were identified by the supervision procedure. The shadow did not cover the sensor irradiance, but a part of the PV generator was affected.

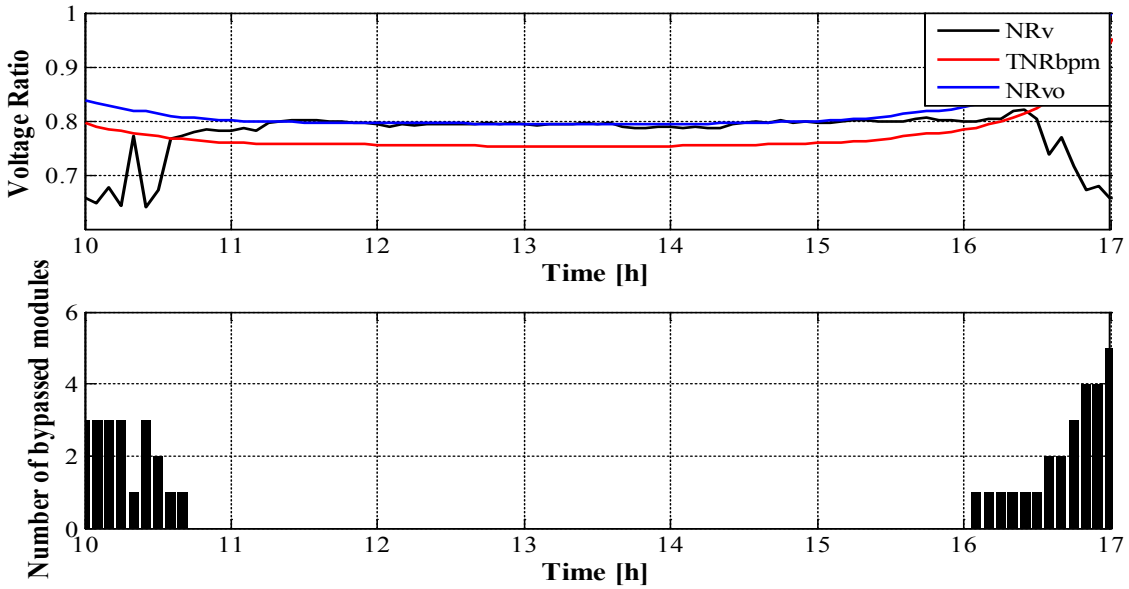

Figure 3.3. 8 Sub-generator 1. Evolution of the Voltage ratios and number of bypassed modules.

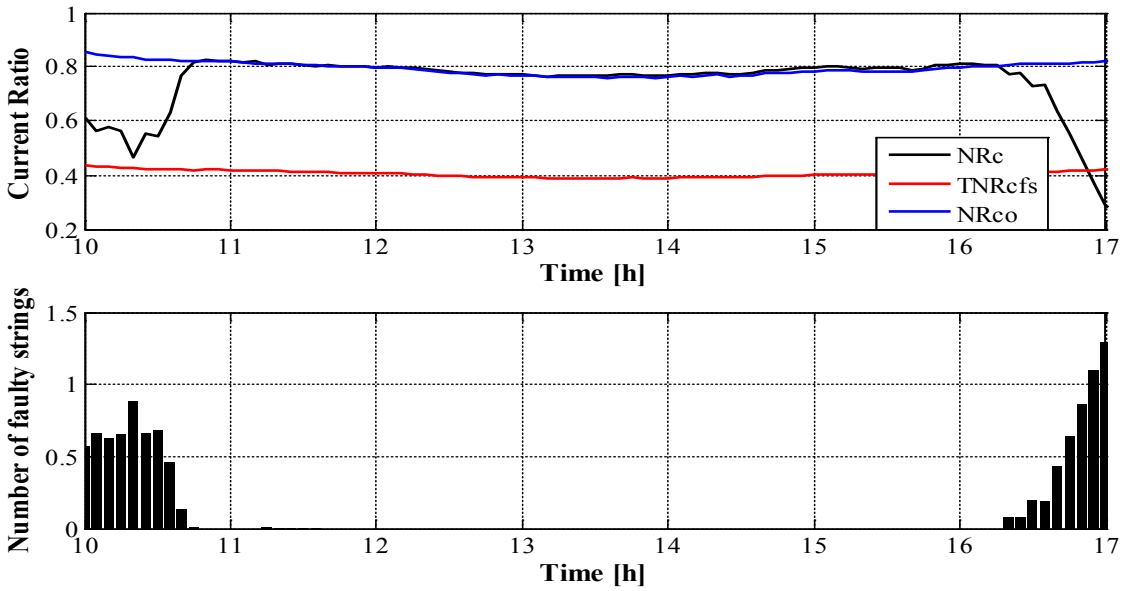

Figure 3.3. 9 Sub-generator 1: Evolution of the Current Ratios and equivalent number of faulty strings.

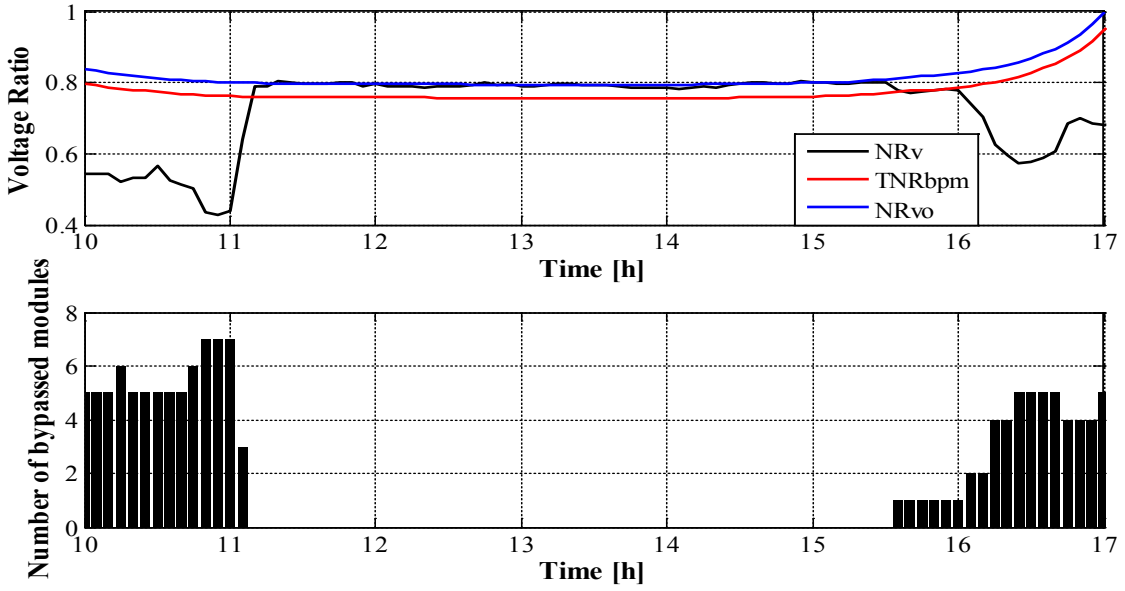

Figure 3.3. 10 Sub-generator 2: Voltage ratio and number of bypassed modules.

The sub-generator 1 is affected by shadows at the beginning and also at the end of the day. Fig. 3.3.8 shows that between 10.00 a.m. and 11.00 a.m. as well as from 16.00 p.m. to 17.00 p.m. the voltage indicator, *NRv*, is below the threshold *TNRbpm* and up to 2.5 PV modules are bypassed as effect of a partial shadow on the array. The number of bypassed PV modules is not an integer because three bypass diodes are included in each of the PV modules present in the PV array. This effect causes a reduction on the output voltage of the PV generator and also a reduction of the output current that is clearly identified by the current indicator analysis shown

in Fig. 3.3.9. Both indicators *NRc* and *NRv* demonstrate that the sub-generator 1 is highly affected by the shadows in the morning period. At the end of the day, the indicator of current, *NRc*, goes below the threshold, *TNRcfs,* and the reduction in output current is equivalent to one faulty string in this sub-generator.

On the other hand, the shadow effects are also the cause of the low *PR* observed in sub-generator 2 indicated in table 3.3.5. In this case the effect is more important. The voltage indicator, *NRv*, appears below threshold, *TNRbpm,* from 10.00 a.m. to 11.00 a.m. and after 15.30 p.m., as it can be seen in Fig. 3.3.10. The analysis shows up to seven bypassed modules are detected in the morning and four in the afternoon.

The evolution of the indicators of current shown in Fig. 3.3.11 proclaims a clear reduction in output current in the same periods of time. The effect of shadows on the array of sub-generator 2 is larger than on sub-generator 1 in both cases: Output voltage and current, as it might be expected.

Fig. 3.3.12 shows the evolution of voltage indicators. As it can be seen, the sub-generator 3 is working in normal operation without any problem except in the last time of the afternoon, when the voltage indicator, *NRv*, appears below the threshold *TNRbpm* and it seems to be two bypassed modules in the string. The rest of the day there is no reduction in output voltage due to shadows on the array.

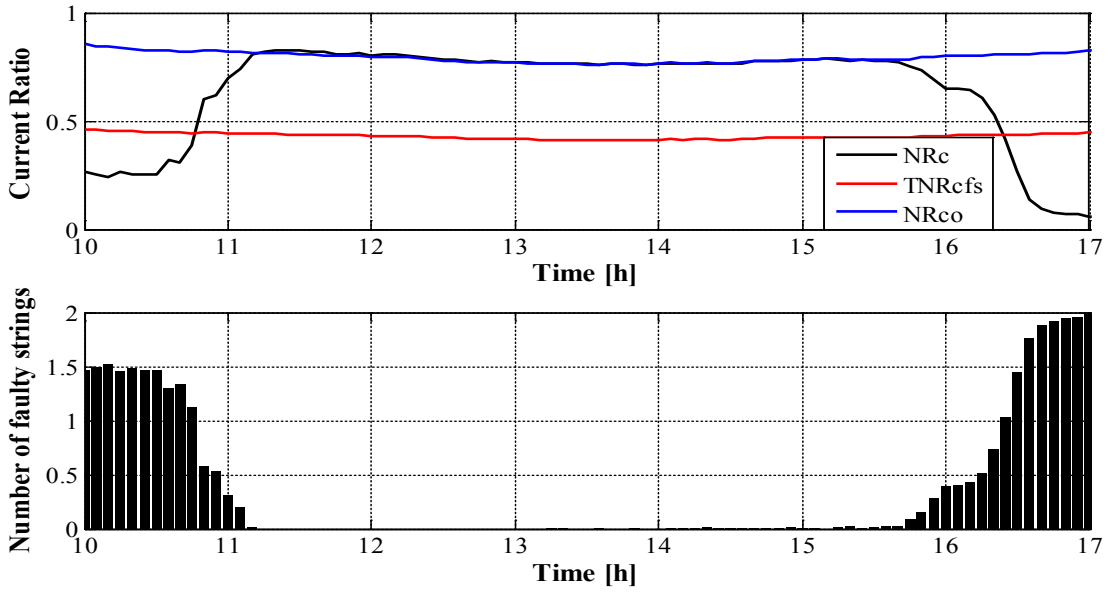

Figure 3.3. 11 Sub-generator 2: Current Ratio and equivalent number of faulty strings.

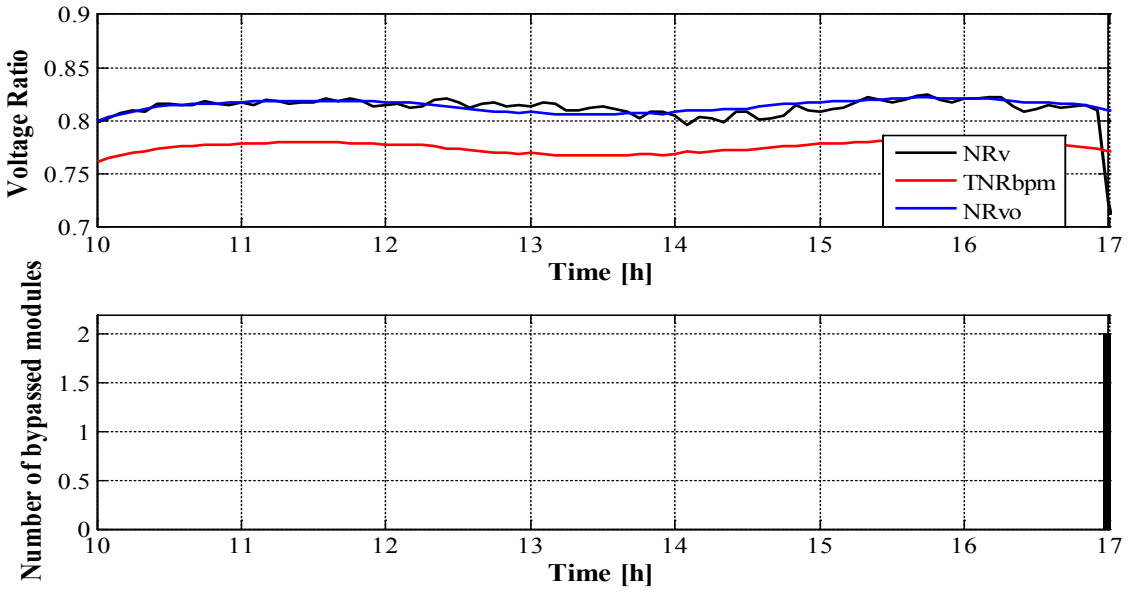

Figure 3.3. 12 Sub-generator 3: Voltage ratios and number of bypassed modules.

The evolution of the current indicator *NRc* given in Fig. 3.3.13 is very similar to the expected value of *NRco* in free fault operation. The current shows a small reduction at the end of the afternoon. However, the indicator of current, *NRc,* remains over the corresponding threshold, *TNRcfs*, and no faulty strings are observed throughout the day.

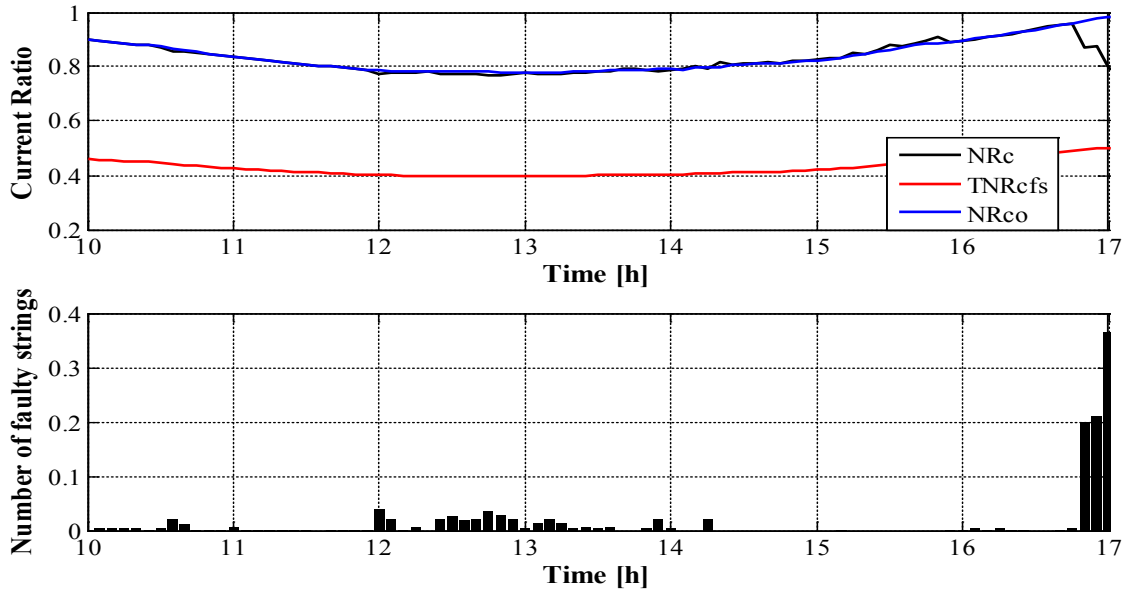

Figure 3.3. 13 Sub-generator 3: Current ratio and equivalent number of faulty strings.

The evolution of *Ploss* along the day, evaluated using Eq. *3.3*-16, is given in Fig. 3.3.14 for the three sub-generators. It must be noted that, as it might be expected, the sub-generator that presents the most important reduction in output power is the sub-generator 2, with a total

reduction of a 32.76% with respect to the expected output power under normal conditions of operation due to the partial shadows on the array at the beginning and also at the end of the day. Sub-generator 1 shows also reduction in output power in the same periods of time. However, the effect due to shadowing is lower and the total reduction in output power is of a 21.41% with respect to the expected one. Finally, sub-generator 3 is the array showing the lowest power losses.

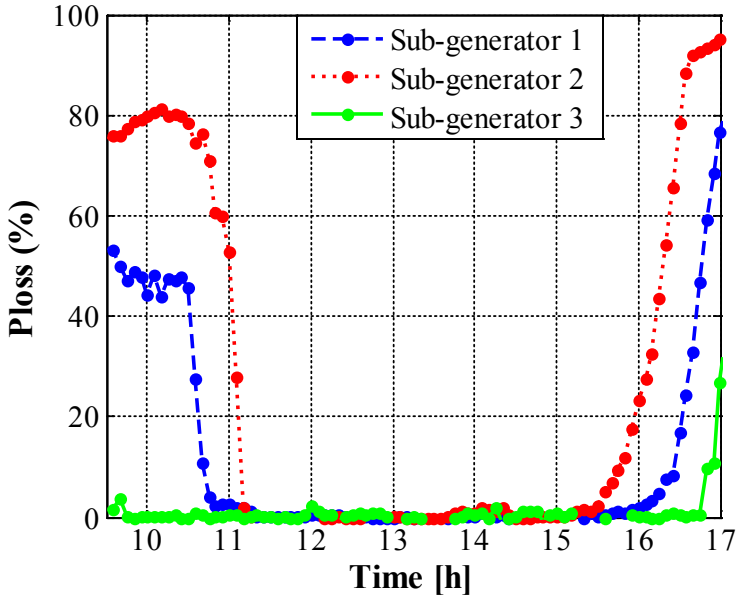

Figure 3.3. 14 Estimated power losses.

The results obtained by using the fault detection analysis by means of OPC monitoring for the rest of the month are very similar to the ones presented as example for December 11th. Neither disconnections of inverters to prevent islanding nor permanent faults in the PV system were detected during the period analysed. The shading effects observed in sub-generator 2, in the morning and afternoon, appear throughout all the month and are responsible for most losses of the PV generation system. Sub-generator 1 is also affected by partial shading at the beginning and at the end of the day, but in this case the duration is shorter and the effect in the total reduction of output power is minor. The repetition of the pattern of shadows in the sub-generators 1 and 2 indicates that the effect of nearby obstacles or even the effect of the shadow of a string of PV modules on another string is its most likely origin. Finally, sub-generator 3 presents the best behaviour and daily yields, being the least affected by shadows.

3.3.4. Conclusions

In this work a procedure for remote supervision and diagnosis of grid connected PV systems by means of OPC monitoring is presented. Monitoring, supervision and fault detection of the PV system are integrated in the same environment.

The supervision is based in the comparison of the monitored data with the expected evolution of the output current, voltage and power of the PV system. In order to obtain the data set corresponding to the expected behaviour of the PV system for actual irradiance and temperature profiles a model of the PV generator is needed. An empirical model is used for this purpose in combination with parameter extraction techniques. The experimental validation results indicated that the model can accurately evaluate the values of output current, voltage and power of the PV system in real conditions of work practically in real time. The RMSE between real monitored data and results obtained from the modelling of the PV array were below 3.6% for all parameters even in cloudy days.

The fault detection procedure used for the diagnosis of the PV system is based on the analysis of the current and voltage indicators evaluated also from monitored data and expected values of current and voltage obtained from the model of the PV generator. Finally, the remote supervision and diagnosis procedure were experimentally verified in real conditions of work in a grid connected PV system formed by three sub-generators connected to inverters with a nominal power of 5 kW each. Results obtained show that the proposed methodology is effective and offers a powerful tool in the field of remote supervision and control of PV systems connected to the grid.

References

[1] Martinez-Marchena I., Mora-Lopez L., Sanchez P.J. and Sidrach-de-Cardona M. Binding machine learning models and OPC technology for evaluating solar energy systems. Lecture notes in computer science 2010; 6098: 606-615.

[2] Martínez-Marchena, Ildefonso; Sidrach-de-Cardona, Mariano; Mora-López, Llanos. Framework for monitoring and assessing small and medium solar energy plants. Journal of Solar Energy Engineering-Transactions of the ASME 2014; 137 (2), 021007.

[3] Alan Gordon. Programación COM y COM+. Anaya Multimedia, 2001.

[4] J. Liu, K.W. Lim, W.K. Ho, K.C. Tan, A. Tay, and R. Srinivasan. Using the opc standard for real-time process monitoring and control. IEEE Software 2005; 22 (6): 54–59.

[5] D.W. Holley. Understanding and using opc maintenance and reliabi- lity applications. Computing Control Engineering Journal 2004; 15 (1):28 – 31.

[6] C.M. Jarque, A. Bera, and K. Anil. A test for normality of ob- servations and regression residuals. International Statistical Review, 1987; 55 (2):163–172.

[7] Chouder A and Silvestre S. Automatic supervision and fault detection of PV systems based on power losses analysis. Energy Convers Manage 2010; 51: 1929–1937.

[8] Drews A, De Keizer AC, Beyer HG, Lorenz E, Betcke J, Van Sark WGJHM, Heydenreich W, Wiemken E, Stettler S, Toggweiler P, Bofinger S, Schneider M, Heilscher G and Heinemann D. Monitoring and remote failure detection of grid connected PV systems based on satellite observations. Journal of Solar Energy 2007; 81: 548-564.

[9] Firth S.K., Lomas K.J., Rees S.J. A simple model of PV system performance and its use in fault detection. Solar Energy 2010; 84: 624-635.

[10] Vergura S, Acciani G, Amoruso V, Patrono GE and Vacca F. Descriptive and inferential statistics for supervising and monitoring the operation of PV plants. IEEE Trans. on Industrial Electronics 2009: 56-11: 4456-4464.

[11] Leloux J, Narvarte L, Luna A, Desportes A. Automatic fault detection on BIPV systems without solar irradiation data. In: Proc. of the: 29th European Photovoltaic Solar Energy Conference and Exhibition; 2014. p. 1-7.

[12] Coleman A, Zalewski J. Intelligent fault detection and diagnostics in solar plants. In: Intelligent Data Acquisition and Advanced Computing Systems (IDAACSs); 2011. p. 948–53.

[13] Wu Y., Lan Q, Sun Y. Application of BP neural network fault diagnosis in solar photovoltaic system. In: Mechatronics and Automation (ICMA); 2009. p. 2581–5.

[14] Silvestre S, Aires da Silva M, Chouder A, Guasch D and Karatepe E. New procedure for fault detection in grid connected PV systems based on the evaluation of current and voltage indicators. Energy Convers Manag 2014; 86: 241-249.

[15] Silvestre S, Kichou S, Chouder A, Nofuentes G and Karatepe E. Analysis of current and voltage indicators in grid connected PV(photovoltaic) systems working in faulty and partial shading conditions. Energy 2015; 86: 42-50.

[16] Chine W, Mellit A, Pavan AM, Kalogirou SA. Fault detection method for grid connected photovoltaic plants. Renew Energy 2014; 66:99-110.

[17] Martínez-Marchena, I. Marco de trabajo para la generación de software para la gestión de sistemas de energía solar. Universidad de Málaga. PhD Thesis. Universidad de Málaga, junio 2015.

[18] King D L, Kratochvil JA and Boyson WE. Photovoltaic array performance model. Sandia Report: SAND2004-3535 (2004). USA, Department of Energy.

[19] Peng J, Lu L, Yang H and Ma T. Validation of the Sandia model with indoor and outdoor measurements for semi-transparent amorphous silicon PV modules. Renewable Energy 2015; 80: 316-323.

3.4. Published paper in Energy 96 (2016)

Energy 96 (2016) 231 – 241

http://dx.doi.org/10.1016/j.energy.2015.12.054

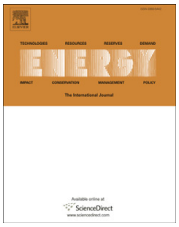

Characterization of degradation and evaluation of model parameters of amorphous silicon photovoltaic modules under outdoor long term exposure

Sofiane Kichou[1], Santiago Silvestre[1], Gustavo Nofuentes[2], Miguel Torres-Ramírez [2], Aissa Chouder[3], Daniel Guasch[4]*

[1] MNT Group, Electronic Engineering Department, UPC-BarcelonaTech. Barcelona, C/ Jordi Girona 1-3, Mòdul C4 Campus Nord UPC, 08034 Barcelona, Spain.

[*] Corresponding author: E-mail addresses: kichousofiane@gmail.com

[2] IDEA Research Group, University of Jaén, Campus de Las Lagunillas, 23071, Jaén, Spain.

[3] Univ. M'sila, Fac. Technologies, Dep. Génie Electrique, BP 166 Ichbelia 28000 M'sila, Algeria.

[4] Departament d'EnginyeriaTelemàtica. Universitat Politécnica de Catalunya (UPC) BarcelonaTech. EDIFICI VG1 (EPSEVG). Avda. Víctor Balaguer, 1. 08800 Vilanova i la Geltrú, Spain.

ARTICLE INFO

Article history:

Received 16 September 2015
Received in revised form 14 December 2015
Accepted 15 December 2015

Keywords:

a-Si PV (photovoltaic) modules,
Model parameters extraction,
Degradation rate.

ABSTRACT

The analysis of the degradation of thin-film single junction a-Si photovoltaic (PV) modules and its impact on the output power of a PV array under outdoor long term exposure located in Jaén (Spain), a relatively dry and sunny inland site with a Continental-Mediterranean climate is addressed in this paper. Furthermore, a new procedure of solar cell model parameters extraction experimentally validated is presented. The parameter extraction procedure allows obtaining main model parameters of the solar cells forming the PV array from monitored data of the PV system in real operation of work. Results obtained of the evolution of each one of the solar cell model parameters along the PV system outdoor long term exposure campaign are analysed in order to achieve a better understanding of the performance changes of the PV modules and the behaviour of the output power of the PV array.

3.4.1. Introduction

The photovoltaic (PV) market continues to grow steadily worldwide. PV systems are replacing conventional energy sources becoming a major source of power generation due to their environment friendly and renewable nature [1].

PV modules are a key element of PV systems and allow conversion of solar energy directly into electrical energy. Several factors influence their performance such as solar irradiance and its spectral distribution [2], mismatches, soiling [3] and operating module temperature [4–7]. Moreover, PV modules tend to degrade after long term outdoor exposition. The degradation rate is mainly associated to the PV module technology and several studies have reported analysis of outdoor performance and degradation of PV modules of different technologies [8–11].

Crystalline silicon (c-Si) and polycrystalline PV modules supply most part of the global photovoltaic energy production with a 90 % of the total annual production in 2013, while thin-film (TF) PV modules are in third position with a 10 % of market share [12]. TF PV modules use materials such as amorphous silicon (a-Si), CdTe, copper indium gallium selenide sulfide (CIGS) and copper indium diselenide (CIS) among others. The main advantages of TF PV modules are their lower production costs and lower temperature coefficients relative to the c-Si and polycrystalline PV modules. However, TF PV modules present higher degradation rates than polycrystalline and c-Si [9,13]. Recently, the TF a-Si PV modules market share noted a regression probably due to this fact and to their lower module conversion efficiency [12]. Additionally, problems related to the bankability of these technologies still persist.

The a-Si PV modules present light-induced degradation (LID) due to the Staebler-Wronski effect (SWE) [14–17]. The electrical performance degradation of these modules is very important during the initial exposure to outdoor light due to changes in photoconductivity and dark conductivity. This effect gradually tends to stabilize at power rates ranging from 10% to 30 % of the nominal power of the PV module. However, thermal annealing of the a-Si for several hours at 150°C reverses these effects [17]. Moreover, a lower temperature annealing also allows recovering the initial performance but takes a longer amount of time [19,20].

Several works have been conducted in attempt to explain the real performance characterization of the a-Si PV modules when deployed outdoors. The degradation rate can be based on the comparison of the monitoring outdoor performance with the initial indoor

measurements taken as references [21–24], or by applying Linear Regression (LR) and Classical Seasonal Decomposition (CSD) methods with temperature correction [25,26].

The studies presented in references [22–24] demonstrate that TF hydrogenated single-junction amorphous silicon (a-Si-H) PV modules are degraded mainly by the SWE effect, when compared to other TF technologies. This degradation affects especially the internal parameters of the solar cell as the short-circuit current, ideality factor, saturation current and series and shunt resistances [18,27].

Understanding the origin of these degradation modes and how they affect the performance of PV modules is essential to improve the reliability of PV modules, and selecting the best technology for each specific climatic condition. In this paper we analyse the behaviour of TF a-Si PV modules under outdoor long term exposure in Jaén (Spain, Latitude: 37º 47' 14.35" N, Longitude: 3º 46' 39.73" W, Altitude: 511 m), a relatively dry and sunny inland site with a Continental-Mediterranean climate. The period under scrutiny ranges from late July 2011 to October 2014.

On the other hand, the variation of main solar cell model parameters is also evaluated by means of parameter extraction techniques. We present a new parameter extraction procedure to obtain main model parameters of the solar cells forming the PV system. The parameter extraction has as input the daily monitored data of the PV system in real operation of work and calculates the temporal evolution of main solar cell model parameters.

The paper is organized as follows: An overview of the degradation analysis methodology and parameter extraction technique followed in the study is given in Section 3.4.2. Section 3.4.3 describes the PV array used in this study and details of the monitoring system. The results and discussion are presented in Section 3.4.4. Finally, the conclusions of the study are given in Section 3.4.5.

3.4.2. Methodology

3.4.2.1. PV Array model

The PV array output is based in the well-known ‘‘five parameter” model of the solar cell in which the relationship between output current and voltage is given by the following nonlinear implicit equation [28–30]:

$$I = I_{ph} - I_O \left[exp\left(\frac{V + R_s I}{nVt}\right) - 1 \right] - \frac{V + R_s I}{R_{sh}} \quad (3.4\text{-}1)$$

where the five solar cell model parameters are: Photocurrent I_{ph}; diode reverse saturation current I_o; ideality factor n; R_s and R_{sh} the series and shunt resistances respectively. I and V are the output current and voltage and Vt is the thermal voltage.

Eq. (*3.4*-1) can also be written as follows,

$$I = I_{ph} - I_d - I_{sh} \quad (3.4\text{-}2)$$

where I_d and I_{sh} are the currents across the diode and shunt resistance respectively.

Generally, PV modules are formed by parallel strings of solar cells connected in series. However, at present most PV modules include one single string of solar cells. Therefore, the model of the solar cell can be scaled up to the model of the PV array taking into account the configuration of the PV array: Number of PV modules connected in series by string and the number of parallel strings forming part of the PV array as well as the internal configuration of the PV module.

Several studies based on the simulation of PV systems applying this model were reported in the literature. The simulations were carried out in software environments as: Pspice [30–33], Matlab [34–36], or LabView [37,38] and results obtained were experimentally validated with success. In this study we have used Matlab/Simulink for the simulations and the parameter extraction.

3.4.2.2. Parameter extraction technique

One of the objectives of this work is the investigation of the variation of the solar cell model parameters for single junction a-Si PV modules in real conditions of work. Therefore, this study includes parameter extraction techniques in order to find the set of solar cell model parameters able to reproduce the actual behaviour of the whole photovoltaic system with a good accuracy degree.

Monitored electrical parameters: Current, voltage and power at the DC output of the PV array together with in-plane irradiance (G) and cell temperature (T_c) profiles are needed in order to estimate the set of model parameters of the solar cells forming the PV array.

Considering the number of parallel strings of solar cells present in the PV array, Np, Eq. (*3.4*-2) becomes:

$$I = N_p(I_{ph} - I_d - I_{sh}) \tag{3.4-3}$$

where I is the DC output current of the PV array.

For any arbitrary value of G and T_c, the photocurrent, I_{ph}, is given by:

$$I_{ph} = \frac{G}{G^*} I_{scc} + k_i(T_c - T_c^*) \tag{3.4-4}$$

where G^* and T^*_c are respectively the irradiance and cell temperature at standard test conditions (STC): 1000 W/m^2 (AM1.5) and 25ºC, k_i is the temperature coefficient of the current and I_{scc} is the solar cell short-circuit current at STC.

Each one of the strings of the PV array is formed by Ns solar cells connected in series. The shunt current, I_{sh}, included in Eq. (*3.4*-2) can be calculated from:

$$I_{sh} = \frac{\frac{V}{N_s} + \frac{I\,R_s}{N_p}}{R_{sh}} \tag{3.4-5}$$

where V is the Therefore DC output voltage of the PV array.

The diode current, I_d, included in Eq (*3.4*-2) is given by:

$$I_d = I_o[\, e^{\left(\frac{\frac{V}{N_s}+\frac{IR_s}{N_p}}{n\,V_t}\right)} - 1] \tag{3.4-6}$$

where I_o is the saturation current of the diode.

The saturation current of the diode presents a strong dependence on temperature and it is usually given by:

$$I_o = I_{oref} e^{\left(\frac{E_{go}}{V_{to}} - \frac{E_g}{V_t}\right)} \left(\frac{T_c}{T_c^*}\right)^3 \tag{3.4-7}$$

where I_{oref} and V_{to} are the saturation current and thermal voltage at STC, respectively, E_g the energy bandgap of the semiconductor and E_{go} is the energy bandgap at T=0 K.

Eq. (*3.4*-7) can also be written, substituting I_{oref} as a function of the short-circuit current: I_{sc} and open-circuit voltage: Voc of the solar cell, as follows:

$$I_o = \frac{I_{sc}\, e^{\left(\frac{E_{go}}{V_{to}} - \frac{E_g}{V_t}\right)}}{e^{\left(\frac{Voc}{n\,Vto}\right)} - 1} \left(\frac{T_c}{T_c^*}\right)^3 \tag{3.4-8}$$

The value of the energy bandgap of the semiconductor at any cell temperature T_c is given by:

$$E_g = E_{go} - \frac{\alpha gap\, T_c^2}{\beta gap + T_c} \qquad (3.4\text{-}9)$$

where α_{gap} and β_{gap} are fitting parameters characteristic of the semiconductor.

The parameter extraction algorithm evaluates: I_{ph}, R_s, R_{sh}, I_o and n by using Eqs. (*3.4*-4) – (*3.4*-9). Daily profiles of monitored electrical parameters–namely, current and voltage at the DC output of the PV array, together with G and T_c - are used as inputs of the parameter extraction algorithm.

A nonlinear regression algorithm based on the Levenberg–Marquardt method was applied to both data sets: The daily monitored data from the PV array in real conditions of work and simulation results generated by using the described model, in order to minimize the following quadratic function [39,40]:

$$S(\theta) = \sum_{i=1}^{N} [Ii - I(Vi, \theta)]^2 \qquad (3.4\text{-}10)$$

where $\theta = f(I_{ph}, I_o, R_s, R_{sh}, n)$.

The toolbox has been interfaced with Simulink as illustrated in Fig. 3.4.1.

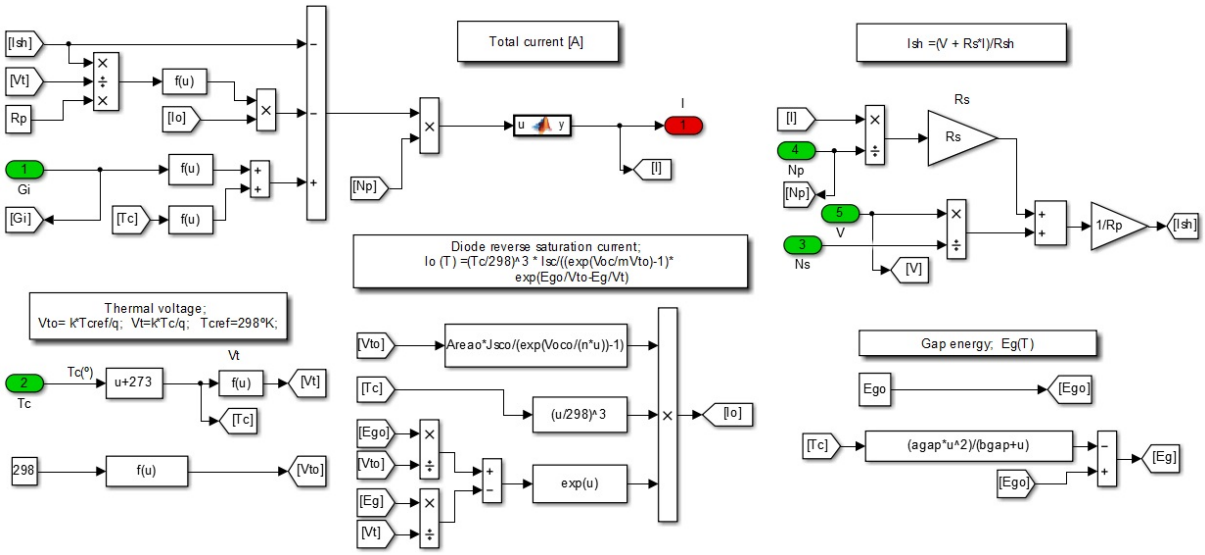

Figure 3.4. 1 Simulink block diagram of the parameter extraction algorithm.

The result of the parameter extraction algorithm is a set of solar cell model parameters that allow the best approach to the daily evolution of output current and voltage of the PV array.

3.4.2.3. Output power of the PV array

The effective peak power of a PV array, P^*_M, at STC is given by the following equation [41,42]:

$$P_M^* = \frac{G^* P_{DC}}{G\,[1 + \gamma(T_c - T_c^*)]} \qquad (3.4\text{-}11)$$

where P_{DC}, G and T_c are the DC output power of the PV array, the irradiance and cell temperature respectively, γ is the power temperature coefficient of the PV modules and G^* and T_c^* are the irradiance and temperature at STC, respectively.

The power coefficient temperature, γ, is normally stated in the PV manufacturer's datasheet. Nevertheless, it can be calculated as follows [6]:

$$\gamma = \frac{1}{P_{max}} \frac{\partial P_{max}}{\partial T} \qquad (3.4\text{-}12)$$

where P_{max} is the maximum power of PV modules at STC and the reference temperature is 25 ºC.

Outdoor monitoring is subject to continuously changing operating conditions as irradiation, temperature and spectrum. The evaluation of P^*_M requires a previous filtering of irradiance values: $G < 800$ W/m^2, in order to avoid the influence of operational anomalies, such as shade on the PV array, inverter saturation, inverter–off, low irradiances, etc [41,42]. So, we eliminated the data where irradiance is too low in our monitoring profiles before the calculation of P^*_M values.

As detailed in the next section, measurements of G are taken by using a pyranometer. However, no spectral effects have been included in Eq. (*3.4*-11) as the solar spectrum distribution at in-plane irradiance levels above 800 W/m^2 closely matches that of the AM 1.5G standard reference spectrum in the city of Jaén [44].

3.4.3. Experimental

3.4.3.1. Climate characterization of the site and PV system description

As commented in section 3.4.1, Jaén is a dry and sunny inland site, with a Continental-Mediterranean climate. In this sense, Table 3.4.1 may help provide a succinct climate characterization. The PV system which has provided the necessary experimental support to this work is located in Jaén and it is shortly described below.

Table 3.4. 1 Annual average values of some relevant meteorological parameters recorded in Jaén over 30 years [45]

Horizontal irradiation ($kWh \cdot m^{-2}$)	Ambient temperature (ºC)	Minimum ambient temperature (ºC)	Maximum ambient temperature (ºC)	Relative humidity (%)	Rainfall (mm)	Barometric pressure (hPa)
2038	16.9	11.4	22.4	63	558	954.1

The 900-Wp PV field comprises 15 a-Si:H TF PV modules, with 5 parallel-connected strings of 3 series-connected PV modules each (Np = 5, Ns = 3). The main electrical characteristics at STC of this PV field are gathered in Table 3.4.2. It is worth noting that the PV modules are fixed to an equator-facing open rack with a tilt angle of 35º. This tilt angle was intended to maximize the collection of annual on-plane irradiation. This criterion is widely followed when planning PV grid-connected systems, unless constraints such as those imposed by architectural integration may deter the PV project developer from following it. Bearing this in mind, the optimal tilt angle for Madrid (Spain, latitude 40º24'N, longitude 3º42'W) lies precisely at 35º [46]. This figure may be assumed for Jaén (Spain, latitude 37º47'N, longitude 3º46'W) with no significant error.

The PV field is connected to a single-phase grid-tied SMA™ Sunny Boy SB1200 inverter. Two SMA™ Sunny SensorBox devices were installed on a metal plate in the same plane as the PV field to measure cell and ambient temperatures together with wind speed. Two Pt 100 resistive thermal detectors (RTD) are used as module temperature sensors being glued to the rear surface of the PV modules. The in-plane irradiance comes from a Kipp & Zonen™ CMP21 pyranometer, which is also installed on a metal plate, coplanar with the PV field. Onsite measurements of DC voltage and current are recorded at the inverter input. Data were taken at 5-minute intervals.

Table 3.4. 2 Main electrical characteristics at STC of the analysed PV field. Values derived from the PV module manufacturers' data sheet.

Maximum power (W)	Open-circuit voltage (V)	Short-circuit current (A)	Voltage at maximum power point (V)	Current at maximum power point (A)
900	276	5.95	201	4.50

3.4.4. Results and discussion

3.4.4.1. Evolution of the effective peak power of the PV array

The effective peak power of the PV array, P^*_M, and the monthly radiation, H, along the monitoring campaign are shown in Fig. 3.4.2. An important initial decrease of P^*_M can be

observed due to the LID phenomenon and then the decrease occurred more slowly. On the other hand, a seasonal variation of P^*_M is clearly shown in Fig. 3.4.2. This seasonal variation in a-Si PV modules behaviour has been described by a number of authors [14,20,24,25]. The initial decrease in output power of the array is followed by an increase over the summer months, a decrease over winter months and once again an increase over summer months. The regeneration on summer months can be attributed to spectral effects [47], to thermal regeneration[17,20,48] and light-induced annealing [22].

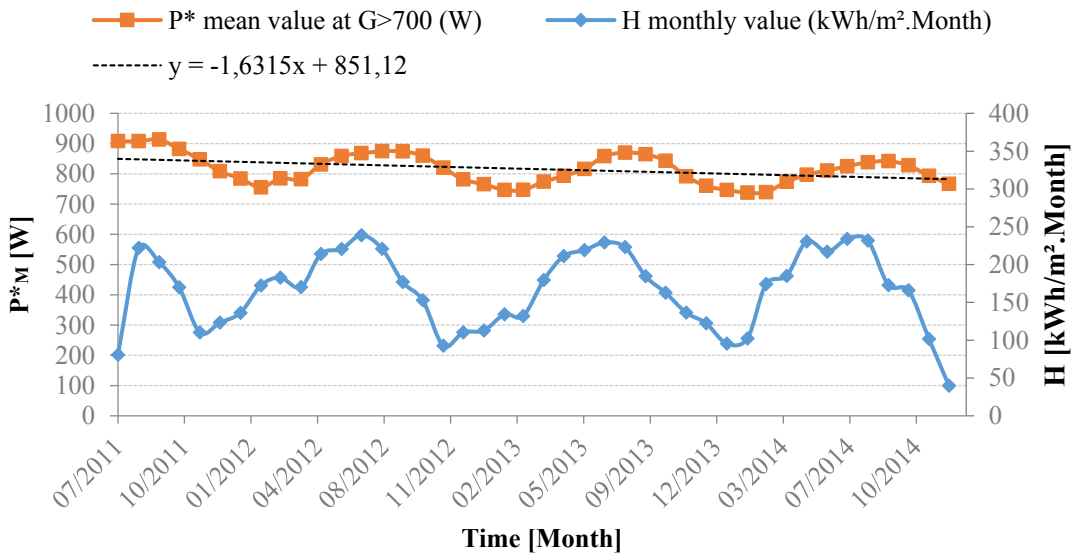

Figure 3.4. 2 The effective peak power of the PV array P^*_M (for G > 700 W/m²), and the monthly radiation, H along exposure period.

The sun's elevation angle (γ_s, in degrees) at solar noon in Jaén varies from 90º - Φ – 23º27' = 28º46' in winter solstices to 90º - Φ + 23º45' = 75º40' in summer solstices, where Φ [º] is the latitude. At solar noon, γ_s = 52º13' in autumnal and vernal equinoxes. Regarding the angle of incidence between the rays of the sun and the normal to the surface (θ_s, in º) it should be kept in mind that the tested PV array was deployed in the Northern Hemisphere on an equator-facing surface with an inclination (35º) angle very close to the latitude (37º47'N). Hence, it may be assumed that [49]:

$$\cos \theta_s \approx \cos \delta \ \cos \omega \qquad (3.4\text{-}13)$$

where δ [º] is the solar declination and ω [º] is the true solar time. Given that ω = 0º at noon, θ_s varied very approximately from 0 (equinoxes) to 23º (solstices) in our experimental campaign at this time of the day.

The degradation rate, R_D, can be analysed by a linear least square fitting method. This method is applied to the monthly effective peak power of the PV array, P^*_M, calculated by using Eq. (*3.4*-14) and monitored data. Using the trend line, the degradation per year can be calculated by linear regression (LR) as follows [3,25]:

Equation of the trend line:

$$y = mx + c \qquad (3.4\text{-}14)$$

where m is the slope of line and c is the y intercept, thus the degradation per year: R_D(%) can be calculated as follows [3]:

$$R_D = 100\frac{12m}{c} \qquad (3.4\text{-}15)$$

The degradation rate calculated from the trend line is found to be: -2.30 ± 0.15 %/year. The analytical uncertainty reported along with the degradation rate was determined from the standard errors of the linear fit. The value obtained for R_D is in the range of previous results presented in the literature for a-Si PV modules [9,25]. The highest degradation rates have been reported in Korea and the Mediterranean region [25].

The stabilized power in a-Si PV modules is achieved when the power does not decrease more than 1% in a month [13]. However, the amount of LID phenomenon depends on the distribution of light and temperature at the specific location of the PV array.

In order to analyse the stabilization period of the PV array, a second monitoring data filtering process was carried out following the procedure used in previous reported studies [14]. One point for each month of the monitored data for the tilted irradiance and working PV module temperature in the range of 900 W/m^2 < G < 905 W/m^2 and 48.6 ºC < T < 54 ºC was selected.

From the data obtained in the filtering process shown by Fig. 3.4.3, the stabilization period was observed to start after 16 months of operation in Jaen. Stabilization periods around 16 months have been also reported for single junction a-Si PV modules under Malaysia's outdoor exposure [14].

The trend line in Fig. 3.4.3 is obtained by sixth polynomial correlation with R^2 equal to 0.9575. In the first month, it is observed a strong initial degradation respect to the other monitored months. The DC power was degraded by about 11.2% in the first 70 days. In November 2012 the DC power exhibited a decline by the relative percentage of 18.8% and then is stabilized.

As commented in section 3.4.3.1, the in-plane irradiance was recorded by means of a pyranometer coplanar with the PV field. Values of G ranging from 900 to 905 W/m^2 correspond to a true solar time interval comprised between ω = -30º and ω = 30º, when the sun elevation is then higher than that of the rest of the day. Consequently, the impact of the solar elevation on the measurements and the angle of incidence dependence may be neglected.

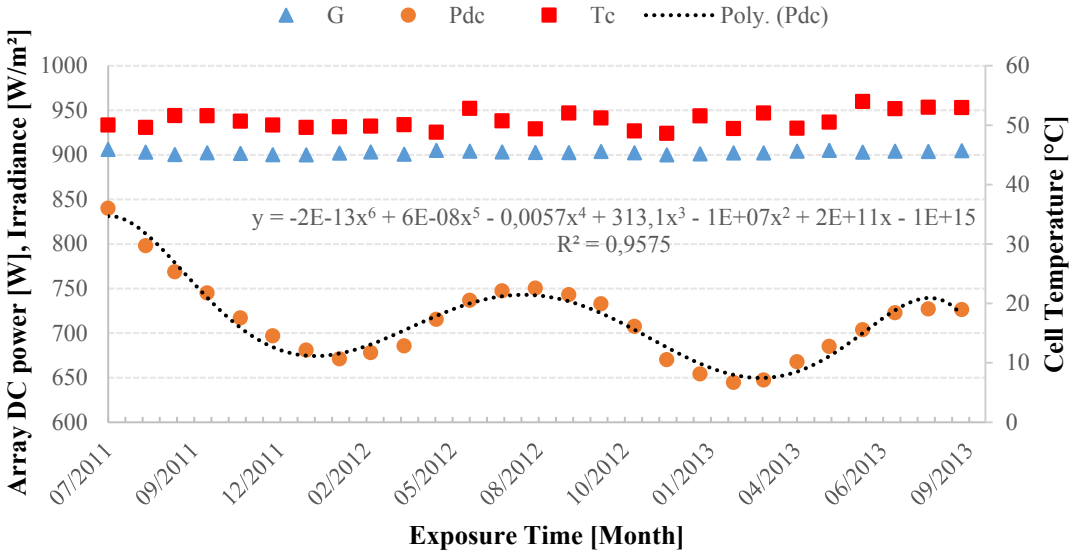

Figure 3.4. 3 Monthly trend line outdoor stabilization process obtained with the selected data of irradiance and cell temperature in the range of 900 W/m² < G < 905 W/m² and 48.6 ºC < T < 54 ºC.

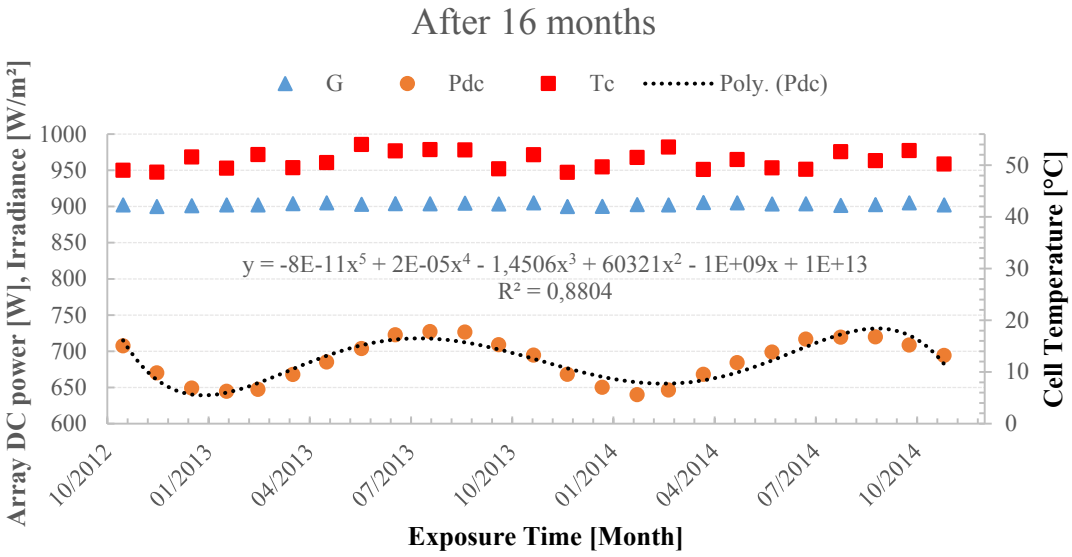

Figure 3.4. 4 Trend line outdoor stabilization process after 16 months using the selected data of irradiance and cell temperature in the range of Wm² < G < 905 W/m² and 48.6 ºC < T < 54 ºC.

Fig. 3.4.4 shows the set of data after the first 16 months of operation and the trend line for the DC output power of the array obtained by fifth polynomial correlation with R^2 equal to 0.88. The stabilized level of DC output power of the array is around 682 W in the range of G and Tc considered in data filtering process. In the following months, it demonstrates as a sinusoidal form attributable to the annealing effects. The effect of seasonal oscillation remains after the stabilization period for about 5 % variation from the stabilized level of DC power.

3.4.4.2. Parameter extraction procedure validation

The parameter extraction algorithm calculates the five model parameters of the solar cell: *Iph, Rs, Rsh, Io* and *n* by using Eqs. (*3.4*-4) – (*3.4*-9) described in section 3.4.2.2. The daily monitored data: Output DC current and voltage, irradiance and temperature of the PV array in real conditions of work are used as input data of the algorithm and it is executed until function S(θ), given by Eq. (*3.4*-10), is minimized. An average number of 10 iterations are needed to find the set of solar cell model parameters for an input data set corresponding to one day of real operation of the PV array, the extracted parameters are given in the table below.

Table 3.4. 3 Extracted solar cell model parameters

Day	*n*	R_s [Ω]	R_{sh} [Ω]	I_{ph} [A]	I_o [A]
23/12/2011	1.1286	0.0307	7.482	0.999	$1.09\ 10^{-15}$

Fig. 3.4.5 and 3.4.6 depict the electrical monitored data recorded during December 23rd, 2011: DC output current and voltage, compared with the simulation results obtained by using the set of solar cell model parameters evaluated by the parameter extraction algorithm. The DC output power of the array is obtained as a product of current and voltage in both real and simulated results and the obtained result is illustrated in Fig. 3.4.7. It should be remembered that the PV array located in Jaén (Latitude 37º 45') is inclined at 35º from the horizontal plane.

As it can be seen a good agreement is found between simulation results and monitored data. The coefficient of variation of the root mean square errors, CV(RMSE) between both data sets are given in Table 3.4.4 for the current, voltage and power respectively.

Table 3.4. 4 CV(RMSE) obtained for main output electrical parameters of the PV array.

P_{DC} [%]	I [%]	V [%]
1.71	1.71	5.21

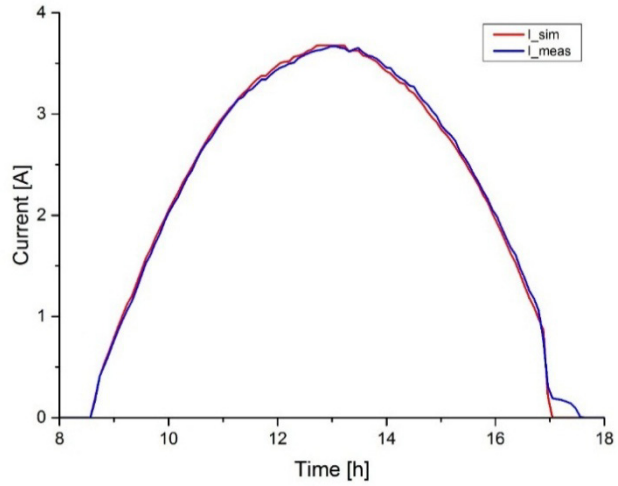

Figure 3.4. 5 Monitored and simulated DC output current obtained by using the set of parameters estimated by the extraction parameter algorithm.

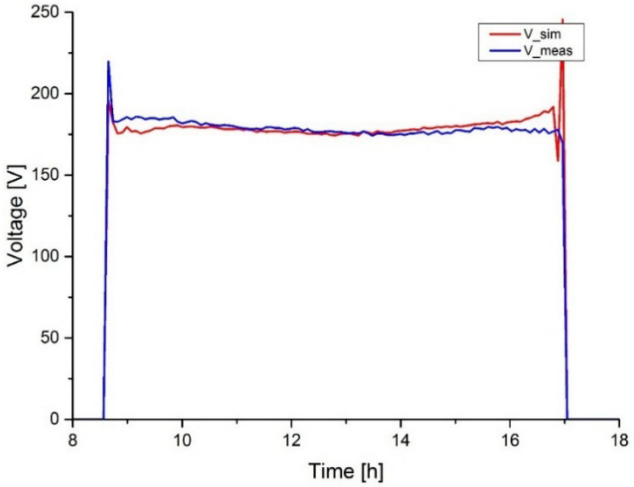

Figure 3.4. 6 Monitored and simulated DC output voltage obtained by using the set of parameters estimated by the extraction parameter algorithm.

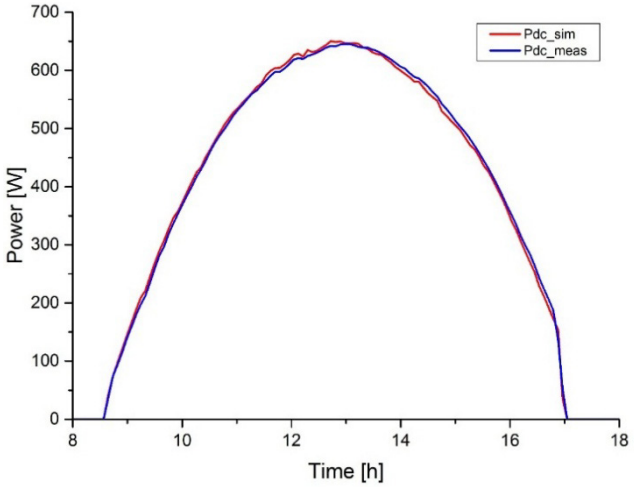

Figure 3.4. 7 Monitored and simulated DC power obtained by using the set of parameters estimated by the extraction parameter algorithm.

3.4.4.3. Evolution of solar cell model parameters

The seasonal variation of a-Si PV modules behaviour can be also observed in the evolution of the solar cell model parameters. The monthly average value of each one of the model parameters was calculated for the whole monitoring campaign included in this study.

Fig. 3.4.8 shows the evolution of the values obtained for the ideality factor, *n*, by using the extraction parameter technique. It can be seen in that the values of *n* show an increase over the winter months, a decrease over the summer months and once again an increase over the winter months.

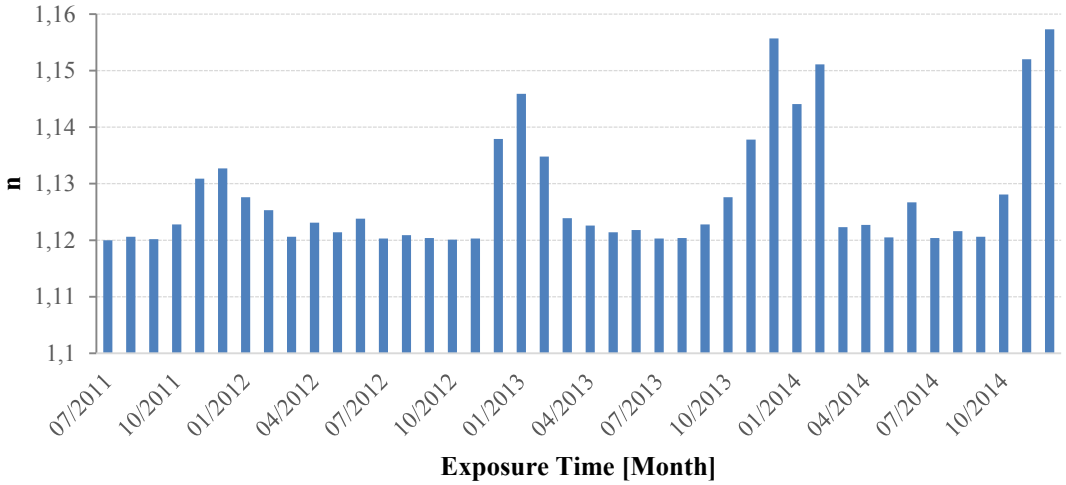

Figure 3.4. 8 Average values of n obtained by using the parameter extraction algorithm.

In summer, a-Si solar cells experience higher temperatures and an improvement occurs in material characteristics. There is an increase in charge carrier lifetime and a reduction in band gap [22,24]. The improvement in carrier lifetime due to a reduction of recombination effects in summer is the main responsible of the evolution of *n*. As can be seen in Fig. 3.4.9, *n* is closer to 1 in summer periods. On the other hand in winter periods there is a deterioration of the p–n junction quality as can be seen from the increase in *n* due to an increase in recombination current [24]. The maximum seasonal variation of n observed is of 3.4 %.

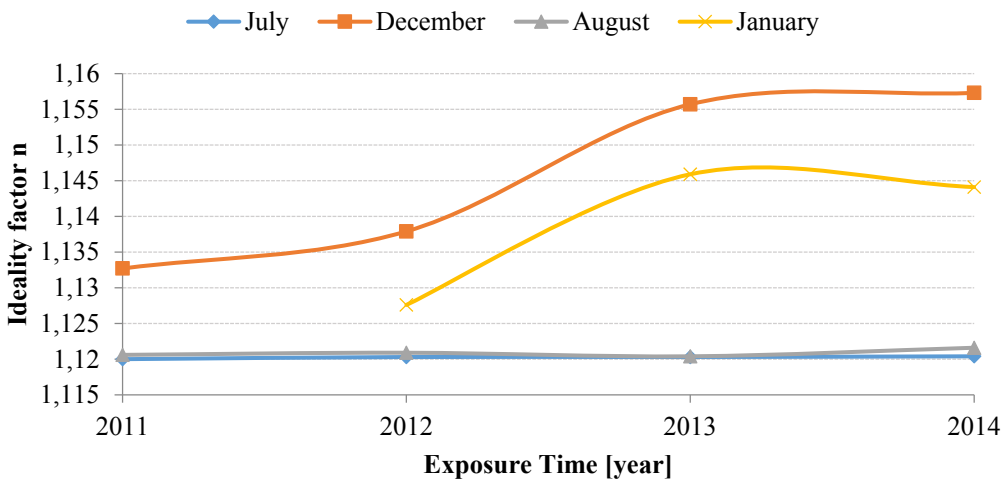

Figure 3.4. 9 Trend of the ideality factor, n, over December, January, July and August from 2011 to 2014.

The variation obtained for the saturation current, I_o, given by Fig. 3.4.10 shows an opposite trend to the variation of n. Eq. (*3.4*-9) gives the variation of the bandgap as a function of temperature. The higher temperatures in summer period decrease the bandgap resulting in a decrease in open-circuit voltage [24]. Temperature has also a strong effect on the variation of the saturation current as shown in Eq. (*3.4*-8). The combination of bandgap reduction and strong increase of temperature in summer periods along with the increase in short-circuit current due to LID effect lead to an increase of the saturation current despite the reduction of recombination effects in summer. As can be seen in Fig. 3.4.10, I_o varies from values in the order of 10^{-12} A to values around 10^{-16} in winter periods.

The continuing decrease in short-circuit current, I_{sc}, throughout the first 16 months of the deployment period can be observed in Fig. 3.4.11. After that it shows a more stable trend. However, the seasonal effect on I_{sc} is also clearly shown in Fig. 3.4.11, being the predominant factor contributing to the large improvement in output power during summer time. There is an important decrease in AM from winter to summer and a favourable spectral distribution of the solar irradiance during summer especially in the ultraviolet region. The improvement in output current during summer time is due to the effect of solar spectral irradiance and to thermal-recovery of the LID [24,46]. The reduction of I_{sc} in the worst winter months is approximately 83% from the peak value of this parameter in the months of August. The lower temperature in winter also reduces the thermal recovery rate for the a-Si solar cells.

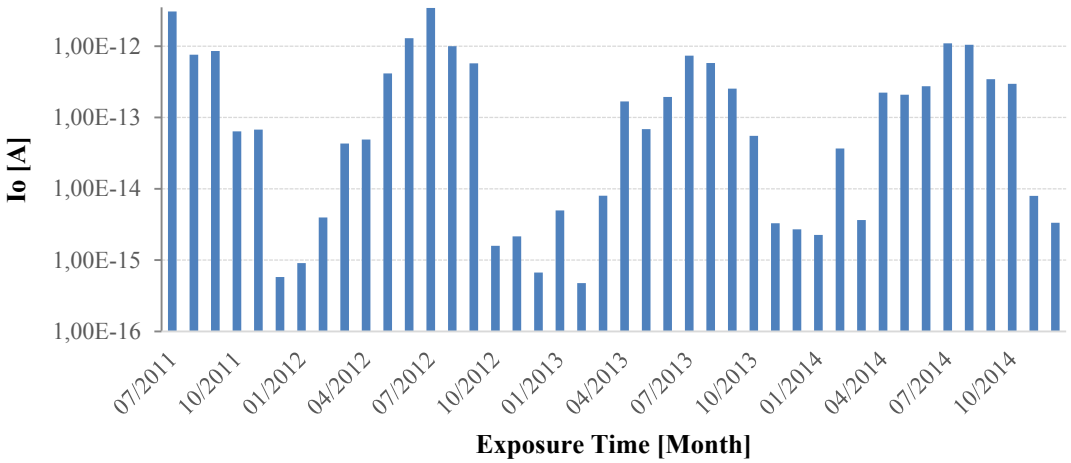

Figure 3.4. 10 Evolution of Io: Average values obtained by using the parameter extraction algorithm.

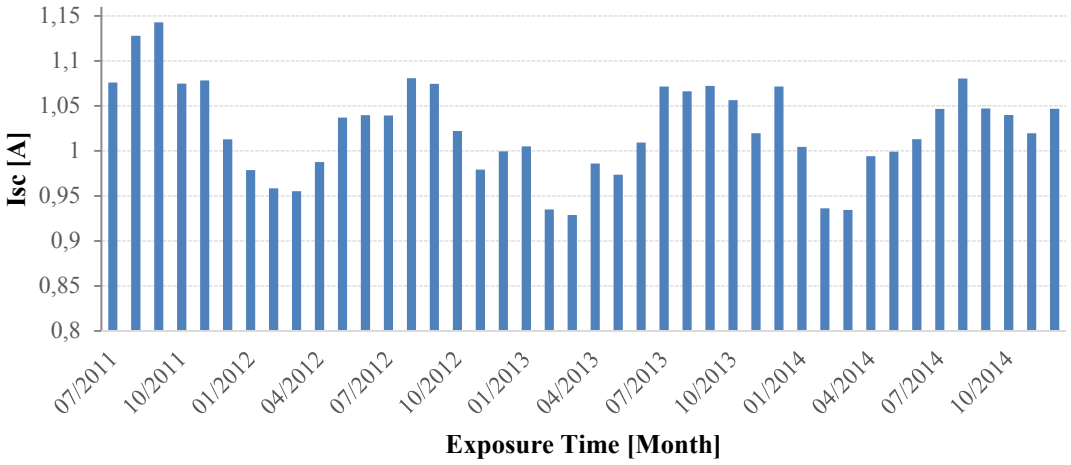

Figure 3.4. 11 Evolution of Isc: Average values obtained by using the parameter extraction algorithm.

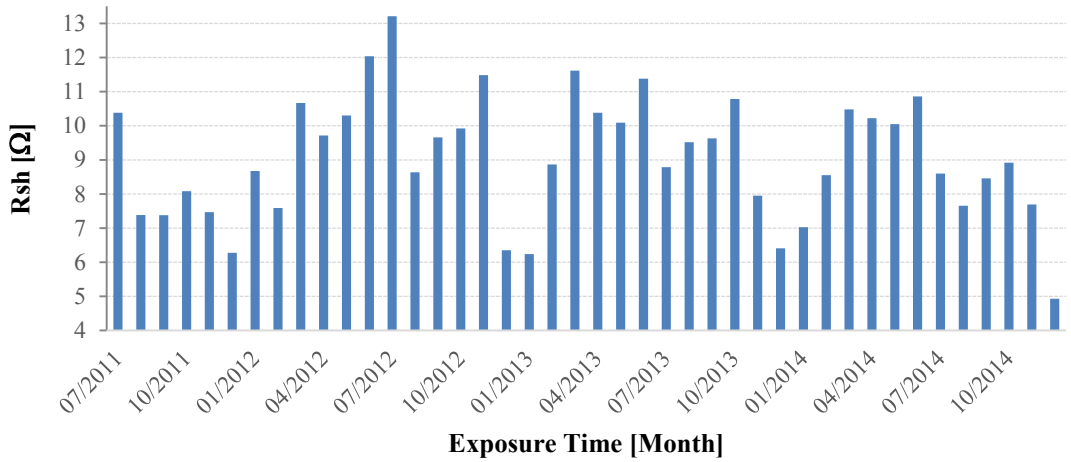

Figure 3.4. 12 Evolution of R_{sh}: Mean monthly values obtained.

Fig. 3.4.12 shows the evolution of the mean monthly value obtained by the parameter extraction algorithm for the shunt resistance, R_{sh}, along the monitoring period. There is an average constant decrease of 0.19 %/year in R_{sh} values that finally reduces to a 50% of its initial value. The reduction of R_{sh} in TF solar cells under outdoor exposure for long periods of time has been previously reported [18,24]. On the other hand, the evolution of R_{sh} shows the same seasonal trend that the evolution of the output power of the PV array and I_{sc} as expected.

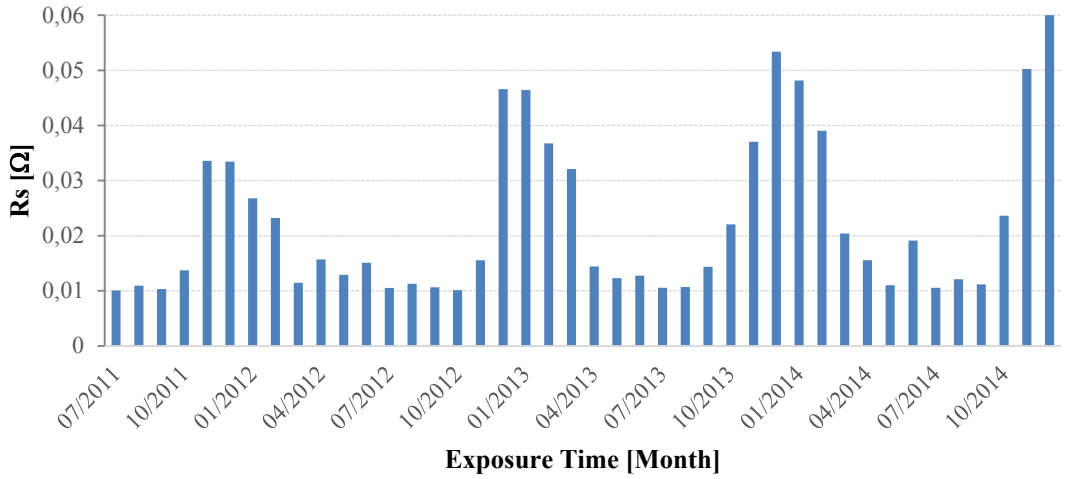

Figure 3.4. 13 Evolution of R_s: Mean monthly values obtained.

A continuing increase in the value of the series resistance, R_s, is found along the monitoring campaign. The values of R_s go from an initial value of 10 mΩ to a final value of 60 mΩ. The seasonal effect is observed again in the trend of R_s that present higher values in winter, with maximum values in the month of December, and reduced values in summer, with minimum values in the month of August. The behaviour of R_s shown by Fig. 3.4.13 is in accordance with precious works reported in the literature for TF solar cells [18,24]. Moreover, the reduction of I_{sc} observed in winter is partially due to the increase of R_s. Eq. (*3.4*-1) can be particularized in short-circuit conditions, V= 0, and rewritten as follows:

$$I_{sc} = I_{ph} - \frac{I_{sc}R_s}{R_{sh}} \qquad (3.4\text{-}16)$$

As can be seen in Eq. (*3.4*-16), the combination of higher values of R_s and lower values of R_{sh} in winter periods results in a decrease of I_{sc}. The effect is the opposite in summer periods, where R_{sh} presents higher values while R_s and I_{sc} decrease.

3.4.5. Conclusion

The degradation modes of TF single junction a-Si PV modules and how they affect the performance of PV modules in a relatively dry and sunny inland site with a Continental-Mediterranean climate is addressed in this paper. The data used in this study was obtained under outdoor long term exposure of the PV system in Jaén from late July 2011 to October 2014.

A reduction of the DC power of the PV array by about 11.2% was observed in the first 70 days of outdoor deployment. The stabilization period was observed to start after 16 months of operation with a decline of the DC power by the relative percentage of 18.8% and then it is stabilized. However, the effect of seasonal oscillation remains after the stabilization period for about 5% variation from the stabilized level of DC power.

Solar cell parameters identification is also addressed in this paper by using a new parameter extraction technique. The sets of solar cell model parameters obtained by using the parameter extraction technique are able to reproduce the behaviour of the PV array in real conditions of work with a good accuracy degree. The parameter extraction technique is able to evaluate the temporal evolution of main solar cell model parameters and helps to understand the evolution of the entire system at PV module level.

The seasonal variation of a-Si PV modules behaviour was also observed in the evolution of the solar cell model parameters. The evolution of each one of the model parameters along the outdoor long term exposure of the PV system has been analysed and allows achieving a better understanding of the performance changes of the PV modules and the evolution of the output power of the PV array.

References

[1] EPIA Report, 2014. Global Market Outlook for Photovoltaics 2014-2018 <http://www.epia.org/news/publications/global-market-outlook-forphotovoltaics-2014-2018/>.

[2] Nann S, Emery K. Spectral effects on PV-device rating. Sol Energy Mater Sol Cells 1992;27:189–216. doi:10.1016/0927-0248(92)90083-2.

[3] Sharma V, Sastry OS, Kumar A, Bora B, Chandel SS. Degradation analysis of a-Si, (HIT) hetro-junction intrinsic thin layer silicon and m-C-Si solar photovoltaic technologies under outdoor conditions. Energy 2014;72:536–46.

doi:10.1016/j.energy.2014.05.078.

[4] Evans DL. Simplified method for predicting photovoltaic array output. Sol Energy 1981;27:555–60. doi:10.1016/0038-092X(81)90051-7.

[5] Pierro M, Bucci F, Cornaro C. Full characterization of photovoltaic modules in real operating conditions: theoretical model, measurement method and results. Prog Photovoltaics Res Appl 2014;23:443–61. doi:10.1002/pip.

[6] Spataru S, Hacke P, Sera D, Packard C, Kerekes T, Teodorescu R. Temperature-dependency analysis and correction methods of in situ power-loss estimation for crystalline silicon modules undergoing potential-induced degradation stress testing. Prog Photovoltaics Res Appl 2015;23:1536–49. doi:10.1002/pip.2587.

[7] Torres-Ramírez M, Nofuentes G, Silva JP, Silvestre S, Muñoz JV. Study on analytical modelling approaches to the performance of thin film PV modules in sunny inland climates. Energy 2014;73:731–40.

[8] Chandel SS, Nagaraju Naik M, Sharma V, Chandel R. Degradation analysis of 28 year field exposed mono-c-Si photovoltaic modules of a direct coupled solar water pumping system in western Himalayan region of India. Renew Energy 2015;78:193–202. doi:10.1016/j.renene.2015.01.015.

[9] Jordan DC, Kurtz SR. Photovoltaic degradation rates - An Analytical Review. Prog Photovoltaics Res Appl 2013;21:12–29. doi:10.1002/pip.1182.

[10] Kaplanis S, Kaplani E. Energy performance and degradation over 20 years performance of BP c-Si PV modules. Simul Model Pract Theory 2011;19:1201–11. doi:10.1016/j.simpat.2010.07.009.

[11] Sharma V, Chandel SS. Performance and degradation analysis for long term reliability of solar photovoltaic systems: A review. Renew Sustain Energy Rev 2013;27:753–67. doi:10.1016/j.rser.2013.07.046.

[12] Photovoltaics Report, 2014. Freiburg, 24 October 2014 <http://www.ise.fraunhofer.de/de/downloads/pdffiles/aktuelles/photovoltaics-report-in-englischer-sprache.pdf>.

[13] Muñoz-García M a., Marin O, Alonso-García MC, Chenlo F. Characterization of thin film PV modules under standard test conditions: Results of indoor and outdoor measurements and the effects of sunlight exposure. Sol Energy 2012;86:3049–56. doi:10.1016/j.solener.2012.07.015.

[14] Hussin MZ, Shaari S, Omar a. M, Zain ZM. Amorphous silicon thin-film: Behaviour of light-induced degradation. Renew Sustain Energy Rev 2015;43:388–402. doi:10.1016/j.rser.2014.10.093.

[15] Staebler D, Wronski C. Reversible conductivity changes in discharge-produced amorphous Si. Appl Phys Lett 1977.

[16] Meyer EL, E.d. van Dyk, "Assessing the Reliability and Degradation of Photovoltaic Module Performance Parameters," IEEE Trans. Reliability 2004;vol:53no1pp83–92.

[17] Yamawaki T, Mizukami S, Yamazaki A, Takahashi H. Thermal recovery effect on light-induced degradation of amorphous silicon solar module under the sunlight. Sol Energy Mater Sol Cells 1997;47:125–34. doi:10.1016/S0927-0248(97)00033-0.

[18] van Dyk EE, Meyer EL. Analysis of the effect of parasitic resistances on the performance of photovoltaic modules. Renew Energy 2004;29:333–44. doi:10.1016/S0960-1481(03)00250-7.

[19] Aziz T, Ketjoy N, Sirisamphanwong C. Determination of PV Module Power Output Degradation after Long Term Operation 2014:19–21.

[20] Ruther R, Del Cueto J, Tamizh-Mani G, Montenegro a. a., Rummel S, Anderberg a., et al. Performance test of amorphous silicon modules in different climates - Year four: Progress in understanding exposure history stabilization effects. Conf Rec IEEE Photovolt Spec Conf 2008.

[21] Kleiss G, Bucher K, Ragot P, Chantant M. Monitoring outdoor performance and photodegradation of a-Si:Hmodules by evaluation of continuously measured I-V curves. Proc 1994 IEEE 1st World Conf Photovolt Energy Convers - WCPEC (A Jt Conf PVSC, PVSEC PSEC) 1994;1:531–4.

[22] Meyer EL, van Dyk EE. Characterization of degradation in thin-film photovoltaic module performance parameters. Renew Energy 2003;28:1455–69. doi:10.1016/S0960-1481(02)00062-9.

[23] van Dyk EE, Audouard A., Meyer EL, Woolard CD. Investigation of the degradation of a thin-film hydrogenated amorphous silicon photovoltaic module. Sol Energy Mater Sol Cells 2007;91:167–73. doi:10.1016/j.solmat.2006.08.001.

[24] Radue C, van Dyk EE. A comparison of degradation in three amorphous silicon PV module technologies. Sol Energy Mater Sol Cells 2010;94:617–22. doi:10.1016/j.solmat.2009.12.009.

[25] Phinikarides A, Kindyni N, Makrides G, Georghiou GE. Review of photovoltaic degradation rate methodologies. Renew Sustain Energy Rev 2014;40:143–52. doi:10.1016/j.rser.2014.07.155.

[26] Phinikarides A, Makrides G, Georghiou GE. Comparison of analysis methodes for the calculation of degradation rates of different photovoltaic thechnologies 2013:2–5.

[27] Voswinckel S, Wesselak V, Lustermann B. Behaviour of amorphous silicon solar modules: A parameter study. Sol Energy 2013;92:206–13. doi:10.1016/j.solener.2013.03.006.

[28] AlHajri MF, El-Naggar KM, AlRashidi MR, Al-Othman a. K. Optimal extraction of solar cell parameters using pattern search. Renew Energy 2012;44:238–45. doi:10.1016/j.renene.2012.01.082.

[29] Ikegami T, Maezono T, Nakanishi F, Yamagata Y, Ebihara K. Estimation of equivalent circuit parameters of PV module and its application to optimal operation of PV system. Sol Energy Mater Sol Cells 2001;67:389–95. doi:10.1016/S0927-0248(00)00307-X.

[30] Castañer, L., Silvestre, S., Modelling Photovoltaic systems using Pspice.Wiley. 2002.

[31] Chine W, Mellit A., Pavan a. M, Kalogirou S a. Fault detection method for grid-connected photovoltaic plants. Renew Energy 2014;66:99–110.

[32] Di Vincenzo MC, Infield D. Detailed PV array model for non-uniform irradiance and its validation against experimental data. Sol Energy 2013;97:314–31.

[33] Moreno A., Julve J, Silvestre S, Castañer L. SPICE macromodeling of photovoltaic systems. Prog Photovoltaics Res Appl 2000;8:293–306.

[34] Chouder A., Silvestre S. Automatic supervision and fault detection of PV systems based on power losses analysis. Energy Convers Manag 2010;51:1929–37. doi:10.1016/j.enconman.2010.02.025.

[35] Chouder A, Silvestre S, Sadaoui N, Rahmani L. Modeling and simulation of a grid connected PV system based on the evaluation of main PV module parameters. Simul Model Pract Theory 2012;20:46–58.

[36] Tsai HL. Insolation-oriented model of photovoltaic module using Matlab/Simulink. Sol Energy 2010;84:1318–26.

[37] Chouder A, Silvestre S, Taghezouit B, Karatepe E. Monitoring, modelling and simulation of PV systems using LabVIEW. Sol Energy 2013;91:337–49. doi:10.1016/j.solener.2012.09.016.

[38] Yu T, Lin Y, Chang F. Establishment of the photovoltaic simulation system using mixed programming with LabVIEW and simulink. Intell Technol Eng 2013.

[39] Chouder A., Silvestre S. Analysis Model of Mismatch Power Losses in PV Systems. J Sol Energy Eng 2009;131:024504. doi:10.1115/1.3097275.

[40] Durisch W, Mayor J-C. Application of a generalized current/voltage model for solar cells to outdoor measurements on a SIEMEN SM 110-module. 3rd World Conf onPhotovoltaic Energy Conversion, 2003 Proc 2003;2:1956–9.

[41] Martínez-Moreno F, Lorenzo E, Muñoz J, Moretón R. On the testing of large PV arrays. Prog Photovoltaics Res Appl 2012;20:100–5. doi:10.1002/pip.1102.

[42] Muñoz J, Lorenzo E, Carrillo JM, Moretón R. Design of a twin capacitive load and its application to the outdoor rating of photovoltaic modules. Prog Photovoltaics Res Appl 2015;23:247–52. doi:10.1002/pip.2425.

[43] Brendel R, Aberle A., Cuevas A., Glunz S, Hahn G, Poortmans J, et al. Considering the Distributed Series Resistance in a Two-diode Model. Energy Procedia 2013;38:167–75. doi:10.1016/j.egypro.2013.07.264.

[44] Nofuentes G, García-Domingo B, Muñoz J V., Chenlo F. Analysis of the dependence of the spectral factor of some PV technologies on the solar spectrum distribution. Appl Energy 2014;113:302–9. doi:10.1016/j.apenergy.2013.07.044.

[45] National Institute of Meteorology, 1997. Guía resumida del clima en España (1961-1990). Series estadísticas. Madrid: Ministry of the Environment, Government of Spain. 1997.

[46] Deutsche Gesellschaft für Sonnenenergie, Planning and installing photovoltaic systems. A guide for installers, architects and engineers. 3rd ed. Gosport: Routledge; 2013

[47] Carlson DE. Monolithic amorphous silicon alloy solar modules. Sol Energy Mater Sol Cells 2003;78:627–45. doi:10.1016/S0927-0248(02)00455-5.

[48] Del Cueto J a., Von Roedern B. Temperature-induced changes in the performance of amorphous silicon multi-junction modules in controlled light-soaking. Prog Photovoltaics Res Appl 1999;7:101–12.

[49] A. Luque and S. Hegedus, "Handbook of PV science and engineering," 2nd Ed., Wiley: Chichester, pp. 991-1009, 2011.

3.5. Published paper in Energy Conversion and Management 120 (2016)

Energy Conversion and Management
120 (2016) 109 – 119
http://dx.doi.org/10.1016/j.enconman.2016.04.093

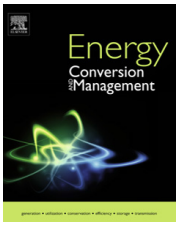

Study of degradation and evaluation of model parameters of micromorph silicon photovoltaic modules under outdoor long term exposure in Jaén, Spain

Sofiane Kichou[1], Elif Abaslioglu[1], Santiago Silvestre[1], Gustavo Nofuentes[2], Miguel Torres-Ramírez[2], Aissa Chouder[3]*

[1] MNT Group, Electronic Engineering Department, UPC-BarcelonaTech. Barcelona, C/ Jordi Girona 1-3, Mòdul C4 Campus Nord UPC, 08034 Barcelona, Spain.

[*] Corresponding author: E-mail addresses: kichousofiane@gmail.com

[2] IDEA Research Group, University of Jaén, Campus de Las Lagunillas, 23071, Jaén, Spain.

[3] Univ. M'sila, Fac. Technologies, Dep. Génie Electrique, BP 166 Ichbelia 28000 M'sila, Algeria.

ARTICLE INFO

Article history:

Received 30 January 2016
Received in revised form
1 April 2016
Accepted 25 April 2016

Keywords:

Micromorph PV modules,
Model parameters extraction,
Degradation rate.

ABSTRACT

The analysis of the degradation of tandem micromorph thin-film photovoltaic (TFPV) modules and its impact on the output power of a PV array under outdoor long term exposure located in Jaén (Spain) is addressed in this work. Furthermore, the evolution of main solar cell model parameters is evaluated by means of parameters extraction techniques from monitored data of the PV system in real operation of work. The degradation rate and the stabilization period of micromorph TFPV modules are evaluated. The analysis of the degradation rate, together to results obtained for the evolution of each of the solar cell model parameters along the outdoor long-term exposure allow a better understanding of changes in performance of micromorph TFPV modules and the behaviour of the output power of the PV generator.

5.3.1. Introduction

Thin-film photovoltaic (TFPV) technologies based on cadmium-telluride (CdTe), copper indium gallium selenide (CIGS) and silicon take around 10% of the global PV market that is mainly dominated by crystalline silicon (c-Si) PV modules. Thin-film silicon PV modules are based on either amorphous silicon (a-Si:H) or microcrystalline silicon (μc-Si:H) and have plenty of advantages such as lower temperature coefficient relative to c-Si and polycrystalline PV modules, low quantity silicon usage as raw material, low-cost manufacturing process and flexibility in product design. However, several weaknesses and challenges in TFPV technologies have been discussed such as low conversion efficiency and long term technological risks in the field performance in terms of durability when compared with the crystalline technology [1].

A list of studies reported analysis of outdoor performance and degradation of PV modules of several technologies under different climatic conditions [2–6]. Likewise, performance evaluation of specific TFPV modules based on: CIGS [7], CdS/CdTe [8], a-Si:H and μc-Si:H [9] were also reported. These studies showed that the degradation rate is mainly associated to the PV module technology and, in addition, TFPV modules present higher degradation rates than polycrystalline and c-Si PV modules [3,10]. On the other hand, a-Si:H suffers from a performance degradation called light-induced degradation (LID) due to the Staebler-Wronski effect (SWE) [11,12]. It was demonstrated that a-Si:H TFPV modules are degraded mainly by the SWE effect, when compared to other TFPV technologies [13–15]. This degradation phenomenon is also present but is much less severe in μc-Si:H TFPV.

Micromorph TFPV modules are formed by micromorph tandem (a-Si:H/μc-Si:H) solar cells that allow a more effective use of the solar spectrum than c-Si solar cells because the band-gaps of both materials form an ideal combination; a-Si:H has a band-gap in the range of 1.7–1.8 eV, while μc-Si:H has the same band-gap as a c-Si wafer, i.e. 1.12 eV [16]. In order to mitigate the degradation of the a-Si:H top cell due to the SWE effect, it needs to be as thin as possible, typically 0.2-0.3 μm. However, a thinner a-Si:H layer limits the short-circuit current of the solar cell if a good matching with the short-circuit current density of the bottom cell is not achieved. For this purpose, an intermediate reflecting layer (IRL) is typically implemented between the top and bottom cells in order to reflect back part of the light that is not absorbed during its first passage through the top a-Si:H cell. Then, the IRL enables a reduction of the a-Si:H solar cell thickness, while keeping its short-circuit current density matched with the one of the bottom cell [1].

In this work, the behaviour of micromorph TFPV modules under outdoor long term exposure in Jaén, Spain, is analysed. The period under scrutiny ranges from late July 2011 to December 2014.

On the other hand, the variation of main solar cell model parameters is also evaluated by means of parameter extraction techniques. The parameter extraction has as input the daily monitored data of the PV system in real operation of work and calculates the temporal evolution of main solar cell model parameters able to reproduce the actual behaviour of the whole PV system with a good accuracy.

The remainder of this paper is organized as follows: An overview of the PV array under study and its model is given in section 3.5.2. The parameter extraction technique, as well as the degradation analysis methodology is also introduced in Section 3.5.2. Section 3.5.3 describes the experimental PV validation of the parameter extraction algorithm array used in this study. The results and discussion are presented in Section 3.5.4. Finally, the conclusions of the study are given in Section 3.5.5.

3.5.2. Methodology

3.5.2.1 Description of the PV system

The PV system under study is sited in Jaén. Jaén is a dry and sunny inland Spanish city with a Continental-Mediterranean climate. Table 3.5.1 summarizes main climate parameters of that city sited in the south of Spain. Fig. 3.5.1 shows its placement in the Iberian Peninsula.

Table 3.5. 1 Annual average values of main meteorological parameters recorded in Jaén over 30 years[17].

Horizontal irradiation ($kWh \cdot m^{-2}$)	Ambient temperature (ºC)	Minimum ambient temperature (ºC)	Maximum ambient temperature (ºC)	Relative humidity (%)	Rainfall (mm)	Barometric pressure (hPa)
1788	16.9	11.4	22.4	63	558	954.1

The PV array comprises 8 micromorph TFPV modules, with 2 parallel-connected strings of 4 series-connected PV modules each ($N_{pm} = 2$, $N_{sm} = 4$). Main electrical characteristics at STC of this PV field are given in Table 3.5.2.

Table 3.5. 2 Main electrical characteristics of the PV array at STC.

PV module	Configuration N_{sm} x N_{pm}	Maximum power (W)	Open-circuit voltage (V)	Short-circuit current (A)	Voltage at maximum power point (V)	Current at maximum power point (A)
a-Si:H/µc-Si	4 x 2	880	284	5	216	4.08

Figure 3.5. 1 City of Jaén: Latitude: 37º 47' 14.35" N Longitude: 3º 46' 39.73 " W, Altitude: 511 m.

The PV system was installed outdoors at the beginning of July 2011 in a south oriented 30º tilted open rack located on the flat roof of the High Technical School building in the University of Jaen (UJA) in Jaén itself and it is connected to a single-phase grid-tied SMA™ Sunny Boy SB1200 inverter. Two SMA™ Sunny SensorBox devices installed on a metal plate in the same plane as the PV field were used to measure cell and ambient temperatures together with wind speed. Moreover, two Pt 100 resistive thermal detectors (RTD) are used as module temperature sensors. The in-plane irradiance was monitored by means of a Kipp & Zonen™ CMP21 pyranometer, which is also installed on the PV array plane. Onsite measurements of DC voltage and current are recorded at the inverter input with a sampling rate of 5 minutes.

3.5.2.2 PV Array model and parameter extraction

The well-known one diode five parameter model is considered in this work for modelling the micromorph solar cell, where the relation between the output current and voltage is defined as follows:

$$I = I_{ph} - I_o\left[exp\left(\frac{V + R_s I}{nV_t}\right) - 1\right] - \frac{V + R_s I}{R_{sh}} \qquad (3.5\text{-}1)$$

where: I_{ph} is the photocurrent (A), I_o is the diode reverse saturation current (A), n is the diode ideality factor, R_s and R_{sh} are the series and shunt resistances respectively (Ω), V_t is the thermal voltage (V). I and V are the output current (A) and voltage (V).

The model of the solar cell described by Eq. (*3.5*-1) can be scaled up to the model of the PV array taking into account the configuration of the PV array: Number of PV modules connected in series by string: N_{sm}, and the number of parallel strings forming part of the PV

array: N_{pm}, as well as the internal configuration and the number of solar cells contained in the PV module [18].

Several studies based on the simulation of PV systems on different software environments have applied this model and results obtained were experimentally validated with success [19–24]. In this work Matlab/Simulink environment is used for the simulations and the parameter extraction.

In our study we are interested in the investigation of the variation of the solar cell model parameters of the micromorph silicon PV modules when exposed outdoors. Therefore, a parameter extraction technique is included in order to find the set of solar cell model parameters able to reproduce the actual behaviour of the whole PV system with the best accuracy.

The parameter extraction technique used in this study is the same used in [25], where the monitored data: Current, Voltage and Power at the DC output of the PV array together with the in-plane irradiance: G, in W/m^2 and cell temperature: T_c, in ºC profiles, are used as inputs for the parameter extraction algorithm in order to estimate the set of model parameters of the solar cells forming the PV array.

Considering the number of parallel strings of solar cells present in the PV array, N_p, Eq. (*3.5*-1) can be written as follows:

$$I = N_p(I_{ph} - I_d - I_{sh}) \qquad (3.5\text{-}2)$$

where I is the DC output current of the PV array (A), I_d is the diode current (A) and I_{sh} is the shunt current (A).

For any arbitrary value of G and T_c, the photocurrent, I_{ph}, is given by:

$$I_{ph} = \frac{G}{G^*} I_{scc} + ki\ (T_c - T_c^*) \qquad (3.5\text{-}3)$$

where G^* and T^*_c are respectively the irradiance and cell temperature at standard test conditions (STC) respectively, 1000 W/m^2 (AM1.5) and 25ºC, ki (ºC^{-1}) is the temperature coefficient of the current and I_{scc} (A) is the solar cell short-circuit current at STC.

The diode current, I_d, included in Eq. (*3.5*-2) is given by:

$$I_d = I_o[\, e^{\left(\frac{\frac{V}{N_s}+\frac{IR_s}{N_p}}{n\,V_t}\right)} - 1] \qquad (3.5\text{-}4)$$

where I_o (A) is the saturation current of the diode and N_s is the number of solar cells connected in series in each string.

The saturation current of the diode depends strongly on temperature and it is given by:

$$I_o = \frac{I_{scc}\, e^{\left(\frac{E_{go}}{V_{to}} - \frac{E_g}{V_t}\right)}}{e^{\left(\frac{Voc}{n\, V_{to}}\right)} - 1} \left(\frac{T_c}{T_c^*}\right)^3 \qquad (3.5\text{-}5)$$

where I_{scc} and Voc are the short-circuit current and the open-circuit voltage of the solar cell respectively, V_{to} is the thermal voltage at STC, E_g the energy bandgap of the semiconductor and E_{go} is the energy bandgap at T=0 K.

The value of the energy bandgap of the semiconductor at any cell temperature T_c is given by:

$$E_g = E_{go} - \frac{\alpha gap\, T_c^2}{\beta gap + T_c} \qquad (3.5\text{-}6)$$

where α_{gap} and β_{gap} are fitting parameters characteristic of the semiconductor.

Finally, the shunt current, I_{sh}, included in Eq. (*3.5*-2) can be calculated from:

$$I_{sh} = \frac{\frac{V}{N_s} + \frac{I\, R_s}{N_p}}{R_{sh}} \qquad (3.5\text{-}7)$$

where V is the DC output voltage of the PV array.

The parameter extraction algorithm evaluates: I_{ph}, I_o, R_s, R_{sh}, and n by using Eqs. (*3.5*-2) – (*3.5*-7) and actual daily profiles of monitored electrical parameters–namely, current and voltage at the DC output of the PV array, together with G and T_c. Then, a nonlinear regression algorithm based on the Levenberg–Marquardt method was applied to both data sets: The daily monitored data from the PV array in real conditions of work and simulation results generated by using the described model, in order to minimize the following quadratic function [25–27]:

$$S(\theta) = \sum_{i=1}^{N} [Ii - I(Vi, \theta)]^2 \qquad (3.5\text{-}8)$$

where $\theta = f\,(I_{ph}, I_o, R_s, R_{sh}, n)$

More details about the parameter extraction technique can be found elsewhere [25].

3.5.2.3 Effective peak power of the PV array

The degradation analysis is based on the variation of the output power of the PV array along the monitoring campaign. The effective peak power of a PV array, P^*_M, at STC may be measured as follows [28,29]:

$$P_M^* = \frac{G^* P_{DC}}{G\,[1 + \gamma(T_c - T_c^*)]} \quad (3.5\text{-}9)$$

where P_{DC} (W) is the DC output power of the PV array, G^* and T_c^* are the irradiance and temperature at STC, respectively, and γ (ºC^{-1}) is the power temperature coefficient of the PV modules.

The power coefficient temperature, γ, can be calculated as follows [30]:

$$\gamma = \frac{1}{P_{max}} \frac{\partial P_{max}}{\partial T} \quad (3.5\text{-}10)$$

where P_{max} is the maximum power of PV modules at STC and the reference temperature is 25 ºC.

The evaluation of P^*_M requires a previous filtering of irradiance values in order to avoid the influence of operational anomalies [28,29]. In this study the data corresponding to low levels of irradiance (G < 700 W/m^2) are discarded before the calculation of P^*_M values. As the solar spectrum distribution at in-plane irradiance levels above 700 W/m^2 closely matches that of the AM 1.5G standard reference spectrum in the city of Jaén [31], Eq. (*3.5*-9) does not take into account any spectral effects.

3.5.2.4 Power-Irradiance technique

In this work, the technique presented by Hussin et al [12] was considered. This technique allows assessing the degradation of PV modules exposed under outdoor conditions, by observing the transition of the real output power between two boundaries indicators; predicted initial and stabilized data values of PV array DC power outputs.

The predicted initial, Pdc_{init}, and stabilized, Pdc_{stab}, data values depend on the measured plane-of-array irradiance (G), module temperature (T_c), and can be calculated by using the following equations:

$$Pdc_{init} = N_{sm}.N_{pm}.Pm_{init}.\eta.G_{eff}.(1 + kv.\Delta T).(1 - ki.\Delta T) \quad (3.5\text{-}11)$$

$$Pdc_{stab} = N_{sm}.N_{pm}.Pm_{stab}.\eta.G_{eff}.(1 + kv.\Delta T).(1 - ki.\Delta T) \quad (3.5\text{-}12)$$

$$G_{eff} = \frac{G}{G_n} \quad (3.5\text{-}13)$$

$$\Delta T = T_c - T_n \quad (3.5\text{-}14)$$

where N_{sm} and N_{pm} are the number of PV modules connected in series and parallel respectively, Pm_{init} is the initial measured peak power of PV module, kv and ki are the voltage and current

temperature coefficients respectively provided in the manufacturer's data sheet ($^oC^{-1}$), Pdc_{stab} is the predicted array DC power referred to stabilized, Pm_{stab} is the stabilized peak power of the PV module found in the manufacturer's data sheet, η is the efficiency referred to all general system losses which changes between 0.89 in summer and 0.86 in winter months, G_n and T_n are the reference irradiance and cell temperature respectively at STC .

As it has been previously mentioned, a data filtering process was carried out in order to avoid problems of uncertainties caused by low values of irradiance ($G < 700$ W/m^2).

Linear regression equations are obtained by using a Linear Correlation Approach (LCA) from the actual PV array DC output power for each month described by the following empirical equation:

$$Pdc = A_{Gr}.G + C \qquad (3.5\text{-}15)$$

where Pdc is the array DC output power, A_{Gr} is the gradient, G is the plan-of-array irradiance and C is the ordinate value of Pdc at $G = 0$.

Finally, the monthly gradient values of each empirical equation can be plotted to observe the degradation rate and determine the stabilization period upon this type of micromorph PV modules [12].

3.5.3. Experimental

3.5.3.1 Parameter extraction procedure validation

The parameter extraction algorithm calculates the set of values for the five model parameters of the solar cell: I_{ph}, R_s, R_{sh}, I_o and n by using Eqs. (*3.5*-2) – (*3.5*-7) described in section 3.5.2.2 that allow reproducing the actual behaviour of the PV array. For this purpose, the daily monitored data set: Output DC current and voltage, irradiance and temperature of the PV array in real conditions of work are used as input data for the algorithm and it is executed until function S(θ), given by Eq. (*3.5*-8), is minimized. Table 3.5.3 shows the set of solar cell model parameters obtained corresponding to October 6th, 2011.

Table 3.5. 3 Extracted solar cell model parameters.

Day	I_o [A]	I_{ph} [A]	R_{sh} [Ω]	R_s [Ω]	n
06/10/2011	9.15 10^{-8}	2.1811	9.6602	0.0455	1.2642

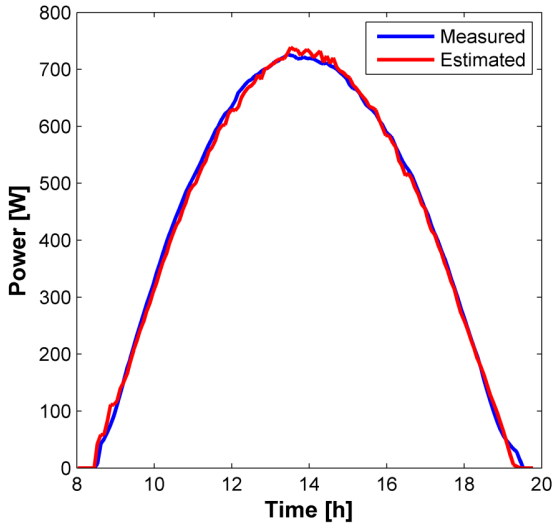

Figure 3.5. 2 Measured versus estimated DC output power obtained by using the set of the extracted solar cell model parameters.

Fig. 3.5.2 shows a comparison of the DC output power of the PV array, monitored and evaluated by using the set of model parameters obtained from the parameter extraction algorithm for that day. As it can be seen a good agreement is found between simulation results and monitored data. The coefficient of variation of the root mean square errors, (CVRMSE) between both data sets, monitored and calculated by using the set of model parameters, are given in Table 3.5.4 for the DC output current, voltage and power of the PV array respectively.

Table 3.5. 4 (CVRMSE) obtained for main electrical parameters of the PV array.

RMSE_Current [%]	RMSE_Voltage [%]	RMSE_Power [%]
1.29	2.44	2.60

3.5.4. Results and discussion

3.5.4.1 Evolution of the effective peak power of the PV array

The evolution of the effective peak power of the PV array, P^*_M, and the monthly radiation, H, along the monitoring campaign are shown in Fig. 3.5.3.

As it can be seen, an initial important decrease of the effective peak power can be clearly identified and after that, the variation of the P^*_M follows the climate seasonal changes.

The initial decrease in output power of the array is followed by an increase over the summer months, a decrease over winter months and once again an increase over summer months. As the solar cells contain a thin film amorphous layer, the regeneration on summer

months can be assigned to light-induced annealing [13], spectral effects [32] and to the thermal regeneration [33,34].

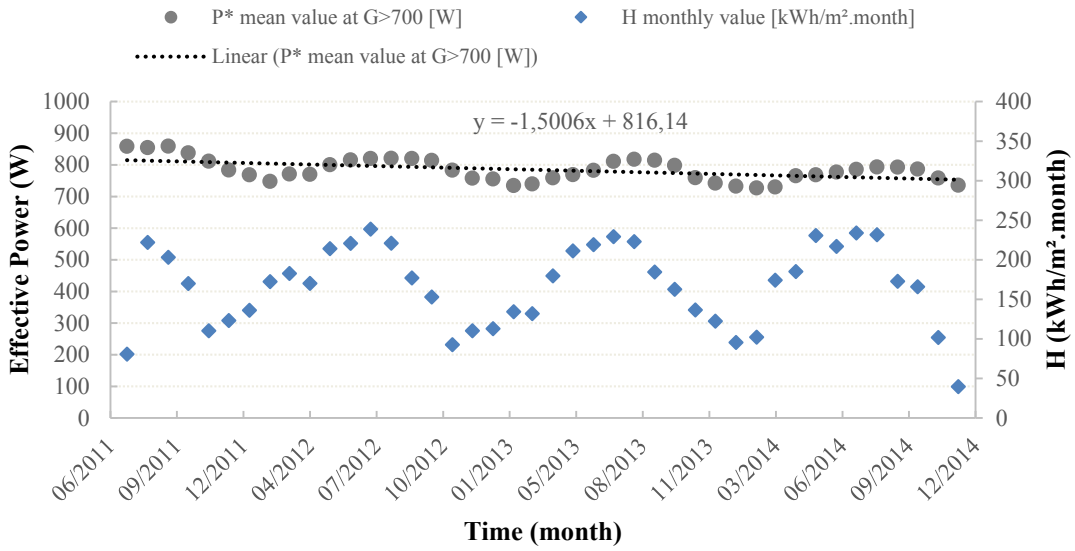

Figure 3.5. 3 The effective peak power of the PV array P*M (W) (for G > 700 [W/m²]), and the monthly radiation, H along exposure period.

A linear least square fitting method was used to estimate de degradation rate, R_D. This method was applied to the monthly effective peak power, P^*_M, calculated by using Eq. (*3.5*-16) and monitored data. The degradation per year can be calculated by linear regression (LR) as follows [35,36]:

The equation of the trend line is:

$$y = mx + c \qquad (3.5\text{-}16)$$

where m (W/month) is the slope of the line, x is the month and c (W) is the initial power output, when time is zero.

Thereby, the degradation per year: R_D (%) can be calculated as follows [36]:

$$R_D = 100\frac{12m}{c} \qquad (3.5\text{-}17)$$

The degradation rate calculated from the trend line is found to be: -2.20±15 %/year. The analytical uncertainty reported along with the degradation rate was determined from the standard errors of the linear fit. A second monitoring data filtering process was carried out following the procedure used in previous reported studies in order to analyse the stabilization period of the PV array [12]. In this second filtering process, one point for each month of the

monitored data for tilted irradiance in the range of 900 W/m^2 < G < 920 W/m^2 and working PV module temperature in the range 53 ºC < T_c < 60 ºC was selected.

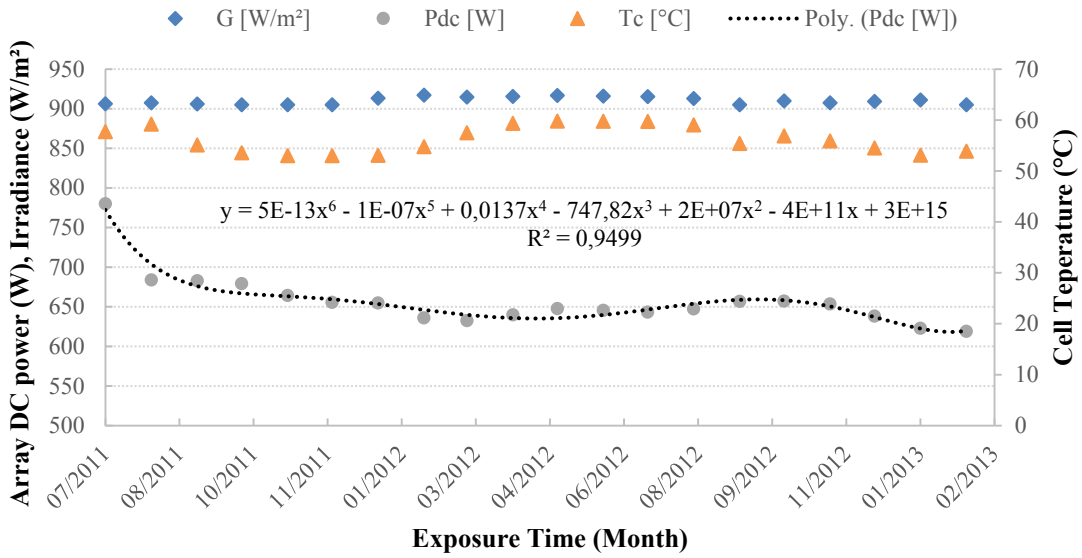

Figure 3.5. 4 Monthly trend line outdoor stabilization process obtained with the selected data of irradiance and cell temperature in the range of 900 W/m² < G < 920 W/m² and 53 °C < Tc < 60 °C.

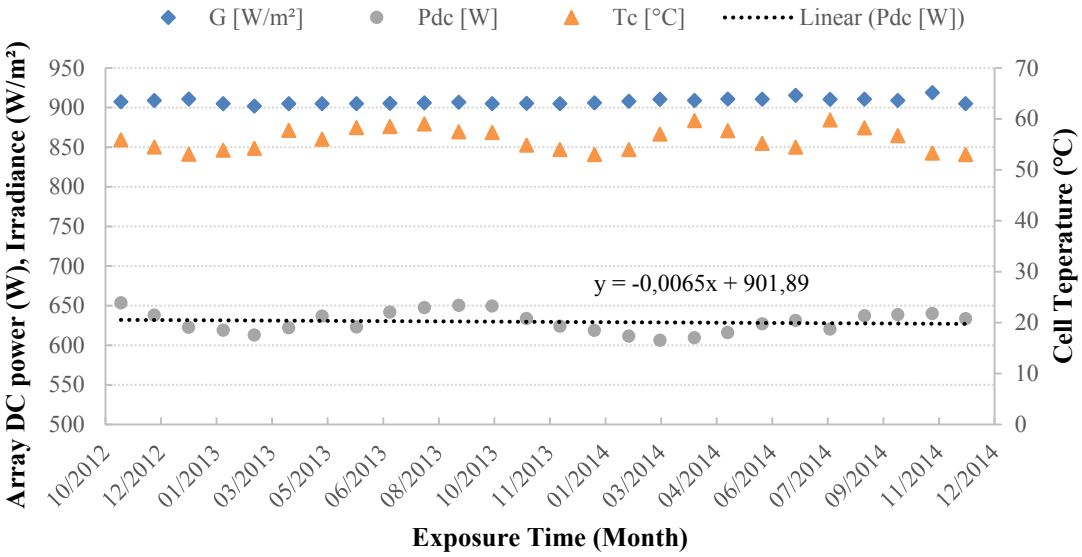

Figure 3.5. 5 Trend line showing the stabilization after 14 months of outdoor operation obtained from the selected data of irradiance and cell temperature in the range of 900 W/m² < G < 920 W/m² and 53 ºC < Tc < 60 ºC.

From results obtained in the filtering process shown by Fig. 3.5.4, the stabilization period was observed to start after four months of operation under the climatic conditions of Jaén. A previous work [12] based on the data supplied by the PV modules manufacturer indicated

stabilization periods up to two months for this kind of TFPV modules. The results obtained show that under Spanish climate conditions the stabilization period of these PV modules is greater. A strong initial degradation is observed in the first month of operation, respect to the other monitored months, where the DC power was degraded by about 12.51%. The trend line in Fig. 3.5.4 is obtained by sixth polynomial correlation with R^2 equal to 0.9499.

Fig. 3.5.5 shows the set of data after the first 14 months of operation, when the PV modules are totally stabilised, after a power loss of 16.66% due to the degradation. The linear trend line with a very small slope, demonstrates that the stabilization level of the PV array output DC power is around 635 W in the range of G and T_c considered in data filtering process. In the following months, it shows a sinusoidal trend attributable to the annealing effects. The effect of seasonal oscillation remains after the stabilization period with variations about 3.18% from the stabilized level of DC output power.

5.3.4.2. Power-Irradiance technique results

The Power-Irradiance technique was applied to assess the degradation rate and the stabilization period of the micromorph TFPV PV modules deployed under outdoor conditions from July 2011 to December 2014.

The measured DC output power of the PV array (blue points), delimited by the two boundaries defined as; initial (red circles) and stable (green stars) obtained from equations Eqs. (*3.5*-11) – (*3.5*-14), are plotted in function of the plane-of-array measured irradiance (G) values for each month of the second semester of each year of the experimental period as illustrated in Fig. 3.5.6 – 3.5.9.

From the Figs. 3.5.6 – 3.5.9 it can be seen that, the measured DC array output power changes the tendency from the expected initial values to the stabilized ones in the course of time.

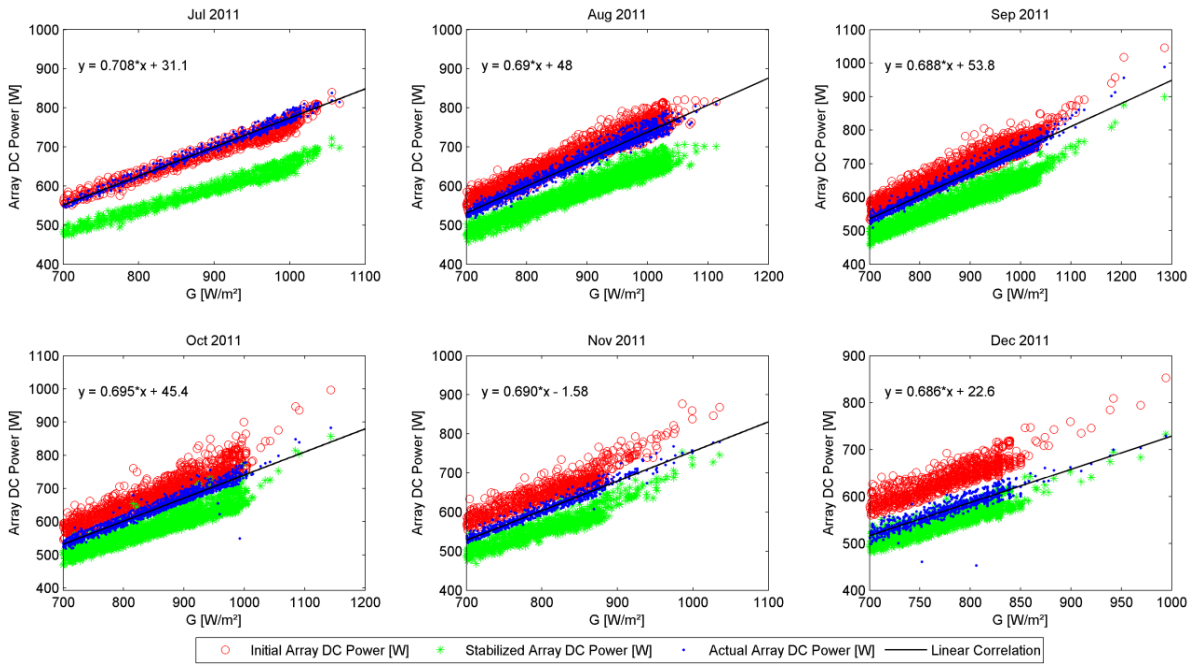

Figure 3.5. 6 DC output power evolution from July 2011 to December 2011.

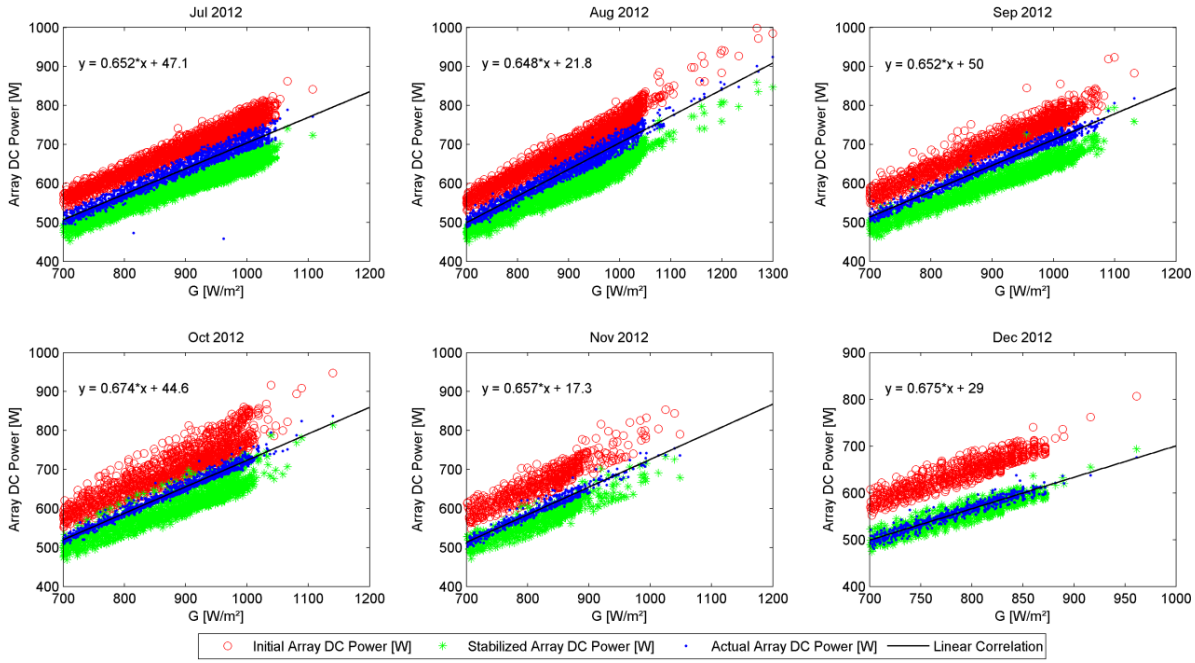

Figure 3.5. 7 DC output power evolution from July 2012 to December 2012.

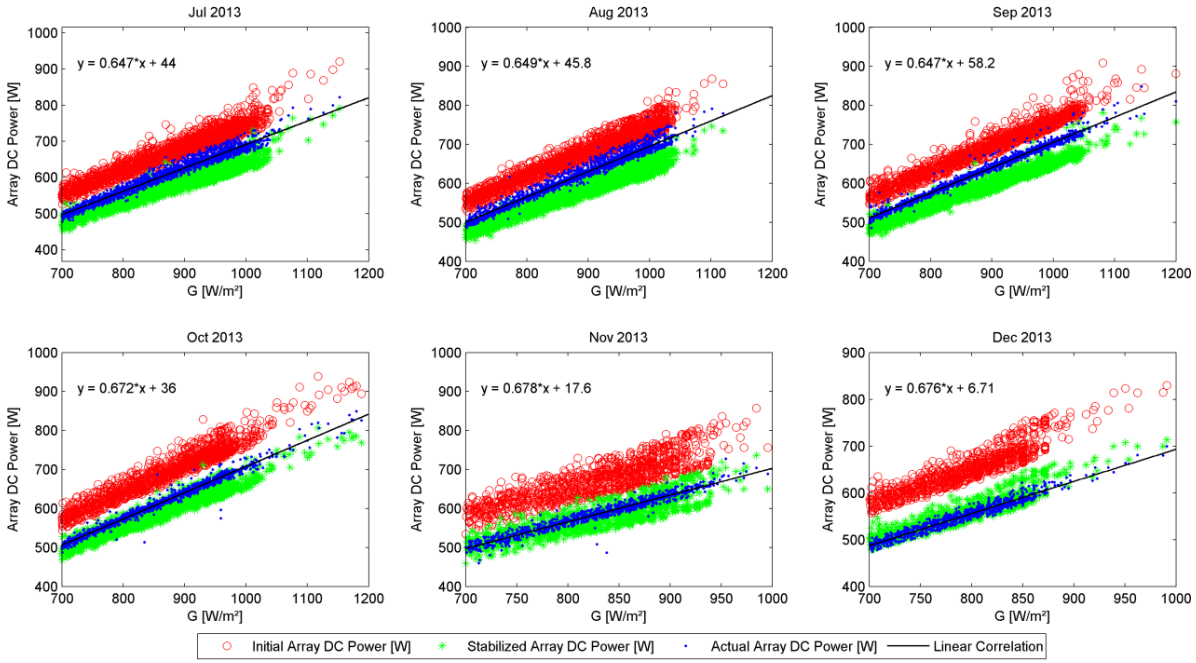

Figure 3.5. 8 DC output power evolution from July 2013 to December 2013.

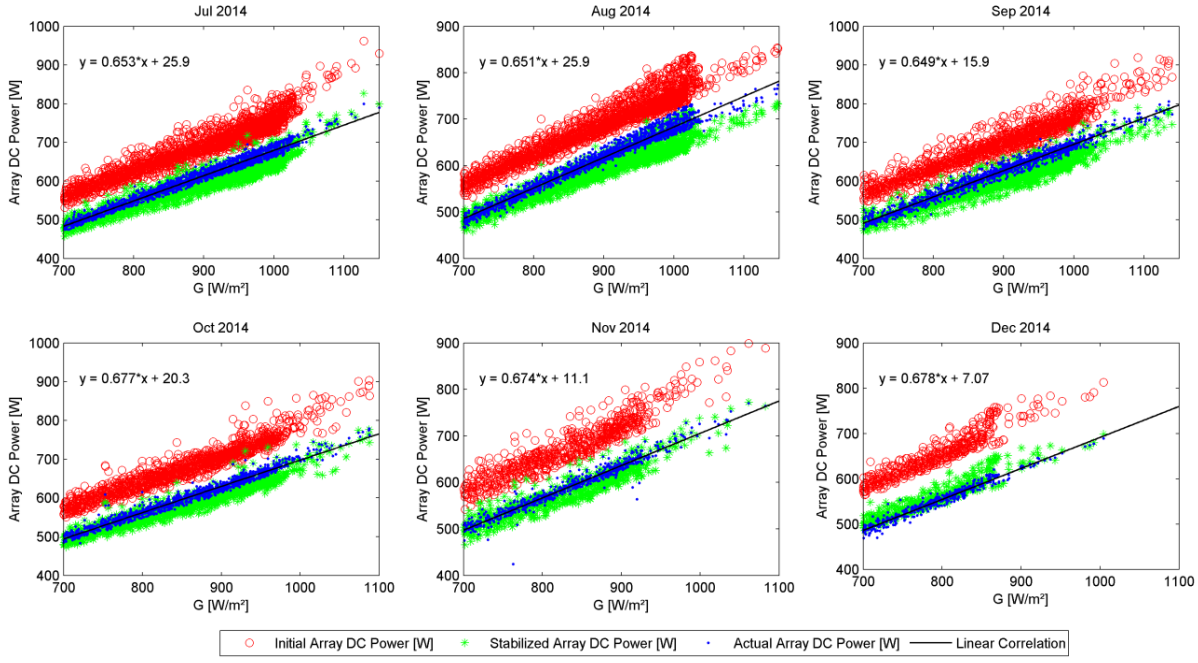

Figure 3.5. 9 DC output power evolution from July 2014 to December 2014.

Table 3.5.5 illustrates the empirical equations obtained by the LCA applied to the measured PV array DC power output allowing the identification of the degradation and stabilization periods.

The stabilization period can be estimated by plotting the gradient values obtained from the empirical equation of each month listed in Table 3.5.5. As it can be seen from Fig. 3.5.10, the gradient magnitude demonstrates a diminution by 2.54% of the initial value after the first month of exposure of the PV modules under outdoor conditions. After that, the evolution of the gradient magnitude shows a continue decrease during the next months until reach a sinusoidal trend. Due to seasonal variation, the gradient magnitudes oscillate around the value 0.664, which represents a 6.47% of reduction of the first value.

Table 3.5. 5 Monthly empirical equation based on LCA.

Month	Gradient	R^2	Empirical Equation
Jul-11	0.708	0.9859	$Pdc = 0.708*G + 31$
Aug-11	0.690	0.9714	$Pdc = 0.690*G + 48$
Sep-11	0.688	0.9788	$Pdc = 0.688*G + 53.8$
Oct-11	0.695	0.9579	$Pdc = 0.695*G + 45.4$
Nov-11	0.690	0.9595	$Pdc = 0.690*G - 1.58$
Dec-11	0.686	0.8045	$Pdc = 0.686*G + 22.6$
Jan-12	0.680	0.9390	$Pdc = 0.680*G - 2.52$
Feb-12	0.673	0.9756	$Pdc = 0.673*G + 27.83$
Mar-12	0.669	0.9816	$Pdc = 0.669*G + 35.3$
Apr-12	0.658	0.9786	$Pdc = 0.658*G + 31.1$
May-12	0.657	0.9699	$Pdc = 0.657*G + 34$
Jun-12	0.650	0.9632	$Pdc = 0.650*G + 27.9$
Jul-12	0.652	0.9563	$Pdc = 0.652*G + 47.1$
Aug-12	0.648	0.9638	$Pdc = 0.648*G + 21.8$
Sep-12	0.652	0.9809	$Pdc = 0.652*G + 50$
Oct-12	0.674	0.9795	$Pdc = 0.674*G + 44.6$
Nov-12	0.657	0.9636	$Pdc = 0.657*G + 17.3$
Dec-12	0.675	0.9352	$Pdc = 0.675*G + 29$
Jan-13	0,674	0.9459	$Pdc = 0.674*G + 6.61$
Feb-13	0,672	0.9768	$Pdc = 0.672*G + 12.3$
Mar-13	0,671	0.9738	$Pdc = 0.671*G + 23$
Apr-13	0,658	0.9804	$Pdc = 0.658*G + 44.4$
May-13	0,657	0.9799	$Pdc = 0.657*G + 30.7$
Jun-13	0,653	0.9693	$Pdc = 0.653*G + 32.1$
Jul-13	0,647	0.9668	$Pdc = 0.647*G + 44$
Aug-13	0,649	0.9683	$Pdc = 0.649*G + 45.8$
Sep-13	0,647	0.9820	$Pdc = 0.647*G + 58.2$
Oct-13	0,672	0.9776	$Pdc = 0.672*G + 36$
Nov-13	0,678	0.9462	$Pdc = 0.678*G + 17.6$
Dec-13	0,676	0.9439	$Pdc = 0.676*G + 6.71$
Jan-14	0,675	0.9741	$Pdc = 0.675*G + 13.2$
Feb-14	0,669	0.9672	$Pdc = 0.669*G + 19.1$
Mar-14	0,665	0.9775	$Pdc = 0.665*G + 27.5$
Apr-14	0,656	0.9756	$Pdc = 0.656*G + 24$
May-14	0,656	0.9772	$Pdc = 0.656*G + 25.1$
Jun-14	0,652	0.9820	$Pdc = 0.652*G + 29$
Jul-14	0,653	0.9761	$Pdc = 0.653*G + 26$
Aug-14	0,651	0.9748	$Pdc = 0.651*G + 25.9$
Sep-14	0,649	0.9744	$Pdc = 0.649*G + 15.9$
Oct-14	0,677	0.9727	$Pdc = 0.677*G + 20.3$
Nov-14	0,674	0.9534	$Pdc = 0.674*G + 11.1$
Dec-14	0,678	0.9593	$Pdc = 0.678*G + 7.07$

Fig. 3.5.11 confirms that, the stabilization period of these TFPV modules requires four months of exposure under real conditions of solar irradiance and temperature corresponding to the climate of Jaén. This result agrees with the stabilization period obtained in the study of the evolution of the effective peak power of the PV array presented in the previous section.

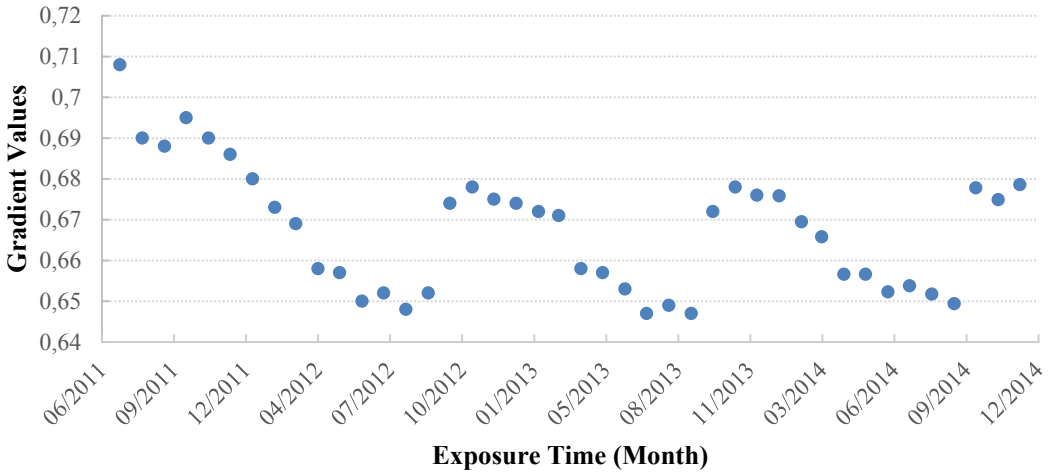

Figure 3.5. 10 Gradient values obtained along the monitoring campaign.

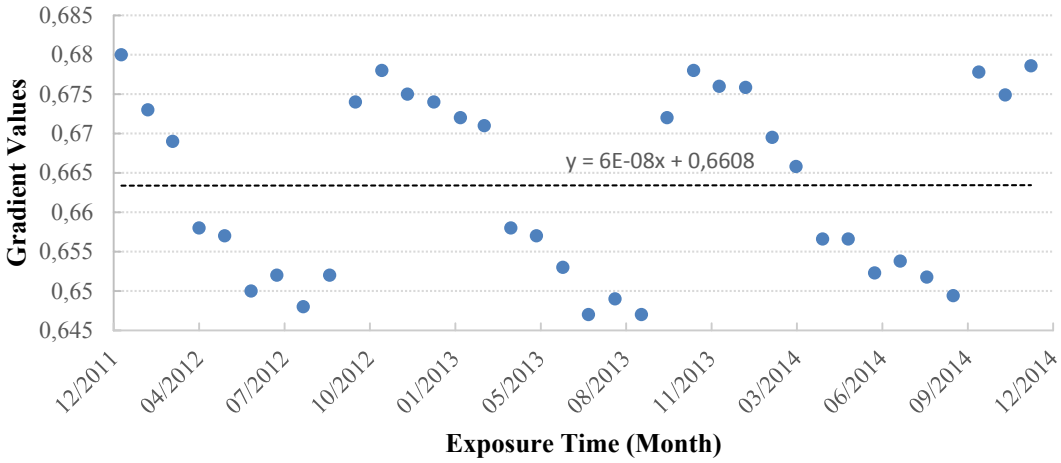

Figure 3.5. 11 Gradient values obtained after the stabilization period.

3.5.4.3. Evolution of solar cell model parameters

The evolution of the solar cell parameters reflects the behaviour of the TFPV modules under seasonal climatic variation. The following figures show the monthly average value of each one of the solar cell model extracted parameters during the whole monitoring period.

Fig. 3.5.12 illustrates the evolution of the ideality factor *n*, obtained by the parameter extraction technique. It can be seen that the variation of the values obtained is very small and

follows the seasonal changes. The ideality factor shows a small reduction in summer while it increases in winter periods. However, the value of *n* fluctuates around a mean value of *n* = 1.2 and the seasonal variations are small. This fact indicates that the diode included in the equivalent circuit of the solar cell corresponding to the five parameter model is dominated by the μc-Si:H substrate [37].

In summer months, it can be seen that there is an improvement in the material characteristics especially in the amorphous layer, caused by the higher temperatures reached by the solar cells. This improvement is due to an increase in charge carrier lifetime and a reduction in band gap [13,15], that's why the values of *n* are reduced. On the other hand, in winter months, the extracted values of the ideality factor *n* are increased due to the increase of the recombination current [15].

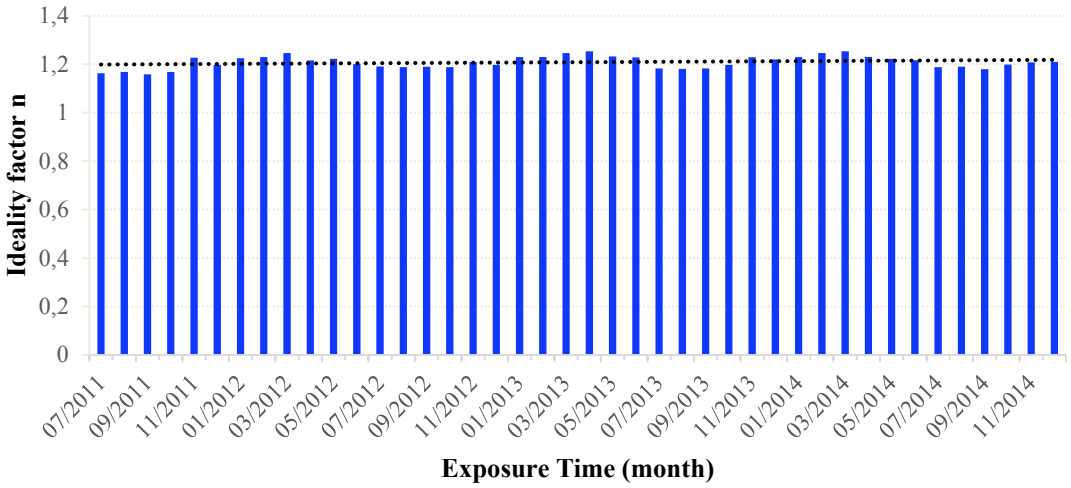

Figure 3.5. 12 Average values of n obtained by using the parameter extraction algorithm.

The evolution of the saturation current, I_o *(blue colour)*, shown in Fig. 3.5.13 demonstrates how the variations of the temperature can affect the bandgap of the solar cell material given by the Eq. (*3.5*-5). The evolution of I_o is opposite to the trend shown by the ideality factor, *n*, as expected.

The open-circuit voltage is decreased due to the decrease of the bandgap caused by the higher temperatures in summer season [15]. The combination of bandgap reduction and strong increase of temperature in summer periods along with the increase in short-circuit current due to LID effect lead to an increase of the saturation current despite the reduction of recombination effects in summer. As can be seen in Fig. 3.5.13, I_o varies from values in the order of 10^{-7} A to

values around 10^{-8} A in winter periods. This variation of about one order of magnitude also explains the small seasonal changes observed in the value of the ideality factor.

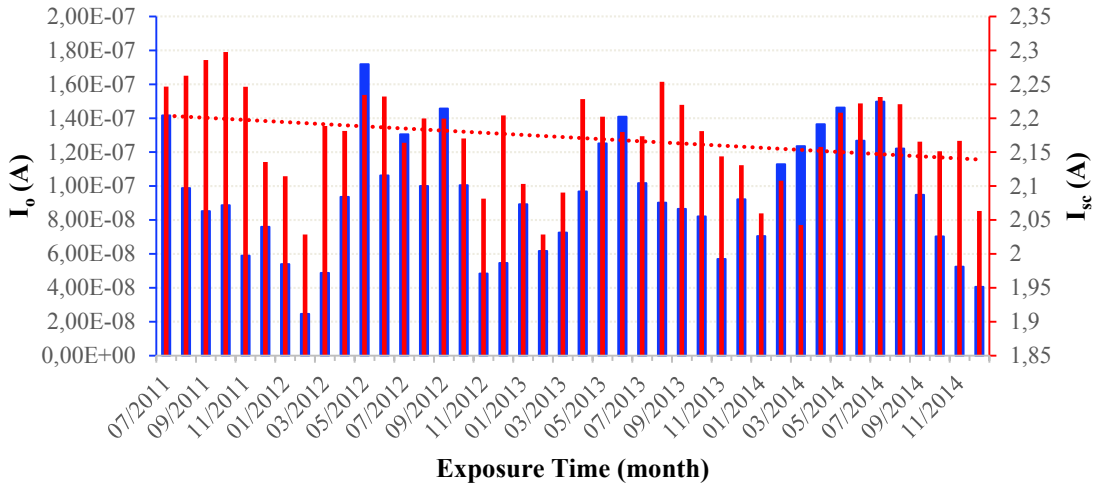

Figure 3.5. 13 Evolution of I_o (blue colour) and I_{sc} (red colour); Average values obtained by using the parameter extraction algorithm.

The continuing decrease in short-circuit current, I_{sc}, throughout the first four months of the deployment period can be observed in Fig. 3.5.13. After that it shows a more stable trend following the seasonal changes.

The improvement in output current during summer time is due to the effect of solar spectral irradiance and to thermal-recovery of the LID affecting the thin film amorphous layer [15,32]. The lower temperatures in winter also reduce the thermal recovery rate for the a-Si solar cells. The minimum value of I_{sc} in the worst winter months is approximately 12% less than the peak value of this parameter for the a-Si:H/µc-Si solar cells. This reduction is very small compared to the observed on a-Si PV modules in outdoor conditions of work at the same location [25].

Fig. 3.5.14 shows the evolution of the mean monthly values obtained by the parameter extraction algorithm for the shunt and series resistances, R_{sh} *(red colour) and* R_s *(blue colour)*, along the monitoring period. An important decrease of R_{sh} can be observed after the first four months of exposure under outdoor conditions, where the value of R_{sh} is reduced by 56% respect to its initial value.

The reduction of R_{sh} in TF solar cells under outdoor exposure for long periods of time has been previously reported [15,38]. On the other hand, after the stabilization period, the evolution of R_{sh} shows the same seasonal trend that the evolution of the output power of the PV array and I_{sc} as expected.

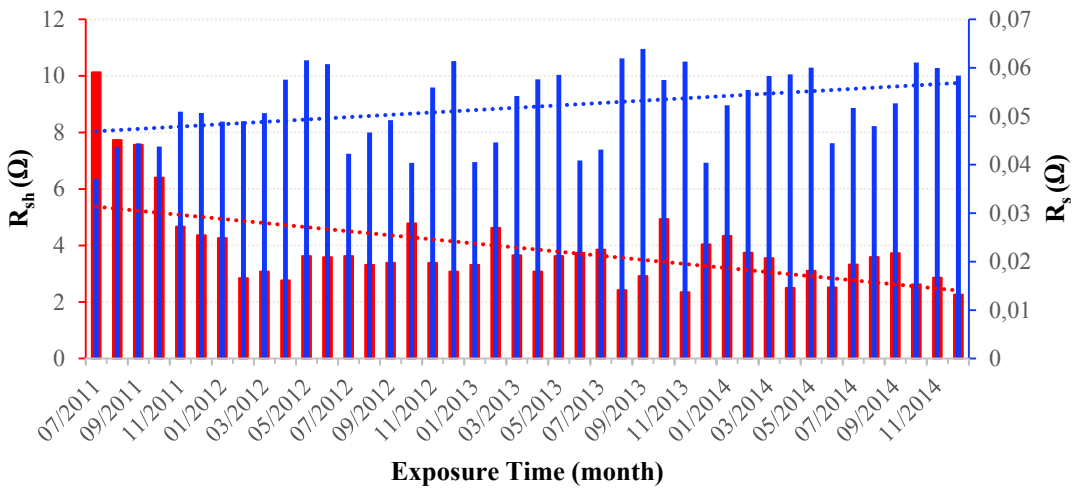

Figure 3.5. 14 Evolution of R_{sh} (red colour) and R_s (blue colour): Mean monthly values obtained.

The series resistance, *R_s (blue colour)*, shows a continuing increase along the first months of the monitoring campaign. The variation of the values of R_s is very small and it goes from an initial value of 3 mΩ to a final value of 6 mΩ. After the stabilization period, the seasonal effect can also be observed in the trend of R_s that presents higher values in winter, with maximum values in the month of December, and reduced values in summer, with minimum values in the month of August. The range of the variation is around 30% between the peak to peak values of R_s in winter and summer. The behaviour of R_s shown in Fig. 3.5.14 is in accordance with previous works reported in the literature for TF solar cells [15,38].

3.5.5. Conclusion

The behaviour of a grid connected PV array formed by micromorph TFPV modules situated in Jaén is reflected by the monitored data obtained under outdoor long term exposure of the PV system from July 2011 to December 2014. The degradation modes of the micromorph solar cells and how they affect the performance of the TFPV modules in a relatively dry and sunny inland site with a Continental-Mediterranean climate are addressed in this paper.

From the analysis of the obtained results, by about 12.51% of reduction of the DC output power of the PV array was observed after the first month of exposure under outdoor conditions. On the other hand, the stabilization period was observed to start after four months of operation with a total reduction of the PV array DC output power of 16.66%. The effect of seasonal oscillation remains after the stabilization period with variations about 3.18% from the stabilized

level of DC output power. This seasonal oscillation is lower than typical values observed in the behaviour of a-Si:H TFPV modules, in the range of 5%, due to the effect of the μc-Si:H substrate present in the micromorph TFPV modules

The extracted sets of solar cell model parameters obtained by using the parameter extraction technique are able to reproduce the behaviour of the PV array in real conditions of work with a good accuracy degree. With the proposed approach it is possible to describe the time evolution of all model parameters along the outdoor long term exposure period of the PV system. Moreover, the temporal evolution of each one of the model parameters permits achieving a better understanding of the performance changes of the PV modules and the evolution of the output power of the PV array and the degradation rate. Furthermore, the seasonal variation of micromorph PV modules behaviour was also observed in the evolution of the solar cell model parameters. It must be noted that the μc-Si:H bottom cell dominates the evolution of most solar cell parameters, mainly the ideality factor and saturation current, while the evolution of the short-circuit current seems to be more related to the behaviour of the a-Si:H top cell.

References

[1] Čampa A, Meier M, Boccard M, Mercaldo LV, Ghosh M, Zhang C, et al. Micromorph silicon solar cell optical performance: Influence of intermediate reflector and front electrode surface texture. Sol Energy Mater Sol Cells 2014;130:401–9.

[2] Kaplanis S, Kaplani E. Energy performance and degradation over 20 years performance of BP c-Si PV modules. Simul Model Pract Theory 2011;19:1201–11. doi:10.1016/j.simpat.2010.07.009.

[3] Jordan DC, Kurtz SR. Photovoltaic degradation rates - An Analytical Review. Prog Photovoltaics Res Appl 2013;21:12–29. doi:10.1002/pip.1182.

[4] Sharma V, Chandel SS. Performance and degradation analysis for long term reliability of solar photovoltaic systems: A review. Renew Sustain Energy Rev 2013;27:753–67. doi:10.1016/j.rser.2013.07.046.

[5] Chandel SS, Nagaraju Naik M, Sharma V, Chandel R. Degradation analysis of 28 year field exposed mono-c-Si photovoltaic modules of a direct coupled solar water pumping system in western Himalayan region of India. Renew Energy 2015;78:193–202. doi:10.1016/j.renene.2015.01.015.

[6] Bouraiou A, Hamouda M, Chaker A, Sadok M, Mostefaoui M, Lachtar S. Modeling and Simulation of Photovoltaic Module and Array Based on One and Two Diode Model Using Matlab/Simulink. Energy Procedia 2015;74:864–77.

[7] Al-Otaibi A, Al-Qattan A, Fairouz F, Al-Mulla A. Performance evaluation of photovoltaic systems on Kuwaiti schools' rooftop. Energy Convers Manag 2015;95:110–9. doi:10.1016/j.enconman.2015.02.039.

[8] Rawat R, Kaushik SC, Sastry OS, Singh YK, Bora B. Energetic and exergetic performance analysis of CdS/CdTe based photovoltaic technology in real operating conditions of composite climate. Energy Convers Manag 2016;110:42–50.

[9] Tripathi B, Yadav P, Rathod S, Kumar M. Performance analysis and comparison of two silicon material based photovoltaic technologies under actual climatic conditions in Western India. Energy Convers Manag 2014;80:97–102.

[10] Muñoz-García M a., Marin O, Alonso-García MC, Chenlo F. Characterization of thin film PV modules under standard test conditions: Results of indoor and outdoor measurements and the effects of sunlight exposure. Sol Energy 2012;86:3049–56.

[11] et al. DLS. Reversible conductivity changes in discharged-produced amorphous Si. Appl Phys Lett 1977;31:274–92.

[12] Hussin MZ, Shaari S, Omar a. M, Zain ZM. Amorphous silicon thin-film: Behaviour of light-induced degradation. Renew Sustain Energy Rev 2015;43:388–402. doi:10.1016/j.rser.2014.10.093.

[13] Meyer EL, van Dyk EE. Characterization of degradation in thin-film photovoltaic module performance parameters. Renew Energy 2003;28:1455–69.

[14] van Dyk EE, Audouard A., Meyer EL, Woolard CD. Investigation of the degradation of a thin-film hydrogenated amorphous silicon photovoltaic module. Sol Energy Mater Sol Cells 2007;91:167–73. doi:10.1016/j.solmat.2006.08.001.

[15] Radue C, van Dyk EE. A comparison of degradation in three amorphous silicon PV module technologies. Sol Energy Mater Sol Cells 2010;94:617–22.

[16] Shah A, Moulin E, Ballif C. Technological status of plasma-deposited thin-film silicon photovoltaics. Sol Energy Mater Sol Cells 2013.

[17] Spanish National Institute of Meteorology, 1997. Guía resumida del clima en España. Series estadísticas (1961-1990). Madrid: Ministry of the Environment, Government of Spain.

[18] Silvestre S, Silva MA Da, Chouder A, Guasch D, Karatepe E. New procedure for fault detection in grid connected PV systems based on the evaluation of current and voltage indicators. Energy Convers Manag 2014;86:241–9.

[19] Chouder A., Silvestre S. Automatic supervision and fault detection of PV systems based on power losses analysis. Energy Convers Manag 2010;51:1929–37.

[20] Chouder A, Silvestre S, Sadaoui N, Rahmani L. Modeling and simulation of a grid connected PV system based on the evaluation of main PV module parameters. Simul Model Pract Theory 2012;20:46–58.

[21] Chouder A, Silvestre S, Taghezouit B, Karatepe E. Monitoring, modelling and simulation of PV systems using LabVIEW. Sol Energy 2013;91:337–49.

[22] Yu TC, Lin Y Bin, Chang FS. Establishment of the photovoltaic simulation system using mixed programming with labview and simulink. Lect Notes Electr Eng 2013;234 LNEE:383–94. doi:10.1007/978-1-4614-6747-2_46.

[23] Di Vincenzo MC, Infield D. Detailed PV array model for non-uniform irradiance and its validation against experimental data. Sol Energy 2013;97:314–31.

[24] Chine W, Mellit A., Pavan A. M, Kalogirou S A. Fault detection method for grid-connected photovoltaic plants. Renew Energy 2014;66:99–110.

[25] Kichou S, Silvestre S, Nofuentes G, Torres-Ramírez M, Chouder A, Guasch D. Characterization of degradation and evaluation of model parameters of amorphous silicon photovoltaic modules under outdoor long term exposure. Energy 2016;96:231–41. doi:10.1016/j.energy.2015.12.054.

[26] Chouder A., Silvestre S. Analysis Model of Mismatch Power Losses in PV Systems. J Sol Energy Eng 2009;131:024504. doi:10.1115/1.3097275.

[27] Durisch W, Mayor J-C. Application of a generalized current/voltage model for solar cells to outdoor measurements on a SIEMEN SM 110-module. 3rd World Conf onPhotovoltaic Energy Conversion, 2003 Proc 2003;2:1956–9.

[28] Martínez-Moreno F, Lorenzo E, Muñoz J, Moretón R. On the testing of large PV arrays. Prog Photovoltaics Res Appl 2012;20:100–5. doi:10.1002/pip.1102.

[29] Muñoz J, Lorenzo E, Carrillo JM, Moretón R. Design of a twin capacitive load and its application to the outdoor rating of photovoltaic modules. Prog Photovoltaics Res Appl 2015;23:247–52. doi:10.1002/pip.2425.

[30] Spataru S, Hacke P, Sera D, Packard C, Kerekes T, Teodorescu R. Temperature-dependency analysis and correction methods of in situ power-loss estimation for crystalline silicon modules undergoing potential-induced degradation stress testing. Prog Photovoltaics Res Appl 2015;23:1536–49. doi:10.1002/pip.2587.

[31] Nofuentes G, García-Domingo B, Muñoz J V., Chenlo F. Analysis of the dependence of the spectral factor of some PV technologies on the solar spectrum distribution. Appl Energy 2014;113:302–9. doi:10.1016/j.apenergy.2013.07.044.

[32] Carlson DE. Monolithic amorphous silicon alloy solar modules. Sol Energy Mater Sol Cells 2003;78:627–45. doi:10.1016/S0927-0248(02)00455-5.

[33] Yamawaki T, Mizukami S, Yamazaki A, Takahashi H. Thermal recovery effect on light-induced degradation of amorphous silicon solar module under the sunlight. Sol Energy Mater Sol Cells 1997;47:125–34. doi:10.1016/S0927-0248(97)00033-0.

[34] Ruther R, Del Cueto J, Tamizh-Mani G, Montenegro A. A., Rummel S, Anderberg A., et al. Performance test of amorphous silicon modules in different climates - Year four: Progress in understanding exposure history stabilization effects. Conf Rec IEEE Photovolt Spec Conf 2008.

[35] Phinikarides A, Kindyni N, Makrides G, Georghiou GE. Review of photovoltaic degradation rate methodologies. Renew Sustain Energy Rev 2014;40:143–52. doi:10.1016/j.rser.2014.07.155.

[36] Sharma V, Sastry OS, Kumar A, Bora B, Chandel SS. Degradation analysis of a-Si, (HIT) hetro-junction intrinsic thin layer silicon and m-C-Si solar photovoltaic technologies under outdoor conditions. Energy 2014;72:536–46. doi:10.1016/j.energy.2014.05.078.

[37] Brammer TÃ, Stiebig H. Applying analytical and numerical methods for the analysis of microcrystalline silicon solar cells. Sol Energy Mater Sol Cells 2006;90:3021–30. doi:10.1016/j.solmat.2006.06.010.

[38] van Dyk EE, Meyer EL. Analysis of the effect of parasitic resistances on the performance of photovoltaic modules. Renew Energy 2004;29:333–44.

3.6. Published paper in Solar Energy 139 (2016)

Solar Energy 139 (2016) 599 – 607

http://dx.doi.org/10.1016/j.solener.2016.10.030

Degradation analysis of thin film photovoltaic modules under outdoor long term exposure in Spanish continental climate conditions

Santiago Silvestre[1], Sofiane Kichou[1], Letizia Guglielminotti[1], Gustavo Nofuentes[2,3] and Miguel Alonso-Abella[4].*

[1] *MNT Group, Electronic Engineering Department, UPC-BarcelonaTech. Barcelona, C/ Jordi Girona 1-3, Mòdul C4 Campus Nord UPC, 08034 Barcelona, Spain*

[*] *Corresponding author: E-mail addresses: Santiago.silvestre@upc.edu*

[2] *IDEA Research Group, University of Jaén, Campus de Las Lagunillas, 23071 Jaén, Spain*

[3] *Centre for Advanced Studies in Energy and Environment, University of Jaén, Campus Las Lagunillas, 23071 Jaén, Spain*

[4] *CIEMAT/DER, Avda. Complutense, 22, 28040 Madrid, Spain*

ARTICLE INFO

Article history:

Received 11 July 2016
Received in revised form 3 October 2016
Accepted 18 October 2016

Keywords:

Thin-film,
PV modules,
Degradation rate (DR),
Performance ratio (PR).

ABSTRACT

The present study analyses the degradation of thin film photovoltaic modules corresponding to four technologies: a-Si:H, a-Si:H/µc-Si:H, CIS and CdTe, under 5 years of outdoor long term exposure in Leganés, Spain. The period of outdoor exposure ranges from January 2011 to December 2015. The degradation rate and the stabilization period are analysed by using two different techniques. Moreover, the evolution of the fill factor and performance ratio is assessed. The CdTe module was found to have the highest degradation rate: -4.45 %/year, while the CIS module appears to be the most stable with a degradation rate of -1.04 %/year. The a-Si:H and a-Si:H/µc-Si:H modules present stabilization periods of 24 and 6 months respectively. The CdTe module degrades significantly for a period of 32 months, while the CIS module is the least degraded PV specimen over the whole experimental campaign.

3.6.1. Introduction

Nowadays thin film photovoltaic (TFPV) modules cover a 10% of market share with an annual production of 2.4 GWp in 2014 [1]. The most common PV materials used in the mass production of TFPV modules are cadmium telluride (CdTe), copper indium gallium selenide sulphide ($Cu(In,Ga)Se_2$, CIGS) and amorphous silicon (a-Si), presenting an annual production in 2014 of 1.9 GWp, 1.7 GWp and 0.8 GWp respectively [1].

The main advantages of TFPV modules are their lower production costs and lower temperature coefficients relative to the crystalline (c-Si) and polycrystalline silicon PV modules [2,3]. On the other hand, main problems of TFPV modules are the degradation phenomena after long term outdoor exposure [4–7] and the lower efficiencies in the comparison to c-Si PV modules.

Hydrogenated amorphous silicon (a-Si:H) and hydrogenated amorphous silicon/hydrogenated microcrystalline silicon hetero-junction (a-Si:H/μc-Si:H) TFPV modules have conversion efficiencies in the range of 8–13% and present low production costs and energy pay-back times. However, these TFPV modules are strongly affected by spectral and temperature effects when deployed outdoors [8–10]. The so called Staebler-Wronski effect (SWE) is the cause of light-induced degradation (LID) that strongly affects a_Si:H and also has effects on (a-Si:H/μc-Si:H) TFPV modules. It determines the amount of dangling bonds created depending on the operating temperature [11–13].

CdTe TFPV modules are well adapted to the spectrum of solar radiation due to their band gap of 1.45 eV. The theoretical efficiency limit for CdTe technology is 29% [7]. However, the average commercial PV module efficiencies are around 10–11% and the highest efficiency to-date is 17.5% [14]. Main degradation mechanisms identified in these PV modules are related to Cu diffusion from the back contact of the cells [15] and to the reduction of the fill factor as a result of shunting effects [16].

Cu $(In,Ga)Se_2$ (CIGS) chalcopyrite semiconductors such as $Cu(In)Se_2$(CIS) are direct-gap polycrystalline semiconductors, having very high optical absorption coefficients [17]. PV modules based on CIS and CIGS technologies are generally considered to be quite stable and TFPV module efficiencies up to 17.5% have been recently reported [1]. However, it is estimated that the initial power may decrease by up to 3% before stabilization [7].

Reliability and lifetime of PV modules are two crucial issues as they are the key for overall system performance and warranty to improve the energy generated. For the case of TFPV

modules, the behaviour under outdoor exposure is still not fully understood and is currently object of research. A better understanding on this topic would be important for selecting the best PV technology for each specific climatic condition and for improving the reliability and performance of TFPV modules.

The objective of this work is the analysis of behaviour of TFPV modules of four technologies under outdoor long term exposure in a relatively dry and sunny inland site. The period under scrutiny ranges from January 2011 to December 2015.

This paper is organized as follows. Section 3.6.2 describes the PV modules used in the study and details the monitoring system. An overview of the degradation analysis methodologies followed in the study is given in Section 3.6.3. The results and discussion are presented in Section 3.6.4. The conclusions of the study are given in Section 3.6.5.

3.6.2. PV modules and experimental setup

The Four PV modules considered in this work correspond to the following thin film technologies: a-Si:H, a-Si:H/µc-Si:H, CIS and CdTe. The modules were deployed in Leganés, a city 16 km south east of Madrid (Spain, Latitude: 40°19′ 42″N, Longitude: 3º 45' 55" W, Altitude: 666m) which lies within the metropolitan area of the latter. Leganés has a Mediterranean climate with strong continental influences and experiences pollution episodes and occasional Saharan dust intrusions as in the case of Madrid. The PV modules were mounted on an equator-facing open rack with a tilt angle of 30°. The tilt angle selected for the open rack was meant to maximize the collection of annual on-plane irradiation. The main parameters of the TMPV modules at standard test conditions (STC): G=1000W/m^2 AM1.5G, Tc=25°C, used in this study are given in Table 3.6.1.

An automatic test and measurement system was used to scan both the electrical and environmental parameters every five minutes over the whole experimental campaign. The experimental setup was intended to scan the current-voltage *(I-V)* curves of each of the four TFPV modules under study together with some environmental parameters that influence their outdoor performance. A PC-based system controlled by LabVIEW™ managed the acquisition and storage of data for their subsequent processing. Thus, *I-V* curves were traced using a PVE PVPM 2540C capacitive load so that 128 current-voltage data points were retrieved from this device in each scan. Additionally, the four PV modules could be tested sequentially using this

setup, by means of a switchgear box of solid state relays driven by a multipurpose Agilent 34970A data acquisition/data logger switch unit.

Table 3.6. 1 Main parameters of PV modules derived from the PV module manufacturers' datasheet.

	PV module			
	Sharp NA-121	Shell Powermax™ Ultra 80C	First Solar FS-270	Kaneka GEA 60
Technology	a-Si:H/μc-Si:H	CIS	CdTe	a-Si:H
Peak power (W)	121	80	72.5	60
Isc (A)	3.34	2.68	1.19	1.19
Voc(V)	59.2	46.6	90	92
Temperature coefficient- power δ (%/°C)	-0.24	-0.43	-0.25	-0.23
η(%)	8.5	12.7	10	6.3

Some external environmental parameters such as the horizontal and on-plane incident irradiance together with its spectral distribution, module temperature, relative humidity, ambient temperature, wind speed and barometric pressure were registered with the above data acquisition/data logger switch unit, so that these parameters were recorded simultaneously with the *I-V* curve tracing. The in-plane irradiance came from a Kipp&Zonnen CMP 21 pyranometer with directional response (up to 80° with 1000 W/m^2 beam) < 10W^2 while the spectral irradiance distribution was measured by means of a weatherproof EKO MS700 grating spectroradiometer whose specifications include a 10-nm spectral resolution. T thermocouples pasted to the rear side of each PV module were used to measure the module temperature, while the relative humidity and ambient temperature were measured by a Young 41382VC relative humidity/temperature probe with an accuracy at 23ºC of ±1% for relative humidity and ±0.3ºC for temperature. Finally, a Young 05305VM anemometer with an accuracy of ±0.2 m/s of wind speed and ±3 degrees of wind direction and a Vaisala barometric pressure sensor with an accuracy at +20 °C of ±0.10 hPa completed the experimental setup.

Table 3.6.2 summarizes a brief statistic of the meteorological parameters recorded for the period of measurements.

Table 3.6. 2 Annual average values of some meteorological parameters along the monitoring campaign.

Accumulated horizontal irradiation (kWh/m^2)	Average ambient temperature (ºC)	Minimum ambient temperature (ºC)	Maximum ambient temperature (ºC)	Relative humidity (%)
1774	15.0	2.7	32.1	57

3.6.3. Methodology

The two techniques applied in this study to all modules under test, based on the analysis of the output power of the PV modules, are described in this section. The combination of these two techniques allows a good approach to understand the degradation effects and helps to identify better the degradation rates, stabilization periods and seasonal variations.

3.6.3.1. Effective peak power of the PV modules

The effective peak power of a PV module, P^*_M, at STC is given by the following equation [18-19] :

$$P_M^* = \frac{G^* P_{DC}}{G} TF \qquad (3.6\text{-}1)$$

where P_{DC}, G and G^* are the DC output power of the PV module, the irradiance, and irradiance at STC respectively. TF is the thermal factor defined as follows:

$$TF = \frac{1}{[1 + \delta(T_m - T_m^*)]} \qquad (3.6\text{-}2)$$

where T_m is the PV module temperature, T_m^* is the module temperature under STC (25°C), and δ is the power temperature coefficient of the PV modules.

The evaluation of P^*_M from the monitoring data set was performed after a disregarding data recorded at low irradiance values. Specifically, only measurements taken at $G > 700$ W/m^2 were used. Thus, the shape of varying solar spectra recorded in Leganés above this irradiance threshold closely resembles that of the spectral AM1.5G reference spectrum and consequently no spectral effects are taken into account in Eq. (*3.6*-1). This agreement between recorded spectra and AM 1.5G reference spectrum is based on the criteria adopted by the International Electrotechnical Commission to state the spectral match of a solar simulator [20], defined by the deviation from the standard spectrum. The experimental assessment of such spectral match is far from being obvious, Thus, the reader is referred to Annex A at the end of this paper where this empirical evaluation can be found.

The monthly average value of P^*_M was evaluated along the five years of the monitoring campaign.

The degradation rate, *DR* (%/year), of the TFPV modules is evaluated by means of a linear least square fitting method of the P^*_M by using Eq. (*3.6*-3).

$$DR = 100\frac{12m}{c} \quad (3.6\text{-}3)$$

where m is the slope of line and c is the y intercept of the trend line obtained for P^*_M [21]:

$$y = mx + c \quad (3.6\text{-}4)$$

The analysis of the stabilization period of TFPV modules is based on a second monitoring data filtering process following the procedure used in previous works [9-10, 22]. The average monthly value of the monitored P_{DC} output power of the PV modules was evaluated for restricted ranges of tilted irradiance and working PV module temperature.

3.6.3.2. Power-Irradiance technique

The power-irradiance (P-G) technique is the second method used in this study to analyse the behaviour of the TFPV modules. This method proposed by Hussin et al. [22] was applied with success to study the degradation of a-Si:H [9,24] and a-Si:H/µc-Si:H TFPV modules [10].

A Linear Correlation Approach (LCA) was used to obtain linear regression equations from the actual PV modules DC outputs, $P_{DC,}$ as a function of the irradiance, G, by means of the following equation:

$$P_{DC} = A_{Gr}.G + C \quad (3.6\text{-}5)$$

where P_{DC} is the PV module DC output power, A_{Gr} is the gradient, G is the plan-of-array irradiance and C is the ordinate value of P_{DC} at $G = 0$.

A data filtering process was carried out in order to avoid problems caused by low values of irradiance (G<700 W/m^2) as in the evaluation of the *DR* presented in previous section. Eq. (*3.6*-5) is only valid for values of G>700 W/m^2.

Finally, the monthly gradient values, A_{Gr}, of each empirical equation can be plotted to determine the stabilization period [22].

3.6.3.3. Fill Factor and Performance Ratio

The performance ratio, *PR(%)*, is used as an indicator of outdoor modules performance and is given by [25]:

$$PR = \frac{P_m}{P_{mSTC}} \Big/ \frac{G}{G^*} \quad (3.6\text{-}6)$$

where P_m is the measured maximum output power of the PV module and P_{mSTC} is the nominal output power of the PV module.

On the other hand, the Fill Factor, *FF*(%), is given by the following equation :

$$FF = \frac{P_m}{Voc \quad Isc} \qquad (3.6\text{-}7)$$

where *Isc* and *Voc* are the short-circuit current and open-circuit voltage of the PV modules respectively.

The evolution of the monthly values of *PR* and *FF* was analysed in all modules under test along the monitoring campaign.

3.6.4. Results and discussion

3.6.4.1. Evolution of the effective peak power of the PV array

The evolution of the effective peak power of the four PV modules calculated by using the Eq. (*3.6*-1) and monitored data is plotted in Fig. 3.6.1. As it can be seen, the decrease rate of the effective peak power, P^*_M, along the monitoring campaign strongly depends on the PV module technology.

Regarding the a-Si:H and micromorph PV modules, an important initial decrease of P^*_M can be observed during the first months of exposure under outdoor conditions due to the LID phenomenon. After a period of time, the decrease is less significant and P^*_M fluctuates around a constant value following climatic seasonal changes. A decrease of P^*_M is observed during the winter months while an increase is observed over the summer months. This seasonal variation in the output power of the a-Si:H and micromorph PV modules is mainly attributed to the effect of temperature on the amorphous material, and has been described previously in several studies [16-18,21-23]. Thus, the regeneration in summer months can be assigned to the light-induced annealing [5], spectral effect [26] and thermal regeneration [13,27].

The evolution of P^*_M of the CdTe PV module presents a continue decrease along the exposure period. As it is shown in Fig. 3.6.1, the decrease of P^*_M over the first and second year is more significant than the decrease of P^*_M over the last three years of the analysis period. The effective peak power value is decreased by 22.15% during the five years of the monitoring campaign. The seasonal variation observed in the trend of P^*_M of the CdTe PV module is smaller than the observed in previous works published in the literature [28].

Finally, form Fig. 3.6.1, it can be observed that P^*_M corresponding to the CIS PV module exhibits a stable evolution during the exposure period compared to the others technologies.

Several works presented in literature confirm the stability of the CIS PV modules when exposed outdoor [29-31]. Moreover, a slight seasonal variation can be observed in the trend of P^*_M, where, the output power increases during the winter months and decreases over the summer months. This can be explained with the relatively high power temperature coefficient of the CIS PV module given in Table 3.6.1. The obtained values of *DR* calculated from the trend line of each PV module are given in Table 3.6.3.

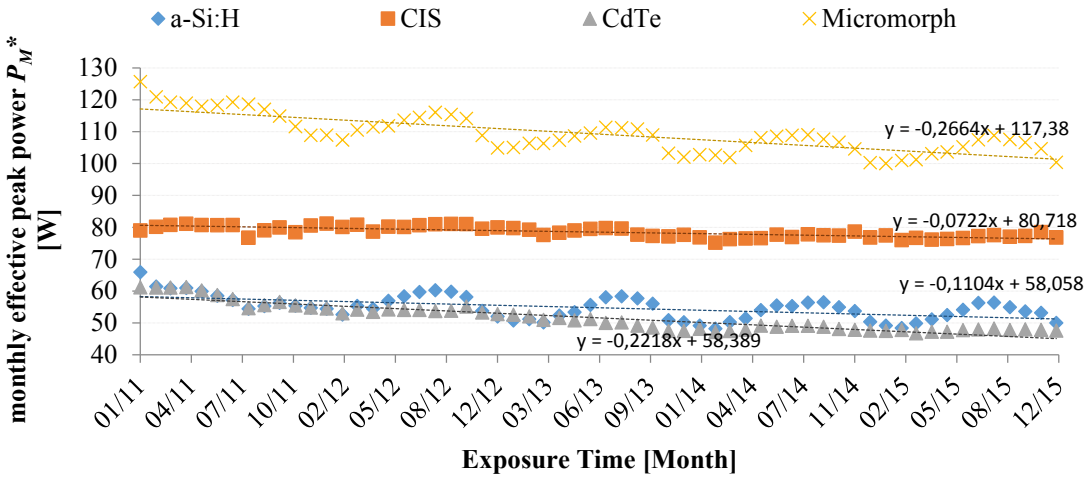

Figure 3.6. 1 Evolution of P^*_M (for G>700 W/m²) of the four PV modules along the monitoring campaign.

Table 3.6. 3 Degradation rates of the PV modules.

PV module	a-Si:H	CIS	CdTe	Micromorph
DR [%/year]	- 2.28	- 1.04	- 4.55	- 2.72

a) a-Si:H PV module

The *DR* of the a-Si:H PV module presented in Table 3.6.3 is in the range of previous results presented in the literature [4,9,32]. The value of *DR* in a work presented by Kichou et al. is around -2.30%/year [9], while Jordan and Kurtz report *DR* of a-Si:H PV modules up to -4.5%/year [4].

In most cases mean values obtained for the *DR* are in the range of -1%/year to -2%/year. These values are similar to *DR* of -1.9%/year reported for mono-crystalline PV modules in Indian climatic conditions [33]. Moreover, Phinikarides et al. refer to *DR* below -2.4%/year for a-Si:H PV modules [32]. The highest degradation rates have been reported in Korea and the Mediterranean region.

The result obtained by applying the filtering process of restricted interval of solar irradiance and cell temperature values is shown in Fig. 3.6.2. After one month of exposure

under outdoor conditions, a strong initial degradation can be observed, where, the DC output power of the PV module is decreased by around 8.61%. From the second month till April 2012, the DC output power of the a-Si:H PV module is reduced by 18.26%. During the summer months of 2012, a regeneration of 5% can be distinguished in the performance of the PV module, and after that, the output power is decreased by the same percentage in winter months.

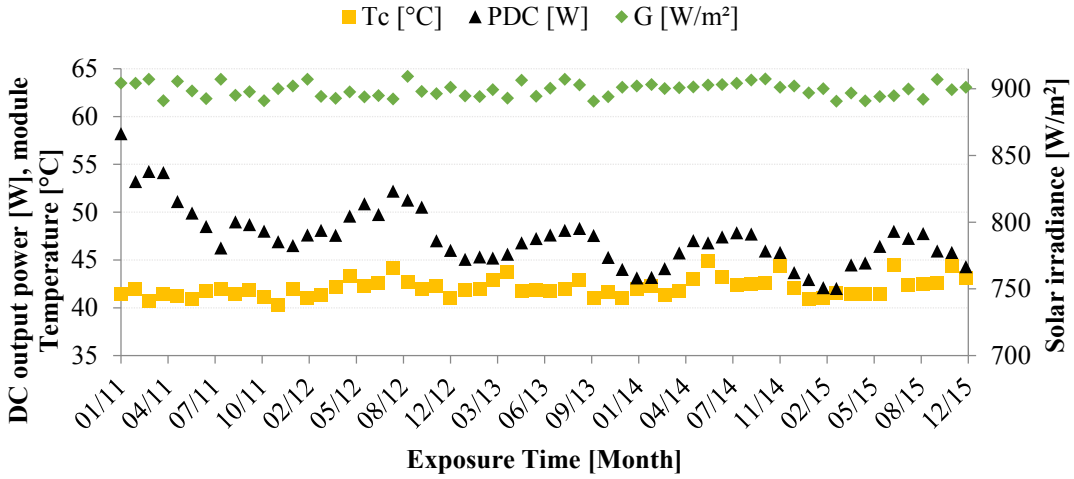

Figure 3.6. 2 Monthly values of the DC output power of the a-Si:H PV module obtained by G and Tc data in the range of: 890 W/m²< G < 910 W/m² and 40 °C < Tc < 45 °C.

The stabilization of the DC output power of the a-Si:H PV module occurs after a period of 24 months of operation under the climate of Madrid. In previous works, stabilization periods of 16 months were reported for a-Si:H PV modules under a Continental-Mediterranean climate [9] and Equatorial climate [22].

The stabilized level of DC output power of the PV module is around 45 W taking into account the range of *G* and *Tc* considered in the data filtering process. In the following months, the DC power demonstrates a sinusoidal trend attributable to the annealing effects. The effect of seasonal oscillation remains after the stabilization period for about 5.5% variation from the stabilized level of DC power. A similar result, 4%, was reported in Rome climatic conditions [34].

b) micromorph PV module

The *DR* of the micromorph PV module is found to be -2.72%/year. This value of *DR* is in the range of results obtained in a previous work where *DR* values of -2.20%/year were reported [10].

The analysis of the stabilization period of the micromorph PV module is carried out by following the same steps presented above. In the second monitoring data filtering process, the selected ranges of *G* and *Tc* are the same as those selected for the a-Si:H PV module, 890 W/m^2<*G* < 910 W/m^2 and 40 °C <*Tc*< 45 °C.

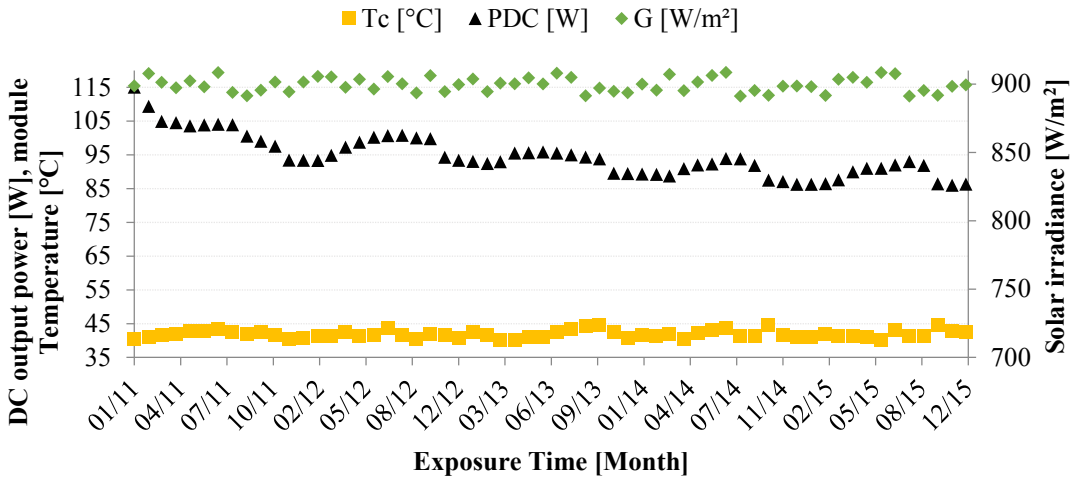

Figure 3.6. 3 . Monthly values of the DC output power of the micromorph PV module obtained by G and Tc data in the range of: 890 W/m^2<G< 910 W/m^2 and 40 °C <Tc< 45 °C.

The evolution of the filtered DC output power of the micromorph PV module over the time is shown in Fig. 3.6.3. Similarly, to the case of a-Si:H, a strong initial decrease of the DC output power is observed after the first months of exposure followed by a smooth variation according to the seasonal climate changes. After four months of deployment under outdoor conditions, the DC output power generated by the micromorph PV module was degraded by about 8.83%. This degradation is mainly associated to the LID that affects the top amorphous layer of the solar cell. In the following months, the DC output power shows a sinusoidal trend attributable to the annealing effects.

Previous works based on the study of degradation of micromorph PV modules commercialized by Kaneka indicate that the stabilization period is from two weeks till a few months [22], and around four months under a Continental-Mediterranean climate [10].

The P_{DC} values of January 2011 and January 2012 are equal to 115.06 W and 93.38 W respectively; this means that the output power of the PV module was degraded by 18.84%. On the other hand, the P_{DC} values of August 2011 and August 2012 are equal to 103.93 W and 100.81 W respectively; this leads to degradation of 3%. Therefore, by comparing the difference

between the values of *DR* obtained from winter and summer months, the stabilization period is identified to be equal to four months after a decrease of 17.4% in the P_{DC} value.

After three years of exposure under outdoor conditions, a reduction of the output power of around 5.6% from the stabilized value was observed leading to a total degradation of 23%.

The effect of seasonal oscillation remains after the stabilization period with variations about 3.7% from the stabilized level of DC output power. Compared with the a-Si:H PV module, the LID phenomenon and the seasonal variation are less significant due to the effect of the μc-Si:H layer.

c) CdTe PV module

From Table 3.6.2 it can be seen that the CdTe PV module presents the highest *DR* compared to the other technologies. Previous works available in the literature present *DR* of -1.5%/year and -3.5%/year using the same linear regression method adopted in this study [4,32].

The analysis of the stabilization period of the CdTe PV module is carried out by following the same method presented in the previous section, with the same ranges of *G* and *Tc* selected previously in the second monitoring data filtering process.

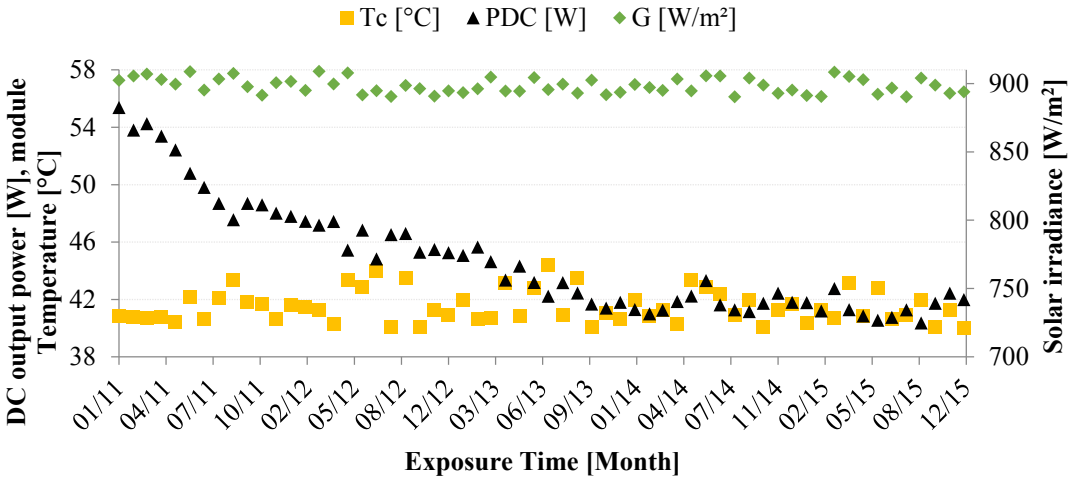

Figure 3.6. 4 Monthly values of the DC output power of the CdTe PV module obtained by G and Tc data in the range of: 890 W/m²<G< 910 W/m² and 40 °C <Tc < 45 °C.

Fig. 3.6.4 displays the results obtained after the filtering process. As it can be seen, the DC output power generated by the CdTe PV module presents a strong steady decrease during the first two years of exposure under outdoor conditions. The output power degraded of around 21.9% in two years and a half. A significant decrease in the performance of CdTe PV modules

is also reported in the literature by Carlsson and Brinkman [35], where the CdTe PV modules degraded of around 13% in a period of 18 months.

After a period of 30 months, the degradation of the CdTe PV module is very slight and the stabilization can be observed in the trend of the output power generated by the PV module.

The stabilization of the DC output power of the CdTe PV module can be estimated to occur after a period of 32 months of operation under the climate of Madrid. With the selected ranges of *G* and *Tc* chosen in the data filtering process, the DC output power of the CdTe PV module stabilizes around 41.6 W. However, a slight seasonal variation can be still be observed, but very small: ±2% of the stabilized DC output power.

d) CIS PV module:

The *DR* obtained for the CIS PV module is -1.04%/year, as it is shown in Table 3.6.3. This value of *DR* is in the range of other works previously developed for different locations: -0.5%/year [4] and -2.72%/year [32].

The analysis of the stabilization period of the CIS PV module is carried out by following the same steps presented in previous sections. In the second monitoring data filtering process, the selected ranges of *G* and *Tc* are: 890 W/m^2<*G* < 910 W/m^2 and 50 °C <*Tc*< 55 °C.

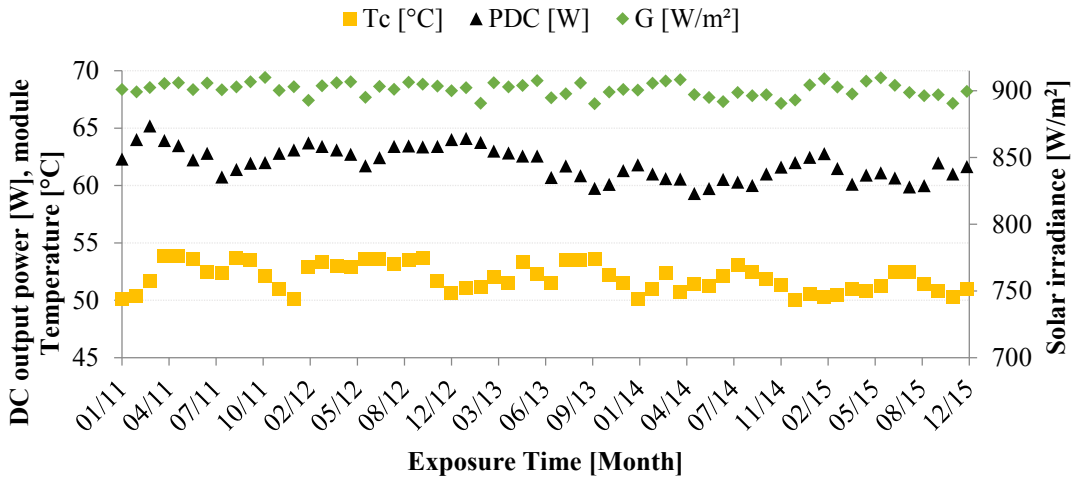

Figure 3.6. 5 DC output power of the CIS PV module obtained by G and Tc data in the range of: 890 W/m^2<G< 910 W/m^2 and 50 °C <Tc< 55 °C.

The result obtained is depicted in Fig. 3.6.5. The DC output power generated by the CIS PV module presents a stable trend during the monitoring campaign. No significant degradation can be observed compared to the other technologies presented above. A slight degradation can

be noticed after a period of 3 years, where the DC output power value is decreased of 2.66%. Moreover, a slight seasonal variation can be observed in the trend of the DC output power. The output power decreases with the increase of temperature and vice versa, and this can be explained by the relative high value of the temperature coefficient of power of the CIS PV module.

3.6.4.2. Power-irradiance technique

The Power-Irradiance method was used as a second technique to estimate the stabilization period of the four TFPV modules used in this work.

Table 3.6. 4 Gradient values and empirical equations obtained for the a-Si:H and micromorph PV modules.

	a-Si:H			micromorph		
Month	**Gradient**	**R^2**	**Empirical equation**	**Gradient**	**R^2**	**Empirical equation**
Jan-11	0.0680	0.950	P_{DC} =0.0680 G + 3.701	0.1343	0.969	P_{DC} =0.1343 G – 3.250
May-11	0.0517	0.947	P_{DC} =0.0517 G + 4.938	0.1071	0.967	P_{DC} =0.1071 G + 3.451
Sep-11	0.0573	0.930	P_{DC} =0.0573 G + 6.242	0.1031	0.962	P_{DC} =0.1031 G + 5.155
Jan-12	0.0504	0.934	P_{DC} =0.0504 G + 0.901	0.1117	0.931	P_{DC} =0.1117 G – 4.411
May-12	0.0511	0.964	P_{DC} =0.0511 G + 1.860	0.1045	0.967	P_{DC} =0.1045 G + 0.474
Sep-12	0.0506	0.963	P_{DC} =0.0506 G + 2.469	0.1022	0.956	P_{DC} =0.1022 G + 4.779
Jan-13	0.0470	0.934	P_{DC} =0.0470 G – 1.253	0.1152	0.966	P_{DC} =0.1152 G – 2.225
May-13	0.0491	0.970	P_{DC} =0.0491 G + 1.794	0.1037	0.964	P_{DC} =0.1037 G – 0.284
Sep-13	0.0510	0.958	P_{DC} =0.0510 G + 1.539	0.0981	0.975	P_{DC} =0.0981 G + 4.317
Jan-14	0.0474	0.883	P_{DC} =0.0474 G + 1.462	0.1064	0.928	P_{DC} =0.1064 G – 3.666
May-14	0.0503	0.912	P_{DC} =0.0503 G + 1.356	0.0946	0.962	P_{DC} =0.0946 G – 3.770
Sep-14	0.0501	0.971	P_{DC} =0.0501G + 2.213	0.0975	0.979	P_{DC} =0.0975 G – 0.039
Jan-15	0.0476	0.923	P_{DC} =0.0476 G – 1.006	0.1058	0.972	P_{DC} =0.1058 G + 0.556
May-15	0.0473	0.965	P_{DC} =0.0473 G + 2.253	0.0931	0.955	P_{DC} =0.0931 G + 4.055
Sep-15	0.0503	0.949	P_{DC} =0.0503 G + 3.419	0.0962	0.957	P_{DC} =0.0962 G + 4.226

Table 3.6. 5 Gradient values and empirical equations obtained for the CdTe and CIS PV modules.

	CdTe			CIS		
Month	**Gradient**	**R^2**	**Empirical equation**	**Gradient**	**R^2**	**Empirical equation**
Jan-11	0.0578	0.946	P_{DC} =0.0578 G + 3.297	0.0692	0.930	P_{DC} =0.0692 G + 5.619
May-11	0.0517	0.947	P_{DC} =0.0517 G + 4.938	0.0637	0.911	P_{DC} =0.0637 G + 5.102
Sep-11	0.0453	0.931	P_{DC} =0.0453 G + 6.241	0.0592	0.914	P_{DC} =0.0592 G + 8.088
Jan-12	0.0489	0.887	P_{DC} =0.0489 G + 3.342	0.0708	0.890	P_{DC} =0.0708 G + 3.887
May-12	0.0485	0.937	P_{DC} =0.0485 G + 2.500	0.0721	0.920	P_{DC} =0.0721 G – 2.264
Sep-12	0.0439	0.922	P_{DC} =0.0439 G + 5.804	0.0612	0.914	P_{DC} =0.0612 G + 7.219
Jan-13	0.0449	0.908	P_{DC} =0.0449 G + 3.132	0.0801	0.866	P_{DC} =0.0801 G – 2.858
May-13	0.0452	0.961	P_{DC} =0.0452 G + 3.867	0.0667	0.943	P_{DC} =0.0667 G + 3.963
Sep-13	0.0432	0.911	P_{DC} =0.0432 G + 5.107	0.0598	0.905	P_{DC} =0.0598 G + 6.058
Jan-14	0.0434	0.822	P_{DC} =0.0434 G + 2.520	0.0752	0.894	P_{DC} =0.0752 G – 1.023
May-14	0.0435	0.926	P_{DC} =0.0435 G + 0.257	0.0733	0.904	P_{DC} =0.0733 G – 4.826
Sep-14	0.0423	0.903	P_{DC} =0.0423 G + 3.511	0.0600	0.941	P_{DC} =0.0600 G + 7.170
Jan-15	0.0434	0.838	P_{DC} =0.0434 G – 0.567	0. 0745	0.879	P_{DC} =0.0745 G – 1.922
May-15	0.0407	0.937	P_{DC} =0.0407 G + 5.903	0. 0583	0.911	P_{DC} =0.0583 G + 6.979
Sep-15	0.0408	0.906	P_{DC} =0.0408 G + 6.143	0. 0590	0.935	P_{DC} =0.0590 G + 6.784

From the plots of the monthly P_{DC} as a function of irradiance the trend line defined by Eq. (*3.6*-5) is extracted with a LCA. The stabilization period can be estimated by plotting the gradient values obtained from Eq. (*3.6*-5).

Tables 3.6.4 and 3.6.5 summarise several gradient values and empirical equations obtained by the LCA for each PV module. One value for each month is given in the tables.

a) a-Si:H PV module.

The evolution of the gradient values along the monitoring campaign obtained for the a-Si:H PV module is shown in Fig. 3.6.6. The gradient values represent clearly the instability of the PV module during the first months of deployment under outdoor conditions. A strong initial decrease can also be observed. The decrease of the gradient values continues during the next months till reaching a sinusoidal trend caused by the seasonal variation.

After a period of 24 months the stabilization of the a-Si:H PV module occurs. This stabilization period matches the stabilization period obtained in section 3.6.4.1 by the first method.

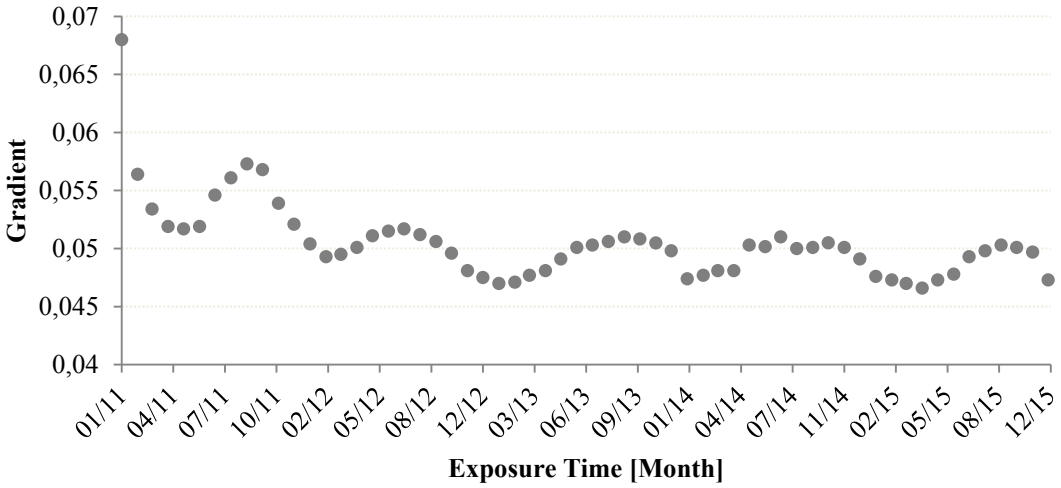

Figure 3.6. 6 Evolution of the gradient values obtained for a-Si:H PV module.

b) micromorph PV module

Fig. 3.6.7 depicts the evolution of the gradient values obtained for the micromorph PV module along the exposure period of five years. After the strong initial decrease observed during the first months, the gradient values keep decreasing following the seasonal variation. In this case the rise of the gradient values is observed to occur during the winter months due to the domination of the temperature effects in the μc-Si:H layer.

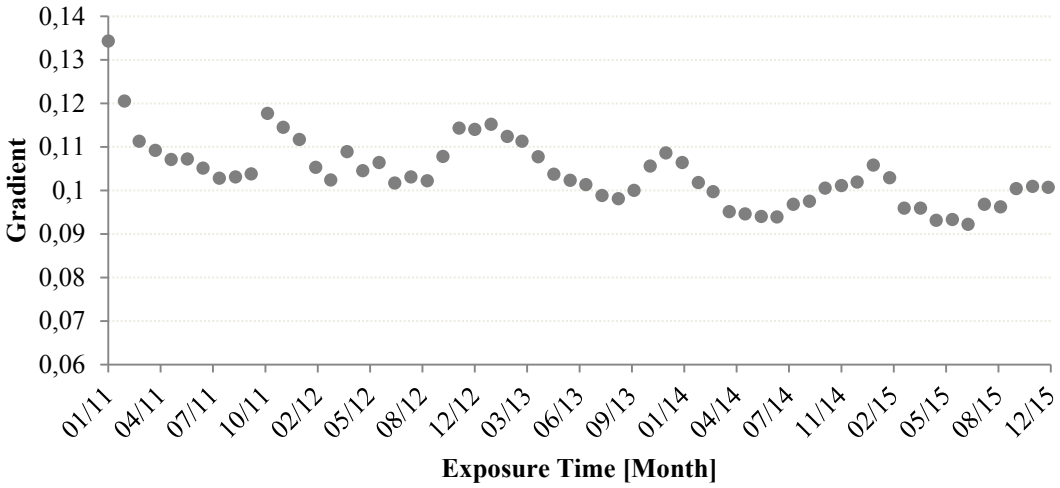

Figure 3.6. 7 Evolution of the gradient values obtained for micromorph PV module.

Concerning the stabilization period, the result obtained is four months, identical to the value obtained in section 3.6.4.1.

c) CdTe PV module

From the evolution of the gradient values for the CdTe PV module plotted in Fig. 3.6.8, it can be observed a continue decrease in the trend of the gradient. After a long period of 32 months, the evolution of the gradient values stabilizes around the value 0.0425, reflecting the stabilization of the output power generated by PV module. The stabilization period obtained by the P-G technique coincide with the stabilization period obtained by the first method presented above.

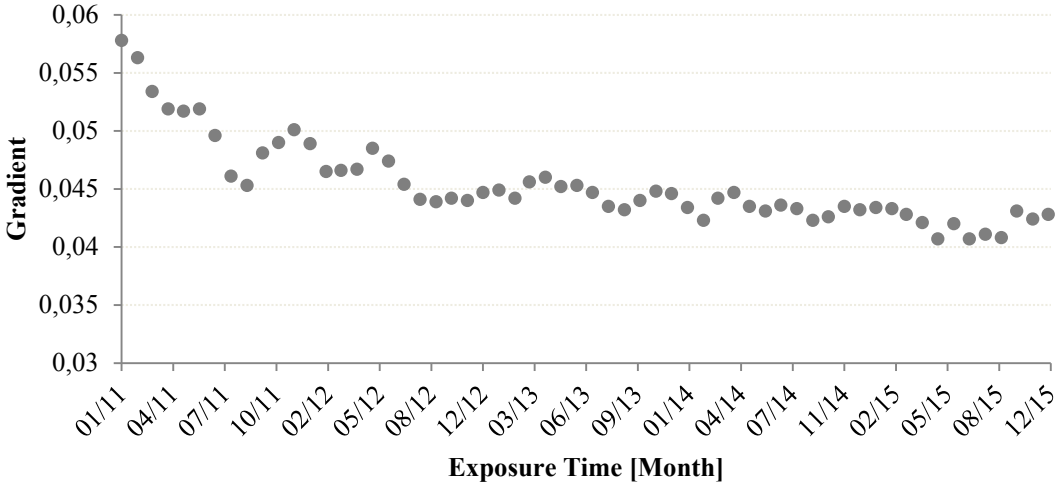

Figure 3.6. 8 Evolution of the gradient values obtained for CdTe PV module.

d) CIS PV module

Finally, the evolution of the gradient values obtained for the CIS PV module is shown in Fig. 3.6.9. After a period of five years of deployment, no significant degradation can be observed, while a sinusoidal trend is present due to the seasonal variation. The results obtained using both methods confirm the stability of the CIS PV module and it can be observed that the PV module performs better during winter months. However, the DC output power value is decreased of 2.66% after a period of 3 years, has it was shown in Fig. 3.6.5. Moreover, a slight seasonal variation of ± 2.1% can be observed in the trend of the DC output power in Fig. 3.6.5.

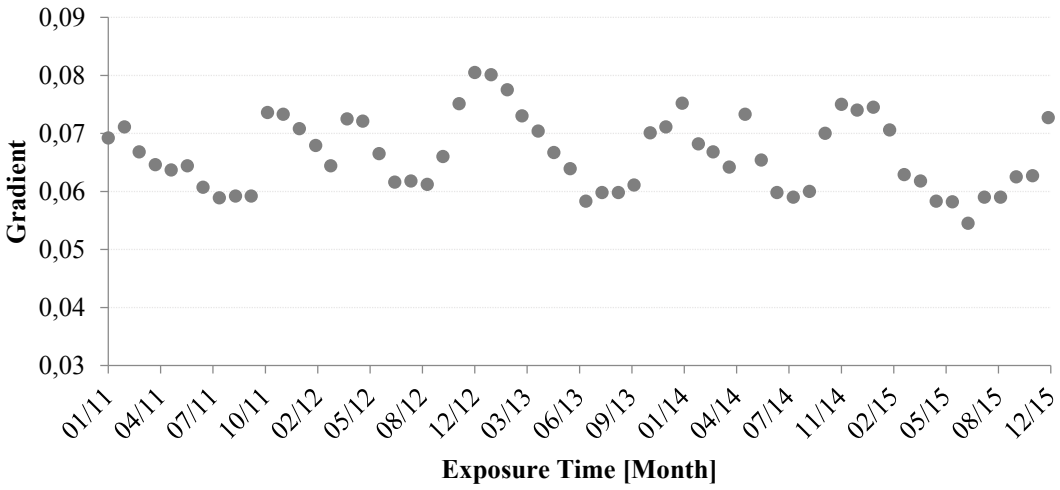

Figure 3.6. 9 Evolution of the gradient values obtained for CIS PV module.

3.6.4.3. *Fill Factor and Performance Ratio evolution.*

The evolution of the monthly fill factor values, *FF*(%), calculated for each PV module, is shown in Fig. 3.6.10. It can be seen that the evolution of the monthly FF of each PV module is in accordance with the results obtained in the previous sections.

Regarding the a-Si:H and the micromorph PV modules, the initial degradation and the seasonal variation are also present in the evolution of their monthly *FF*. The stabilized value of the *FF* for the a-Si:H PV module is around 57%. For the micromorph PV module, the *FF* firstly stabilizes around 62% and, after a period of three years, diminishes to 60%. Comparing these two PV modules, the effect of the μc-Si:H bottom layer can be clearly seen in the enhanced performance of the micromorph PV module.

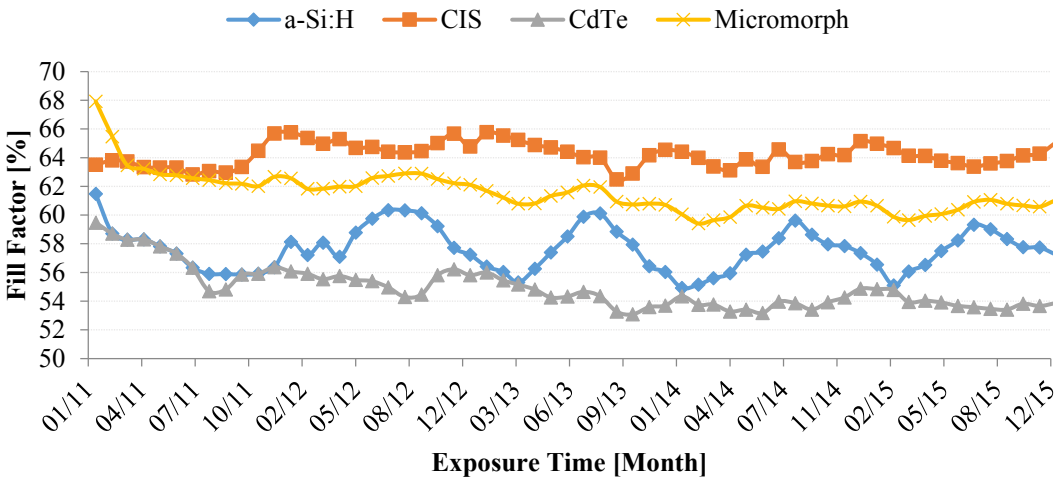

Figure 3.6. 10 Evolution of the FF along the exposure period.

The trend of the monthly FF obtained for the CdTe PV module demonstrates a continue degradation in the performance of the PV module. The value of the *FF* stabilizes around 53% representing the worst value compared to the other PV module technologies.

Finally, the high values of the monthly *FF* obtained for the CIS PV module reflect the stability in the performance of this PV module. It can be seen from Fig. 3.6.10 that the monthly *FF* values fluctuate around 64% following the seasonal variation previously observed for the CIS PV module.

The monthly values of the performance ratio, *PR*, calculated using Eq (*3.6*-6) are plotted in Fig. 3.6.11. As it can be seen, the same trends of degradation are obtained.

For the a-Si:H PV module the initial degradation is also observed in the trend of the *PR* shown in Fig. 3.6.11. The *PR* stabilizes around the 85% following the seasonal variation. These seasonal *PR* fluctuations are around the 10%, similar to results reported in the literature in Rome climatic conditions [36].

From the trend of the *PR* obtained for the micromorph PV module, it can be seen an initial degradation, followed by a first stabilization around 89% and a further reduction of 5.61% after a period of three years. *PR* of 91% with an important seasonal variation was reported for micromorph PV modules after one-year operation in temperate climates [37].

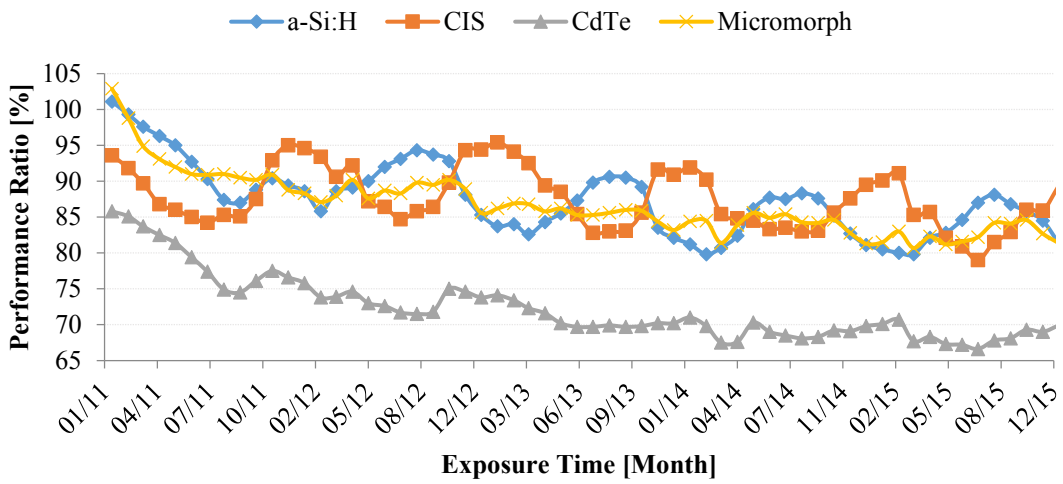

Figure 3.6. 11 Evolution of the PR along the exposure period.

The evolution of the *PR* calculated for the CIS PV module demonstrates stable fluctuations around the value of 90% following the seasonal variation.

Finally, for the CdTe PV module, it can be seen from Fig. 3.6.11 that the continue degradation along a period of 32 months clearly affects the performance of the PV module, with a *PR* degrading from 85% to 69%.

3.6.5. Conclusion

The evaluation of performance degradation under 5 years of outdoor exposure of four TFPV modules corresponding to four different technologies: a-Si:H, a-Si:H/µc-Si:H, CdTe and CIS, was addressed in this work. The PV modules were deployed in Leganés, a city within the metropolitan area of Madrid (Spain). This is a dry and sunny inland site with a Continental-Mediterranean Climate. The results obtained are referred to one PV module for each of the technologies tested so that these results cannot be considered as general results.

The values of *DR* were evaluated by linear regression from the evolution of the modules effective peak power. The stabilization periods were assessed by observing the evolution of the output P_{DC} and through the power-irradiance technique.

The values of *DR* for all the technologies were found to be in the range of previous studies except for the CdTe PV module. This module presents a higher degradation rate than expected, as well as a very high loss of effective peak power over the five years. The CIS PV module is found to be the most stable, presenting the lowest values of *DR* and power loss.

Regarding the stabilization period, the a-Si:H and micromorph silicon modules present results in good agreement with the literature, even if stabilization periods found in previous studies for a-Si:H TFPV modules are slightly shorter. In both a-Si:H and micromorph technologies, a strong degradation is observed during the first month of outdoor exposure, where the DC output power drops of 8.61% and 8.42% respectively. In both technologies the instability is mainly due to the a-Si:H layer. In the micromorph TFPV module, however, the layer of a-Si:H is significantly thinner than in the a-Si:H module. This fact, together with the presence of the more stable μc-Si:H bottom layer, allows the micromorph module to have a significantly shorter stabilization period than that of the a-Si:H module. The CdTe PV module degrades steadily for a very long period, during which the output P_{DC} degrades over 22% before showing stabilization. This result is in disagreement with previous works reported in the literature, which state CdTe to be a stable technology. On the other hand, the CIS PV module shows a very stable trend, with only 2.66% of P_{DC} loss over the 5 years of experimental campaign lasted and a *DR* of -1.04%/year.

As a summary, the CIS PV module was found to be the most stable of the four PV modules, under long term outdoor exposure in a dry and sunny inland site. The amorphous and micromorph modules also perform quite well, showing degradation rates and stabilization periods similar to the expectations. However, their performances appear to be lower than what stated in the manufacturer datasheets, especially regarding the values of stabilized effective peak power. The CdTe module shows poor performances, with high degradation rate and power losses, and the power output is always well below the datasheet value.

Finally, the evolution of the monthly values obtained for the *FF* and *PR* is in line with degradation trends observed for all TFPV modules analysed.

Acknowledgements

The authors sincerely thank the financial support provided by the Spanish Science and Innovation Ministry and the ERDF within the frame of the project ‘Estimacion de la energia generada por módulos fotovoltaicos de capa delgada: influencia del espectro’ under expedient code ENE2008-05098/ALT. This work was also supported by the Centre for Advanced Studies in Energy and Environment (University of Jaén) within the frame of the project ‘Caracterización y modelado de las irradiancias espectrales global sobre plano inclinado y directa normal mediante técnicas estadísticas y de inteligencia artificial’.

Appendix A. Experimental assessment on the spectral match of spectra recorded in Leganés at values of irradiance above 700 W/m^2

A.1. Introduction

This annex is intended to show how spectral measurements corresponding to irradiances above 700 W/m^2 recorded in Leganés over the course of the experimental campaign match the AM 1.5G reference spectrum according to similar criteria to those used by the IEC to evaluate the spectral mismatch of a solar simulator [20]. The analysed spectral instances were collected from January 2012 to December 2013 totalizing 40,554 samples, including those scanned below 700 W/m^2. This is a number of samples which suffices to assess the spectral matching over the whole data collection period which ranges from January 2011 to December 2015.

A.2. Methodology

The average photon energy (APE, in eV) was originally proposed by Jardine et al. [38], as the average energy of all photons from a given solar spectrum distribution. Since then it has become a popular and widespread index to assess whether blue light or red light is enhanced in an actual spectrum when compared with the AM1.5G reference spectrum. Thus, APE may be written as follows:

$$\mathrm{APE} = \frac{\int_a^b E\ (\lambda) d\lambda}{q\int_a^b \phi(\lambda) d\lambda} \tag{1}$$

where $E(\lambda)$ [W·m^{-2}·nm^{-1}] is the spectral irradiance, $\Phi(\lambda)$ [m^{-2}·nm^{-1}·s^{-1}] is the spectral photon flux density, q is a constant that numerically equals the electronic charge [J·eV^{-1}], a [nm] and b [nm] are the lower and upper wavelength limits, respectively, of the waveband under study. The latter two limits are usually determined by the measurement range of the spectro-radiometer used. Specifically, in our case, a = 350 nm and b = 1050 nm. Thus, APE for the AM1.5G reference spectrum equals 1.88 eV for this measurement range. Therefore, higher values of this index imply spectra shifted to shorter wavelengths ('blue shifted') whilst lower ones imply spectra shifted to longer wavelengths ('red shifted').

The methodology used by the IEC [20] to classify a solar simulator according to its spectral match is summarized in what follows. First, the waveband ranging from 400 to 1000 nm in a spectrum generated by a solar simulator is divided in six 100-nm bands each contributing a certain percentage to the the integrated irradiance. Then, the percentage values to the total

irradiance for each spectral band of the spectrum produced by a solar simulator and the AM1.5G reference spectrum are obtained. If the deviation of the percentages of the spectrum produced by a solar simulator from those of the AM 1.5 reference spectrum lie within ±25%, the simulator obtains 'A-Class' regarding spectral match. This spectral matching requirement has been adopted in this work to analyse natural sunlight spectrum matching at values of irradiance above 700 w/m2 in Leganés, following the methodology of some other previous contributions [39,40].

A.3. Results and conclusion

Over 97% of all the spectral instances collected from January 2012 to December 2013 corresponding to $G > 700$ W/m^2 yield values of APE ranging from 1.84 to 1.90 eV. As it can be easily derived from above, spectra scanned with APE lying within 1.85 ± 0.01 eV and 1.89 ± 0.01 eV correspond to "reddest" and "bluest" ones, the former are usually recorded in winter when the sun elevation is low, while the latter are measured during clear days in late spring and early summer when the sun elevation is high.

The broadband irradiance was integrated for each data binned in the above two sets of spectral measurements between 350 and 1050 nm using the trapezoidal rule. Then, the wavelength range was divided into fourteen 50-nm bands so that the percentage contribution (R_c) of each band to the calculated broadband irradiance was obtained. Mean values of R_c ($\langle R_c \rangle$) in each 50-nm band were calculated for both APE intervals. The standard deviation was also calculated for each of these bands to estimate the dispersion in the values of R_c around its mean value within these two APE intervals.

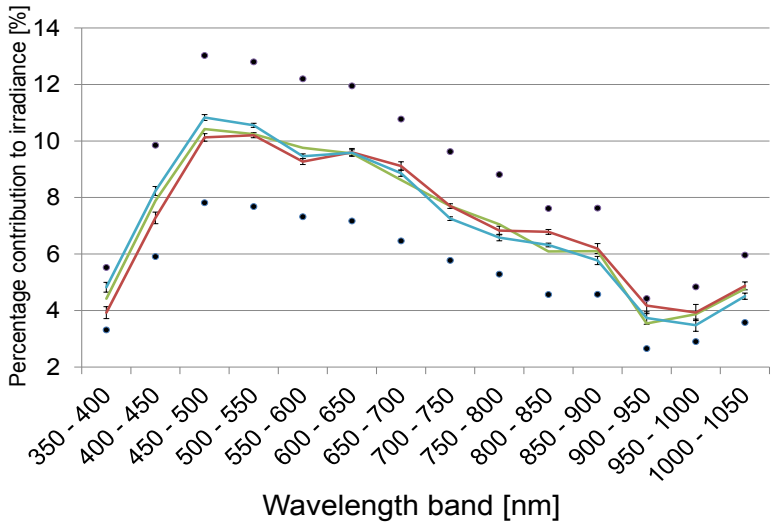

Fig. A. 1 Average Rc values of each 50-nm spectral band for the spectra binned in the APE intervals 1.85 ± 0.01 eV (red line) and 1.89 ± 0.01 eV (blue line). The standard deviation related to each value of <Rc> is shown by means of error bars. Values of Rc of each value of <R_c> is shown by means of error bars. Values of R_c of each

50-nm spectral band for the AM1.5G reference spectrum are depicted by a green line while black dots show a deviation of ±25% from the latter.

The blue and red line in Fig. A.1 show the average R_c values for every 50-nm band for the two APE intervals under consideration while error bars indicate the standard deviation related to each value of $<R_c>$. The green line indicates values of R_c for the AM1.5G reference spectrum –restricted to the 350-1050 nm waveband- across all 50-nm bands. Black dots above and below the green line indicate the ±25% deviation allowed for Class-A simulators according to the requirements stated by the IEC. Obviously, spectral measurements binned in the APE interval ranging from 1.88 to 1.90 eV show higher percentage contributions to the integrated irradiance in 50-nm bands with shorter wavelengths. Conversely, percentage contributions in 50-nm bands with longer wavelengths are enhanced for spectral data grouped in the APE interval ranging from 1.84 to 1.86 eV. These results are in close agreement with those obtained by Minemoto et al. [39] and Norton et al. [40], who carried out a similar analysis –although aimed at a different goal- to that presented here in Kusatsu city (Japan), Golden, Colorado (USA) and Ispra (Italy).

Fig. A.1 clearly shows how values of $<R_c>$ corresponding to the spectra with the most enhanced short wavelengths –blue line- and the most enhanced long wavelengths –red line- fit very well the allowable deviation of ±25% -black dots- from percentage contributions across all 50-nm bands to the integrated irradiance of the AM1.5G spectrum. Additionally, such values of $<R_c>$ are in very close agreement with those of the AM1.5G reference spectrum for R_c.

In view of the above results, no spectral correction has been used in Eq. (1). Indeed, spectra corresponding to irradiance levels exceeding 700 W/m^2 in Leganés may be considered similar to the AM1.5G spectrum according to the criteria adopted in this work.

References

[1] Fraunhofer Institute for Solar Energy Systems, ISE. Photovoltaics Report. Freiburg, 11 March 2016. https://www.ise.fraunhofer.de/de/downloads/pdf-files/aktuelles/photovoltaics-report-in-englischer-sprache.pdf

[2] Tossa Alain K, Y.M. Soro YM, Thiaw L, Azoumah Y, Lionel Sicot, Yamegueu D. Claude Lishou, Coulibaly Y, Guillaume Razongles, 2016. Energy performance of different silicon photovoltaic technologies under hot and harsh climate. Energy 103 : 261–270.

[3] Virtuani A, Pavanello D, Friesen G. Overview of temperature coefficients of different thin film photovoltaic technologies. 25th European photovoltaic solar energy

conference and exhibition/5th World conference on photovoltaic energy conversion. Proc. 2010; 6-10.

[4] Jordan DC, Kurtz, SR, 2013. Photovoltaic degradation rates - An Analytical Review. Prog. Photovoltaics Res. Appl. 21: 12–29.

[5] Meyer EL, van Dyk EE, 2003. Characterization of degradation in thin-film photovoltaic module performance parameters. Renew. Energy 28:1455–1469.

[6] Mendoza-Pérez R, Sastre-Hernández J, Contreras-Puente G, Vigil-Galán O, 2009. CdTe solar cell degradation studies with the use of CdS as the window material. Solar Energy Materials & Solar Cells 93:79–84.

[7] Muñoz-García M, Marin O, Alonso-García MC, Chenlo F, 2012. Characterization of thin film PV modules under standard test conditions: Results of indoor and outdoor measurements and the effects of sunlight exposure. Sol. Energy 86: 3049–3056.

[8] Virtuani A, Fanni L, 2014. Seasonal power fluctuations of amorphous siliconthin-film solar modules: distinguishing between different contributions. Prog. Photovoltaics Res. Appl. 22: 208-217.

[9] Kichou S, Silvestre S, Nofuentes G, Torres-Ramírez M, Chouder A, Guasch D, 2016. Characterization of degradation and evaluation of model parameters of amorphous silicon photovoltaic modules under outdoor long term exposure. Energy 96: 231-241.

[10] Kichou S, Abaslioglu E, Silvestre S, Nofuentes G, Torres-Ramírez M, Chouder A, 2016. Study of degradation and evaluation of model parameters of micromorph silicon photovoltaic modules under outdoor long term exposure in Jaén, Spain. Energy Conversion and Management 120:109–119.

[11] Staebler D, Wronski C, 1977. Reversible conductivity changes in discharge-produced amorphous Si. Appl Phys Lett 31(4):292-294.

[12] Van Dyk EE, Audouard A, Meyer EL, Woolard CD. Investigation of the degradationof a thin-film hydrogenated amorphous silicon photovoltaic module. Solar Energy Materials & Solar Cells 2007;91: 167-73.

[13] Yamawaki T, Mizukami S, Yamazaki A, Takahashi H, 1997. Thermal recovery effecton light-induced degradation of amorphous silicon solar module under thesunlight. Solar Energy Materials & Solar Cells 47:125-34.

[14] Green MA, Emery K, Hishikawa Y, Warta W and Dunlop ED, 2015. Solar cell efficiency tables (Version 45). Prog. Photovoltaics Res. Appl. 23:1–9.

[15] Romeo N, Bosio A, Tedeschi R, Canevari V, 2000. Back contacts to CSS CdS/CdTe solar cells and stability of performances. Thin Solid Films 361–362: 327–329.

[16] Mendoza-Pérez R, Sastre-Hernández J, Contreras-Puente, G and Vigil-Galán O, 2009. CdTe solar cell degradation studies with the use of CdS as the window material. Solar Energy Materials & Solar Cells 93(1): 79-84.

[17] Shah A, Torres P, Tscharner R, Wyrsch N, Keppner H, 1999;.Photovoltaic technology: the case for thin-film solar cells. Science 285(5428): 692-698.

[18] Martínez-Moreno F, Lorenzo E, Muñoz J, Moretón R, 2012. On the testing of large PV arrays. Prog. Photovoltaics Res. Appl. 20:100–5.

[19] Nofuentes G, Aguilera J, Santiago RL, De La Casa J, Hontoria L. 2006; A reference-module-based procedure for outdoor estimation of crystalline silicon PV module peak power. Prog Photovoltaics Res Appl. 14: 77–87.

[20] IEC 60904-9 (Ed. 2.0), Photovoltaic devices - Part 9: Solar simulator performance requirements. Geneva, 2007.

[21] Sharma V, Sastry OS, Kumar A, Bora B, Chandel SS, 2014. Degradation analysis of a-Si, (HIT) hetro-junction intrinsic thin layer silicon and m-C-Si solar photovoltaic technologies under outdoor conditions. Energy 72:536-546.

[22] Hussin MZ, Shaari S, Omar AM, Zain ZM, 2015. Amorphous silicon thin-film: behaviour of light-induced degradation. Renew Sustain Energy Rev 43:388–402.

[23] Cañete C, Carretero J and Sidrach-de-Cardona M, 2014. Energy performance of different photovoltaic module technologies under outdoor conditions. Energy 65: Pages 295–302.

[24] Kichou S, Silvestre S, Nofuentes G, Torres-Ramírez M, Chouder A, Guasch D, 2016. Behavioral data of thin-film single junction amorphous silicon (a-Si) photovoltaic modules under outdoor long term exposure. Data in Brief 7; 366-371.

[25] Ishii T, Otani K, Takashima T and Ikeda K, 2014. Change in I–V characteristics of thin-film photovoltaic (PV) modules induced by light soaking and thermal annealing effects. Prog. Photovoltaics Res. Appl. 22:949–957.

[26] Carlson DE. 2003. Monolithic amorphous silicon alloy solar modules. Solar Energy Materials & Solar Cells 78: 627–645.

[27] Rüther R, Del Cueto J, Tamizh-Mani G, Montenegro A A, Rummel S, Anderberg A, & Von Roedern B. (2008, May). Performance test of amorphous silicon modules in different climates-year four: Progress in understanding exposure history stabilization effects. In Photovoltaic Specialists Conference, 2008. PVSC'08. 33rd IEEE (pp. 1-5). IEEE.

[28] De la Parra Í, Garcia MA, Marcos J & Marroyo L. (2013, September). A comparative study of degradation and performance of thin film photovoltaic generators versus a multi-crystalline generator. In Energy Conversion Congress and Exposition (ECCE), 2013 IEEE, pp. 4511-4517.

[29] Deibel C, Dyakonov V, Parisi J, Palm J, Zweigart S, Karg F, 2002. Influence of damp heat testing on the electrical characteristics of Cu (In, Ga) (S, Se) 2 solar cells. Thin Solid Films 404: 325–330.

[30] Ullal HS, Zwelbel K & Von Roedern B. (1997, September). Current status of polycrystalline thin-film PV technologies. In Photovoltaic Specialists Conference, 1997, Conference Record of the Twenty-Sixth IEEE (pp. 301-305). IEEE.

[31] Del Cueto JA, Rummel S, Kroposki B, Osterwald C, & Anderberg A. (2008, May). Stability of CIS/CIGS modules at the outdoor test facility over two decades. In Photovoltaic Specialists Conference, 2008. PVSC'08. 33rd IEEE (pp. 1-6). IEEE.

[32] Phinikarides A, Kindyni N, Makrides G, Georghiou GE, 2014. Review of photovoltaic degradation rate methodologies. Renew. Sustain. Energy Rev. 40: 143–152.

[33] Pramod Rajput, G.N. Tiwari, O.S. Sastry, Birinchi Bora, Vikrant Sharma, 2016. Degradation of mono-crystalline photovoltaic modules after 22 years of outdoor exposure in the composite climate of India. Solar Energy 134:32–44.

[34] Pierro M., Bucci F., and Cornaro C. 2015. Full characterization of PV modules in real operating conditions: theoretical model, measurement method and results. Progress in Photovoltaics: Research and Applications Vol. 23, 4: 443-461.

[35] Carlsson T and Brinkman A, 2006. Identification of Degradation Mechanisms in Field-tested CdTe Modules. Prog. Photovoltaics Res. Appl. 14:213–224

[36] Pierro M., Bucci F., and Cornaro C. 2015. Impact of light soaking and thermal annealing on amorphous silicon thin film performance. Progress in Photovoltaics: Research and Applications Vol.23, 11:1581-1596.

[37] Niccolò Aste, Claudio Del Pero, Fabrizio Leonforte, 2014. PV technologies performance comparison in temperate climates. Solar Energy 109: 1-10.

[38] Jardine C, Betts T, Gottschalg R, Infield DG, Lane K. Influence of spectral effects on the performance of multijunction amorphous silicon cells. In: Proc of PV in Europe - From PV Technology to Energy Solutions, Rome, Italy 2002.

[39] Minemoto T, Nakada Y, Takahashi H, Takakura H. Uniqueness Verification of Solar Spectrum Index of Average Photon Energy for Evaluating Outdoor Performance of Photovoltaic Modules. Sol Energy 2009;83(8):1294–99.

[40] Norton M, Gracia Amillo AM, Galleano R. Comparison of Solar Spectral Irradiance Measurements Using the Average Photon Energy Parameter. Sol Energy 2015;120: 337–44.

4. Results and discussion

This chapter details main results obtained that have been presented in the published works related to modelling, parameters extraction techniques, fault detection and study of degradation of several TFPV modules/arrays. The findings obtained through the procedures previously described in the methodology chapter are exposed and discussed.

4.1. PV modelling

Regarding the PV models used in the present work, the implementation of the PV models in MATLAB/Simulink presents good results in simulating and forecasting the behaviour of the PV systems in real conditions of work.

Several PV systems with different PV modules technologies were simulated using the SAPM and the one-diode (five-parameter) PV models. Both PV models showed good performance in reproducing the real behaviour of the PV systems in different conditions of work [1–5].

In despite of the weather conditions, PV system configuration and PV modules technology, a good agreement between the real measured data and the SAPM predicted data was always found. Where, DC-output power RMSE values below the 6% were reported in the published works [1,3]. However, as the SAPM is an empirical model, it allows simulating just the outputs of the PV cell/module, moreover, the information provided by this model concerning the solar cell has no physical meaning.

Contrariwise to the SAPM, the one-diode (five-parameter) model simulates not only the outputs of the solar cell but also permits understanding the physical behaviour of the solar cell reflected by the values of the five model parameters (I_{ph}, I_o, n, R_s and R_{sh}). The one-diode model

presents a good trade-off between complexity and accuracy. The model performed well in simulating and predicting the outputs of grid-connected PV systems including different types of PV module technologies [1,4,5]. Depending on the estimation method of its model parameters, DC-output power RMSE values obtained including the case of worst weather conditions are below the 13%, otherwise, the RMSE values obtained for clear sky days doesn't exceed 3% [1].

4.2. Parameter extraction

The accuracy of the PV cell models in reproducing the real behaviour of the PV systems strongly depends on the estimation of the model parameter values.

The parameter extraction methods based on the algorithms described in section 2.3 were used in the simulation of three grid-connected PV systems of different PV cell technologies, and the obtained results were experimentally validated with real measured data [1].

From the published works [1,4,5], it can be seen that the efficiency and the performance of the PV cell models changes from an algorithm to another one. Moreover, the metaheuristic algorithms (GA, PSO, DE and ABC) provide better results than the numerical algorithms based on LMA especially in worst weather conditions. Moreover, the shortcoming present in the numerical method based on LMA related to the importance choice of the initial conditions is avoided in the bio-inspired algorithms. The comparison of the five algorithms used for the estimation of the PV models parameters published in [1] offers a clear idea about how the algorithms perform under different weather conditions. Where, from the obtained results it can be seen that the ABC algorithm provides the best accuracy in the simulation results.

The PV models parameters were extracted from the measured data of the dynamic response of the PV systems in real conditions of work. However, in order to see how these techniques perform in static behaviour, Fig. 4.2.1 illustrates a comparison between measured data and result obtained by applying these algorithms for the extraction of the one-diode PV model parameters from a measured I-V characteristic of an ISOFOTON 106/12 PV modules.

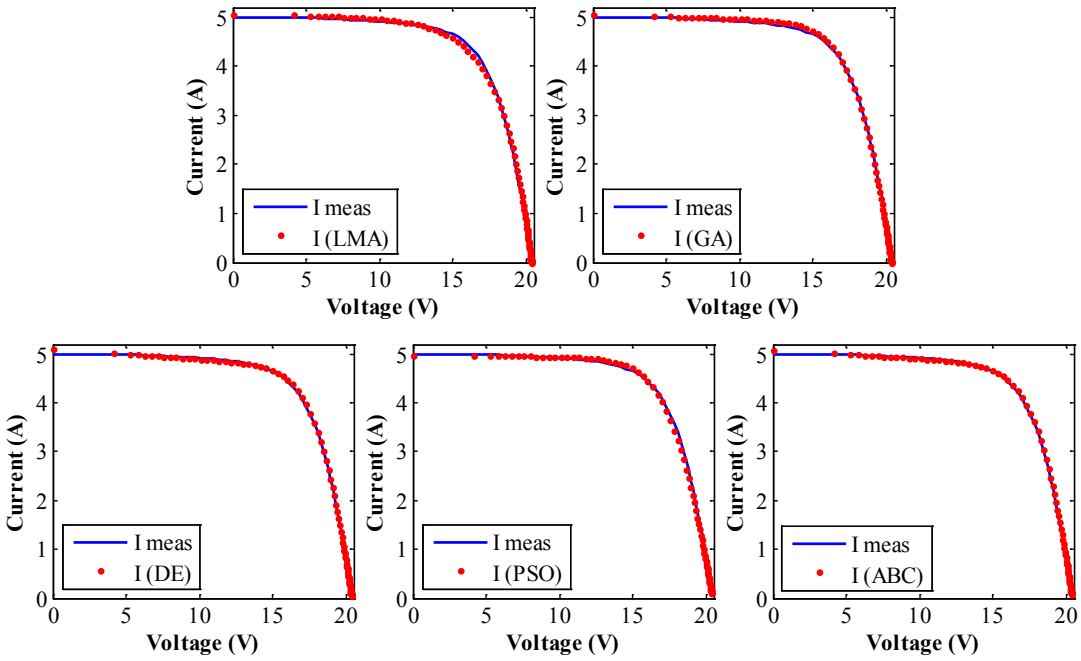

Figure 4.2. 1 Simulation of the I-V curve using the one-diode PV model based on five different algorithms.

As it can be seen from Fig. 4.2.1, the I-V curves simulated by the one-diode model based on the five algorithms are in accordance with the real measured data. The five algorithms perform well in the estimation of the one-diode model parameters. The calculated RMSE values between measured and simulated I-V curve listed in Table 4.2.1 confirm that the metaheuristic algorithms are more accurate than the LMA, and once again, the ABC algorithms is the most accurate.

Table 4.2. 1 RMSE values using one-diode model based on five different algorithms.

	LMA	GA	DE	PSO	ABC
RMSE (A)	0,0421	0,0336	0,0304	0,0321	0,0271
RMSE (%)	0,84	0,67	0,60	0,64	0,54

4.3. OPC monitoring and fault detection procedure

The fault detection procedure relied on the current and voltage indicators provided good performance in detecting and identifying main faults present in the DC-side of the PV systems. From the results obtained in the works [2,3], it can be seen that the procedure is able to detect several faults related to shadows, inverter disconnection, faulty strings and bypassed PV modules.

The enhancement of the method allows it to provide an equivalent number of bypassed PV modules and faulty strings. Moreover, for each detected fault the equivalent power losses are quantified.

The procedure was experimentally validated in three grid-connected PV systems having different sizes, topologies, locations and based on different PV modules technologies [2,3].

As an application, the fault detection method presented in this thesis was successfully integrated in a platform based on OPC used for remote supervision and diagnosis of a grid-connected PV system.

From the obtained results [3], it can be seen that, the fault detection method performs well on OPC platforms for the detection and the identification of failures occurred in the PV system under study. Moreover, the reliability of the monitored data by means of OPC standard is confirmed by the accordance between predicted yields and measured ones given in [3].

4.4. Degradation study

The study of the degradation of TFPV modules has been carried out using the two different techniques described previously in the methodology chapter.

The evolution of the effective peak power along the monitoring period allows calculating the degradation rate. Moreover, the stabilization period is estimated form the data obtained from the narrow filters carried out on the solar irradiance and cell temperature.

The power-irradiance technique is added as a second method permitting the estimation of the stabilization period. The method is based on the plot of the monthly gradients obtained from the plots of the DC-output power in function of on-plane solar irradiance.

The two techniques were applied for the study of degradation of several types of TFPV technologies. The degradation of two PV arrays situated in Jaén (Spain) based on a-Si:H and micromorph PV modules respectively, and four TFPV modules (a-Si:H, micromorph, CdTe and CIS) situated in Madrid (Spain) were studied in the published works [4–6].

4.4.1. Amorphous PV modules (a-Si:H)

Regarding the a-Si:H PV module/array, the study of degradation carried out in [4,6] illustrates un important initial decrease of the performance of the module/array after the first

months of exposure under outdoor conditions. This initial strong decrease of the output power generated by the PV modules is due to the light induced degradation (LID) phenomenon known also as Staebler-Wronski Effect (SWE) [7]. The amount of LID phenomenon depends on the distribution of light and temperature at the specific location of the PV module/array.

After the first initial decrease of the performances, the variation of the DC-output power follows the climatic seasonal changes. The initial decrease in output power is followed by an increase over the summer months, a decrease over winter months and once again an increase over summer months. As the PV modules are based on amorphous solar cells, the regeneration of the performance in summer months can be assigned to light-induced annealing [8], spectral effects [9] and to the thermal regeneration [10,11].

The obtained results in the study of degradation of an a-Si:H PV array published in [4] and the study of degradation of an a-Si:H PV module published in [6] provide degradation rate values, $R_{D,}$ in the range of -2.28%/year -2.30%/year. The obtained values for the R_D are in the range of previous results presented in the literature for a-Si:H PV modules [12,13]. The highest degradation rates have been reported in Korea and in the Mediterranean region [12].

The stabilization period of PV array was observed to start after 16 months of operation in Jaen (Spain), after a total degradation of 18.80% of the DC-output power [4]. From the study of degradation of one amorphous PV module deployed under the climate of Madrid, after a total reduction of 18.26% of the DC-output power, a stabilization period of 24 months is found [6]. The discrepancy between the two stabilization periods is due to the climate conditions which are different in Madrid and Jaén. In previous works reported in the literature, a stabilization period of 16 months was obtained for a-Si:H PV modules working under Equatorial climate [14].

After the stabilisation period, the effect of the seasonal variations could be observed from the trend of the generated DC-output power. Indeed, it can be observed that the variations between summer and winter are around ±5% of the stabilisation value [4,6].

4.4.2. Micromorph PV modules (a-Si:H/µc-Si:H)

An initial important decrease in the performance of micromorph PV module/array was also observed in the published works [5,6]. After that, the trend of the generated DC-output power of the micromorph PV modules follows the seasonal variations; the generated DC-output power increases over the summer months and decreases over the winter months.

As the micromorph solar cell contain an amorphous layer, the important initial decrease of the performance is attributed to the LID phenomenon, and the regeneration of the performance over the summer months can be assigned to light-induced annealing [8], spectral effects [9] and to the thermal regeneration [10,11].

A degradation rate, $R_{D,}$ of -2.20%/year is found in the published paper [5] related to the study of degradation of a micromorph PV system sited in Jaén. This R_D value corresponds also with the result obtained in the degradation analysis of a single micromorph PV module deployed in Madrid [6].

The stabilisation period of the micromorph PV modules is observed to start after four months of operation under outdoor conditions. This stabilization period occurs after a total DC-output power reduction of 16.66% (case of the PV array situated in Jaén) and 17.4% (case of PV module situated in Madrid).

The effect of seasonal oscillations remains after the stabilization period with variations about of ±3.18% (case of the PV array situated in Jaén) and ±3.7% (case of PV module situated in Madrid) from the stabilized level of DC-output power. Comparing with the a-Si:H PV module, the LID phenomenon and the seasonal variation are less significant due to the effect of the μc-Si:H layer.

4.4.3. Cadmium telluride PV module (CdTe)

The study of degradation of CdTe PV module carried out in [6], demonstrates a continue decrease of the performance of the CdTe PV module along the exposure period under the climate of Madrid. Moreover, it is found that the CdTe PV module presents the highest degradation rate value: R_D = -4.55%/year compared to the other TFPV cells technologies. Previous works available in the literature report R_D values of -1.5%/year and -3.5%/year by using the same linear regression method adopted in this thesis [12,15].

The evolution of the DC-output power generated by the CdTe PV module shows a strong steady decrease during the first two years of exposure under outdoor conditions. The output power degraded of around 21.9% in two years and a half. After a period of 30 months, the degradation of the CdTe PV module is very slight and the stabilization can be observed in the trend of the output power generated by the PV module.

A significant decrease in the performance of CdTe PV modules is also reported in [16], where the CdTe PV modules degraded of around 13% in a period of 18 months. Several studies were performed on the degradation of CdTe PV modules, and conclude that the efficiency and long term stability of CdTe solar cells presents a strong dependence on the materials used for the back contact [17–21].

The stabilization period of the DC-output power for the CdTe PV module can be estimated to occur after a 32 months of operation under the climate of Madrid [6]. However, a slight seasonal variation can still be observed, but it remains below the ±2% of the stabilized DC-output power.

4.4.4. Copper indium diselenide PV module (CIS)

Finally, the evolution of the performance of a CIS PV module under outdoor long term exposure was reported in [6]. The generated output power experiences a much slighter degradation in comparison to the TFPV modules presented above. Several works presented in the literature confirm the stability of CIS PV modules when deployed outdoor [22–24].

The degradation rate, R_D, obtained in [6] for the CIS PV module is of 1.04%/year under Madrid climate. Previous works carried out in different locations provide R_D values of -0.5%/year [15] and -2.72%/year [12].

Moreover, a slight seasonal variation can also be observed in the trend of the DC-output power generated by CIS PV modules [6]. Where, the DC-output power decreases with the increase of temperature and vice versa, and this can be explained by the relative high value of the temperature coefficient of power of the CIS PV module.

4.5. Evolution of solar cell model parameters

Furthermore, parameter extraction techniques allow analysing the evolution of the PV module/solar cell model parameters in real working conditions. Results obtained for a-Si:H PV modules allow to a better understanding of the physical effects related to the degradation of this PV modules when exposed outdoor.

The five parameters of the one-diode model have been extracted from the dynamic response of two PV generators based on a-Si:H and micromorph PV modules respectively, and evaluated along the monitoring campaign.

From the results obtained published in [4,5], it can be seen that, the evolution of the extracted model parameters reflects the degradation of the PV modules under outdoor exposure period.

The evolutions of the diode ideality factor, n, along the monitoring campaign obtained for both PV generators show a decrease over the summer months and an increase over the winter months following the seasonal changes. Where, in summer months, it can be seen that there is an improvement in the material characteristics especially in the amorphous layer, caused by the higher temperatures reached by the solar cells. This improvement is due to an increase in charge carrier lifetime and a reduction in bandgap [8,25], that's why the values of n are reduced. On the other hand, in winter months, the extracted values of the diode ideality factor n are increased due to the increase of the recombination current [25].

The variation obtained for the saturation current I_o shows an opposite trend to the variation of n. The higher temperatures in summer period decrease the bandgap resulting in a decrease in open-circuit voltage [12,25]. Temperature has also a strong effect on the variation of the saturation current as shown in Eq. (*2.2*-11). The combination of bandgap reduction and strong increase of temperature in summer periods along with the increase in short-circuit current due to LID effect lead to an increase of the saturation current despite the reduction of recombination effects in summer.

The evolution of the short-circuit current I_{sc} shows a continuing decrease until reach the stabilization period. After that it shows a more stable trend following the seasonal changes. The improvement in output current during summer time is due to the effect of solar spectral irradiance and to the thermal-recovery of the LID affecting the TF amorphous layer [9,13]. The lower temperatures in winter also reduce the thermal recovery rate for the a-Si:H solar cells and the amorphous layer of the micromorph cells. The decrease of I_{sc} values in the worst winter months for the micromorph PV modules is very small compared to the reduction observed on a-Si:H PV modules, and this is thanks to the micro-crystalline (µc-Si:H) layer present in the micromorph PV cell.

A decrease of the shunt resistance value, $R_{sh,}$ was reported in [4,5]. The reduction of R_{sh} in TF solar cells under outdoor exposure for long time was previously reported [25,26]. Moreover, the evolution of R_{sh} follows the same seasonal trend that the evolution of the output power of the PV array and I_{sc} as expected.

Finally, the evolution of the series resistance, $R_{s,}$ shows an increase of its value according to the degradation of the PV modules [4,5]. The seasonal effect is observed again in the trend of R_s that presents higher values in winter and reduced values in summer months. The lower values of R_s obtained in summer months are due to the regeneration of the performance caused by temperature effects.

References

[1] Kichou S, Silvestre S, Guglielminotti L, Mora-López L, Muñoz-Cerón E. Comparison of two PV array models for the simulation of PV systems using five different algorithms for the parameters identification. Renew Energy 2016;99:270–9. doi:10.1016/j.renene.2016.07.002.

[2] Silvestre S, Kichou S, Chouder A, Nofuentes G, Karatepe E. Analysis of current and voltage indicators in grid connected PV (photovoltaic) systems working in faulty and partial shading conditions. Energy 2015;86:42–50. doi:10.1016/j.energy.2015.03.123.

[3] Silvestre S, Mora-López L, Kichou S, Sánchez-Pacheco F, Dominguez-Pumar M. Remote supervision and fault detection on OPC monitored PV systems. Sol Energy 2016;137:424–33. doi:10.1016/j.solener.2016.08.030.

[4] Kichou S, Silvestre S, Nofuentes G, Torres-Ramírez M, Chouder A, Guasch D. Characterization of degradation and evaluation of model parameters of amorphous silicon photovoltaic modules under outdoor long term exposure. Energy 2016;96:231–41. doi:10.1016/j.energy.2015.12.054.

[5] Kichou S, Elif A, Silvestre S, Nofuentes G, Torres-Ramírez M, Chouder A. Study of degradation and evaluation of model parameters of micromorph silicon photovoltaic modules under outdoor long term exposure in Jaén, Spain. Energy Convers Manag 2016;120:109–19. doi:10.1016/j.enconman.2016.04.093.

[6] Silvestre S, Kichou S, Guglielminotti L, Nofuentes G, Alonso-Abella M. Degradation analysis of thin film photovoltaic modules under outdoor long term exposure in Spanish continental climate conditions. Sol Energy 2016;139:599–607. doi:10.1016/j.solener.2016.10.030.

[7] Staebler DL, Wronski CR. Reversible conductivity changes in discharge-produced amorphous Si. Appl Phys Lett 1977;31:292. doi:10.1063/1.89674.

[8] Meyer EL, van Dyk EE. Characterization of degradation in thin-film photovoltaic module performance parameters. Renew Energy 2003;28:1455–69. doi:10.1016/S0960-1481(02)00062-9.

[9] Carlson DE. Monolithic amorphous silicon alloy solar modules. Sol Energy Mater Sol Cells 2003;78:627–45. doi:10.1016/S0927-0248(02)00455-5.

[10] Yamawaki T, Mizukami S, Yamazaki A, Takahashi H. Thermal recovery effect on light-induced degradation of amorphous silicon solar module under the sunlight. Sol Energy Mater Sol Cells 1997;47:125–34. doi:10.1016/S0927-0248(97)00033-0.

[11] Ruther R, Del Cueto J, Tamizh-Mani G, Montenegro A. A., Rummel S, Anderberg A., et al. Performance test of amorphous silicon modules in different climates - Year four: Progress in understanding exposure history stabilization effects. Conf Rec IEEE Photovolt Spec Conf 2008. doi:10.1109/PVSC.2008.4922773.

[12] Phinikarides A, Kindyni N, Makrides G, Georghiou GE. Review of photovoltaic degradation rate methodologies. Renew Sustain Energy Rev 2014;40:143–52. doi:10.1016/j.rser.2014.07.155.

[13] Tripathi B, Yadav P, Rathod S, Kumar M. Performance analysis and comparison of two silicon material based photovoltaic technologies under actual climatic conditions in Western India. Energy Convers Manag 2014;80:97–102. doi:10.1016/j.enconman.2014.01.013.

[14] Hussin MZ, Shaari S, Omar AM, Zain ZM. Amorphous silicon thin-film: Behaviour of light-induced degradation. Renew Sustain Energy Rev 2015;43:388–402. doi:10.1016/j.rser.2014.10.093.

[15] Jordan DC, Kurtz SR. Photovoltaic degradation rates - An Analytical Review. Prog Photovoltaics Res Appl 2013;21:12–29. doi:10.1002/pip.1182.

[16] Carlsson T, Brinkman A. Identification of degradation mechanisms in CdTe modules. Prog Photovoltaics Res … 2006;14:213–24.

[17] Hegedus SS, McCandless BE, Birkmire RW. Analysis of stress-induced degradation in CdS/CdTe solar cells. Conf Rec IEEE Photovolt Spec Conf 2000;2000–Janua:535–8. doi:10.1109/PVSC.2000.915891.

[18] Compaan AD, Sites J, Birkmire R, Ferekides C, Fahrenbruch AL. Critical Issues and Research needs for CdTe-based Solar Cells. Renew Energy 1999.

[19] Ross M, Rich G, Petacci L, Klammer J, Llc FS. IMPROVEMENT IN RELIABILITY AND ENERGY YIELD PREDICTION OF THIN-FILM CdS / CdTe PV MODULES 2006:2148–51.

[20] Marion B, del Cueto JA, McNutt P, Rose D. Performance Summary for the First Solar CdTe 1 kW System 2001:1–4.

[21] Harju R, Karpov VG, Grecu D, Dorer G. Electron-beam induced degradation in CdTe photovoltaics. J Appl Phys 2000;88:1794–801. doi:10.1063/1.1305857.

[22] Deibel C, Dyakonov V, Parisi J, Palm J, Zweigart S, Karg F. Influence of damp heat testing on the electrical characteristics of Cu (In , Ga)(S , Se) 2 solar cells. Thin Solid Films 2002;404:325–30.

[23] Ullal HS, Zwelbel K, Roedern B Von. Current status of polycrystalline thin-film PV technologies. Conf Rec Twenty Sixth IEEE Photovolt Spec Conf - 1997 1997:0–4. doi:10.1109/PVSC.1997.654089.

[24] del Cueto JA, Rummel S, Kroposki B, Osterwald C, Anderberg A. Stability of CIS / CIGS Modules at the Outdoor Test Facility over Two Decades Preprint. Photovolt Spec Conf 2008 PVSC '08 33rd IEEE 2008:1–6. doi:10.1109/PVSC.2008.4922772.

[25] Radue C, van Dyk EE. A comparison of degradation in three amorphous silicon PV module technologies. Sol Energy Mater Sol Cells 2010;94:617–22. doi:10.1016/j.solmat.2009.12.009.

[26] van Dyk EE, Meyer EL. Analysis of the effect of parasitic resistances on the performance of photovoltaic modules. Renew Energy 2004;29:333–44. doi:10.1016/S0960-1481(03)00250-7.

5. Conclusions

The overall objectives of the present thesis planted in the introduction related to supervision and diagnosis of photovoltaic systems, modelling of the PV system components and the study of degradation of different thin film PV (TFPV) modules were achieved in the published works carried out during the investigation period.

Two PV module/array models have been used in the present thesis for simulation purposes: The one-diode (five-parameter) PV model and the Sandia Array Performance Model (SAPM). These models were used to reproduce the behaviour of grid-connected PV systems of different topologies and solar cell technologies.

The SAPM model demonstrated a high accuracy degree in the simulation of the PV systems behaviour independently of the PV module technology. On the other hand, the SAPM model is an empirical model including a set of model parameters in which some of them have little physical meaning.

The one-diode model allowed simulating the dynamic behaviour of several PV systems of different solar cell technologies with an acceptable accuracy degree for applications of supervision and forecasting of energy production. In addition, the advantage of the one-diode model is the physical meaning of the set of model parameters that provides relevant information about the PV module/array and allows an easy comparison between different PV modules.

The accuracy of the PV cell models in reproducing the real behaviour of the PV systems depends strongly on the estimation of the model parameter values. From the comparison of different algorithms, it can be seen that the metaheuristic algorithms are more efficient than the numerical LMA algorithm in estimating the unknown parameters of both PV module models, essentially in worst weather conditions. The GA is less accurate compared to the other bio-

inspired algorithms. The ABC algorithm provides the best results and it is slightly more accurate than the DE and PSO algorithms.

Both PV models performed well when used in the automatic fault detection procedure and the prediction of the outputs of grid-connected PV systems.

The fault detection procedure used for the diagnosis of PV systems is based on the analysis of the current and voltage indicators evaluated also from monitored data and expected values of current and voltage obtained from the model of the PV generator.

An experimental validation of the proposed procedure is shown in the study of three grid-connected PV systems having different sizes, topologies, and different solar cell technologies. From the obtained results it can be seen that, main faults as short-circuited PV modules, bypassed strings, inverter disconnection and partial shading could be detected in real time by the evaluation of the current and voltage indicators. Moreover, an equivalent number of faulty strings and bypassed PV modules as well as the amount of power losses can be estimated from the values of both indicators. Furthermore, the obtained results show that the integration of the fault detection procedure in an OPC platform is effective and offers a powerful tool in the field of remote supervision and control of PV systems connected to the grid.

The study of degradation of TFPV modules/arrays corresponding to four different technologies (a-Si:H, micromorph, CdTe and CIS) was addressed in this thesis. The degradation study was carried out on PV modules/arrays deployed outdoor for long term exposure in dry and sunny inland sites (Jaén and Madrid) with a Continental-Mediterranean Climate.

The values of degradation rates, R_D, were evaluated by linear regression from the evolution of the modules effective peak power. The stabilization periods were assessed by observing the evolution of the filtered DC-output power, and through the power-irradiance technique. The obtained values of degradation rates, R_D, for all the technologies are in the range of previous studies available in the literature except for the CdTe PV module which presented a higher R_D value than expected.

In both a-Si:H and micromorph technologies, a strong degradation is observed during the first months of outdoor exposure under a Continental-Mediterranean Climate, where the DC-output power of the PV module/array drops by around 10% from the initial value. This strong initial decrease of the generated power is not observed in the case of CdTe PV module, however, the trend of its DC-output power presents a steadily decrease for a very long period of 32

months. The CIS PV module is found to be the most stable, presenting the lowest value of R_D and power losses.

The instability of a-Si:H and micromorph PV modules is mainly due to the amorphous layer. In the micromorph TFPV module, the amorphous layer is significantly thinner than in the a-Si:H module. This fact, together with the presence of the more stable μc-Si:H substrate, allows the micromorph module to have a significantly shorter stabilization period than that of the a-Si:H PV module. Moreover, for the micromorph PV module/array, the effect of seasonal variations remains after the stabilization period with variations about 3% from the stabilized value of DC-output power. These seasonal oscillations are lower than those observed in the behaviour of a-Si:H PV module/array (seasonal variation of 5%) thanks to the effect of the μc-Si:H layer present in the micromorph TFPV modules.

As a summary, the CIS PV module was found to be the most stable compared to the other technologies, when deployed under long term outdoor exposure in a dry and sunny inland site with a Continental-Mediterranean Climate. The a-Si:H and micromorph PV modules also perform quite well, showing degradation rates and stabilization periods similar to the expectations. However, their performances appear to be lower than what stated in the manufacturer datasheets, especially regarding the values of stabilized power which are decreased by 18% from the initial values. Lastly, the CdTe module shows poor performances, with high degradation rate, long stabilization period of 32 months and the total drop of the output power is of 25% below the datasheet value.

Finally, the parameter extraction technique based on LMA is also addressed in the study of degradation of TFPV modules. The parameter extraction technique is able to evaluate the temporal evolution of main solar cell model parameters and helps to understand the evolution of the entire system at PV cell/module level. The seasonal variation effect was also observed in the evolution of the model parameters. The evolution of each one of the model parameters along the scrutiny period has been analysed and allows achieving a better understanding of the performance changes of the PV modules and the evolution of the output power of the PV array.